GDAŃSK UNIVERSITY OF TECHNOLOGY

The author of the doctoral dissertation: Iga Szpunar
Scientific discipline: Material Science

DOCTORAL DISSERTATION

Title of doctoral dissertation: The lanthanide influence on selected properties of $BaLnCo_2O_{6-\delta}$

Title of doctoral dissertation (in Polish): Wpływ lantanowca na wybrane właściwości $BaLnCo_2O_{6-\delta}$

Supervisor signature	Auxiliary supervisor signature
dr hab. inż. Aleksandra Mielewczyk-Gryń	dr inż. Sebastian Wachowski

Gdańsk, year 2022

GDAŃSK UNIVERSITY OF TECHNOLOGY

STATEMENT

The author of the doctoral dissertation: Iga Szpunar

I, the undersigned, declare that I am aware that in accordance with the provisions of Art. 27 (1) and (2) of the Act of 4th February 1994 on Copyright and Related Rights (Journal of Laws of 2021, item 1062), the university may use my doctoral dissertation entitled:
Xxx
for scientific or didactic purposes[1].

Gdańsk, 22.08.2022 ……..

Signature of the PhD student

Aware of criminal liability for violations of the Act of 4th February 1994 on Copyright and Related Rights and disciplinary actions set out in the Law on Higher Education and Science(Journal of Laws 2021, item 478),3as well as civil liability, I declare, that the submitted doctoral dissertation is my own work.

I declare, that the submitted doctoral dissertation is my own work performed under and in cooperation with the supervision of dr hab. inż. Aleksandra Mielewczyk-Gryń, and the auxiliary supervision of dr inż. Sebastian Wachowski.

This submitted doctoral dissertation has never before been the basis of an official procedure associated with the awarding of a PhD degree.

All the information contained in the above thesis which is derived from written and electronic sources is documented in a list of relevant literature in accordance with Art. 34 of the Copyright and Related Rights Act.

I confirm that this doctoral dissertation is identical to the attached electronic version.

Gdańsk, 22.08.2022 ……..

Signature of the PhD student

I, the undersigned, agree to include an electronic version of the above doctoral dissertation in the open, institutional, digital repository of Gdańsk University of Technology.

Gdańsk, 22.08.2022 ……..

Signature of the PhD student

[1] Art 27. 1. Educational institutions and entities referred to in art. 7 sec. 1 points 1, 2 and 4–8 of the Act of 20 July 2018 – Law on Higher Education and Science, may use the disseminated works in the original and in translation for the purposes of illustrating the content provided for didactic purposes or in order to conduct research activities, and to reproduce for this purpose disseminated minor works or fragments of larger works. 2. If the works are made available to the public in such a way that everyone can have access to them at the place and time selected by them, as referred to in para. 1, is allowed only for a limited group of people learning, teaching or conducting research, identified by the entities listed in paragraph 1.

GDAŃSK UNIVERSITY OF TECHNOLOGY

DESCRIPTION OF DOCTORAL DISSERTATION

The Author of the doctoral dissertation: Iga Szpunar

Title of doctoral dissertation: The lanthanide influence on selected properties of $BaLnCo_2O_{6-\delta}$

Title of doctoral dissertation in Polish: Wpływ lantanowca na wybrane właściwości $BaLnCo_2O_{6-\delta}$

Language of doctoral dissertation: English

Supervisor: dr hab. inż. Aleksandra Mielewczyk-Gryń

Auxiliary supervisor: dr inż. Sebastian Wachowski

Date of doctoral defense:

Keywords of doctoral dissertation in Polish: podwójne perowskity, kobaltyty, uwodnienie, ogniwa paliwowe

Keywords of doctoral dissertation in English: double perovskite**,** cobaltites, hydration, fuel cells

Summary of doctoral dissertation in Polish:

Przedmiotem badań niniejszej rozprawy są tlenki kobaltu o strukturze perowskitu, o wzorze ogólnym $BaLnCo_2O_{6-\delta}$, gdzie Ln to La, Pr, Nd, Sm, Gd, Tb, Dy. Celem pracy było zweryfikowanie zdolności tych materiałów do tworzenia defektów protonowych, a także zidentyfikowanie czynników warunkujących tę zdolność. W ramach pracy wytworzono oraz scharakteryzowano materiały z zaproponowanej grupy. W celu zweryfikowania postawionych hipotez badawczych wykorzystano następujące metody pomiarowe: proszkową dyfrakcję rentgenowską, dyfrakcję rentgenowską ze źródłem synchrotronowym, proszkową dyfrakcję neutronów, skaningową i transmisyjną mikroskopię elektronową, analizę termograwimetryczną, miareczkowanie jodometryczne oraz rentgenowską spektroskopię absorpcyjną. Wzrost masy w atmosferze zawierającej parę wodną, który może wskazywać na wbudowywanie się do struktury materiału defektów protonowych, zaobserwowano jedynie w $BaLaCo_2O_{6-\delta}$ i $BaGdCo_2O_{6-\delta}$. Wykazano również, że efekt ten nie jest związany z istnieniem lub powstawaniem faz obcych. Zauważono, że czynnikiem determinującym zdolność materiału do tworzenia defektów protonowych jest struktura elektronowa materiału, wynikająca z oddziaływania pomiędzy orbitalami 4f lantanowca, oraz 3d kobaltu i 2p tlenu.

Summary of doctoral dissertation in English:

The subject of research of this dissertation are cobalt oxides with a double perovskite structure with a general formula $BaLnCo_2O_{6-\delta}$, where Ln stands for La, Pr, Nd, Sm, Gd, Tb, Dy. The aim of the study was to verify the ability of these materials to form the protonic defects, as well as to identify the factors determining this ability. As part of the work, materials from the proposed group were synthesised and

characterized. To verify the research hypotheses the following techniques were used: powder x-ray diffraction, synchrotron radiation x-ray diffraction, powder neutron diffraction, scanning and transmission electron microscopy, thermogravimetry, iodometric titration, and x-ray absorption spectroscopy. The increase in mass in the atmosphere containing water vapour, which may indicate the incorporation of protonic defects into the material structure, was observed only in $BaLaCo_2O_{6-\delta}$ i $BaGdCo_2O_{6-\delta}$. It has also been shown that this effect is not related to the existence or formation of secondary phases. It was observed that the factor determining the material's ability to form the protonic defects is the electronic structure of the material, resulting from the interaction between the lanthanide 4f orbitals, and the 3d cobalt and 2p oxygen orbitals.

Lilianie

Żebyś zawsze miała odwagę spełniać marzenia

Acknowledgements

It is very difficult to express my gratitude to all of to all those who had an impact on the presented dissertation.

First of all, I would like to thank my supervisors: ***Professor Aleksandra Mielewczyk-Gryń*** *and* ***Dr. Sebastian Wachowski****, for all your help, guides, and inspiration. You both showed me how fascinating science can be, and helped me to overcome my chaos.*

The substantive contribution of ***Professor Maria Gazda*** *cannot be overestimated either. Professor, like no one else, is able to notice any inaccuracies, and her guidelines are always very accurate and extremely valuable.*

This work would never have been created without the joint efforts of the entire international team. At this point, I would like to thank my partners from Spain: ***Professor José Serra,*** *and* ***Dr. María Balaguer,*** *Norway:* ***Professor Truls Norby****, and* ***Dr. Magnus Sørby****. Essentially I would like to thank* ***Dr. Ragnar Strandbakke****, for the enormous number of ideas, many discussions and also for believing in me. I would always like to keep your enthusiasm.*

For the absolutely unique working atmosphere I would like to thank to ***Dr. Sebastian Wachowski*** *and* ***Dr. Tadeusz Miruszewski****.*

I would also like to thank all the members of our research group ***Dr. Wojciech Skubida, Dr. Kacper Dzierzgowski, Dr. Piotr Winiarz, mgr inż. Daniel Jaworski, mgr inż. Daria Balcerzak, mgr inż. Jagoda Budnik, mgr inż. Arkadiusz Dawczak, mgr inż. Francis Oseko,*** *and* ***mgr inż. Joanna Pośpiech.***

I would like to thank my friend ***Asia*** *for always being able to rely on you.*

Finally, I would like to thank my family, husband ***Krzysztof****, parents, sister, and brother. Without all of you, I wouldn't have gotten to this point.*

Special thanks go to my daughter ***Liliana****, thanks to you every day is better.*

The research has been supported by the National Science Centre Poland (2016/22/Z/ST5/00691), the Spanish Government (PCIN-2017-125), and the Research Council of Norway (Grant nº 272797 "GoPHy MiCO") through the M-ERA.NET Joint Call 2016.

The SR-PXD and NPD research were conducted with the assistance from the staff of the Swiss–Norwegian Beamline (SNBL), at the European Synchrotron Radiation Facility (ESRF), Grenoble, France. Dr Cheng Li is at POWGEN, SNS, Oak Ridge, US and Dr Chiu C. Tang at beamline I11 at Diamond, Didcot, UK.

The research was supported by CERIC-ERIC Consortium by the access to MCX beamline at Elettra Sinchrotrone Trieste and TEM at National Institute of Material Physics in Romania (proposal no 20187079). We also acknowledge Solaris National Radiation Centre Poland for access to the XAS/PEEM beamline (proposal no 181MS001).

Table of contents

Abstract

This dissertation presents the results of research on materials with a double perovskite structure with the general formula $BaLnCo_2O_{6-\delta}$, where the symbol Ln replaces the following rare earth metals: lanthanum, praseodymium, neodymium, samarium, gadolinium, terbium, and dysprosium. In the literature, there are reports on the protonic defect formation and protonic conductivity in those materials. So far, however, no consensus has been reached as to whether protonic defects actually arise in this group of materials. There are works that both provide evidence for their existence and contradict them. The main purpose of the study was to verify these reports, as well as to identify the factors determining the ability to incorporate water into the structure and the concentration of proton defects. As part of the work, two research hypotheses, presented in chapter 1, were formulated.

To verify the hypotheses the in-depth analysis of crystallographic structure that complements the knowledge available in the literature was carried out. The following diffraction methods were applied: powder x-ray diffraction, synchrotron radiation powder x-ray diffraction and neutron powder diffraction, supported with Rietveld refinement. The diffraction studies were supported with microscopy studies, including scanning and transmission electron microscopy. Oxygen nonstoichiometry at room temperature was determined by the means of iodometric titration, while thermogravimetry was used at elevated temperatures. Thermogravimetry was also used to screen the ability to incorporate water into the structure of the materials. X-ray absorption spectroscopy was used to investigate the electronic structure.

All investigated materials exhibit the ordering of A-site cations and oxygen vacancies, wherein the crystallographic parameters scale with the difference in ionic radii of barium and lanthanide. A similar relation was observed when determining the average oxidation state of cobalt and the oxygen content in the materials, which at room temperature increase with the ionic radius of the rare earth metal. Transmission electron microscopy provided direct evidence of the ordering of oxygen vacancies. As part of the dissertation, the chemical expansion coefficients of the investigated materials were determined, and due to the developed model of chemical expansion, it was possible to separate the effect from the reduction of cobalt and the formation of oxygen vacancies. Mass increase upon exposure to atmosphere containing water vapor was observed only in w $BaLaCo_2O_{6-\delta}$, $BaGdCo_2O_{6-\delta}$, and to a small extent in

$BaDyCo_2O_{6-\delta}$. Simultaneously, the relation to the existence or formation of secondary phases was eliminated. The ability to incorporate water was not correlated with any structural parameter or the concentration of oxygen vacancies. However, it was noticed that in barium lanthanum cobaltite the total mass increase under the humidified atmosphere is different in materials with an ordered and disordered A-site cations sublattice. This suggests a dependence of the protonic defects concentration on the degree of order and concentration of oxygen vacancies. The study of the electronic structure has shown that the density of unoccupied states at the O 2p level in materials exhibiting mass increase in humidified atmospheres is lower comparing to materials in which this increase was not observed. This suggests the dependence of the material's ability to form protonic defects on the electronic structure and the nature of the lanthanide species. Moreover, the proton defect modifies the electronic structure of the material.

The thesis has been divided into 6 parts. Chapter 1 presents the aim of the work and formulated research hypotheses. Chapter 2 contains a description of the current state of knowledge in the presented research topic. Chapter 3 covers the theoretical basis and technical parameters of the research techniques used. The results of the research are presented in Chapter 4. This chapter began with the results of structural studies, then the results of thermal and spectroscopic studies were presented. Chapter 5 presents a discussion of the obtained research results. Chapter 6 summarizes the thesis. The thesis also includes a list of symbols and abbreviations used, a list of figures and tables, as well as a list of references to literature. The dissertation was supplemented with three appendices, which presented a list of results not presented in chapter 4 (appendix 1), an analysis of the parameters describing the structure stability (appendix 2), and a methodology for the separation of oxidation and incorporation of water (appendix 3).

The presented dissertation is part of the project „Governing Principles in Hydration of Mixed Conducting Oxides" co-financed by the National Science Centre under contract no. UMO-2016/22 / Z / ST5 / 00691. This project was carried out under the M-ERA.NET Joint Call 2016 agreement in cooperation with the University of Oslo and the Institute for Energy Technology in Norway, as well as Consejo Superior de Investigaciones in Spain.

Streszczenie

Niniejsza rozprawa przedstawia wyniki badań materiałów o strukturze podwójnego perowskitu o wzorze ogólnym $BaLnCo_2O_{6-\delta}$, gdzie symbol *Ln* zastępuje następujące metale ziem rzadkich: lantan, prazeodym, neodym, samar, gadolin, terb, oraz dysproz. W literaturze napotkać można doniesienia o zdolności materiałów z tej grupy do tworzenia defektów protonowych w strukturze i przewodnictwa protonowego. Jak dotąd jednak, nie wypracowano konsensusu, co do tego, czy faktycznie defekty protonowe powstają w omawianej grupie materiałów. W literaturze znajdują się zarówno prace dostarczające dowodów na ich istnienie, jak również zaprzeczające im. Głównym celem pracy było zweryfikowanie tych doniesień, a także określenie czynników warunkujących zdolność do wbudowywania wody w strukturę oraz koncentrację defektów protonowych. W ramach pracy postawiono dwie hipotezy badawcze.

W celu zweryfikowania postawionych hipotez przeprowadzono dogłębną analizę struktury krystalicznej badanych materiałów, będącą uzupełnieniem wiedzy dostępnej w literaturze. Zastosowano kombinację następujących metod dyfrakcyjnych: proszkowej dyfrakcji rentgenowskiej, proszkowej dyfrakcji rentgenowskiej ze źródłem synchrotronowym, oraz proszkowej dyfrakcji neutronów, wraz z analizą Rietvelda. Wyniki badań dyfrakcyjnych zostały wsparte badaniami mikroskopowymi przy wykorzystaniu skaningowej i transmisyjnej mikroskopii elektronowej. Stechiometrię tlenową w temperaturze pokojowej wyznaczono za pomocą miareczkowania jodometrycznego, zaś w podwyższonych temperaturach w tym celu wykorzystano analizę termograwimetryczną. Metoda ta została wykorzystana również do zweryfikowania zdolności tworzenia defektów protonowych w badanych materiałach. Rentgenowską spektroskopię absorpcyjną zastosowano do zbadania struktury elektronowej.

We wszystkich badanych materiałach zaobserwowano porządkowanie kationów w podsieci A oraz porządkowanie wakansów tlenowych, przy czym właściwości strukturalne skalują się z różnicą promieni jonowych baru i lantanowca. Podobną zależność zaobserwowano przy wyznaczaniu średniego stopnia utlenienia kobaltu i zawartości tlenu w materiałach, które w temperaturze pokojowej rosną wraz z rozmiarem promienia jonowego metalu ziem rzadkich. Transmisyjna mikroskopia elektronowa dostarczyła bezpośrednich dowodów na porządkowanie wakansów tlenowych. W ramach rozprawy wyznaczono współczynniki rozszerzalności chemicznej badanych materiałów, a dzięki opracowanemu modelowi rozszerzalności chemicznej możliwe było odseparowanie wpływu od redukcji kobaltu i powstawania wakansu tlenowego. Wzrost masy w atmosferze zawierającej parę wodną

zaobserwowano jedynie w $BaLaCo_2O_{6-\delta}$, $BaGdCo_2O_{6-\delta}$, oraz w nieznacznym stopniu $BaDyCo_2O_{6-\delta}$. Jednocześnie wykluczono, aby było to związanie z istnieniem lub powstawaniem faz obcych. Zdolność do wbudowywania wody nie została skorelowana z żadnym parametrem strukturalnym, ani koncentracją wakansów tlenowych. Zauważono jednak, że w kobaltycie lantanowo barowym całkowity wzrost masy pod wpływem atmosfery zawierającej parę wodną jest różny w materiałach o uporządkowanej i nieuporządkowanej podsieci kationów A. Sugeruje to zależność koncentracji defektów protonowych od stopnia uprządkowania i koncentracji wakansów tlenowych. Badania struktury elektronowej wykazały, że gęstość nieobsadzonych stanów na poziomie O 2p w materiałach, w których zaobserwowano wzrost masy w atmosferach zawierających parę wodną, jest niższa w odniesieniu do materiałów, w których tego wzrostu nie obserwowano. Sugeruje to zależność zdolności materiału do tworzenia defektów protonowych od struktury elektronowej oraz natury lantanowca. Co więcej powstanie defektu protonowego modyfikuje strukturę elektronową materiału.

Rozprawę podzielono na 6 części. W rozdziale 1 przedstawiono cel pracy oraz postawiono hipotezy badawcze. Rozdział 2 zawiera opis dotychczasowego stanu wiedzy w prezentowanej tematyce badawczej. Rozdział 3 to podstawy teoretyczne i parametry techniczne wykorzystywanych technik badawczych. Wyniki prowadzonych badań przedstawiono w rozdziale 4. Rozdział ten rozpoczęto od wyników badań strukturalnych, następnie przedstawiono wyniki badań termicznych i spektroskopowych. W rozdziale 5 zaprezentowano dyskusję otrzymanych wyników badań. W rozdziale 6 przedstawiono podsumowanie rozprawy. Praca zawiera również zestawienie użytych symboli i oznaczeń, spis rysunków i tabel, a także spis odnośników do literatury. Rozprawę uzupełniono o trzy dodatki, w których zaprezentowano zestawienie wyników nieprzedstawionych w rozdziale 4 (appendix 1), analizę parametrów opisujących stabilność struktury (appendix 2), oraz metodologię separacji procesów utlenienia i wbudowywania wody (appendix 3).

Prezentowana rozprawa jest częścią projektu „*Podstawy zjawisk związanych z uwodnieniem tlenków o mieszanym przewodnictwie*” współfinansowanego ze środków Narodowego Centrum Nauki w ramach umowy nr. UMO-2016/22/Z/ST5/00691. Projekt ten realizowany był we współpracy Uniwersytetem w Oslo oraz Institut for Energy Technology w Norwegii, a także Consejo Superior de Investigaciones w Hiszpanii.

Glossary and Abbreviations

Abbreviations

AFC	alkaline fuel cell
CN	coordination number
BCZ	$BaCe_{1-x}Zr_xO_{3-\delta}$
BCZY	$Ba(Ce,Zr,Y)O_{3-\delta}$
BCZYYb	$Ba(Ce,Zr,Y,Yb)O_{3-\delta}$
BDC	$BaDyCo_2O_{6-\delta}$
BGC	$BaGdCo_2O_{6-\delta}$
BLC	$Ba_{0.5}La_{0.5}CoO_{3-\delta}$/ $BaLaCo_2O_{6-\delta}$
BNC	$BaNdCo_2O_{6-\delta}$
BPC	$BaPrCo_2O_{6-\delta}$
BSC	$BaSmCo_2O_{6-\delta}$
BSCF	$Ba_{1-x}Sr_xCo_{1-y}Fe_yO_{3-\delta}$
BTC	$BaTbCo_2O_{6-\delta}$
EDS	energy dispersive x-ray spectroscopy
EELS	electron Energy Loss Spectroscopy
EXAFS	extended x-ray absorption fine structure
HAADF	high-angle annular dark-field imaging
HRTEM	high resolution transmission electron microscopy
HS	high spin state
IS	intermediate spin state
IT	iodometric titration
LS	low spin state
LSCF	$La_{1-x}Sr_xCo_{1-y}Fe_yO_{3-\delta}$
LSCM	$La_{1-x}Sr_xCr_{1-y}Mn_yO_{3-\delta}$
LSGM	$La_{1-x}Sr_xGa_{1-y}Mg_yO_{3-\delta}$
LSM	$LaMnO_3$
LSTF	$La_{1-x}Sr_xFe_{1-y}Ti_yO_{3-\delta}$
MCFC	molten carbonate fuel cell
MIEC	mixed ionic-electronic conductor
NPD	neutron Powder Diffraction
ORR	oxygen reduction reaction

PAFC	phosphoric acid fuel cell
PCFC	protonic ceramic fuel cell
SAED	selective Area Electron Diffraction
SOFC	solid oxide fuel cell
SR-PXD	synchrotron Radiation Powder X-ray Diffraction
STEM	scanning transmission electron microscopy
TEC	Thermal expansion coefficient
TGA	thermogravimetry Analysis
TOF-NPD	time-of-flight Neutron Powder Diffraction
TPB	triple-phase boundary
XANES	x-ray absorption near edge structure
XAS	x-ray absorption spectroscopy
XRD	powder X-ray diffraction
YSZ	yttria-stabilized zirconia

SYMBOLS

a,b,c	unit cell parameters (Å)
Co_{AVG}	average cobalt oxidation state
d_{hkl}	interplanar distance (Å)
E_A	activation energy (eV)
h	Planck's constant (J·s)
p_{H_2O}	water vapour partial pressure
r	ionic radius (Å)
t	Goldschmidt tolerance factor
T_C	Curie temperature
δ	oxygen nonstoichiometry
λ	wavelength (m)
μ	linear absorption coefficient
Θ_{hkl}	reflected angle

1. The aim of the work

The aim of this study was to establish a general relations between water uptake and fundamental properties of mixed ionic-electronic conducting perovskite oxides. The general formula of the investigated materials is $BaLnCo_2O_{6-\delta}$, where Ln stands for the lanthanide: La, Pr, Nd, Sm, Gd, Tb, and Dy. A few reports of water uptake in those materials have previously been published in the literature, however, this issue remains controversial. The provided evidence confirming the ability to form protonic defects is insufficient. Moreover, no explanation of what parameter is responsible for the water uptake phenomenon in these materials has been proposed so far. Therefore it is very important to verify the ability to incorporate protonic defect, to identify the factors that determine this phenomenon. This knowledge is necessary for the future materials development.

The very phenomenon of water uptake is important from both fundamental and application points of view because the protonic defect formation is a necessary condition for the proton conductivity to occur in materials in which hydrogen is not a constituent element. Mechanically and chemically stable materials with high proton transfer numbers are very desirable for electrochemical devices technology. Such materials are used as both electrolyte, and electrode materials. The branch of hydrogen technology is developing very dynamically due to the high demand for sustainable and environmentally friendly energy systems. One kind of electrochemical devices are fuel cells, in which the chemical energy of fuel, usually hydrogen, is directly converted into electricity. Hydrogen is considered to be the most promising renewable energy source. This is mainly due to the independence of hydrogen technologies from constraints by weather and local geographic conditions, high efficiency, and the possibility of integration with other technologies.

Protonic ceramic electrochemical devices, based on the proton conducting electrolyte, are the type that recently attracts much attention, but its development is limited by the lack of sufficient mixed ionic electronic electrode materials. The most anticipated materials for this application are conductors with three mobile charge charier, like oxygen ions, electron holes, and protons. Designing materials for specific applications requires a thorough understanding of the mechanisms that govern the observed processes. In case of triple conducting oxides, it is necessary to understand why some materials with similar chemical

compositions and structures show the ability to build a proton defect, while others do not. Such a rules are well known for pure proton conducting perovskite oxides, in which the competing interaction between defects are negligible. Hydration enthalpy can be related to the symmetry tolerance factor[1] and chemical properties of constituent elements, like oxide basicity[2] and difference in electronegativity of A- and B-site cations[3]. In case of mixed ionic-electronic conductors it is much more difficult, for example those materials offer the equilibrium between hydration and oxidation, what introduce new variables to be considered. Due to the application potential of these materials, it was decided to take up the challenge of explaining the mechanisms governing the phenomenon of protonic defect formation in double perovskite cobaltites. In the layered structure alternate layers consist of different cations what alternates its acidity and basicity, what affects the ability to incorporate protons.

Within the project the following research hypotheses were made:

- It is possible to synthesise the A-site ordered double perovskite cobaltites, with general formula $BaLnCo_2O_{6-\delta}$ in the wide range of lanthanides, including La, Pr, Nd, Sm, Gd, Tb, and Dy.
- Layered perovskite structure, which consist of acidic and basic layers, affect the water uptake. The presence of oxygen vacancies in more acidic Co-O layer, surrounded by more basic Ba-O and Ln-O sites will create a local environment more suitable for water splitting and hydration.

To verify the stated research hypotheses the detailed characterization of crystallographic and electronic structure, supported with thermal studies were applied.

2 Introduction

2.1 Perovskites

Perovskites are a group of materials, with the general formula ABX_3, where A and B are cations and X is an anion. The name of the whole group comes from the first discovered representative, $CaTiO_3$, the perovskite mineral. In general, this large group of materials may be divided into organic, and inorganic perovskites. Organic ones have s functional groups at A- and B-site[4],[5]. Typical inorganic perovskite consists of a large 12-coordinated A-site cation, and a smaller 6-coordinated B-site cation. The anion type may serve as the basis for introducing the classification of perovskites into smaller subgroups. The first subgroup that can be distinguished is inorganic perovskite oxides, with the general formula ABO_3. The second group is halide perovskites, where X = F, Cl, Br, I [6]. This group includes also alkali halide perovskites and organometal perovskites [7]. The third group is hydride perovskites, where X = H and the last subgroup that can be distinguished is perovskite hydroxides with the general formula $AB(OH)_6$ [7]. Perovskite oxides attract much attention due to their wide variety of compositions and properties[8].

Perovskite materials may be composed of various combinations of elements with different oxidation states. The cation selection is determined by the constituent anion. Monovalent anion, like F, Cl, and Br requires the choice of monovalent A-site cation and divalent B-site cation[8]. The divalent oxygen as an anion extends the choice of cations, e.g. A^{+1} and B^{+5}, A^{+2} and B^{+4}, or A^{+3} and B^{+3} [8]. This makes the number of compounds in the perovskite group enormous. Figure 2.1 shows the periodic table, with marked elements that can form perovskite structures. As can be seen, a wide variety of elements may be chosen to compose the perovskite material, both as A and B cations. Thus many different compositions can be imagined. Furthermore, many elements, like Pb, and Mg may occupy A-site[9] as well as B- site position[9].

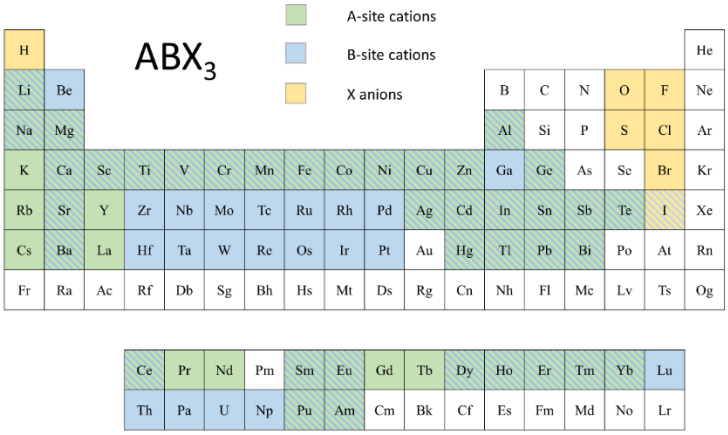

Figure 2.1 Elements that form perovskite structure[7],[10],[11]

The large number of elements that can form a perovskite structure leads to the wide range of physical properties. For instance, they differ in their electrical and magnetic properties. Among this group, both dielectric [12],[13] and highly conducting[14]–[16] materials may be found. What is more, the charge carrier, as well as transport mechanism, differs from compound to compound. $La_{0.8}Sr_{0.2}MnO_{3\pm\delta}$ is an example of a pure electronic conductor[17]–[19], while $La_{2/3-x}Li_{3x}TiO_3$ (for $0.07 \leq x \leq 0.13$)[20] and $(La_{0.9}Nd_{0.1})_{0.8}Sr_{0.2}Ga_{0.8}Mg_{0.2}O_{3-\delta}$[21] are reported to exhibit pure or almost pure oxygen conductivity. Besides, under some specific conditions, perovskite materials, e.g. $Ba_3Sr_{1+x}Ta_{2-x}O_{9-\delta}$[22] and $BaLaIn_{1-x}Y_xO_4$[23] are almost pure proton conductors, however, those materials are not cubic perovskites, but perovskite derivatives. Moreover, many perovskite materials, like $La_{1-x}M_xCo_{1-y}Fe_yO_{3-\delta}$, where M = Sr, Ba, Ca, are mixed conductors[24]–[26].

Magnetic properties also vary among the different representatives of perovskites. This group consists of ferromagnetic[27],[28], antiferromagnetic [29]–[31], as well as ferrimagnetic[32]–[34] materials. Perovskites can exhibit a more complex magnetic nature, like competing interactions of ferromagnetic, and antiferromagnetic sublattices in $La_{0.7}Sr_{0.3}FeO_3/La_{0.7}Sr_{0.3}MnO_3$ solid solution[35], or spin-glass behaviour[36]–[38]. Representatives of perovskites exhibit also giant magnetoresistance[39]–[41].

Due to the variety of their properties, perovskites are widely used in various branches of technology. From the application point of view, perovskite oxides are extremely interesting, because they show great ease in creating oxygen vacancies. The presence of which strongly affects the properties of the perovskite compounds. Such

changes are rarely observed in oxides with different structures. What is more, the concentration of oxygen vacancies may be tailored by doping. The discoveries of some perovskite oxides, like high-temperature superconductors[42], are considered as milestones in material science.

2.1.1 Perovskite structure

The unit cell of ideal ABX_3 perovskite, presented in Figure 2.2, is cubic and belongs to $Pm\bar{3}m$ space group. There are several approaches to describe those structures. Atoms in the unit cell may be listed in two general ways, depending on how the coordinate system is selected. Both A and B cations may be located at the origin of the system. Those two representations are presented in Figure 2.2. Figure 2.2a depicts the unit cell in which the origin was located on the A-site cation, while Figure 2.2b shows the unit cell with the B-site cation at the origin. In Figure 2.2a A-site cations lie at the corners of the unit cell. The B-site cations occupy the centre of the unit cell, surrounded by a regular octahedron of X-anions, which is presented in Figure 2.2c. Coordinates and Wyckoff's positions of atoms in this projection are presented in Table 2.1. In the second projection A-site cations, coordinated to 12 X anions are situated in the centre of the unit cell in the cuboctahedral cage site (Figure 2.2d)[43]. Different location of unit cell origin entails the coordinates of base atoms, which are summarized in Table 2.1.

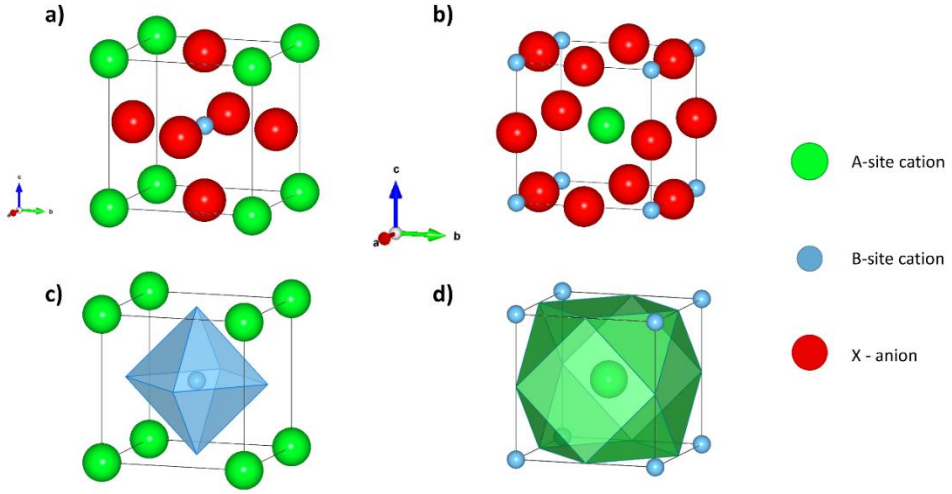

Figure 2.2 Unit cell of ideal ABX_3 perovskite with the A-site cation (a) B-site cation (b) in the 0,0,0 point, (c) and (d) show the coordination polyhedra of the B- and A-cations, respectively.

Table 2.1 Atomic coordinates and Wyckoff positions in the perovskite structure, when the coordinate system origin is located on an A-site cation and B-site cation

Origin	Atom	Wyckoff position	Coordinates
A	A	1a	0,0,0
	B	1b	½,½,½
	X	3d	½,½,0
B	A	1b	½,½,½
	B	1a	0,0,0
	X	3d	½,0,0

Perovskite structure may also be described as a network of corner-sharing BX_6 octahedra (Figure 2.2c). In an ideal perovskite structure, the octahedra axes are parallel to each other, and the X-B-X bonds are linear equal in length. Cubic perovskite structure may be also thought of as the sequence of close-packed AX_3 layers stacked in the ABCABC sequence, laying normal to the unit cell diagonal [111]. The AX_3 plane is presented in Figure 2.3, B site cations lie below and above this plane occupying ¼ of the available octahedral cavities[44].

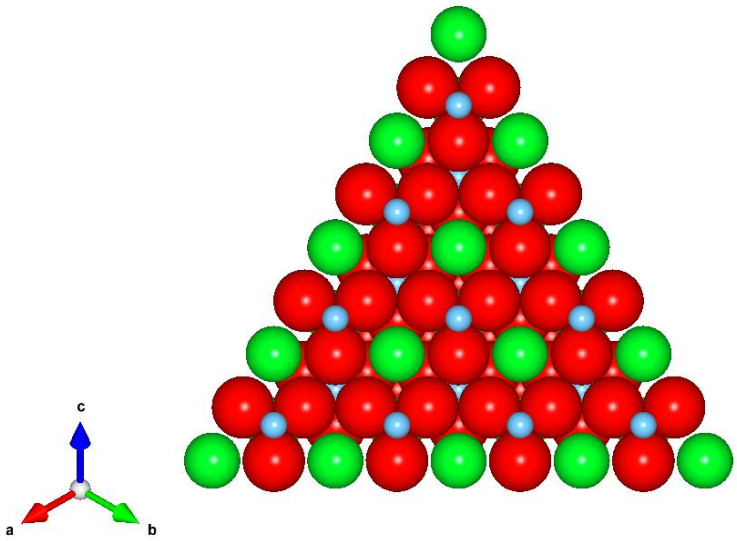

Figure 2.3 Single AX_3 (111) plane in cubic perovskite

Wyckoff position of atoms in perovskite structure is unadaptable, and hence the ideal perovskite structure is inflexible. Thus, any compositional change must be followed by the change in the lattice parameters. In cubic perovskite structure, a simple geometric relation between ionic radii of compositional atoms and lattice parameters may be established. Figure 2.4 shows the scheme of the unit cell of the ideal perovskite structure,

which presents how its space is filled. The sum of B-site cation and anion radii must be equal to the lattice parameter, according to equation 2.1.

$$2r_B + 2r_X = a \tag{2.1}$$

Unit cell diagonal is filled with the A-site cations and X-anion; thus the length of the diagonal must be equal to the sum of those ions' sizes. This relation is presented in equation 2.2.

$$2r_a + 2r_X = a\sqrt{2} \tag{2.2}$$

Based on equations 2.1 and 2.2 it may be stated that in the ideal perovskite structure the relation between ionic radii of component ions must be as it is presented in equation 2.3. It was Goldschmidt who presented this relation for the first time and suggested that it can be used to predict the probability of forming the perovskite structure by two cations. In an ideal perovskite structure ionic radii ratio presented with equation 2.3 must be equal to 1, however, in real cases, deviations from this value are observed. From relation 2.3 a so-called Goldschmidt tolerance factor *t*, presented in equation 2.4, can be derived. This ratio may be treated as a parameter, which describes not only the likelihood of perovskite structure formation but also the stress in the structure. Goldschmidt stated that the perovskite structure may be formed if the tolerance factor value is close to unity. The factor has reasonable predictive power despite its simplicity. It is especially useful in the case of perovskite oxides due to the well-established oxygen ionic radius. The probability of ideal cubic perovskite structure formation is reasonably high if the *t* value ranges from 0.89 to 1.0. Greater deviation of the value of *t* from unity causes the stresses in the structure to be so high that it leads to structural deformation. Generally, a lower value of the t parameter leads to the formation of ilmenite structure[45].

$$\frac{r_A + r_X}{\sqrt{2}(r_B + r_X)} = 1 \tag{2.3}$$

$$t = \frac{r_A + r_X}{\sqrt{2}(r_B + r_X)} \tag{2.4}$$

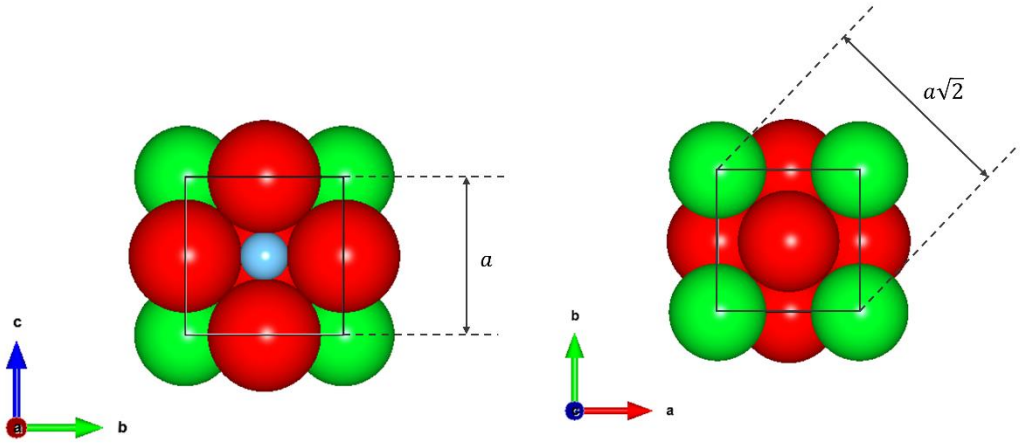

Figure 2.4 The scheme of space-filling of the unit cell of the ideal perovskite

Goldschmidt tolerance factor is a useful, however, it is often insufficient[46]. It does not consider the chemical nature of constituent elements, e.g.; preferred coordination number. Goldschmidt tolerance factor have 83% accuracy in predicting perovskite structure in oxides, and only 33% accuracy for iodides[47]. What is more, the Goldschmidt tolerance factor being derived from geometric constraints does not guarantee that the perovskite structure is a ground state structure for the investigated compound. It only points out that the ionic radius of composing atoms may be commensurate with the perovskite structure, without direct information on the probability of perovskite structure formation. Even if the t value is equal to unity, the compound may not adapt to a perovskite structure, like $NaBeCl_3$[47],[48]. Thus, the new tolerance factor τ, which is presented with the equation 2.5, was recently introduced by Bartel et al[47]. The new tolerance factor τ includes not only ionic radii of composing atoms but also the oxidation state of A-site cation, which in equation 2.5 is denoted as n_A. The authors state that the perovskite structure may be formed if $\tau < 4.18$[47]. The advantage of the τ parameter is that similarly to the Goldschmidt tolerance factor, it only requires the knowledge of the chemical composition of the compound. Factor τ applies to the wide range of single and double perovskites and allows to predict thousands of new perovskite compounds[47]. The τ parameter describes the possibility of perovskite structure formation. However, it is impossible to calculate the τ factor for the compound in which $r_A = r_B$. Nevertheless, the perovskite structure is unlikely to form in materials with equal ionic radii of A- and B-site cations. This can be established based on the Goldschmidt tolerance factor, which is equal to $t = 0.71$ if $r_A = r_B$.

$$\tau = \frac{r_X}{r_B} - n_A\left(n_A - \frac{r_A/r_B}{\ln(r_A/r_B)}\right) \quad (2.5)$$

2.1.2 Distortions in the perovskite structure

Even if the ionic radius of composing ions does not fulfil the geometrical relation, the perovskite materials may be formed. However, it introduces a strain to either the A-O or B-O bonds. If the strain is low enough even the ideal cubic perovskite structure may be formed. If the strain is higher, it may cause structure deformation, which relieves elastic energy. The distortion may cause the formation of both perovskite structure derivative as well as a non-perovskite structure. The number of materials with distorted perovskite structures is much higher than the number of cubic perovskites. Materials with tetragonal[49],[50], orthorhombic[51],[52], rhombohedral[53],[54], triclinic[55],[56], and monoclinic[49],[57] perovskite structures are known. Several mechanisms of perovskite structure deformation are known. The main mechanisms of structure deformation are octahedra distortion, the displacement of a cation within the octahedra, and octahedra tilting[43]. The following subchapters describe each distortion mechanism. Structure distortion is very interesting not only from the crystallography point of view, but it also strongly affects the perovskites' physical properties.

2.1.2.1 Octahedral tilting

In an ideal perovskite structure, the B-site coordination polyhedra form a three-dimensional network of parallel corner-sharing octahedra, but since the inter-octahedra bonds are flexible, a certain amount of tilting and rotation may take place. Octahedral tilting is the most commonly occurring distortion of the perovskite structure, which causes the release of stress resulting from the mismatch of cation sizes. It takes place if the ionic radii of the A-site cation are not big enough to fit the framework of BO_6 octahedra. As a consequence of octahedra tilting around the pseudocubic axes, the size of the A-site cation cavity is reduced, which compensates for the cation size mismatch[43]. The octahedra tilting does not change their corner-sharing connectivity. This type of distortion reduces the length of the A-X bond without the change in the first coordination sphere of the B-site cation[58]. Figure 2.5 presents the scheme of possible octahedra rotations. The octahedra may be tilted about the triad (Figure 2.5a), diad (Figure 2.5b), and tetrad (Figure 2.5c) axes[43]. Those axes are coincident with the aristotype cubic unit cell.

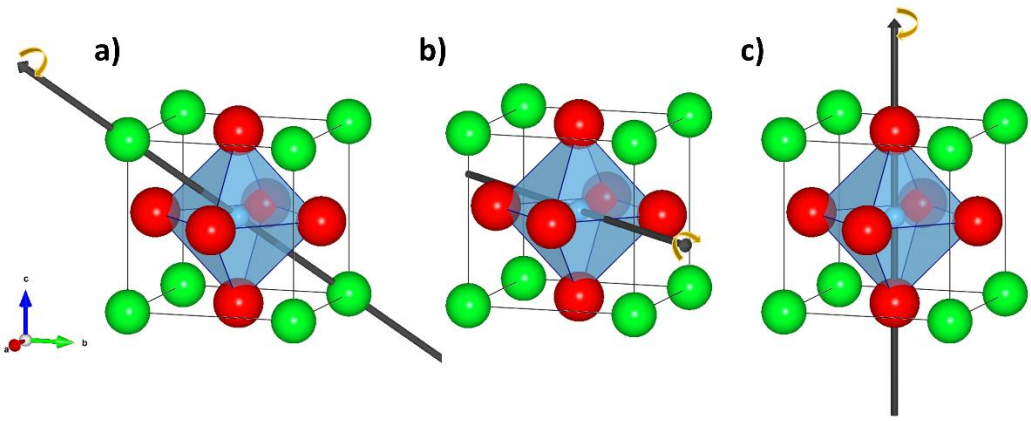

Figure 2.5 The scheme of possible rotation axes of octahedron tilting: triad axis (a), diad axis (b), and tetrad axis (c)

Tilting of one octahedron entails the distortion of the entire octahedra network. Figure 2.6 shows the exemplary tilting of one layer of BX_6 octahedra. In this case, octahedra are rotated only about one, $[001]_p$ axis. The rotation of one octahedron leads to the tilting of four adjacent octahedra at the same angle, but in the opposite direction. Thus, the first octahedra tilting forces the distortion of the whole BX_6 layer. The successive octahedral planes are tilted either in phase or out of phase to the first layer. Those rotations of the sequential octahedra planes reduce the symmetry of the structure from cubic, to tetragonal with space groups P4/mbm, and I4/mcm for in-phase and anti-phase rotations, respectively[46]. Octahedra tilting changes A-site cation coordination and reduces the symmetry of the perovskite[46]. More complicated rotations further lower the symmetry of the system. The external conditions, like temperature and pressure, affect the octahedral tilting. The nomenclature to describe the tilted perovskite structure was developed and introduced by Glazer[59], who identified 23 tilt systems. This number was then reduced to 15 based on the studies of Howard and Stokes[60], who used the group theory. This reduction was possible because the authors proved that tilted angles do not have to be equal in particular space groups.

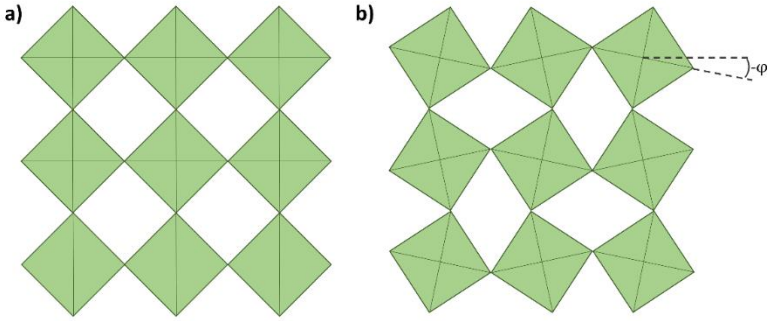

Figure 2.6 Scheme of an exemplary tilt of the plane of BX_6 octahedra

2.1.2.2 Jahn-Teller distortion

Jahn-Teller distortion is one of the best described distortions of the B-site octahedra in perovskite oxides. According to the theory of Jahn-Teller distortion molecules with symmetrical atomic configuration and a degenerate electronic ground state are unstable. Consequently, those molecules tend to distort to remove the electronic degeneracy of the highest occupied molecular orbital[61]. It is applied to the materials with the transition metal at the B-site. Figure 2.7 shows the energy levels of a d-electron metal in different coordinations. In octahedral coordination, d^5 levels are split into two degenerated levels. A lower energy level labelled t_{2g} is triply degenerated and consists of d_{xy}, d_{yz}, and d_{xz} orbitals. The upper, doubly degenerated level, which is labelled as e_g contain $d_{x^2-y^2}$ and d_{z^2}levels. Transition metals in which e_g orbitals are occupied by the odd number of electrons have the degenerate ground state due to two equivalent possibilities of electrons distribution. The Jahn-Teller distortion is manifested by the change in the length of one of the three pairs of B-X bonds in an anion crystal field. The B-X-B in one of its fourfold tetrad symmetry axes may be either elongated or shortened. The octahedron distortion, both elongation and compression lead to the degenerated levels splitting, which enhances the stability of the transition metal, however, it is difficult to predict whether a given compound will tend to shorten or lengthen the octahedron. The change in the bond length causes both the e_g and t_{2g} levels to separate. The energy splitting of t_{2g} orbital is rather small and does not highly affect the perovskite structure, unlike the splitting of e_g orbital, which is significant and leads to octahedral distortion[43].

As a result of Jahn-Teller distortion, the unit cell symmetry is lowered to tetragonal or orthorhombic, even though A- and B-site cations remain in their position in the centre of coordination polyhedra. A significant influence on the magnitude of Jahn-Teller distortion has the size of the A-site cation[46]. Moreover, the level of Jahn-Teller distortion strongly depends on the temperature and pressure. Often, the temperature and pressure elevation eliminates the Jahn-Teller distortion, which increases the symmetry to cubic[43].

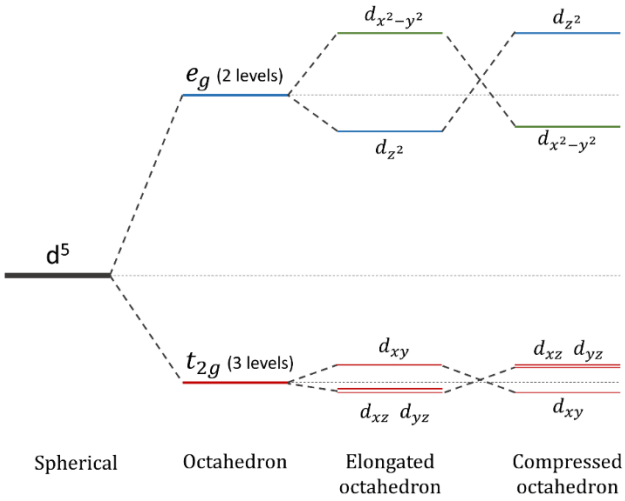

Figure 2.7 Energy levels of d-electron metal in different coordination, prepared based on [43]

2.1.2.3 B-cation displacement

B-site cation displacement in the materials with the perovskite structure consists in changing the position of the B-site cation from the centre of the octahedron along with one of the octahedron symmetry axes. It is attributed to the second order Jahn-Teller effect, which occurs in nonlinear molecules with a nondegenerate electronic ground state and a very low excited state. Symmetry lowering takes place to facilitate the overlapping of the ground and excited electronic state, which leads to the ground state energy lowering[43]. Figure 2.8 shows the three possible directions of B-site cation shifting within the BX_6 octahedra. The B-site cation may be moved along three fourfold (tetrad) axes of rotational symmetry, all of which passes through the opposite vertices of the octahedra. The example of tetrad axis is presented in Figure 2.8a. Such a displacement results in the formation of one elongated and one shortened B-X bond, while the remaining four have intermediate length, however still being elongated relative to the undistorted structure[43]. B-site cation displacement may also occur in six twofold (diad) axes of rotational symmetry, which connect the centres of the opposite edges of the octahedron, presented in Figure 2.8b. Such a displacement results in two short and two long bonds in the plane of the displacement, and two intermediate-length bonds roughly perpendicular to the displacement plane. It is also possible to shift the B-site cation along the four threefold (triad) axes of rotational symmetry passing through the centre of the opposite triangular face of the octahedron[43] presented in Figure 2.8c. In this case, three bonds are shortened, and three are elongated. B-site cation displacement along the above-mentioned axes does not break the symmetry

axis parallel to the direction of the displacement. All of B-site cations may be distorted in the same way, which usually is associated with the A-site cation displacement, or B-site cation displacement may be distorted along different axes. Non-uniaxial B-site cation displacement results in the formation of more complicated derivative structures.

B-site cation displacement is strongly affected by temperature and pressure, a good example of which is $BaTiO_3$, which undergoes phase transitions between cubic, tetragonal, orthorhombic and rhombohedral structures, under the change of temperature and atmosphere[43].

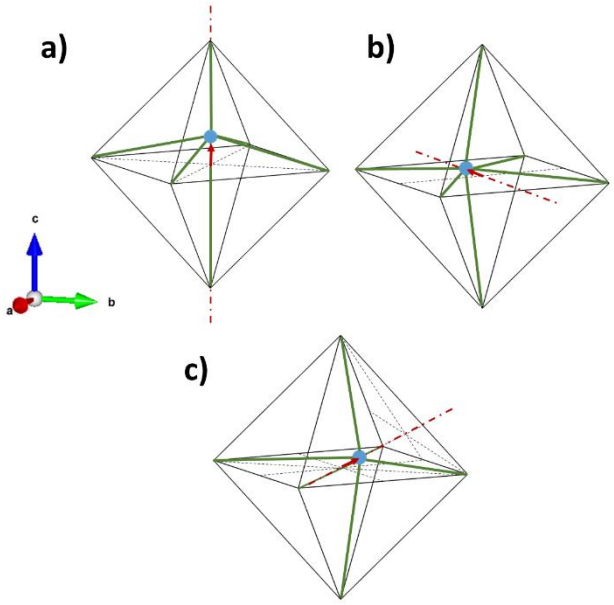

Figure 2.8 B-site cation displacement within the BX_6 octahedron along with the tetrad (a), diad (b), and triad (c) axes

2.1.3 Perovskite structure derivatives

Distortions mentioned in previous sections, octahedral tilting, Jahn-Teller distortion, and B-site cation displacement, lead to the formation of perovskite structure derivatives, but in general, do not change the framework of the coordination polyhedra. BX_6 octahedra remain to be corner-sharing, while the A-site cations are in the cuboctahedral voids. Because of those distortions, the bond lengths and angles vary from the ideal regular perovskite structure. However, due to the very high flexibility of the BX_6 octahedra framework more complex distortion may be observed. Such a distortion may result from differences in ionic radii of constituent cations or deviation from stoichiometry. Thus, the perovskite derivatives may be divided into stoichiometric and nonstoichiometric.

The one type of derivative of the stoichiometric perovskite structure is double perovskites, in which an A-site or B-site lattice is occupied with the combination of two different chemical species, located at the specific crystallographic sites. The ratio between elements occupying the same sublattice may be varied, which influences the general formula of the material. The general formula of double perovskites may be written as $AA'B_2X_6$ or $A_2BB'X_6$ or $A_3BB'_2O_9$[46]. Elements of the same sublattice may be either randomly distributed or form ordering in the crystal lattice. Different types of the ordering of both A- and B-site cations are observed in perovskite derivatives. Random distribution of cations occupying the same sublattice makes their positions undistinguishable, and the $Pm\bar{3}m$ is maintained. Cation ordering results from the difference in ionic radii of cations occupying the same sublattice. It reduces the strain energy and leads to a doubling of unit cell parameter in at least one direction, from which the name of these structures come from[62]. Two specific types of order are known. Coexisting cations may be fully ordered along $(111)_p$ planes, which introduces the long-range order, without cations mixing on their positions and octahedra tilting[46]. This leads to the formation of $Fm\bar{3}m$ unit cell with lattice parameter doubled with the respect to ideal perovskite structure. Such ordering is called a rock salt type-ordering double perovskite. The cation ordering combined with the octahedra tilting leads to the symmetry lowering. This type of ordering leads to the formation of BX_6 and $B'X_6$ altering layers along one direction. Both A- and B-site cations may be simultaneously ordered, what may cause the further unit cell parameters magnification. Such structures are called complex, or quadrupole perovskites.

In this work, the nomenclature of double perovskite is used to describe compounds in which the A-site is occupied by two different species in the 1:1 ratio and the lattice parameter is doubled in at least one crystallographic axis.

A layered perovskite consists of a certain number of BX_6 layers separated by a different structural element. In this group, five main groups may be distinguished, namely Ruddelsden-Popper, Dion-Jacobson, and Aurivillius, $A_nB_nX_{3n+2}$, and $A_{n+1}B_nX_{3n+3}$ phases[63],[64]. The Ruddelsden-Popper structure may be described as ABX_3 perovskite with AX unit added. Thus, the general formula of the Ruddelsden-Popper compound may be written as ($AX+nABX_3$), where *n* stands for the number of corner-sharing BX_6 layers in the stack[46]. Dion-Jacobson's structure is similar to the Ruddelsden-Popper, but the A-site cation is ordered, and it consists of only one layer of inner-slab A-cations[46]. The

Aurivillius materials, the general formula of which is $[Bi_2O_2]^{2+}[A_{n-1}B_nO_{3n+1}]^{2-}$, are constructed of n cubic layers separated with $[Bi_2O_2]^{2+}$ planes. Such a diversity of layered perovskite derivatives gives a lot of possibilities to tailor the properties of those compounds. In the group of layered perovskites, superconducting oxides deserve special attention[65].

Another type of perovskite derivative is materials with partially occupied crystal sites. Among this type seven main groups may be distinguished: A-site vacant hydroxide perovskites, anion deficient Brownmillerites, A-site vacant quadrupole perovskite, B-site vacant single perovskites, B-site vacant inverse single and double perovskites, and anion deficient partly-inverse quadrupole perovskites[66].

The hexagonal perovskites are the derivative of the ideal cubic structure, which is formed when the difference in A- and B-site cations ionic radii is big. The lattice strain induced by the mismatch in cations' size is released with some B octahedra distortion, which starts to share faces instead of corners. In such a case perovskite structure may be viewed as the sequence of the close-packed AO_3 layers[67]. The AO_3 layers aligned along the c direction can be stacked in either cubic 'c' or hexagonal 'h' order. In the first order, the B-cation octahedra share its vertices, while in the second one the faces. The different sequences and ratios of cubic and hexagonal stacking lead to the formation of a wide range of hexagonal perovskites[68].These studies concern the investigation of double perovskite cobaltites with the A-site cations forming alternate layers.

2.1.4 Applications of perovskite oxides

It will not be an overstatement to say that perovskite materials can be used anywhere. It is a result of the high flexibility of the structure, which can adopt most of the chemical elements. Thus, the properties of the perovskite materials can be tailored by the chemical composition of the compound. Even if the chosen elements do not fulfil the geometrical condition to form an ideal cubic perovskite, the structure is very flexible, which gives the possibility to form the distorted structure. By skilful selection of the chemical composition, perovskite materials can be designed for almost all, even very extreme, applications.

Perovskites, both organic and inorganic are widely used in renewable energy and green technologies[69]. Thanks to the high catalytic activity, perovskite materials are widely used in the removal of organic pollutants[70]. The catalytic activity of perovskites is also

used for hydrogen production[71], catalytic combustion of volatile organic compounds[71], water splitting[72],[73], and much more[74]–[77]. Interestingly, materials from the investigated group of double perovskite cobaltites are also studied for their catalytic activity toward water splitting[78]. Perovskite materials are also applied in photovoltaics[79],[80]. Metal halide perovskites are used as absorber materials in solar cells which reach efficiency and durability comparable to silicon-based photovoltaic cells. What is more, lead-free perovskites used in photovoltaics make those devices more environmentally friendly[81].

Optoelectronics also make extensive use of perovskite and perovskite derivative materials[82]. Perovskites are applied in light-emitting diodes and lasers[83]–[85] due to the excellent charge transport and ability to adjust the band gap[84]. Optoelectronic devices based on perovskites reach high external quantum efficiency and current efficiency[85]. However, a great effort is made to increase its long-term operational stability and reduce toxicity hazards[83]. The variety of optical properties of perovskites allows to use them in various types of optical and electrochemical sensors[86]. Perovskites are used to detect carbon monoxide, hydrocarbons, and ethanol, among others[87],[88].

Among perovskites, good conductors, as well as, materials with high dielectric constant, may be found. Dielectric properties of perovskites are used for energy storage in many different application fields, like electronic circuits, microwave communication, hybrid vehicles, distributed power systems, renewable energy, or high-power applications[13],[89]. Piezoelectric perovskites are used in actuators, transducers, and sensors[90]–[92]. The extraordinary magnetic properties of perovskite oxides open up many other application possibilities, like spin-valve devices[93], or biomechanical applications[94],[95]. Finally, widespread cuprates, exhibiting high-temperature superconductivity are perovskite structure derivatives[96].

The amazing variety of chemical compositions and physicochemical properties of perovskites makes the topic of their applications very difficult to exhaust. However, within the scope of this thesis, the application of perovskite oxides in electrochemical devices, like fuel cells and electrolysers is of particular interest.

2.1.4.1 Fuel cells and electrolysers

Fuel cells are electrochemical devices that directly convert chemical energy of fuel into electrical energy. The conversion of chemical energy into electricity takes place

without any intermediate form of energy in the reaction between fuel and oxygen. Hydrogen is the basic fuel, but also different compounds consisting of hydrogen, like hydrocarbons, may be used. The unquestionable advantage of hydrogen technology is the ability to operate the same device in both, fuel cell and electrolyser, modes[97]. Several types of electrochemical cells that differ in design, type of fuel and type of electrolyte can de distinguished. The main fuel cell types are polymer electrolyte fuel cell (PCFC), molten carbonate fuel cell (MCFC), alkaline fuel cell (AFC), phosphoric acid fuel cell (PAFC), and solid oxide fuel cell (SOFC). Despite the differences in construction, the main concept is the same. Hydrogen reacts with oxygen, which is used to produce electricity, heat, and water. Applying fuel other than molecular hydrogen requires the pre-step of fuel decomposition. This reaction may take place in the opposite direction in the mode of water electrolysis leading to hydrogen generation.

Among all types of fuel cells, solid oxide fuel cells seem promising owing to their high reliability, fuel flexibility and high efficiency[98]. The scheme of the solid oxide fuel cell, which is based on the oxygen ion-conducting electrolyte, is presented in Figure 2.9. At the air electrode (cathode) the oxygen is reduced, and then it is transported through the electrolyte towards the anode. At the anode two reactions take place, one is hydrogen oxidation, and the second is water formation. The conduction of oxygen ions through the electrolyte is a thermally activated process, and thus achieving high efficiencies requires a high operating temperature of the cell[98],[99]. Switching to the electrolyser operation mode changes the direction of electron transport in electrodes, thus their names switch. The fuel cell's cathode became the electrolyser's anode and vice versa. Therefore, the nomenclature of 'positrode', and 'negatrode' will be used[2].

A particular type of ion-conducting electrolyte is proton conducting material, which is used as the electrolyte in proton ceramic fuel cell (PCFC), presented in Figure 2.9b. In this device, the hydrogen ion H^+ is transported through the electrolyte from the fuel electrode to the air electrode. In comparison to oxygen conductivity, proton transport is usually characterized by lower activation energy, and thus PCFCs require lower operating

[2] Truls Norby proposed the introduction of 'positrode', and 'negatrode' nomenclature, for the electrode with positive and negative bias respectively. Such nomenclature is independent of the operating mode[100] and has already been used in the literature[101],[102].

temperature. What is more, in this type of fuel cell the fuel is not diluted by the outgoing water[100],[103].

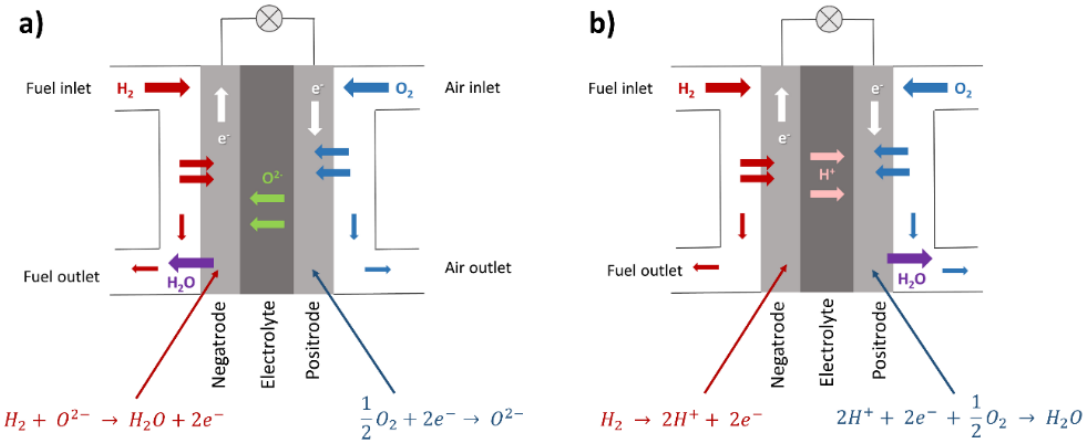

Figure 2.9 The schemes of solid oxide fuel cell (a), and proton ceramic fuel cell (b)

Despite the simple principle of operation, the design and construction of fuel cells are complex. The whole device must be hermetic and mechanically stable, with good non-blocking interfaces. Perovskite materials are used for almost all of the unit cells constituents, electrodes, electrolytes, and interconnectors[104].

Electrolyte materials should exhibit high ionic and low electronic conductivity, chemical and physical stability under both reducing and oxidising conditions at the working temperature, and be easy to densify[105],[106]. Currently, the most commonly used electrolytes with a perovskite structure are oxides with lanthanum and strontium at the A-site and gallium and magnesium at B-site, like $La_{0.9}Sr_{0.1}Ga_{0.8}Mg_{0.2}O_{2.85}$ (LSGM)[106]. Those materials are almost pure ionic conductors [107], which may be manufactured with a density close to the theoretical value[108]. High ion conductivity is a result of lanthanum substitution with strontium, which has a very similar ionic radius but leads to oxygen vacancies concentration. Similarly, gallium substitution with lanthanum also decreases oxygen content. Perovskites containing transition metals, like $La_{1-x}Sr_xCo_{1-y}Fe_yO_{3-\delta}$[109] and $La_{1-x}Sr_xFe_{1-y}Ti_yO_{3-\delta}$[110] are also studied as electrolyte materials so SOFC. PCFCs require the application of a good proton conductor as electrolyte material, the most popular of which is the solid solution of barium cerate and barium zirconate $BaCe_{1-x}Zr_xO_{3-\delta}$. To improve the performance of the electrolyte yttrium $Ba(Ce,Zr,Y)O_{3-\delta}$[111],[112] and ytterbium $Ba(Ce,Zr,Y,Yb)O_{3-\delta}$[112] substitution of the B-site is applied.

Perovskites are also used as negatrode materials in fuel cells and electrolysers. In this case, on the negatrode of both SOFCs and PCFCs, the same reaction of hydrogen ionization takes place. Thus, similar materials may be considered as negatrode material in those two types of fuel cells. However, the final choice depends on the compatibility of the material in question with the electrolyte material. Among the representatives of the perovskites used as negatrodes[113],[114], it is $La_{1-x}Sr_xCr_{1-y}Mn_yO_{3-\delta}$[105] in the first place, however, titanium-based perovskites are also used[115]. Moreover, composite electrodes consisting of an electrolyte oxide and metal, usually nickel, are most commonly used[116],[117].

Perovskite materials are widely used as the positrode material in both SOFCs and PCFCs. However, the choice of proper positrode material is challenging. Positrode materials must meet stringent requirements. It must have high electronic conductivity and electrochemical activity for the efficient oxygen reduction reaction (ORR), and high diffusivity to effectively transport oxide ions through the electrode to the electrolyte. It must exhibit stability under both oxidizing and inert atmospheres. What is more, it must be stable upon steam pressure. Positrode material should fit well with the electrolyte material in terms of compliance with thermal expansion coefficients, chemical reactivity, and good adhesion properties[118]. It is possible, though, to use imperfectly compliant materials, however, the use of buffer layers is necessary. The low cost of cathode fabrication is also an important criterion. The morphology of the electrode plays a crucial role, it must be porous to ensure good gas access and display a large number of reaction sites. The positrode microstructure must not degrade the mechanical stability of the electrode. The scheme of different types of cathodes is presented in Figure 2.10. The ordinary electronic conductor (Figure 2.10a) may be applied as a positrode, however, it limits the electrochemical reactions only to the triple-phase boundary (TPB), which lowers the efficiency of the cell. The application of a mixed ion-electron conductor as the cathode allows the chemically reactive surface to expand to the whole surface of the electrode. Oxygen transport through the electrode may be obtained by application of composite material, consisting of electronic and ionic conducting phases, or the use of mixed-ion electron conductor (MIEC)[118]. Such materials may be found among perovskites and non-perovskites[119]. While choosing a positrode material, one should also pay attention to the operating temperature of the cell, which is determined by the temperature required to achieve sufficient transport through the electrolyte. The harsh environment of high-temperature SOFC makes electrode selection difficult. In this type of SOFC, the composite of strontium-doped $LaMnO_3$ (LSM) and

yttria-stabilized zirconia (YSZ) is used[119]. However, the LSM may also be applied separately, not as a part of the composite[119],[120]. In addition to lanthanum, other lanthanides are also studied as the A-site cation in manganese[121],[122]. Different example of single-phase mixed-conducting material used as the positrode are $La_{1-x}Sr_xCo_{1-y}Fe_yO_{3-\delta}$ (LSCF)[120],[123],[124], $Ba_{1-x}Sr_xCo_{1-y}Fe_yO_{3-\delta}$ (BSCF)[120],[125]–[127]. The reducibility of transition metal provides the catalytic activity of those materials, while the octahedral symmetry of the transition metal promotes a metallic or semiconducting band structure at high temperatures, which is a result of 3d electron level splitting, due to the interaction with the crystal field. As it is described in section 2.1.2.2 in octahedral coordination this energy level splits into two levels separated by a band gap. Metallic or semiconductor nature depends on how those levels are filled with electrons. If a large number of oxygen vacancies is responsible for high ionic conductivity[119].

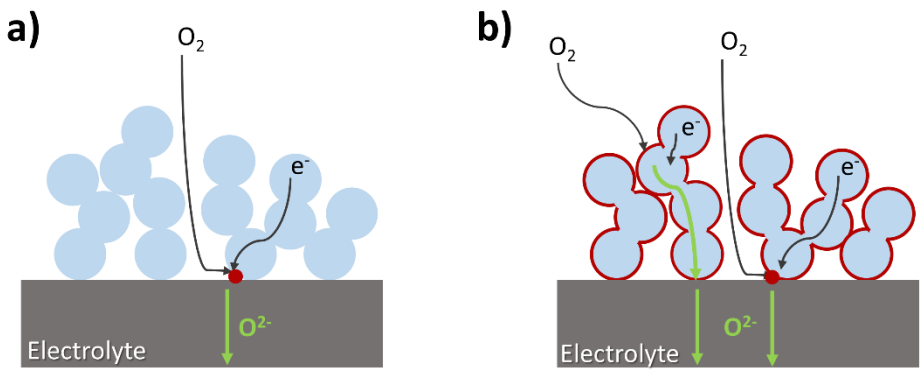

Figure 2.10 The scheme of the interface between cathode and the electrolyte of solid oxide fuel cell with the electron-conducting cathode (a), and mixed ion-electron conducting cathode (b)

Solid oxide electrochemical cell technology is at a very high level of advancement and implementation for general use. Protonic ceramic electrochemical cell technology is less advanced despite many advantages over SOFC. Protonic defect mobility is characterized by lower activation energy than oxygen-ion transport[103],[128],[129], which gives a potential to reduce the operating temperature. Not only the activation energy is usually lower in proton conductors, but also the total ionic conductivity of the PCFC electrolyte is higher at the given temperature than in SOFC[130],[131]. PCFCs are also characterized by a faster startup, less degradation, and lowered cost[132]. A definite advantage of PCFCs is that water is produced at the air electrode (Figure 2.9 b), which does not dilute the fuel as in SOFCs. Water formation on the air electrode is beneficial because unused fuel can be easily recycled for reuse. Another advantage of PCFC is the possibility

of using different fuels[133]. It may operate with pure hydrogen, as well as ammonia[134], and hydrocarbons[135]. What is more, the theoretical maximum efficiency of PCFCs is higher in comparison to SOFC due to the lower operating temperature[133].

Despite the many advantages of PCFCs, their further development is limited by the selection of positrodes. The lowered operating temperature leads to the overpotentials of the electrode-electrolyte interface increase[103],[132]. The positrode reactions usually have a higher energy barrier than negatrode reactions or charge transport via electrolyte so the positrode is usually the element limiting the cell performance. This is because the oxygen reduction reactions are slower than fuel oxidation on the negatrode and ionic transport through the electrolyte[103]. Therefore, the current density at the positrode limits the performance of the whole cell[103]. The application of mixed ion-electron conducting air electrode leads to the extension of a catalytically active zone beyond the TPB. The most desired electrode material for PCFC is a triple conducting material, with electron holes, oxygen ions and protons as mobile charge carriers[132]. However, the mechanical strength and compatibility with the electrolyte must also be met. Thanks to the advantages of PCFCs, and positrode requirements, the search for those materials is a "hot" topic.

Perovskite oxides are widely studied as PCFC positrodes, due to their properties and flexibility. After all, the specific properties of the perovskite can be tailored by appropriate control of the chemical composition. Haile et al. reported the PCFC with double perovskite $PrBa_{0.5}Sr_{0.5}Co_{1.5}Fe_{0.5}O_{5+\delta}$ as a positrode to have, at that moment, one of the highest power density of 1.1 Wcm^{-2} at 650 °C[136]. Perovskites are also used as a component of positrode composites, like in the composite of $BaPrCo_2O_{5+\delta}$ and BZY[136], $BaPrO_3$-$PrNi_{0.5}Mn_{0.5}O_{3-\delta}$[137], or BCZY-BSCF composite[138]. However, single-phase positrodes have an advantage over composites, because the electrochemically active sites may be extended to the whole surface of the electrode if a triple conducting material is applied. The $BaCo_{0.4}Fe_{0.4}Zr_{0.1}Y_{0.1}O_{3-\delta}$ is a promising electrode, in which mixed ion-electron conductivity is obtained by the high concentrations of mix-valance Co and Fe, while the presence of Ba, Zr, and Y promotes the proton transport[139]. Also, $NdBa_{0.5}Sr_{0.5}Co_{1.5}Fe_{0.5}O_{5+\delta}$[139] and $Sr_2Fe_{1.5}Mo_{0.5}O_{6-\delta}$[140] seem to be promising electrode materials. Not only are the chemical substitutions used to tailor the properties of the positrode materials. Ren et al. proposed to introduce A-site cation deficiency in $Ba_xCo_{0.4}Fe_{0.4}Zr_{0.1}Y_{0.1}O_{3-\delta}$[140]. Authors shown that barium deficiency alters the charge

compensation mechanism, leading to additional vacancies to maintain electronic neutrality. An increased number of oxygen vacancies leads not only to oxygen ion and proton transport diffusion but also improves the ORR performance of the material[140].

Triple conducting double perovskites are very promising materials for PCFCs. However, designing materials for this application requires a thorough understanding of the processes governing the transport mechanisms in these materials. What is more, not only the selection of the best material is important, but also its appropriate manufacturing. Bian et al. showed that the simple acid treatment of the surface of the components can strongly increase the performance of the cell, due to the interface improvement[141].

2.2 Cobalt oxides

This study concerns the double perovskite cobaltites, which belong to the family of strongly correlated electron systems. The high complexity of cobalt oxide properties results from the readiness of cobalt to have various oxidation states, spin states and coordination symmetries. Cobalt in crystals exhibit oxidation states such as Co^{2+}, Co^{3+}, Co^{4+} and, especially in ternary oxides, a mixture of Co ions with different valence is observed. The intermediate valence often couples with charge ordering, which makes the magnetism and transport properties of cobalt oxides very complex and interesting. Cobalt in oxides exhibits a wide variety of coordination, including tetrahedral, pyramidal and octahedral coordination, which allows the formation of multiple structures of cobalt oxides. Structure and oxidation flexibility goes in line with the resilience of the oxygen framework, while the oxygen nonstoichiometry strongly influences the properties of the material[142].

Cobalt exhibit not only a variable oxidation state but also adopt different electron structures. The electron configuration schemes of each spin and oxidation state in octahedral coordination are presented in Figure 2.11. In pyramidal coordination, t_{2g} orbitals split into two lower energy e_g' orbitals, and one higher energy a_{1g} orbital. E_g orbitals also lose the degeneration in pyramidal coordination[143]. Generally, as was shown for $LaCoO_3$, the spin state is a result of competition between crystal field splitting and the exchange energy for 3*d* electrons and the occupied orbitals in CoO_6 octahedron and it increases with temperature[144],[145]. Such a variety of cobalt results in a variety of magnetic and transport transitions, often coupled with structural transitions. Very complex transport behaviour in mixed valence cobalt oxide results from the fact that not every electron transition is allowed

in the system. The transition of electron between states with S difference larger than ½ is strongly suppressed[146],[147], since it should involve more than one electron or include a simultaneous flip of other spins[148]. The examples of allowed and not allowed electron transitions are presented in Figure 2.12. The phenomenon of transport blocking due to not allowed spin transition is called spin blockade, and is often observed in cobalt oxides[142].

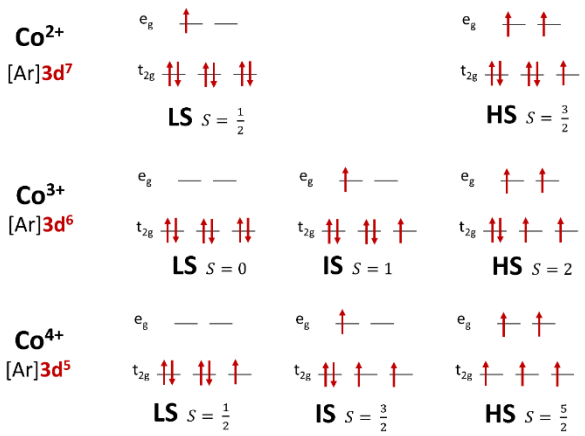

Figure 2.11 Electron configuration of cobalt in each oxidation state

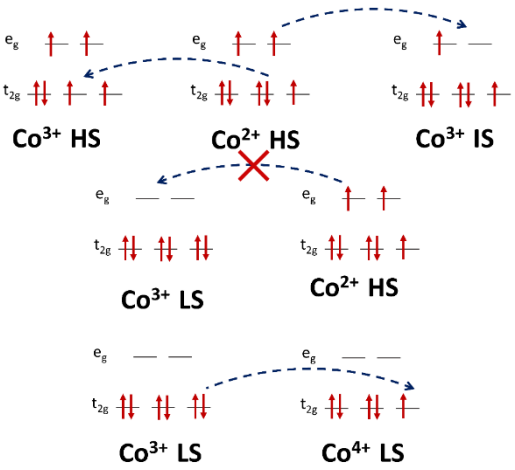

Figure 2.12 The examples of allowed and not allowed electron transitions between cobalt at different spin and oxidation states, based on [147]

This thesis focuses on complex cobalt oxides with perovskite structures. The general formula of this group is $BaLnCo_2O_{6-\delta}$, where Ln = La, Pr, Nd, Sm, Gd, Tb, Dy.

2.2.1 Structure of double perovskite cobaltites

According to the literature barium cobaltites substituted with lanthanide can crystallize in three different space groups, all of which are perovskite structure derivatives.

The structure is directly related to the differences in the ionic radii of barium and lanthanide, as well as oxygen stoichiometry[149],[150]. Lanthanum barium cobaltite crystalizes in the ideal cubic perovskite structure[151],[152]. In such a case, the $Ba_{0.5}La_{0.5}CoO_{3-\delta}$ chemical formula is used, which corresponds to the general perovskite oxide formula ABO_3. The ionic radius of lanthanum is the most similar to barium among all the lanthanides[153], thus it easily occupies the same crystallographic position[151]. This results in a random distribution of lanthanum and barium in the A-site sublattice. The lanthanides contract as their atomic number increases so with the increasing atomic number of the lanthanide occupying A site the difference between the size of barium and lanthanide increases[153]. This difference induces a strain in the lattice, which causes the formation of the separate Ln-O, and Ba-O layers which alternate along the c-axis[154]. This phenomenon is called A-site cation ordering. Since barium and lanthanide positions are not equivalent the unit cell is doubled in the c direction, forming the tetragonal structure with the space group $P4/mmm$[154]–[156]. Not only A-site cation may order in double perovskite cobaltite, but also oxygen vacancies tend to form an ordering[157]. Oxygen vacancies are preferably located in the lanthanide layer. In the case of perfect ordering, every second oxygen position along the b axis in the Ln-O layer is more promoted to form the oxygen vacancy. Cobalt alternates between octahedral and pyramidal coordination. This leads to unit cell doubling along the b-axis. Material, in which oxygen vacancies are ordered adapts an orthorhombic unit cell, with the space group Pmmm[157],[158]. Within the whole dissertation to describe the oxygen position will be described as O1, O2, and O3, what stand for the oxygen atoms placed in Ba-O, Co-O and Ln-O layers, respectively. In orthorhombic structure, the O3a and O3b positions are distinguished, while oxygen vacancies order at the O3b position. Figure 2.13 shows the exemplary XRD patterns of cubic and double perovskite calculated with Vesta software[159] based on crystallographic data reported by Nakajima et al[149]. Due to the unit cell doubling along the c direction, the XRD pattern of double perovskite exhibit characteristic reflection multiplication.

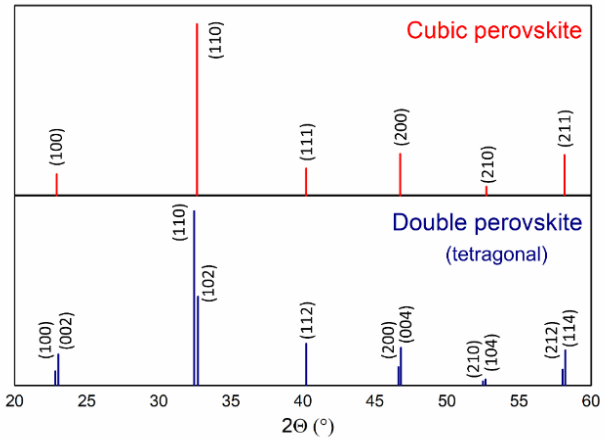

Figure 2.13 The XRD patterns of cubic (top) and double (down) perovskite structure. XRD patterns simulated with VESTA software[159] *on the basis of data from* [149]

2.2.2 Properties of double perovskite cobaltites

The properties of double perovskite cobaltites result mostly from the transition nature of cobalt, variable oxidation and spin state. In those materials, strong electron correlations and coupling between charge, spin, orbital and lattice degrees of freedom are observed. Substitution of divalent barium with trivalent lanthanide enhances the mixed valence of cobalt. Due to the variable cobalt oxidation state, these materials tend to form many oxygen vacancies. High adjustability of oxygen vacancy concentration strongly impacts the properties of double perovskite cobaltites and may be easily tailored by the appropriate heat treatment under different atmospheres[160]–[162]. Lanthanide substituted double perovskite barium cobaltites exhibit very interesting magnetization properties, mixed ionic-electronic conductivity at elevated temperatures, and high catalytic activity towards oxygen reduction.

Very rich magnetic properties of double perovskite cobaltites result from the interaction between incompletely filled 3*d* electron orbitals of cobalt and O 2*p* and/or 1*s* orbitals. Different types of magnetic ordering have been reported in double perovskite cobaltites. According to Nakajima et al. $BaLaCo_2O_6$ undergoes a ferromagnetic transition at T_c = 175 K[149].

The transport properties of double perovskite lanthanides are very complex and interesting. It is strongly affected by oxygen nonstoichiometry. The total conductivity of those materials is high exceeding values of $500\ S \cdot cm^{-1}$ [163],[164]. Despite many studies on transport nature in double perovskite cobaltites, the general agreement on the band structure and even charge transport type is still lacking[165]. The only commonly accepted postulate is that the electronic current conduction is dependent on –O-Co-O- chains in the crystal

structure, similarly as it takes place in other cobalt oxides[166],[167]. $BaLnCoO_{6-\delta}$ according to most of the studies are classified as p-type semiconductors[165] with a band-gap around 0.3 eV[165]. The p-type charge carriers are usually considered as small polarons[168], but it is also disputed. In contrast to that stand the results of Hall effect measurements, which showed the metallic nature of conductivity with itinerant carriers and zero band gap[169],[170]. The dominance of p-type electronic charge carriers is contested also by the results of Telegin et al. who showed negative values of thermopower [171]. The studies on monocrystal showed high anisotropy of transport properties[171]. In those materials, the metal-insulator transitions around 300 K was observed, which indicates the change in transport nature [165],[172],[173]. What is more, Pelosato et al. observed another transition from semiconductor-type to metallic nature at a temperature in the range 673-773 K[165].

The p-type small polaron model is applicable to explain the phenomenon of the observed spin blockade[152], however, the values of mobility calculated with this model seem to be too high for small polaron transport[174]. Vøllestad et al. proposed a model of a two-band conduction mechanism in double perovskites[170]. This model concerns two types of mobile charge carriers. The first is p-type carriers with high mobility in a wide O 2p band. The second one is n-type carriers with a lower mobility in a partially occupied σ*-band, which forms by degenerate spin states of cobalt 3d electrons. However, it is not possible to explain the observed low values of the Seebeck coefficient based on this model. Tsvetkov et al.[175] proposed a similar model of competing highly mobile p-type and less mobile n-type small polarons, but without referring to the band structure. The multitude of approaches to explain the electrical conductivity in double perovskites confirms how complex this issue is.

Double perovskite cobaltites exhibit a significant level of oxygen ion conductivity, which results from high oxygen vacancy concentration and their mobility. As shown before, the oxygen nonstoichiometry in those materials is very flexible and may reach the value of $\delta = 1.25$[176]. The oxygen diffusion across the crystal structure is highly anisotropic, The oxygen transport takes place mostly along the a-b plane with the activation energy of diffusion around 0.5 eV between 800-1400 K[177]. A-site cation ordering was shown to strongly impact the oxygen ion conductivity. In materials with disordered A-site cation, the oxygen diffusion became isotropic, however, the total diffusivity of disordered material decreases in comparison to the ordered counterpart[152],[177]–[180].

High total electronic conductivity, catalytic activity, and mixed ionic-electronic conductivity, however, are not the only criteria that make a given material a potentially good positrode material. Positrode material must be thermomechanically compatible with the electrolyte material. The thermal expansion coefficient of the BZCY, which is the most commonly used electrolyte material is around $9 \cdot 10^{-6}\ K^{-1}$ [181]. This value is significantly lower than values reported for double perovskite cobaltites, which is around $20 \cdot 10^{-6}\ K^{-1}$ [160],[162]. Such mismatch in thermal expansion coefficient is challenging because it causes mechanical strain upon temperature change and results in damage or even failure of the electrochemical devices. Moreover, the literature is not abundant with data on the chemical expansion of these compounds, which is also very important due to the elevated operating temperature of PCFCs and PCECs.

Due to the high total electronic conductivity, mixed ionic-electronic conductivity, possible proton conductivity and high catalytic activity those materials are widely studied as cathodes for electrochemical devices. Nevertheless, its performance still needs to be improved. For this, it is necessary to understand the basic laws that govern the phenomena in these materials.

2.3 Point defects in crystal structures: Kröger-Vink notation

Properties of all materials strongly depend on defects present in the crystal structure, i.e. their type and concentration. Defect engineering is used in different groups of materials and allows obtaining different, extraordinary functional materials[182],[183]. In crystals point defects play a fundamental role in affecting the physical properties[184].

Kröger-Vink notation is used to describe point defects in crystals[185]. It denotes the species and defects in the crystal lattice with the symbols followed by the indexes in the subscript and superscript. The symbol in Kröger-Vink notation takes the following form $\boldsymbol{A_p^c}$. It may also be used for delocalized electronic defects, holes, and electrons. The main symbol A represents the species, it may be both the chemical symbol of the element, or symbol *v* for the vacancy. The subscript *p* describes the *position* that the element occupies. If the element locates at a regular atomic site in the crystal structure *p* takes the value of the chemical symbol of the element, which should be in this location in the perfect crystal. The interstitial position is denoted as '*i*'. The superscript *c* represents the charge that the species has. It may be either the absolute or the effective charge. The effective

charge is the difference between the absolute charge of a defect and the charge of the perfect crystal in this position. Positive relative charges are described with dots, •, negative with slashes, /, and neutral using *X*. The Kröger-Vink notation may be used not only to describe point defects, but also the perfect crystal elements. The examples of point defects in the structure of cobalt (III) oxide, written in Kröger-Vink notation, are presented in Table 2.2.

Table 2.2 Exemplary point defects in cobalt (III) oxide written in Kröger-Vink notation

Defect type	Notation
Cobalt	Co_{Co}^{X}
Oxygen	O_{O}^{X}
Free electron	$e^{/}$
Free hole	$h^{\bullet}$
Fe^{2+} in the cobalt position	$Fe_{Co}^{/}$
Fe^{3+} in the cobalt position	Fe_{Co}^{X}
Fe^{4+} in the cobalt position	$Fe_{Co}^{\bullet}$
Oxygen vacancy	$v_{O}^{\bullet\bullet}$
Cobalt vacancy	$v_{Co}^{///}$
Oxygen interstitial	$O_{i}^{//}$

Kröger-Vink notation enables writing the defect chemistry reactions, which is useful in thermodynamics studies. If the Kröger-Vink symbol is written in square brackets [], it relates to the concentration of the specie described by the symbol. Every reaction of point defect formation may be formulated while adhering to the three basic principles.

- The principle of conservation of mass – on both sides of the reaction, the mass of the reactants must be equal. Electrons and holes, however, are considered massless. Consequently, the mass of ion and neutral elements of the same kind is equal.
- The principle of conservation of charge - the total charge on both sides of the equation must be equal.
- The principle of conservation of the site ratio – if the reaction creates or annihilates any atomic site in the crystal, it must concern all atomic sites that result from the crystal stoichiometry.

Technically, any defect chemistry reaction which satisfies the above rules is correct[186],[187]. The probability of the given reaction is described by the equilibrium constant. The example reaction of oxygen incorporation is presented in equation 2.6. The

incorporation of gaseous oxygen in the position of unoccupied oxygen position is compensated by the generation of two electron holes.

$$\frac{1}{2}O_{2(g)} + V_O^{\bullet\bullet} \leftrightarrow O_O^x + 2h^{\bullet} \tag{2.6}$$

On the basis of equation 2.6 the reaction constant may be written, as it is presented in equation 2.7.

$$K_{Ox} = \frac{p^2}{[V_O^{\bullet\bullet}]p_{O_2}^{\frac{1}{2}}} \tag{2.7}$$

2.4 Water uptake mechanism

In materials, which do not contain hydrogen in the structure proton incorporation is the first necessary condition for proton conductivity to occur. The proton incorporation in this case is always the result of interaction with the surrounding atmosphere. Protons cannot exist in the oxide crystal lattice as separate entities, due to large charge density. In metals, protons interact with the delocalized electron density of the conduction band. In this case, a proton is considered as a part of hydrogen, although it may exhibit some protonic or hydridic character, which depends on the energy difference between the H1s state and the Fermi energy of pure metal. In metals proton may exhibit high coordination number, usually CN=4, or CN=6 in a tetrahedral, or octahedral site, respectively[188].

In non-metallic compounds, protons tend to associate with electronegative atoms, e.g. oxygen. Proton interacts with the valence electron density of one or two nearest neighbours. Attaching a proton to single oxygen creates a positively charged protonic defect $OH_O^{\bullet}$. This bonding may occur when the oxygen ion is well separated from other electronegative species. The O-H bond length in this case is around 100 pm, which is less than the ionic radius of the oxygen ion (r_O =140 pm). This means that the proton situates deeply in the valence electron cloud of the oxygen ion[188]. The situation is different if the distance between two adjacent oxygen atoms is very small, on the order of 240 pm. In this case, the proton is involved in two equivalent hydrogen bonds[188]. In an intermediate case, when the distance between the oxygen ion and the nearest electronegative element is around 250 – 280 nm, the proton is involved in two asymmetrical hydrogen bonds, one short and strong, and the second longer and weaker. A strongly bonded species is called a proton

donor, and the weakly bonded one is a proton acceptor. Such an asymmetrical hydrogen bond (O — H ··· O) exhibits a highly directional character[188].

Two fundamental reactions of proton defect formation may be written for the oxides. The first is called hydration and is presented in equation 2.8. Hydration is an acid-base reaction that does not involve electronic defects. In this reaction, dissociative absorption of water fills oxygen vacancies. The second proton is transferred to a regular lattice oxygen, which creates the second protonic defect. Hydration is the only way for proton incorporation in materials with low redox activity, that is with a large bandgap and low concentration of electronic defects[189]. It is the dominating reaction in the case of protonic electrolytes.

$$H_2O_{(g)} + V_O^{\bullet\bullet} + 2O_O^x \leftrightarrow 2\boldsymbol{OH_O^\bullet} \tag{2.8}$$

In redox-active materials, protons may be incorporated in the redox reaction of hydrogenation, presented in equation 2.9. This reaction describes proton defect formation with the consumption of electron-hole. The reaction of hydrogenation may take place even if the material does not contain oxygen vacancies[189].

$$H_2O_{(g)} + 2O_O^x + 2h^\bullet \leftrightarrow \frac{1}{2}O_{2_{(g)}} + 2\boldsymbol{OH_O^\bullet} \tag{2.9}$$

The reaction of hydrogenation is the combination of reaction 2.8 and reaction of oxidation (eq. 2.10) in which oxygen vacancies are filled with oxygen from the gas phase with the formation of an electron hole. What is more, the oxygen vacancies may be filled by oxygen from the water molecule, which dissociates on the surface of the material, which is presented in equation 2.11, which may be called water-based oxidation. Oxidation and water-based oxidation cause mass increase, however, no proton defect is formed in those reactions. Thus, the mass gain can be misinterpreted as proton defect formation. Pure proton conductors are believed to undergo only the hydration and/or hydrogenation process.

$$\frac{1}{2}O_2 + V_O^{\bullet\bullet} \leftrightarrow O_O^x + 2h^\bullet \tag{2.10}$$

$$H_2O_{(g)} + V_O^{\bullet\bullet} \rightarrow O_O^x + 2h^\bullet + H_{2_{(g)}} \tag{2.11}$$

Moreover, a proton defect can be formed because of interaction with the dry atmosphere, which contains hydrogen H_2. Protons may dissolve in oxide in a direct redox reaction, presented in equation 2.12. The charge in this reaction is compensated by the introduction of two electrons[190].

$$H_2 + 2O_O^x \leftrightarrow 2\boldsymbol{OH_O^\bullet} + 2e' \quad (2.12)$$

Since many different reactions may take place upon exposure of mixed conductors to a humidified atmosphere, the water uptake studies require great care, not to be misinterpreted. For this reason, the hydration of double perovskite cobaltites is a subject of lively scientific discussion. This stems from potential applicability as electrode material in electrochemical devices like fuel cells and electrolysers[191]–[194]. It is established in the literature that double perovskite cobaltites exhibit high mixed oxide ion and electronic conductivity[152],[193],[195],[196] and high catalytic activity for oxygen reduction[192],[197], so their application potential would be further increased if the material exhibited proton conductivity. Therefore great effort has been made to demonstrate that materials from the group $BaLnCo_2O_{6-\delta}$ can be considered as triple conducting oxides[192],[198]–[200].

The effect of change in the mass of material because of exposure to the humidified atmosphere attributed to the proton defect formation was observed in several double perovskite cobaltites. Grimaud et al.[190], Hashimoto et al.[201] and Strandbakke et al.[192] observed proton defects in $BaPrCo_2O_{6-\delta}$. The small amount of incorporated water in $BaPrCo_2O_{6-\delta}$ was also observed by Lozano et al.[202], however, by the means of secondary mass ion spectroscopy, it was determined, that most of the incorporated water is located close to the surface of the material. Nevertheless, the authors do not exclude the formation of point defects in the volume of the material, not only on the surface. A similar effect was also observed in $BaGdCo_2O_{6-\delta}$ [192],[203]. Vøllestad et al.[170] also investigated materials with more than one lanthanide on the A-site, showing the presence of proton defects in $Ba_{1-x}Gd_{0.8}La_{0.2+x}Co_2O_{6-\delta}$. Those reports stand in opposition to the studies of Malyshkin et al. [204] who attributed the water uptake in barium lanthanum gadolinium cobaltites to the hydration of the secondary phase of cubic perovskite $BaCo_{0.8}Gd_{0.2}O_{6-\delta}$. This statement was verified within this study.

2.5 Proton transport mechanism

Two basic mechanisms of proton transport are recognised in proton conductors, the Grotthuss mechanism, and the vehicle mechanism[190]. The schemes of both transport mechanisms are presented in Figure 2.14.

The vehicle mechanism relies on the proton transport with the assistance of bigger species, like H_3O^+, the vehicle. The counter diffusion of unprotonated vehicles leads to net proton transport. In oxides in which protons are incorporated as proton defects, the whole hydroxyl species is diffused through the crystal lattice. What is more, the activation energy of proton defect transport is lower than oxygen ion transfer, due to the smaller size of the hydroxide defect $OH_O^{\bullet}$ in comparison to oxygen ion O_O^x [205]. The vehicle mechanism typically occurs in water-containing materials, like $SnO_2 \bullet nH_2O$, and acids[188] and is rather unlikely to occur in perovskite oxides.

The second type of proton transport mechanism is the Grotthuss mechanism, in which the proton jumps between two neighbouring acceptor sites. This process can be divided into two steps. The first is the reorientation of the proton around the oxygen, and the second is the proton jumping towards the nearest oxygen site. The first step is considered to be very fast, with a low activation energy (E_A < 0.1 eV). The Grotthuss transport is limited by the jump step, which has significantly higher activation energy. Grotthuss mechanism is believed to be the most probable to occur in proton-conducting oxides at elevated temperatures (T > 300°C)[206].

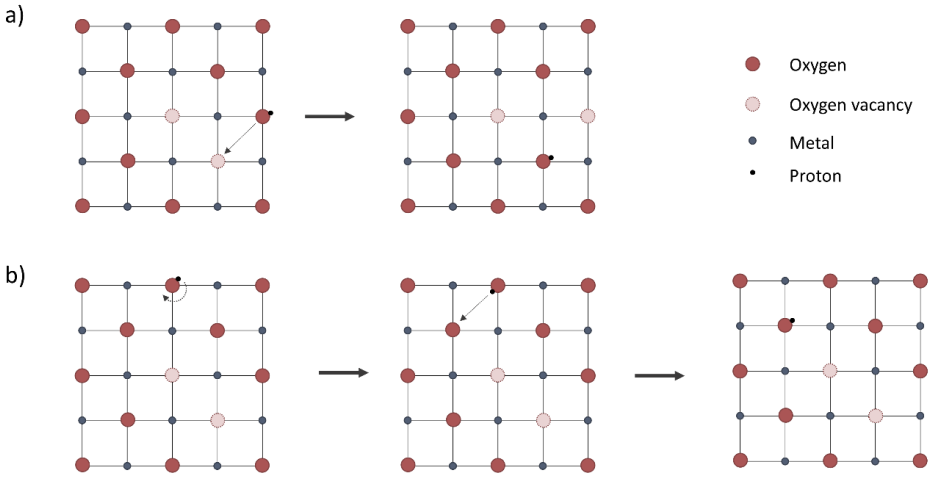

Figure 2.14 The schematic representation of proton transport mechanisms. Vehicle mechanism (a), and Grotthuss mechanism (b)

3. Experimental techniques

The experimental work made within this project may be divided into two main parts. The first one is materials synthesis, while the second is characterization. This section consists of a detailed description of the conducted research, starting from the synthesis, through the physical basis of the applied measuring techniques, to the experimental parameters.

3.1 Synthesis of double perovskite cobaltites

The selection of an appropriate method of synthesis is a prerequisite for the success of material research. The utility of each synthesis method is determined mostly by its effectiveness and reproducibility. However, simplicity, speed, low energy, reagents, and cost consumption are also desirable features. Several techniques are used for perovskite structured compounds preparation, including hydrothermal[207],[208] and sol-gel[209]–[213] methods, mechanosynthesis[214],[215], and solid-state reaction (SSR) technique, which seems to be one of the most popular. The solid-state reaction method fulfils basic requirements for the synthesis method, however, it requires the use of high annealing temperatures. Due to the vague and homogeneity of the materials produced, it was the solid-state synthesis reaction that was chosen as the material synthesis method in the presented work.

The flowchart of the method is presented in Figure 3.1. The stoichiometric amounts of reagents are mixed and either ground in agate mortar or ball-milled using isopropanol as a medium. The dried reagents are then formed into pellets and subjected to high-temperature thermal treatment. At this stage the decomposition of reagents and the formation of the desired structure take place. Solid samples are the result of annealing. The strict control of synthesis parameters, especially the temperature, time, and atmosphere of annealing plays a crucial role in this method. In the next step, the pellets are crushed and reground. The obtained powder is routinely screened with XRD to check phase composition of the fabricated material. If the main phase adopts the desired structure but the material still contains small amounts of unreacted reagents or other impurities, the grinding and high-temperature annealing process can be repeated. If the diffractogram does not indicate the presence of foreign phases, the obtained powder is a finished product, ready for further investigation. For the techniques that require samples in the solid form, the powder may be

pelletized and sintered at a high temperature. At this step no chemical reaction takes place, and the structure of the material remains unchanged.

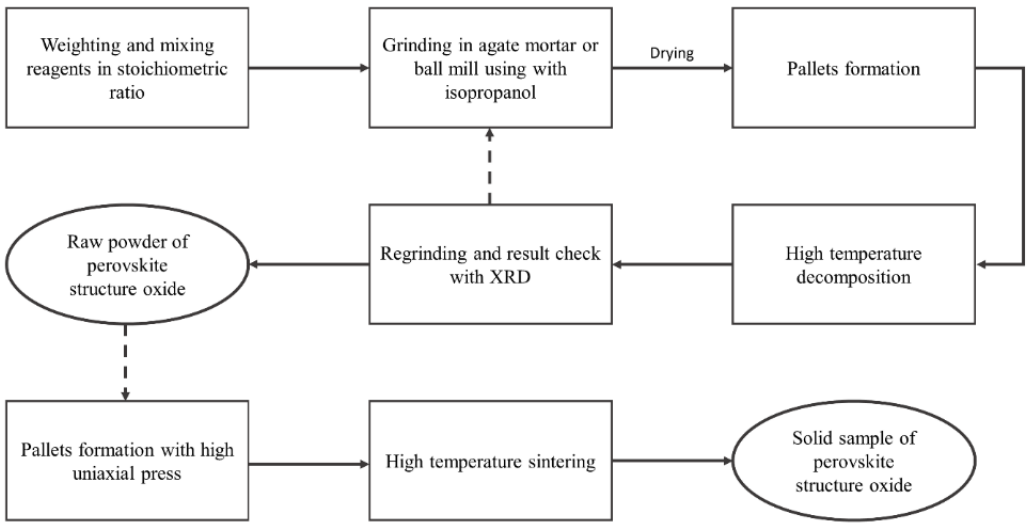

Figure 3.1 The flowchart of the solid-state reaction method pellets, using, high-temperature

In this work, the one-step solid-state synthesis method was applied. The list of used reagents is summarized in Table 3.1. La_2O_3 and Nd_2O_3, before weighing, were preheated at 900°C for 5 hours and kept at 150°C to remove the absorbed water. The green bodies were annealed in static air at 1150 °C for 48 h. The expectation is that $BaLaCo_2O_{6-\delta}$ after the first step of synthesis adopts the cubic perovskite structure. The material has to be reduced to form the double perovskite structure. To do so, the obtained powder of $Ba_{0.5}La_{0.5}CoO_{3-\delta}$ was annealed in Ar flow at 1050°C for 24 hours and then in air flow at 350°C for 3 hours. The solid samples were obtained by uniaxial pressing (p = 220 MPa) and sintered for 24 hours in static air at 1050°C.

Table 3.1 The list of reagents used

Element	Reagent	Producer, purity	Pre-treatment
Ba	$BaCO_3$	*Sigma Aldrich*, 99,9%	preheated at 900 °C for 5 h
Co	Co_3O_4	*Alfa Aesar*, 99.98%	
La	La_2O_3	*Alfa Aesar*, 99.99%	
Pr	Pr_6O_{11}	*Aldrich*, 99.99%	
Nd	Nd_2O_3	*Chempur*, 99.9%	preheated at 900 °C for 5 h
Sm	Sm_2O_3	*Chempur*, 99.9%	
Gd	Gd_2O_3	*Alfa Aesar*, 99.98%	
^{160}Gd	$^{160}Gd_2O_3$	*Trace Sciences International*, 99.7%	
Tb	Tb_4O_7	*Aldrich*, 99.99%	
Dy	Dy_2O_3	*Chempur*, 99.9%	
Lu	Lu_2O_3		

The analogous approach of material synthesis was used to obtain $BaCo_{0.8}Gd_{0.2}O_{6-\delta}$. The formation of material, according to Malyshkin et al.[204], is responsible for hydration in barium lanthanum gadolinium cobaltites.

3.2 Materials characterization

To characterize the materials several techniques were applied. Double perovskite cobaltites are a very complex group of materials, due to the structural diversity and variable nature of cobalt itself. Thus, this research required a holistic view of the properties of the material. The measurement techniques were divided into four main groups, based on the properties that are tested in a given method. Thus, structural studies, studies of the electronic structure, magnetic properties, and thermoanalysis were distinguished. Many of the applied techniques, like diffraction and spectroscopy, are based on the interaction of electromagnetic waves with matter. X-ray electromagnetic wave ($\lambda < 10$ nm) interacts with the electron cloud of a material causing three main effects:

- Elastic (Rayleigh) scattering, which does not change the energy of outgoing photons. Elastic scattering is the base of diffraction on crystalline samples[216]
- Inelastic (Compton) scattering, which lowers the energy of outgoing photons[216]

- Absorption, which causes the transition of the electron to a higher energy level, creates an excited state. The relaxation of this excited state may occur with the emission of electrons and photons of a longer wavelength (fluorescence)[216].

The X-ray flux transmitted through the sample is attenuated by the absorption, which causes the exponential reduction of radiation intensity according to the relation (3.1), where I_t and I_0 are transmitted and incident radiation intensity, μ is a linear absorption coefficient, and l is the sample thickness[216].

$$I_t = I_0 \cdot e^{-\mu l} \tag{3.1}$$

However, absorption is not the only cause of radiation attenuation, the absorption and attenuation coefficients are not usually distinguished in the literature, due to the fact absorption is the first-order effect of X-rays in matter[217]. The absorption properties depend on the chemical composition of the material, thus the investigation of the transmitted radiation is very useful in material studies[216].

The interaction of X-ray radiation with matter is schematically shown in Figure 3.2. A detailed description of each type of interaction is included in the following sections, next to the method based on the given type of interaction.

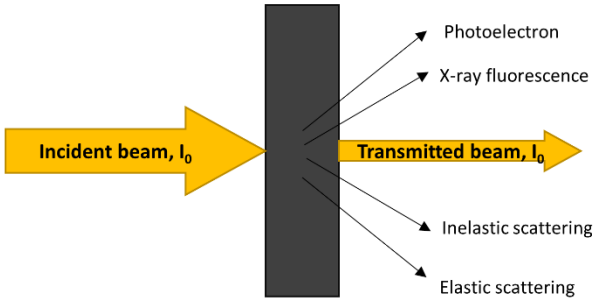

Figure 3.2 Interaction of x-rays with matter, after[216]

3.2.1 Structure characterization

Structural studies aim to provide a complete description of the crystal structure of the material, as well as give information on the macroscopic structural properties of the material, like morphology and grain size. In this group, two main types of technicians can be distinguished, i.e., diffraction and microscopy methods.

3.2.1.1 Diffraction methods

The diffraction techniques are based on the coherent (Rayleigh) scattering of the radiation. The incoming photon collides with the inner-shell electron of the material. Elastic scattering does not change the photon energy[218]. A crystal, as a periodic set of atoms, can be treated as a diffraction grating, thus the observation of diffracted radiation can provide information about the internal structure of the crystal. The explanation of the phenomenon of the interference ray enhancement was proposed by Braggs and Wulff, who treated the outgoing radiation as a beam reflected from the set of parallel lattice planes (hkl), as is schematically shown in Figure 3.3. The incident radiation is partially reflected from the outer plane and partially penetrates deep into the crystal and is then reflected from subsequent lattice planes. Rays reflected from different planes interfere, however, the constructive interference occurs only if the difference in path lengths Δs is equal to the integer multiple of the wavelength. This approach allows the formation of Wulff-Bragg's condition (eq. 3.2)[219].

$$n\lambda = 2 \cdot d_{hkl} \sin \theta_{hkl} \qquad (3.2)$$

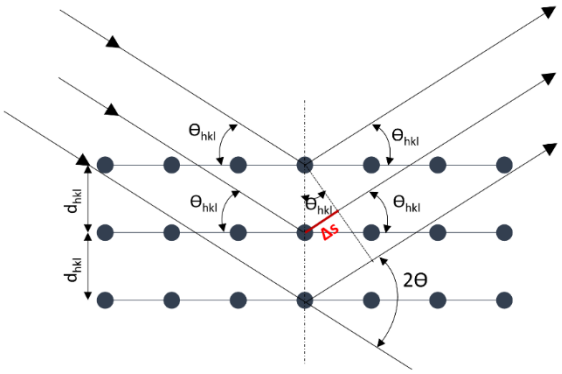

Figure 3.3 Graphical representation of Wulff-Bragg's law

The reflected wave is the secondary radiation of the X-rays illuminated atoms. The Bragg's-Wulff condition determines the direction of the outgoing radiation. The radiation amplification is observed only at the specific angles, which can be directly related to the Miller index of the reflecting planes.

Braggs and Wulff's works focused on the diffraction of X-ray radiation, however, it may be applied to the other types of radiation. The application of different types of radiation

allows us to obtain various information on the structure of the material. In this work the following diffraction techniques were used:

- Powder x-ray diffraction (XRD)
- Synchrotron radiation powder x-ray diffraction (SR-PXD)
- Neutron powder diffraction (NPD)

3.2.1.1.1 Powder x-ray diffraction

Powder x-ray diffraction is a technique for studying the polycrystalline samples. Therefore, it is one of the first-choice methods of materials characterization. It is used to determine the result of synthesis, as well as investigate the fundamental structural parameters of the specimen. The polycrystalline sample may be considered as a set of many randomly oriented lattice plane families; thus, all possible orientations of individual crystallites are equally probable. The sample is illuminated with monochromatic radiation, whereas the angle between the X-ray source, sample, and detector is variable. At the specific angle, when the Bragg-Wulff condition is fulfilled, the intensity of the radiation reaching the detector is significantly increased. One of the most popular geometries of goniometers used in powder X-ray diffraction is Bragg-Brentano geometry, which is schematically shown in Figure 3.4. A sample is placed in the fixed position centre of the circle that incident and diffracted-beam slits move on. The X-ray source and detector rotate relative to the sample, keeping equal source-sample and sample-detector angles[218]–[220].

As a result of the measurement, the diffraction pattern is obtained. In powder diffraction, some information on crystal structure is lost, due to the signal overlapping coming from differently oriented planes with the same d-spacing. Nevertheless, analysing the position, intensity, and shape of the reflections much information on the crystal structure may be obtained, which is summarized in Figure 3.5. The most important information on crystal structure is hidden in the peak position and intensity.

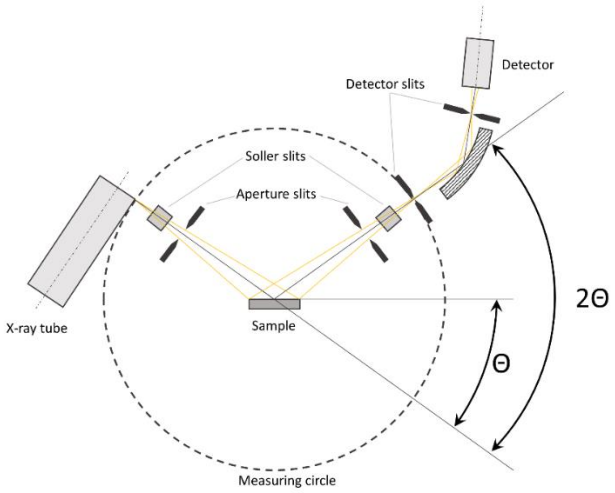

Figure 3.4 The scheme of Bragg-Brentano geometry goniometer in the X-ray diffractometer[218]

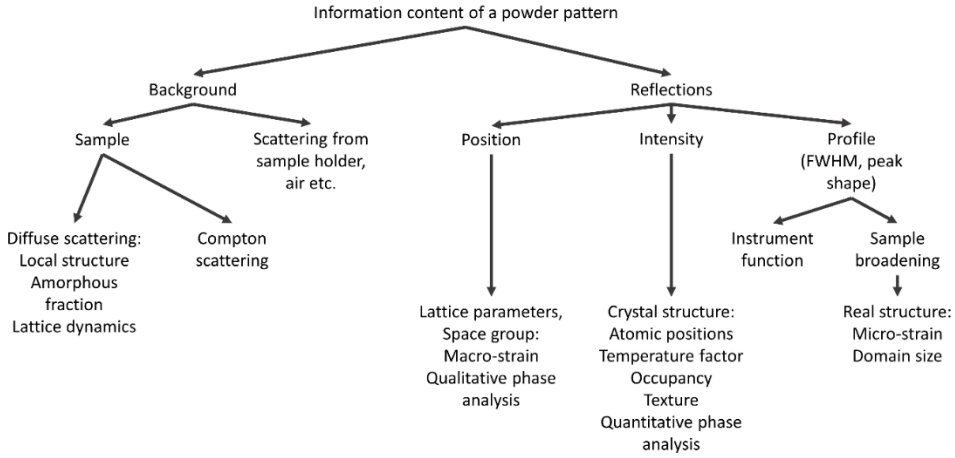

Figure 3.5 General information which may be obtained based on powder diffraction pattern –based on [220]

The x-rays in this technique are produced in the x-ray tube. The origin of the radiation is the collision between high-energy electrons, accelerated in the electric field, and the metal target. The outgoing radiation consists of the characteristic x-rays corresponding to the anode material and a continuous spectrum. To narrow the wavelength range of the incident radiation specific filters are used. In this case Phillips X'Pert Pro diffractometer with Cu K α radiation, proportional counter, and Bragg–Brentano geometry.

3.2.1.1.2 Synchrotron radiation powder x-ray diffraction

Synchrotron radiation powder x-ray diffraction is based on the same principles as laboratory powder x-ray diffraction. The main difference lies in the radiation source. The synchrotron radiation is produced in the specific units, in which accelerated near to the speed of light electrons are moving on the circular path. The direction of the electron change

is forced by the magnetic field. The electromagnetic radiation is emitted as a consequence of the principle of conservation of momentum[216].

In comparison to x-ray produced in the x-ray tube, the synchrotron radiation exhibits high brightness (from 4 to 12 orders of magnitude higher than the conventional x-ray source), which reduces the time of diffraction pattern recording. What is more synchrotron x-ray are characterized with high collimation, wide energy spectrum, and short-pulsed time structure[221]. What is more, the penetration depths of synchrotron radiation are much higher than that of laboratory-scale radiation. The energy of synchrotron radiation may be tailored, which allows experimenting as a function of wavelength instead of an angle. What is more, the experimental parameters may be easily matched to the specific needs of the investigated material. Despite the lower availability of synchrotron radiation SR-PXD is often used due to the much higher resolution of the results[222].

X-ray radiation, regardless of the source, interacts with the electron cloud of the atom in the crystal lattice. The atomic cross-section of Rayleigh scattering is given with the relation 3.3.

$$\frac{\sigma_R}{\rho} \propto \frac{Z}{(h\nu)^2} \tag{3.3}$$

The elastic scattering cross-section is therefore proportional to the atomic number of the element. Thus the intensity of the radiation scattered on light elements is low. It implies insufficient sensitivity of x-ray diffraction methods to the elements with low Z numbers[223]. While oxygen stoichiometry is one of the key properties of perovskite structured oxides, it is difficult to determine the O-site occupancies with XRD or even the SR-PXD method.

The room temperature SR-PXD data were collected at European Synchrotron Radiation Facility (ESRF) in Grenoble and Diamond Light Source in Didcot. ESRF measurements were carried out with Swiss-Norwegian Beamlines (SNBL) BM01[224] and BM31[225] with a Pilatus 2M 2-dimensional (2D) detector (BM01) λ=0.78956 Å, and with a Dexela-Perkin Elmer 2923 CMOS 2D detector (BM31) and λ = 0.31232 Å. Program Bubble[224] was used for 2D diffraction patterns integration to obtain 1D ones. At Diamond 45 photomultiplier detectors, each with a Si(111) analyser crystal, working in a high-resolution mode were used[226]. The data was collected with λ = 0.82657 Å and a step size

of 0.004°. High-temperature synchrotron powder X-ray diffraction (SR-PXD) patterns were collected at the Elettra-Synchrotron Trieste, Trieste, Italy at the Materials Characterization by X-ray Diffraction (MCX) beamline. Diffraction patterns were collected at 20 KeV energy (λ = 0.61992 Å) and 2θ angle range of 1 to 35° at from RT to 1000 °C in air, the heating rate between each temperature step 3 °C/min.

3.2.1.1.3 Neutron powder diffraction

Neutron powder diffraction (NPD) is another type of diffraction technique using the beam of the neutron as a radiation. Usually the thermal neutron beam, with a wavelength comparable to the atomic radius ($\lambda \sim 1 - 2 \cdot 10^{-10}$ m) are applied. The diffraction of those neutrons on the periodic arrangements of atoms is strong and occurs in an analogous way to x-ray diffraction, however, the scattering mechanism differs. While the x-rays interact with the electron cloud, the neutrons are scattered by atomic nuclei[227]. What is more, neutrons possess a magnetic moment, which may interact with the material. The most significant interaction is neutron elastic scattering from magnetic spin or orbital moments in magnetic atoms, which leads to strong diffraction effects on magnetically ordered structures. This is the reason why neutron powder diffraction Is a very useful tool in studying magnetic materials[227].

Two types of neutron powder diffraction experiments are used. The first is time-of-flight neutron powder diffraction (TOF-NPD), which uses a continuous distribution of wavelengths at a fixed angle. The other one is constant wavelength neutron powder diffraction (CW-NPD). Both of these modes have several advantages and disadvantages, providing the same information of material structure[227].

To sum up, neutron powder diffraction is a powerful tool in materials studies, being complementary to many other techniques. However, due to the requirement of a neutron source, it is rarely the method of a first choice. Nevertheless, in comparison to x-ray diffraction, it exhibits several advantages. It is a light element sensitive method, allowing to distinguish elements with similar Z numbers and isotopes. The penetration depth of neutrons is big, therefore it is easy to study the bulk of the material. Moreover, it is a suitable method for determining the magnetic structure of the material[227].

In this work double perovskite cobaltite, substituted with lanthanides, is studied. Naturally occurring isotopes of gadolinium and samarium exhibit exceptionally high cross-

sections for neutron absorption, as shown in Figure 3.6, thus samples containing those two elements are unsuitable to be measured with NPD. This issue was solved with the synthesis of a ^{160}Gd enriched sample, which is a much less neutron-absorbing isotope.

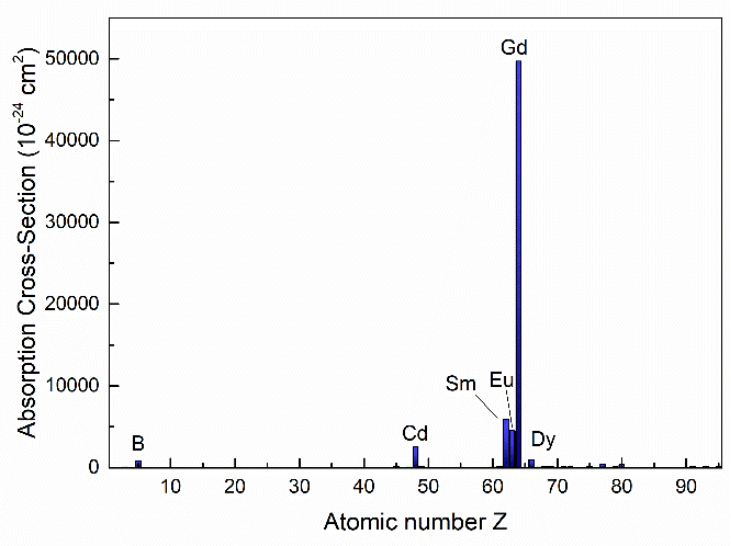

Figure 3.6 Neutron absorption cross-section for 2200 m/s neutrons as a function of Z number[228]

The PND data was collected at two different facilities JEEP II reactor in Kjeller, Norway, and Spallation Neutron Source (SNS) in Oak Ridge U.S. JEEP II uses the constant-wavelength diffractometer PUS (λ =1.555 Å) and vanadium 6 mm diameter cans for sample holding. At SNS the Time-Of-Flight (TOF) instrument POWGEN with 3 mm diameter vanadium canes was applied.

Since more than one facility was used for both synchrotron and neutron diffraction the specification of experimental details is required. Table 3.2 consists of all information where each sample was measured.

Table 3.2 The summary of experimental details of synchrotron and neutron diffraction

Ln	RT SR-PXD	HT SR-PXD	NPD
La	BM01 (SNBL), ESRF	MCX Elettra, Triest	PUS, Kjeller, Norway
Pr	BM01 (SNBL), ESRF	MCX Elettra, Triest	PUS, Kjeller, Norway
Nd	BM01 (SNBL), ESRF	MCX Elettra, Triest	PUS, Kjeller, Norway
Sm	BM01 (SNBL), ESRF	Not Applied	Not Applied
Gd	I11, Diamond	Not Applied	^{160}Gd enriched sample POWGEN, Oak Ridge, USA
Tb	BM31 (SNBL), ESRF	Not Applied	PUS, Kjeller, Norway
Dy	BM31 (SNBL), ESRF	Not Applied	Not Applied

3.2.1.1.4 Rietveld refinement

The diffraction pattern is a result of the powder diffraction experiment regardless of the type of radiation used. As mentioned in chapter 3.2.1.1.1 the position and shape of the may provide much information on crystal structure, which cannot be extracted directly. The Rietveld refinement is the first method of analysing the powder diffraction pattern, which uses the entire pattern. In this technique, the diffraction pattern is simulated based on a mathematical model. What is unique with this method is the fact, that the mathematical model consists not only of structural parameters, like space group, lattice parameters, etc., but also deals with experimental details, like applied geometry, sample shift, and many others. The main concept of this technique is to fit those parameters to, in a series of iterations, minimize the weighted sum of the squared difference between the observed and calculated patterns. Equation 3.4 describes the used least square method. In this equation, W is a weight, and c stands for scale factor[229].

$$M = \sum_i W_i \left(y_i^{obs} - \frac{1}{c} y_i^{calc} \right) \tag{3.4}$$

The result of Rietveld refinement is just the set of mathematical parameters that describes the obtained diffraction pattern in the best way. The compliance of the observed and calculated pattern, which shows the quality of the fit, is described with the parameters given by equations 3.5 and 3.6. R_p is called profile residual, while R_{wp} weighted profile residual. R_{wp} follows directly from the square root of the quantity minimized, scaled by the weighted intensities. What is more, the parameter, describing the best possible fit for the given dataset is introduced, R_{exp}. The R_{exp} is given with equation 3.7, where N is the number of data points, and P is the number of fitted parameters. The other parameter used to describe the refinement quality is the *goodness of fit*, represented with equation 3.8[229].

$$R_{wp}^2 = \frac{\sum_i W_i\left(y_i^{obs} - y_i^{calc}\right)^2}{\sum_i W_i\left(y_i^{calc}\right)^2} \tag{3.5}$$

$$R_p = \frac{\sum_i \left|y_i^{obs} - y_i^{calc}\right|}{\sum_i y_i^{obs}} \tag{3.6}$$

$$R_{exp}^2 = \frac{N - P}{\sum_i W_i\left(y_i^{calc}\right)^2} \tag{3.7}$$

$$GOF = \left[\frac{R_{wp}}{R_{exp}}\right]^2 \tag{3.8}$$

Rietveld refinement may be applied for analysing the patterns obtained using all applied diffraction methods, including the refinement of the magnetic structure using neutron diffraction. Regardless of how useful and powerful this method is, it requires a lot of knowledge and experience from the user. The fitted parameters should be strictly controlled to check their physical change. The quality of fit may be improved based on initial restrictions[229].

The simultaneous Rietveld refinement was applied to analyse the results of synchrotron-radiation powder diffraction, and neutron powder diffraction. The sequential refinement was applied for high-temperature SR-PXD studies. The refinement was performed on the full set of data simultaneously and proceeded as follows: at first, the initial refinement on room-temperature diffraction patterns was performed. The goal of this stage was to obtain the acceptable fit of the background, peak position, and shape. In the next

step, the obtained results were copied to the following diffraction pattern, which was then refined. In this approach the resulting parameters are used as a starting point for the next diffractogram, however, all the diffraction patterns are refined independently. Then, the number of iterations were performed to improve the fit.

3.2.1.2 Microscopic methods

The microscope is one of the earliest used laboratory instruments because the easiest way to understand the object is to take a deep look into it. In this study, two-electron microscope techniques were used. Despite many analogies to optical microscopy, electron microscopy using offers incomparably greater research possibilities.

Electron microscopy uses an electron beam as a radiation. According to the De Broglie hypothesis, the wavelength associated with the beam of electrons of a high momentum is much lower than that of the visible light. It provides significantly higher resolving power in comparison to optical microscopy. To understand the principle of operation the description of the interaction between electron beam and matter is necessary. Figure 3.7 shows schematically, how the electron beam interacts with matter. Electrons collide with the atoms in a material. As a result of this interaction, they could be reflected or absorbed. Absorption leads to an excited state, which relaxes through the emission of secondary electrons or electromagnetic waves. A technique that is based on the examination of the signal reflected from the sample surface is scanning electron microscopy (SEM). However, the word 'reflected' is in this case a kind of a mental shortcut, because the nature of the outgoing signal is not a reflection in itself, but it describes well the direction of the generated radiation. Each type of interaction involves different volumes of the sample material and provides various information on tested material[230]. If the sample thickness is small enough, the electron can be transmitted through the sample, which provides another dose of information on the material. It is transmission electron microscopy (TEM) that examines the signal coming out of the sample[231].

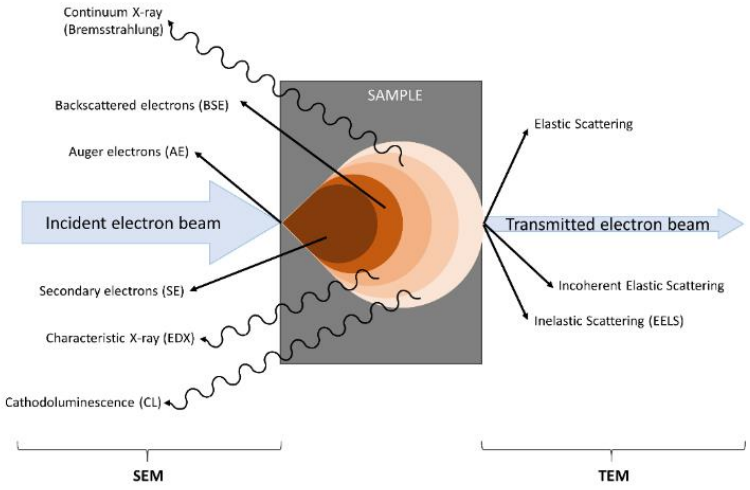

Figure 3.7 The scheme of interaction between an electron beam and matter[230],[231]

3.2.1.2.1 Scanning electron microscopy

Scanning electron microscopy (SEM) is a technique to imagine the investigated material's surface, which is illuminated with the electron beam. This method analyses the signal reflected from the sample, giving basic information on the morphology of the sample. However, according to different types of outgoing signals, much more information on the material can be obtained. Signal coming from the most outer layers of the surface of the material are auger electrons that provide information on the chemical composition of surface layers[232]. From the subsurface layers of the sample secondary electrons are produced in inelastic interaction between the electron beam and the sample. This signal is mainly used for imaging the topography of the surface[233]. As a result of inelastic collisions with atoms in the deeper volume of the material the backscattered electrons are produced. The number of reflected electrons is proportional to the atomic number of the materials components, due to the increased likelihood of collision with larger atoms. This causes differences in the contrast of phases with different chemical compositions, being useful for distinguishing between phases. Backscattered electrons provide also information on crystallography, the topography of the material[234]. Moreover, to types of x-rays are produced, characteristic, and continuum x-rays. The spectrum of characteristic x-rays is unique for each chemical element. Thus EXD provides direct information on the chemical composition of the investigated material [235]. Continuum x-rays are mostly a background signal[235]. The last type of outgoing signal is cathodoluminescence, which is mostly used

for optical properties characterization at nanoscale[236]. In this technique, the electron beam is moved across the surface of the sample to map it.

SEM provides also many types of detectors and imaging modes, making it a powerful tool in surface imaging. The microstructure was investigated with the use of an FEI Quanta FEG 250 Scanning Electron Microscope (SEM). The imaging was performed with secondary electron Everhart-Thornley Detector (ETD) and Backscattered Electrons Detector (BSED).

3.2.1.2.2 Transmission electron microscopy

Transmission electron microscopy (TEM) is a high-resolution microscope technique that is based on the analysis of the signal transmitted through the thin sample radiated with the beam of high-energy electrons. It enables imaging of material structure with atomic resolution. Similarly to the reflected signal, the transmitted one is also of different origin giving a wide range of measuring advantages[231].

- Direct beam
- Coherent elastic scattered electrons
- Incoherent inelastic scattered electrons
- Incoherent elastic forwarded scattered electrons

Analysing each type of outgoing signal much information on the materials is provided. First of all, as mentioned above TEM may be applied to obtain the image of the material at atomic resolution. More information on crystal structure is provided by the transmitted electron diffraction. The chemical composition at the atomic resolution scale may be also investigated with TEM[231].

A probe-corrected JEM ARM 200F instrument provided with Energy Dispersive x-ray Spectroscopy (EDS) and Electron Energy Loss Spectroscopy (EELS) was used in TEM studies. The $BaLaCo_2O_{6-\delta}$, $BaPrCo_2O_{6-\delta}$, $BaNdCo_2O_{6-\delta}$, $BaGdCo_2O_{6-\delta}$ samples were analysed. They were ground in a mortar and dripped on a TEM grid. High-resolution TEM (HRTEM), Scanning Transmission Electron Microscopy (STEM), Selected-Area Electron Diffraction (SAED), EDS EELS, and combined imaging-analytical techniques for chemical mapping at atomic spatial resolution (STEM-EELS-SI) were used in search of possible superstructures. The temDM MSA routine running under Digital Micrograph was

used for the digital processing and signal-to-noise ratio (SNR) enhancement of the EEL Spectrum Images[237]. HRTEM images were simulated with a multislice technique using Crystal Kit and Mac Tempas software kits. The images were generated with the variable thickness t and the defocus of the objective lens, f.

3.2.2 Electronic structure

An electronic band structure is a distribution of energy levels that may be occupied by the electrons in compounds. According to quantum theory electrons in free atoms can have only discrete, well-defined energies. The energy level is defined by quantum numbers. When the atoms form chemical compounds the energy levels mix, creating a molecular orbital. Calculation of energy levels in solids requires considering the interaction between electrons and crystal lattice. Because of this interaction, the ranges of permitted and forbidden energies are formed. Band structure determines the basic properties of the material, inter alia transport, and optical properties. There are many techniques for investigating the band structure. Even though drawing a full band diagram requires studies on a single crystal, techniques studying polycrystalline materials also provide valuable, but not necessarily full information on the electronic band structure. This chapter includes the description of experimental techniques used to investigate the electronic structure of $BaLnCo_2O_{6-\delta}$ compounds[238]. Most applied techniques deal with absorption spectra, which measure the attenuation of the radiation as a function of radiation energy. Lines or bands in such a spectrum represent the energy splitting between two levels. On this basis, the full energy diagram may be a constructed, but it requires a wide theoretical knowledge since many transitions are forbidden, thus they may be not visible in the investigated spectrum[238].

3.2.2.1 X-ray absorption spectroscopy

X-ray absorption spectroscopy is a technique using synchrotron x-rays. The key interaction taking place in this method is an inelastic scattering[222]. When the radiation energy corresponds to the separation of some energy levels a sharp increase in absorption is observed, what is called an absorption edge (Figure 3.8 a)[239]. In the XAS method, the core electrons are excited. Two types of excitation may occur, the core electron may be transferred to an unoccupied state in the valence band or leave the absorbing atom as a wave to a continuum. Those two effects are presented in Figure 3.8 b[216]. Electron transfer to the valence band affects the spectrum close to the absorption edge threshold, including

the pre-edge features. This regime is called x-ray absorption near edge structure (XANES). The virtual valence state occupied by the electron transferred from the core energy level may be both highly localized on the absorbing atom and delocalized onto neighbouring atoms, having charge transfer characteristics[216]. The higher energy of the incident beam may cause the transfer of an electron to the energy continuum. Electron escaping the absorbing atom has an excess of kinetic energy, which provides the photoelectron with its momentum[216]. This effect affects the spectrum at energies higher than the absorption edge threshold. This regime is called extended x-ray absorption fine structure (EXAFS). Analysis of XANES and EXAFS regimes provides much information on the material. XANES gives the information on the electronic structure of specific elements, while EXAFS provides a quantitative description of local coordination geometry and bonding distance[221]. From the point of this study, the investigation of the L-edge of transition metal seems to be of particular importance. This edge is highly sensitive to local electronic structure, which includes its valence state, symmetry, and spin state of the transition metal[221]. Those features are considered as strongly influencing the properties of the double perovskite cobaltites[240].

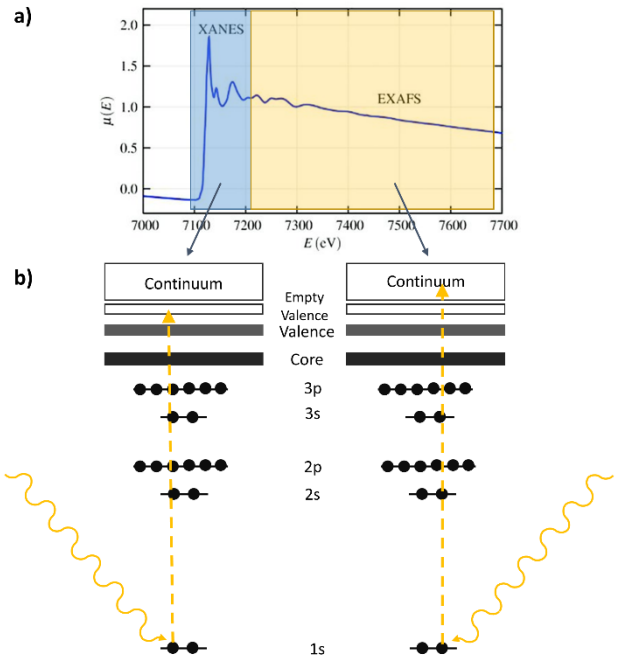

Figure 3.8 Concept of XAS. X-ray absorption spectrum of FeO with marked XANES and EXAFS regions from [239] (a), scheme of transitions in XANES and EXAFS from [216](b)

X-ray Absorption Spectroscopy measurements were performed at the Solaris National Synchrotron Radiation Centre in Kraków, Poland. A dedicated PEEM/XAS

bending magnet beamline was utilized to measure Lanthanide-$M_{4,5}$, Co-$L_{2,3}$, and O-K edges. For measurements. Powder samples were mounted on the carbon tape and placed on the Omicron plates. The measurements were performed under ultra-high vacuum at room temperature.

The Co-$L_{2,3}$, and O-K edges were chosen to be analysed due to the strong dependencies of those edges on cobalt oxidation and spin state. The pre-peak on the OK edge results from the transition of the electrons from the O*1s* core-state to hole-states of p character. In case of transition metal oxides, the O*2p* ligand-hole states are usually mixed with *s*, *p*, and *d* stated of neighbouring atoms. The availability of O*2p* states, which work as dipole-allowed excitation channels, determines the visibility of the states. Thus, the pre-peak structure is not visible in completely ionic oxides[241].

3.2.3 Thermoanalysis

Thermoanalysis is a wide range of methods of studying how the materials' properties change with temperature. It may be divided based on what property is measured. In this study thermogravimetric analysis was applied, which measures the mass change upon temperature changes. This chapter describes also iodometric titration, which is not a thermoanalysis in the strict sense, nevertheless, the results of IT are a starting point for oxidation studies.

3.2.3.1 Iodometry

Titration is a quantitative technique of analytical chemistry. Several types of titrations are known. In this study redox titration, using iodine as an oxidizing agent is used. This method is known as Iodometric titration. It is usually used to determine the concentration of an analysed substance. In this work, however, this method is used to determine the oxidation state of cobalt in the well-specified volume of an investigated compound. This value is used for the oxygen stoichiometry calculation[242].

The analysis is a sequence of strictly controlled chemical reactions. At first, the sample and the excess potassium iodide are dissolved in hydrochloric acid, which results in a solution containing the following ions: Ba^{2+}, Ln^{3+}, O^{2-}, K^{+}, I^{-}. Cobalt may adopt different oxidation states in the perovskite structure; thus the solution may consist of: Co^{2+}, Co^{3+}, Co^{4+}. The whole process takes part in a protective atmosphere because atmospheric oxygen could

oxidize cobalt, distorting the titration result[243]. The iodine reduces cobalt according to the following reactions:

$$2\,Co^{3+} + 3\,I^- \rightarrow 2\,Co^{2+} + I_3^- \quad (3.9)$$

$$Co^{4+} + 3\,I^- \rightarrow Co^{2+} + I_3^- \quad (3.10)$$

In the following step, the strictly controlled amount of sodium thiosulfate ($Na_2S_2O_3$) is added, and the backward reaction of iodine takes place, according to reaction 3.9. This reaction leads to complete discolouration of the solution, which is considered the endpoint of the titration. To make it easier to catch the moment of discolouration of the solution at the very end of the titration, a starch indicator is added[243].

$$I_3^- + 2\,{S_2O_3}^{2-} \rightarrow 3\,I^- + {S_4O_6}^{2-} \quad (3.11)$$

The volume of used sodium thiosulfate is directly dependent on the oxidation state of cobalt, which can be calculated with the formula 3.12, where $V_{N_2S_2O_3}$ stands for volume of thiosulfate used, $c_{N_2S_2O_3}$ is the molar concentration of sodium thiosulfate, $m_{BaLnCo_2O_{6-\delta}}$ and $M_{BaLnCo_2O_{6-\delta}}$ are mass and molar mass of the compound, accordingly.

$$Co_{AVG} = 2 + \frac{V_{N_2S_2O_3} \cdot c_{N_2S_2O_3}}{2 \cdot \frac{m_{BaLnCo_2O_{6-\delta}}}{M_{BaLnCo_2O_{6-\delta}}}} \quad (3.12)$$

Knowing the cobalt average oxidation state, the δ value can be easily found, with the relation 3.13.

$$\delta = 6 - \frac{5 + 2 \cdot Co_{AVG}}{2} \quad (3.13)$$

3.2.3.2 Thermogravimetric analysis

Thermogravimetric analysis is a thermal analysis method that measures changes in the mass of the sample with the changes in temperature and atmosphere. TGA is useful in the investigation of many different chemical processes, like kinetics of decomposition, oxidation, and reduction. In this study, TGA was applied mostly for investigating the water uptake and oxidation/reduction phenomena.

Thermogravimetric analysis is a widely used technique to investigate the proton defect formation in the materials. The ability to incorporate protons manifests itself in the

form of an increase in the mass of the material under the influence of an atmosphere containing water vapor, thermobalance enables to detect this effect. In the literature two different approaches are proposed to study the water uptake, isobaric and isothermal mode. In isothermal mode at constant temperature the water vapor partial pressure is changed upon constant temperature, while in isobaric mode the water vapor partial pressure remains constant at changing temperature. In pure proton conductors the results of isobaric and isothermal measurements are consistent[244]. In mixed conductors, however, the mass gain may result not only from proton defect formation, which leads to overestimation of the results. Figure 3.9 shows the comparison of proton defect concentration in $BaGd_{0.8}La_{0.2}Co_2O_{6-\delta}$ determined by the means of isothermal and isobaric TGA. The measurement conducted under isobaric conditions gave significantly higher results. On the basis of this validation, it was decided to use the isothermal mode, as more relevant for mixed conductors.

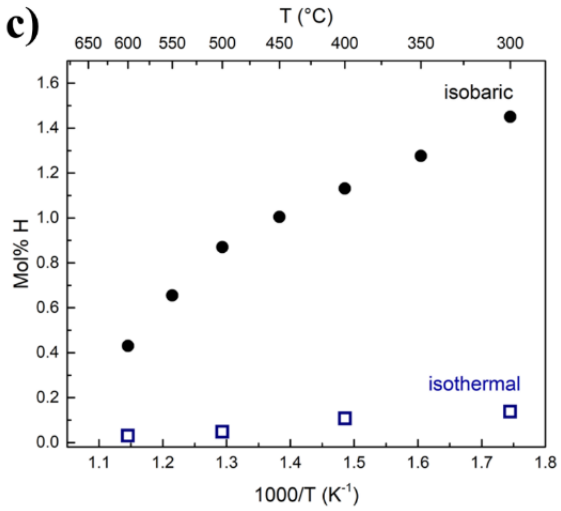

Figure 3.9 Proton defect concentrations in $BaGd_{0.8}La_{0.2}Co_2O_{6-\delta}$ as a function of the inverse of temperature determined by isobaric and isothermal TGA. This validation was performed by Ragnar Strandbakke, and presented by Aleksandra Mielewczyk-Gryń et al. at 5th International Workshop Prospects on Proton Ceramic Cells, Montpellier, France

Netzsch Jupiter® 449 F1 simultaneous thermal analyser was used for water uptake studies. The water uptake was measured in isothermal conditions at 300°C, however, the proper measurement was preceded by the following thermal program. The as-prepared $BaLnCo_2O_{6-\delta}$ powders were at first heated to 800°C with a heating rate of 5°C/min. At this temperature, the sample was kept for 5 hours to remove the residual water. Then the sample was cooled to 300°C, with the same cooling rate, and stabilized for 2 hours. After that, the atmosphere was switched from dry to humidified gas by the change of the water vapour

partial pressure in purge gas ($p_{H_2O} = 0.019$ atm). This atmosphere was maintained for 2 hours after the reverse switch to dry gas was performed. The synthetic air was used as a purge gas and nitrogen as a protective gas. A similar measurement procedure was applied to investigate hydration under a nitrogen atmosphere. The only change was in purge gas, which was replaced with N_2.

Netzsch Tarsus 401 thermobalance was used for oxidation studies. Samples were heated up to 900°C and cooled back to room temperature at 2°C/min. both heating and cooling rates. Similarly to water uptake analysis, synthetic air was used as a purge gas and nitrogen as a protective gas.

4 Results

This chapter contains a summary of the results of the investigation carried out on materials from the group of double perovskite cobaltites with the general formula $BaLnCo_2O_{6-\delta}$.

4.1 Crystal structure

The crystal structure of materials from the $BaLnCo_2O_{6-\delta}$ group was a subject of numerous studies and lively scientific discussion. The following subsections consist of the crystallographic description of the structure of the investigated group of material, determined by the means of diffraction and microscopy studies. The investigated materials were expected to form the derivative perovskite structure with A-site cations forming alternate layers along the c-axis. This results from the big size mismatch between barium and lanthanide cations. The probability of perovskite structure formation is classically described with the Goldschmidt tolerance factor t[47]. Recently also a new tolerance factor has been introduced. In the case of this study calculation of both Goldschmidt tolerance factor t, and new tolerance factor τ is challenging, since both of them are based on the ionic radii of constituent atoms, and the literature does not provide all of the required data. Ionic radii strongly depend on the oxidation state and coordination number. Among all investigated lanthanides the size of ionic radius at 3+ oxidation state, and CN=12 are known only for La, Nd, and Sm[153]. For cobalt, it is even more complicated, because the spin state also affects the ionic radius[153]. A detailed analysis of tolerance factors may be found in Appendix 2.

Figure 4.1 shows unit cells of the structures that were expected to be observed in the family of barium lanthanide cobaltites. This figure shows also the symbols used to describe oxygen positions, which are used within this work.

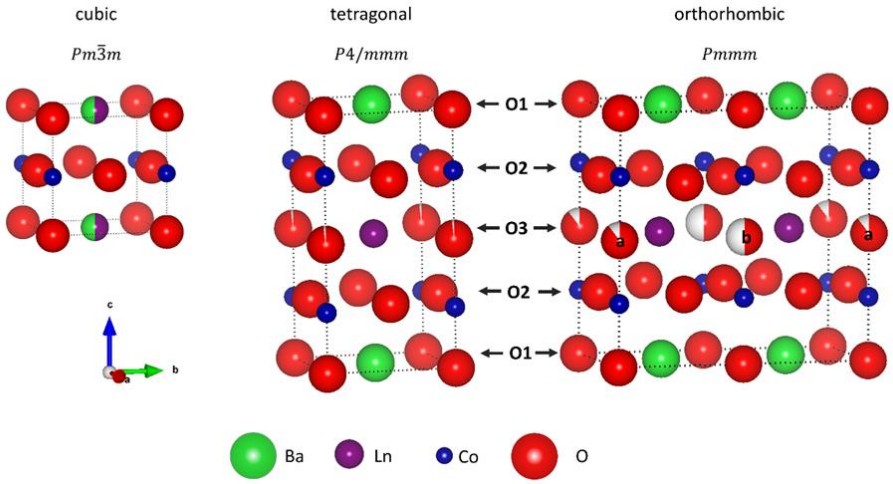

Figure 4.1 Summary of crystal structures adapted by $BaLnCo_2O_{6-\delta}$

Double perovskite structures, both tetragonal and orthorhombic were observed for all investigated lanthanides. Phase transition between the tetragonal and orthorhombic phase is directly related to oxygen stoichiometry, which is presented in Figure 4.2. The orthorhombic phase is observed only at the specific range of oxygen content. Highly oxidised and reduced samples exhibit tetragonal structure since O3a and O3b positions are equivalent. The oxygen content ranges given in Figure 4.2 were reported for $BaPrCo_2O_{6-\delta}$[240], however, for other lanthanides, those ranges should be similar. The presence of oxygen vacancies changes the local neighbourhood of cobalt ions, which coordination changes from octahedral to pyramidal. This affects not only the structure symmetry but also electron configuration, and spin state of cobalt[245].

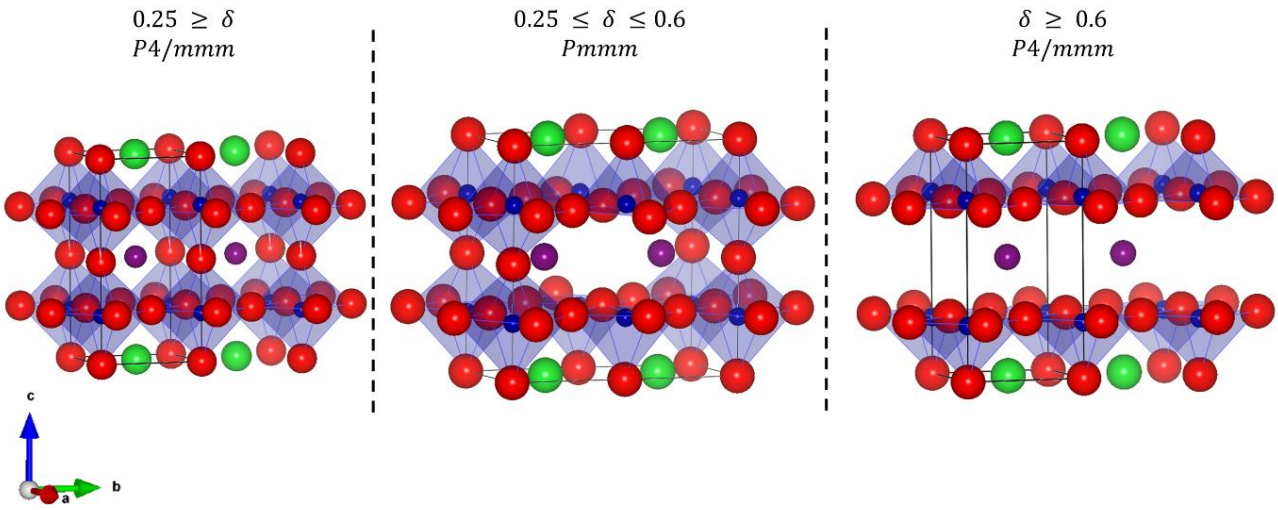

Figure 4.2 Comparison of tetragonal (P4/mmm) and orthorhombic (Pmmm) unit cells with different oxygen stoichiometry. Reprinted from Szpunar et al. 2020[102]

4.1.1 Powder x-ray diffraction

As described in chapter 3.1 laboratory-scale x-ray powder diffraction method was routinely used for every synthesised sample to examine the phase composition and check if the material exhibits the expected perovskite structure. Powder x-ray diffraction patterns are presented in Figure 4.3. In all compositions, the observed reflections are characteristic of a perovskite structure, which suggests that the obtained material does not contain impurity phases. With the increasing atomic number of lanthanides, the unit cell volume decreases since the peak positions shift towards higher angles. Although the positions of the reflections suggest the presence of a perovskite structure, their shape and symmetry change with the change of the lanthanide atomic number. Reflections in the diffraction pattern of lanthanum barium cobaltite, presented in Figure 4.3, are symmetrical and not separated, which indicates a cubic perovskite structure. All observed reflections in this pattern were indexed within the ideal perovskite structure of $Pm\bar{3}m$ space group. In the patterns of the cobaltites containing a lanthanide with a higher atomic number, the main peak splits into multiple reflections. The scale of multiplication varies among the investigated lanthanides. The peak splitting, especially around 32.5° and 58.5°, presented in Figure 4.3b and Figure 4.3c, respectively, confirms the symmetry lowering of the structure of investigated material. This is consistent with the literature reports on c-parameter doubling as a consequence of A-site cations ordering[192],[195],[202].

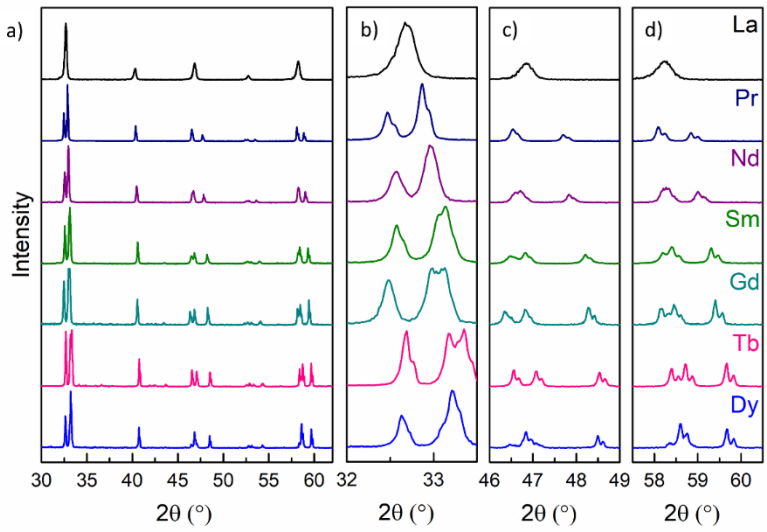

Figure 4.3 X-ray powder diffraction patterns of $BaLnCo_2O_{6-\delta}$ (a) with the characteristic ranges zoomed (b,c,d)

As-synthesised barium lanthanum cobaltite has the cubic perovskite structure with random distribution of Ba and La cations, while the annealing under argon atmosphere leads to A-site cations ordering. The comparison of x-ray diffraction patterns of the BLC sample before and after annealing is presented in Figure 4.4. The patterns are similar one to another with no significant reflection shift between those of as-prepared and reduced BLC. The main peak of the reduced BLC exhibits a shoulder on the lower-angle side indicating a doubling of the unit cell along the c direction. This splitting is more pronounced for the reflections around 47° and 58°. At 47° the reflection corresponding to the (200) plane splits into two components originating from the (200) and (004) planes. Similarly, at 57° the (211) reflection separates into two reflections from the (211) and (114) planes. This indicates the lattice parameter doubling along the c axis, which is a result of alternate layers of Ba-O and La-O formation in this direction.

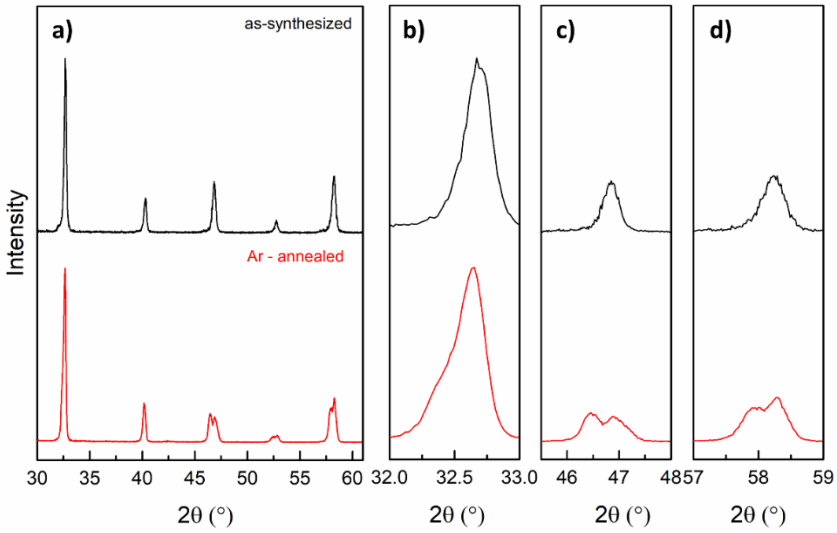

Figure 4.4 X-ray diffraction pattern of as-prepared (top) and reduced (down) BLC (a), with the characteristic ranges zoomed (b,c,d)

In-house x-ray diffraction was used in search of structural changes in the material after exposure to the humidified atmosphere. Figure 4.5 shows the XRD pattern of as-prepared and water-exposed $BaLaCo_2O_{6-\delta}$ and $BaNdCo_2O_{6-\delta}$. The materials were humidified within the TG experiment; thus graphs are labelled as before and after TG. Those materials were chosen as an example of two differently behaving materials in wet atmospheres. The mass increase in the humidified atmosphere was observed in $BaLaCo_2O_{6-\delta}$ while in $BaNdCo_2O_{6-\delta}$ not. However, in both cases, this does not appear to have any influence on the structure of the material and the diffraction pattern remains

unchanged after TGA measurement. This suggests that water uptake has no effect on the structure of the material and does not cause a secondary crystalline phase formation. The formation of the amorphous phase is also unlikely because the background signal remains unchanged. However, it must be emphasized that the laboratory scale x-ray diffraction may not be a sufficient tool to detect slight structural changes. What is more, if the concentration of the secondary phase is below the detection level, it may go undetected. Therefore, it is desirable to use more precise measurement techniques.

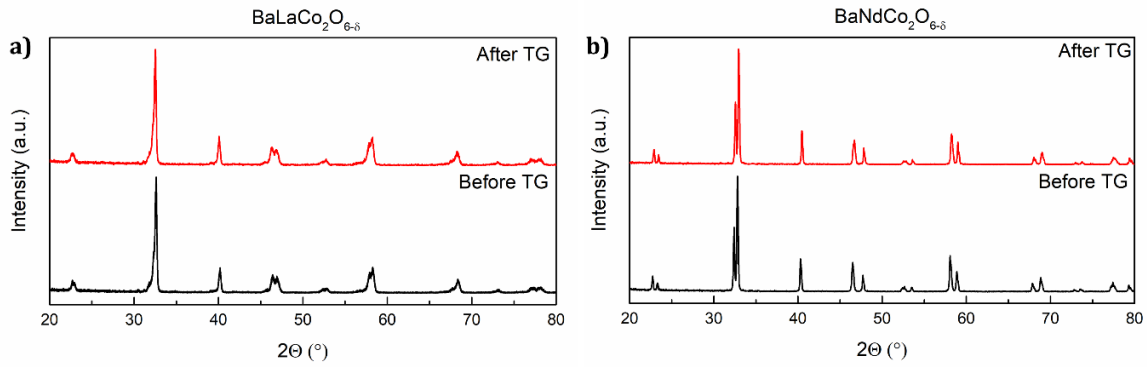

Figure 4.5 X-ray diffraction patterns before and after TG measurements of BLC (a), and BNC (b). Reprinted from Wachowski et al. 2020[246]

4.1.2 Combined synchrotron radiation x-ray diffraction and neutron powder diffraction

Since the diffraction patterns of tetragonal and orthorhombic perovskite structures exhibit a high level of overlapping and laboratory-scale x-ray diffraction is not sufficient to properly evaluate oxygen positions occupancy the combined synchrotron radiation x-ray diffraction and neutron powder diffraction were used to determine the structure of investigated materials.

Figure 4.6 depicts the powder diffraction patterns of as-prepared lanthanum barium cobaltite obtained with NPD (a), and SR-PXD (b). Those patterns were simultaneously refined using the Rietveld method to provide a full description of crystal structure. The Riveted refinement results confirm that the structure is cubic with the space group no. 221 ($Pm\bar{3}m$), and the lattice parameter $a = 3.8845(1)$ Å. All the reflections exhibit slight asymmetry at the low-angle side, which could not be fitted with the modification of the single-phase fit parameters. Therefore, it was decided to add to the model a second cubic phase with a slightly higher lattice parameter. The lattice parameter of this phase is $a = 3.9959(7)$ Å, while the weight phase fraction was 2.6(3) % wt. This value is below the detection level of laboratory-scale x-ray diffraction. In contrast to x-ray diffraction

neutron powder diffraction enables to determine the occupancy of oxygen positions. In the cubic lanthanum barium cobaltite, oxygen occupies only one Wyckoff position, which is in this case, within the uncertainty 0.007, fully occupied. This indicates the average oxidation state of cobalt Co_{AVG} = 3.5.

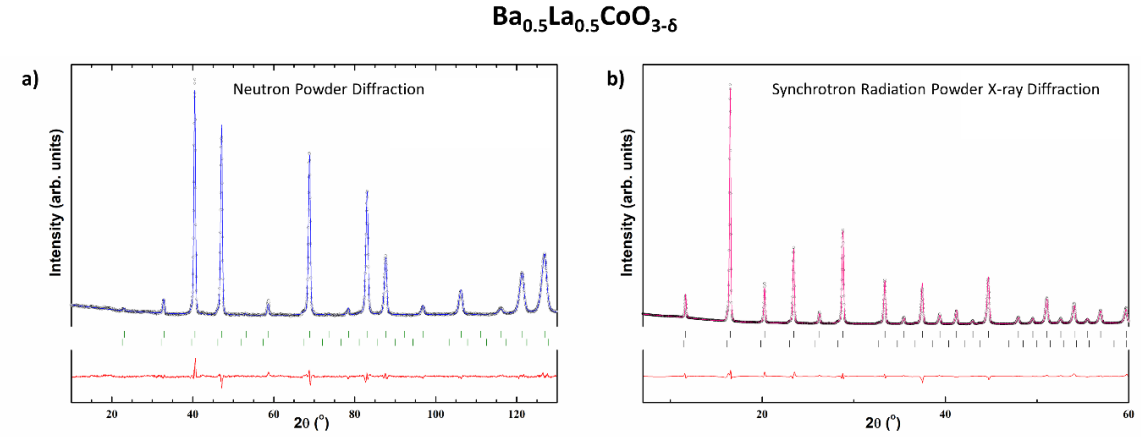

Figure 4.6 Powder diffraction pattern of cubic BLC, neutron powder diffraction (a), synchrotron radiation powder x-ray diffraction (b) with Rietveld refinement. Black points represent the experimental data, the solid line is the simulated pattern while the vertical ticks mark Bragg peak position. The red solid line is the difference plot. Reprinted from Wachowski et al. 2020[246]

Table 4.1 Refined structural parameters of cubic $Ba_{0.5}La_{0.5}CoO_{3-\delta}$, Wyckoff position, atomic coordinates, and site occupancies

ID	Wyck.	Position			Atom	Occ.
		X	Y	Z		
La1	*1a*	0	0	0	La^{3+}	0.5
Ba1	*1a*	0	0	0	Ba^{2+}	0.5
Co1	*1b*	½	½	½	Co^{3+}	1
O1	*3d*	0	½	½	O^{2-}	1.002(7)

In-house x-ray diffraction pointed out that the reduced barium lanthanum cobaltite, as well as the cobaltites containing other investigated lanthanides, exhibit a double perovskite structure, but it did not provide the proper structure description. Figure 4.7 presents the neutron (a) and synchrotron radiation (b) powder diffraction patterns and their Rietveld refinement profiles. $BaLaCo_2O_{6-\delta}$ was chosen as a representative of double perovskite cobaltites, the remaining diffractograms are placed in Appendix 1 (Fig. I.1-I5). For $BaSmCo_2O_{6-\delta}$ and $BaDyCo_2O_{6-\delta}$ only SR-PXD were obtained, due to the high cross-section for neutron absorption of samarium and dysprosium[228]. A tetragonal ($P4/mmm$) structure was expected for barium lanthanum cobaltite, but the refinement with a single tetragonal structure did not give satisfactory results. The mismatch between the intensities of measured and simulated data was significant. What is more, the refinement of a single orthorhombic structure ($Pmmm$) was also insufficient. Thus, it was decided to refine it as

a mixture of two phases, tetragonal and orthorhombic. This approach provided excellent agreement of raw data and the fit. The refined structure parameters for both orthorhombic and tetragonal phases are presented in Table 4.2 and Table 4.3.

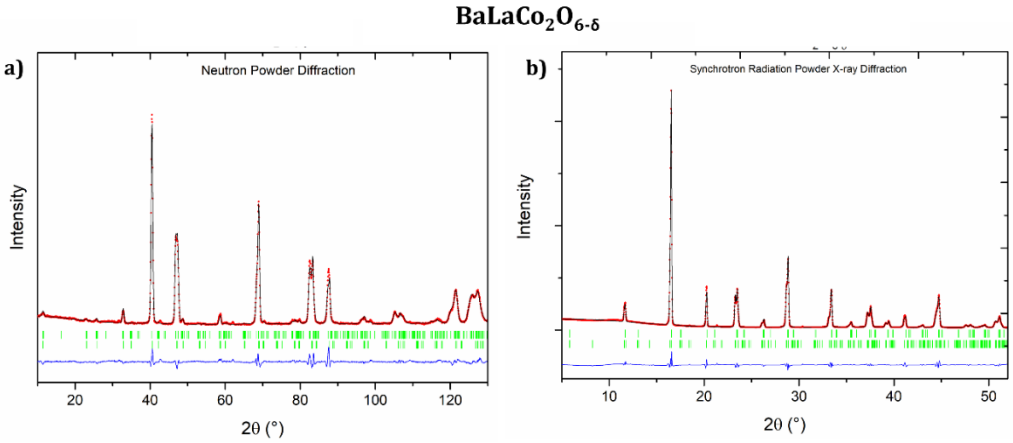

Figure 4.7 Powder diffraction pattern of double perovskite BLC, neutron powder diffraction (a), synchrotron radiation powder x-ray diffraction (b) with Rietveld refinement. Reprinted from Wachowski et al. 2020[246]

Table 4.2 Refined structural parameters of orthorhombic $BaLaCo_2O_{6-\delta}$, Wyckoff position, atomic coordinates, and site occupancies

ID	Wyck.	Position			Atom	Occ	Layer
		X	Y	Z			
La1	*2p*	½	0.249(1)	½	La^{3+}	1	La-O
Ba1	*2o*	½	0.254(1)	0	Ba^{2+}	1	Ba-O
Co1	*2r*	0	½	0.243(3)	Co^{3+}	1	Co-O
Co2	*2q*	0	0	0.253(2)	Co^{3+}	1	Co-O
O1a	*1a*	0	0	0	O^{2-}	1	Ba-O
O1b	*1e*	0	½	0	O^{2-}	1	Ba-O
O2a	*2r*	½	0	0.267(7)	O^{2-}	1.07(8)	Co-O
O2b	*2t*	½	½	0.260(8)	O^{2-}	0.99(7)	Co-O
O2c	*4u*	0	0.252(2)	0.264(7)	O^{2-}	1.02(6)	Co-O
O3a	*1g*	0	½	½	O^{2-}	0.95(8)	La-O
O3b	*1c*	0	0	½	O^{2-}	0.97(7)	La-O

Table 4.3 Refined structural parameters of tetragonal $BaLaCo_2O_{6-\delta}$, Wyckoff position, atomic coordinates, and site occupancies

ID	Wyck.	Position			Atom	Occ.	Layer
		X	Y	Z			
La1	*1b*	½	½	0	La^{3+}	1	La-O
Ba1	*1a*	½	½	½	Ba^{2+}	1	Ba-O
Co1	*2h*	0	½	0.245(2)	Co^{3+}	1	Co-O
O1	*1c*	0	0	½	O^{2-}	1	Ba-O
O2	*4i*	0	½	0.249(2)	O^{2-}	1	Co-O
O3	*1d*	0	0	0	O^{2-}	0.66(4)	La-O

The diffraction pattern of the tetragonal and orthorhombic double perovskite exhibits a high level of overlapping because of the close position of Bragg reflections. This leads to a strong correlation between refinement parameters. The most significant difference between the orthorhombic and tetragonal phase diffraction patterns is observed in the range of 2Θ below 10°, in which the peaks coming only from the orthorhombic Pmmm structure are present. Low angle reflections were observed in all investigated double perovskites, for this reason, the orthorhombic structure was applied for the Rietveld refinement. The orthorhombic perovskite structure, with the space group Pmmm, was determined to be the majority phase in all investigated $BaLnCo_2O_{6-\delta}$.

The agreement of calculated and measured patterns was satisfactory for most of the compounds, excluding $BaSmCo_2O_{6-\delta}$. In the case of BSC, a big difference between the calculated and measured intensities was observed, when the structure was refined with the single-phase orthorhombic structure. Bragg reflections described with the (120), (022) and (102) Miller indices exhibited the highest intensity mismatch. To decrease the level of this inconsistency, a similar approach as for BLC was applied. The BSC pattern was refined as a mixture of tetragonal and orthorhombic phases. The refinement results showed that the orthorhombic BSC is a majority phase, with a phase fraction of 75% wt. The refined structural parameters of $BaLnCo_2O_{6-\delta}$ are presented in Table 4.4. $BaTbCo_2O_{6-\delta}$ contains a small amount (below 3 wt. %) of secondary $CoYbO_3$, $TbCoO_3$, Co_3O_4. All these phases are barium free, which indicates a slight deviation from barium stoichiometry in the majority phase.

Table 4.4 Summary of simultaneous PND and SR-PXD Rietveld refinement, space group, unit cell parameters, and refinement quality.

Ln	Symmetry	Unit cell parameters (Å)	R_{wp}	Comments
La	cubic $Pm\bar{3}m$	a = 3.8850(6)	R_{wp} (SR-PXD) = 5.23% R_{wp} (PND) = 4.22% R_{wp} (total) = 4.71%	As prepared powder
La	tetragonal $P4/mmm$ (35 wt. %) orthorhombic $Pmmm$ (65 wt. %)	a = 3.8767(1) c = 7.7819(3) a = 3.9155(2) b = 7.8142(5) c = 7.7247(3)	R_{wp} (SR-PXD) = 5.82% R_{wp} (PND) = 5.41% R_{wp} (total) = 5.60%	Ar annealed
Pr	orthorhombic $Pmmm$	a = 3.864(2) b = 7.716(3) c = 7.541(3)	R_{wp} (SR-PXD) = 7.94% R_{wp} (PND) = 4.75% R_{wp} (total) = 6.23%	Unit cell parameters reported for PND data
Nd	orthorhombic $Pmmm$	a = 3.9090(1) b = 7.8050(2) c = 7.6163(1)	R_{wp} (SR-PXD) = 6.90% R_{wp} (PND) = 4.47% R_{wp} (total) = 5.50%	
Sm	tetragonal $P4/mmm$ (25 wt. %) orthorhombic $Pmmm$ (75 wt. %)	a = 3.8962(1) c = 7.5757(4) a = 3.8880(1) b = 7.8375(2) c = 7.5603(1)	R_{wp} = 7.83%	NPD not applied
Gd	orthorhombic $Pmmm$	a = 3.8771(1) b = 7.8265(2) c = 7.5338(1)	R_{wp} (SR-PXD) = 11.85% R_{wp} (PND) = 1.45% R_{wp} (total) = 4.19%	
Tb	orthorhombic $Pmmm$	a = 3.8667(2) b = 7.8126(1) c = 7.5126(1)	R_{wp} (SR-PXD) = 4.97% R_{wp} (PND) = 5.49% R_{wp} (total) = 4.96%	Impurities < 3 wt. %
Dy	orthorhombic $Pmmm$	a = 3.8609(1) b = 7.8001(1) c = 7.5020(1)	R_{wp} = 7.62%	NPD not applied

Figure 4.8 shows the unit cell parameters determined with Rietveld refinement. The plots of the relations between lanthanide ionic radii and a-, and c- parameters and unit cell volume includes the data for all space groups, marked with different symbols. The b-parameter is presented only for the materials with the orthorhombic Pmmm unit cell. The a- and c- parameters increase with increasing lanthanide ionic radius. Non-monotonic dependence of the b parameter was observed, but the relative change of this value is less than 1%. Despite the lack of significant changes in the b parameter, changes in the a and c parameters translate into an increase in the volume of the unit cell with the increasing size of the lanthanide, presented in Figure 4.8d. Outstanding values of lattice parameters were obtained for $BaPrCo_2O_{6-\delta}$.

The combined SR-PXD and NPD studies allow for determining the O-site positions occupancies. In the case of all investigated lanthanides, oxygen vacancies tend to locate in

the Ln-O layer. The O1 and O2 positions remain fully occupied, within the measurement uncertainty for all investigated materials. In the tetragonal P4/mmm structure all O3 oxygen positions are equivalent, while in the orthorhombic Pmmm structure oxygen vacancies are ordered along the b direction thus two different oxygen positions O3a, and O3b may be distinguished. Thus, the occupancy ratio of positions O3b and O3a, presented in Figure 4.8e, may be an indicator of orthorhombic distortion, the lower this value, the higher the orthorhombic distortion is. This value increases with increasing the ionic radius of lanthanide from 0.095 for $BaTbCo_2O_{6-\delta}$ to 0.98 for $BaLaCo_2O_{6-\delta}$. The evidence of higher orthorhombic distortion of smaller lanthanide cobaltites is visible in SR-PXD patterns even without the Rietveld refinement. The higher the atomic number of Ln, the more pronounced low-angle reflections are, what can be seen in the figures presented in appendix I (Figure I.1-I.5). Interestingly, the O3b/O3a ratio of the BPC sample, unlike the lattice parameters, fits perfectly into the trend.

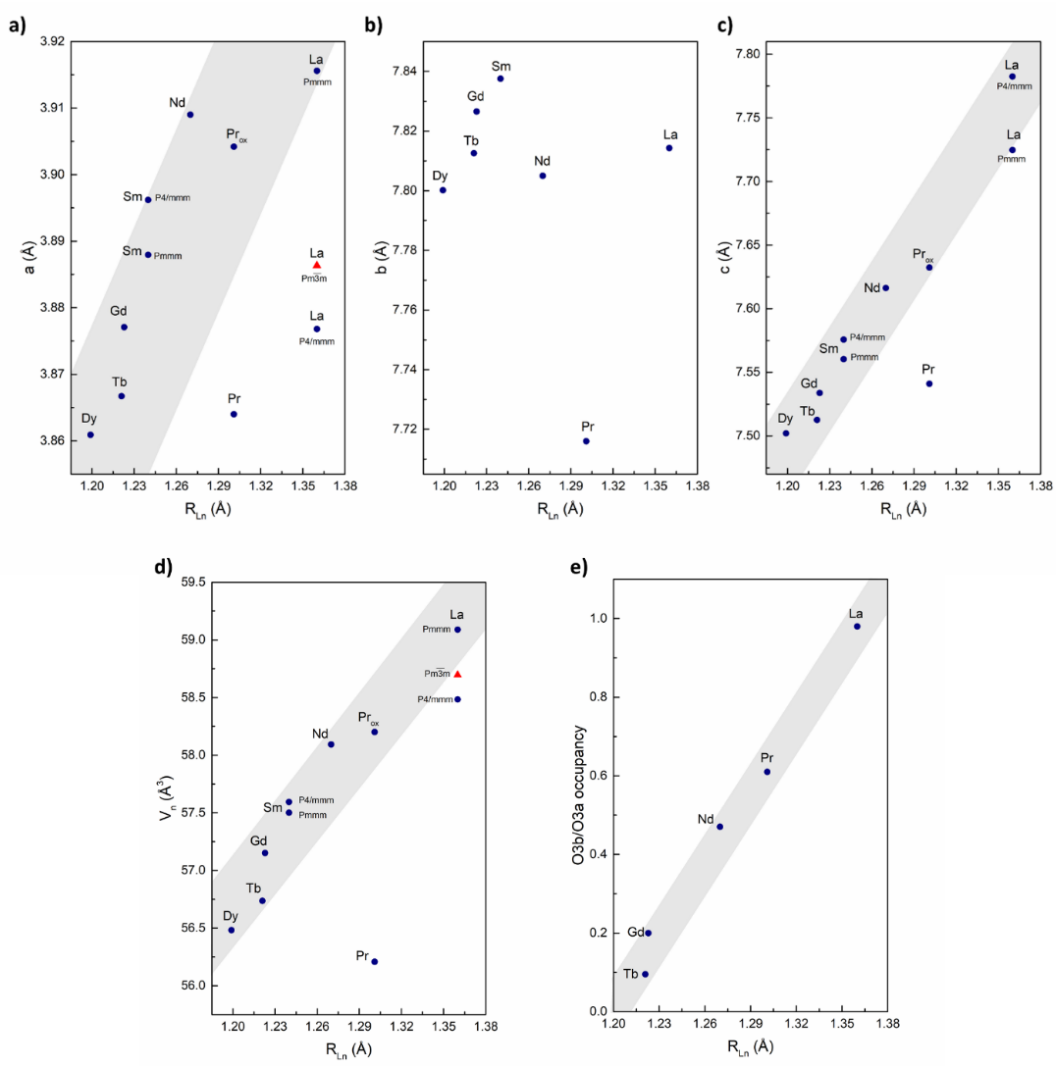

Figure 4.8 Lattice parameters obtained with the simultaneous Rietveld refinement of NPD and SR-PXD patterns as a function of ionic radius of lanthanide: a parameter (a), b parameter (b), c parameter (c), unit cell volume (d), O3b/O3a occupation ratio (e). The grey band is a guide for an eye, showing the general trend, not an actual fit.

Figure 4.9 shows the $Ba_{0.5}La_{0.5}CoO_{3-\delta}$ and $BaNdCo_2O_{6-\delta}$ SR-PXD patterns after annealing in high water vapour partial pressure, which was performed to investigate the stability of double perovskite in the humidified conditions. After annealing for 96 h in pH_2O = 10 bar at 300°C both cubic BLC, and double BNC remains single phase. No trace of secondary phase formation was detected.

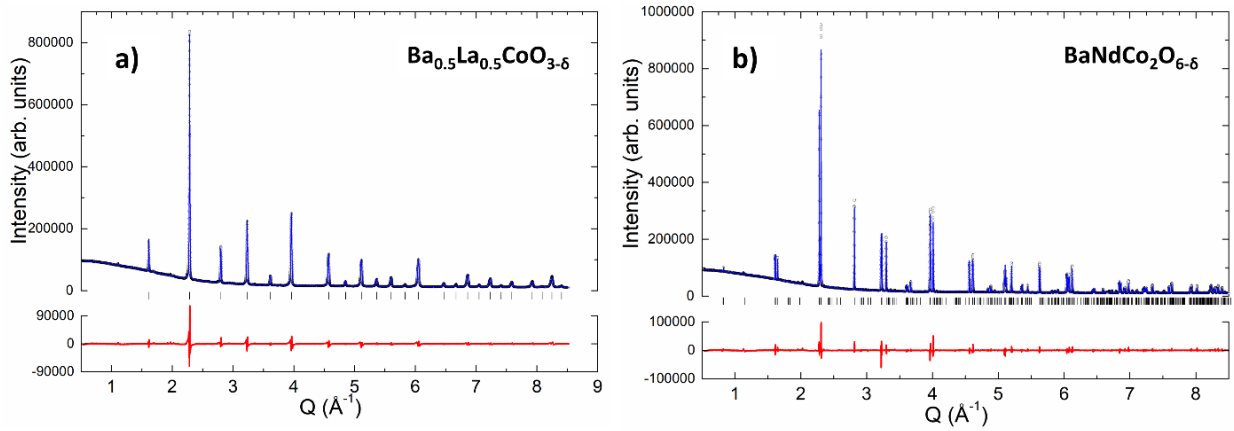

Figure 4.9 SR-PXD pattern with Rietveld refinement of $BaLaCo_2O_{6-\delta}$ (a) and $BaNdCo_2O_{6-\delta}$ (b) after annealing at 300 C, in water vapour partial pressure pH_2O = 10 bar for 96 h. Reprinted from Wachowski et al. 2020[246]

4.1.3 High-temperature synchrotron powder x-ray diffraction

Figure 4.10 shows high-temperature SR-PXD diffraction patterns of $BaLaCo_2O_{6-\delta}$ (a), $BaPrCo_2O_{6-\delta}$ (b), and $BaNdCo_2O_{6-\delta}$ (c), collected in the wide range of temperatures. No significant changes in diffractograms are observed up to 1000°C. No evidence of phase transition is visible in those diffraction patterns, while the reflection positions shift towards the lower angles indicating lattice parameters increase. At the highest temperature, some extra peaks are observed (marked with a '*'), which are characteristic of the quartz capillary specimen holder.

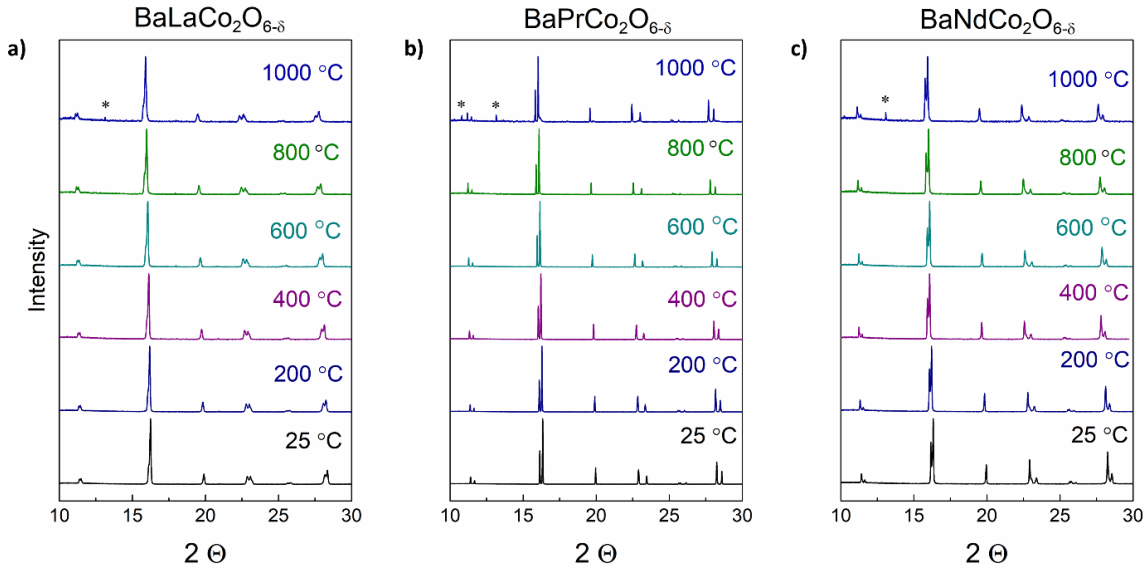

Figure 4.10 High-temperature synchrotron radiation powder x-ray diffraction patterns of $BaLaCo_2O_{6-\delta}$ (a), $BaPrCo_2O_{6-\delta}$ (b), $BaNdCo_2O_{6-\delta}$ (c). Reprinted from Szpunar et al. 2020[102]

The Rietveld refinement was performed on the high-temperature diffraction patterns. Based on room-temperature diffraction studies, it was decided to apply an orthorhombic

(space group Pmmm) structure as a starting model for the refinement. However, a single-phase orthorhombic model was insufficient to refine the diffraction patterns of BLC and BNC. Based on combined SR-PXD – NPD a two-phase model was applied. BLC was well represented by a mixture of tetragonal and orthorhombic phases, while for BNC the best agreement was reached for the combination of cubic and tetragonal phases. Figure 4.11 depicts the exemplary refinements of the room-temperature diffraction data for BLC, BPC and BNC, while diffraction patterns with Rietveld refinement profiles at the elevated temperatures are presented in Appendix 1 (Figures I.6-I.8). The tetragonal and cubic phases were the minority components, respectively, in BLC and BNC in the whole studied temperature range.

Figure 4.12 shows the temperature evolution of the minority phase fraction detected in BLC and BNC. At room temperature, the phase fraction of tetragonal $BaLaCo_2O_{6-\delta}$ is 35%, which is in good agreement with the results of combined SR-PXD-NPD studies. The phase fraction of the minority tetragonal BLC does not change below 400 °C, while above this temperature, a decrease in this phase fraction is observed. The phase fraction of the cubic phase in BNC is below 10% and remains constant within the measurement uncertainty in the whole temperature change.

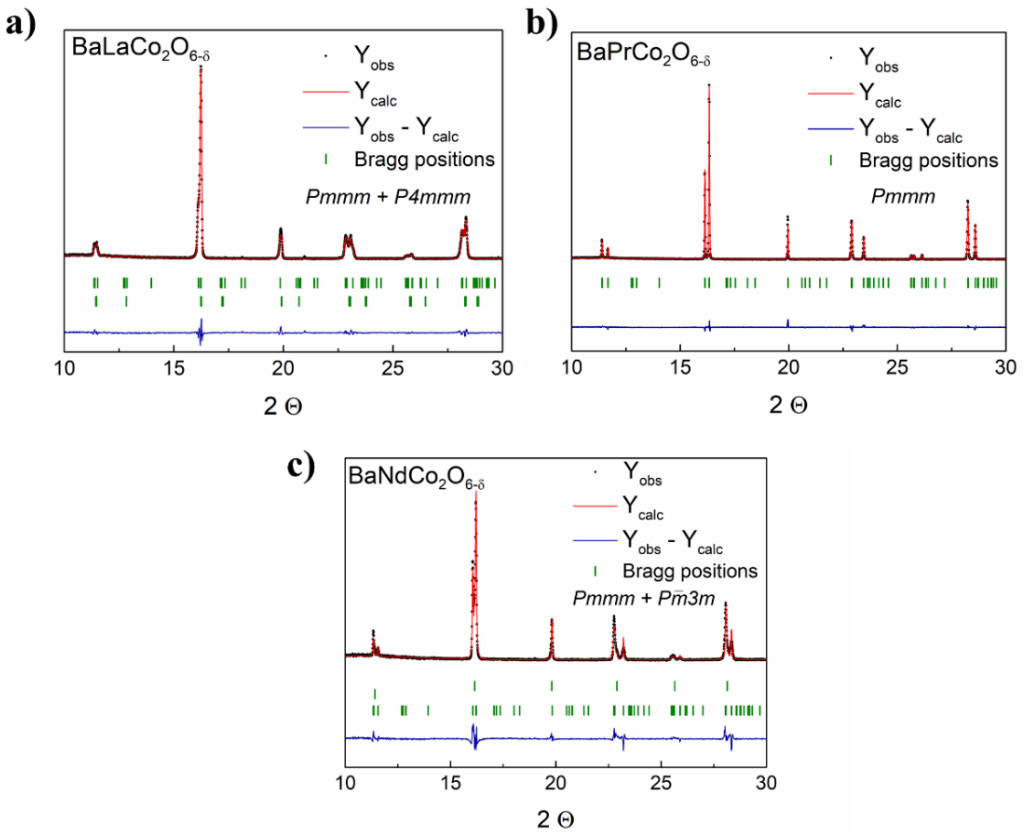

Figure 4.11 Room temperature synchrotron radiation x-ray diffraction patterns and the Rietveld refinement profiles of $BaLaCo_2O_{6-\delta}$, $BaPrCo_2O_{6-\delta}$, $BaLaCo_2O_{6-\delta}$. Measurement data is presented with black points, calculated pattern with the straight red line, the blue line is a difference curve, while green vertical tics show the Bragg peaks positions. Reprinted from Szpunar et al. 2020[102]

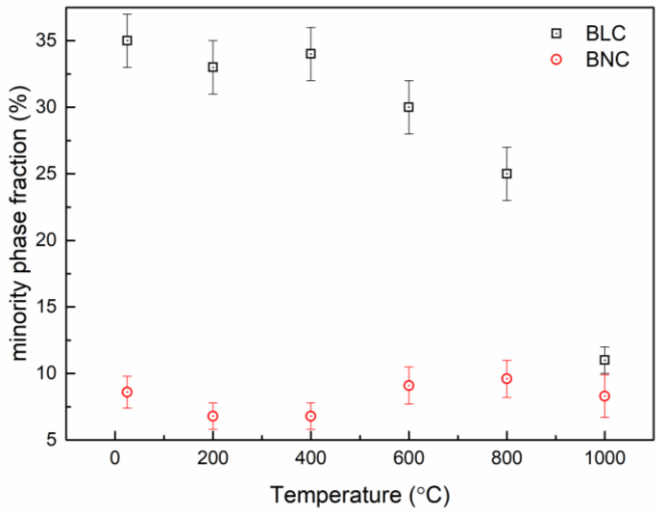

Figure 4.12 Minority phase fraction in BLC and BNC as a function of temperature

Figure 4.13 depicts the temperature evolution of $BaLaCo_2O_{6-\delta}$, $BaPrCo_2O_{6-\delta}$ and $BaNdCo_2O_{6-\delta}$ unit cell parameters determined by the means of Rietveld refinement. All unit cell parameters increase with increasing temperature, however not in all cases those dependencies are linear. In all investigated compounds, except the tetragonal phase of BLC,

the temperature evolution of a-parameter cannot be represented well with one linear function. Similar behaviour is observed in the temperature dependencies of the b-parameter of BPC, and BNC (Figure 4.13d). Unit cell volume of tetragonal BLC, PBC and BNC, shown in Figure 4.13g,h, increases linearly with the temperature.

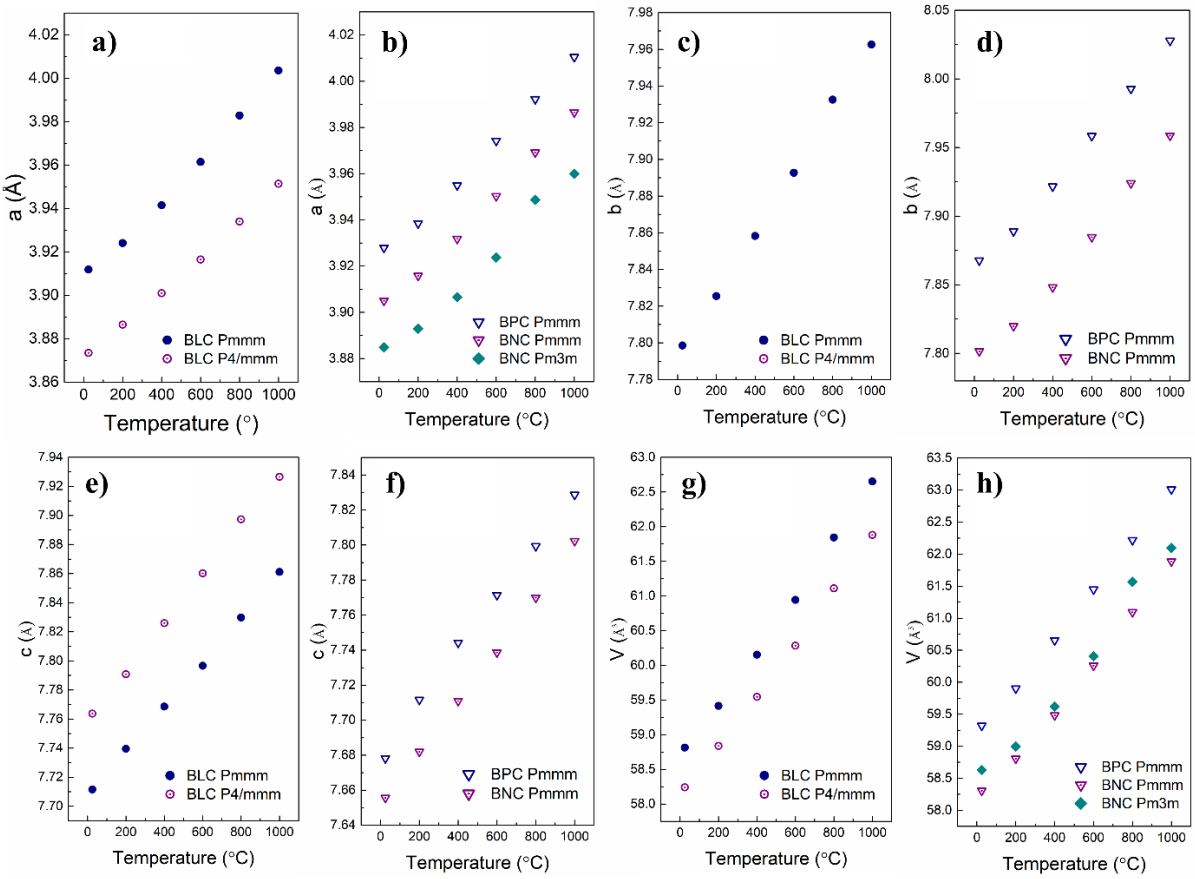

Figure 4.13 Temperature evolution of unit cell parameters. The a parameters of tetragonal and orthorhombic BLC (a); a parameters of orthorhombic BPC and BNC, and cubic BNC (b); b parameter of orthorhombic BLC (c); b parameter of orthorhombic BPC and BNC (d); c parameter of tetragonal and orthorhombic BLC (e); c parameter of orthorhombic BPC and BNC (f), unit cell volume of tetragonal and orthorhombic BLC (g); unit cell volume of orthorhombic BPC and BNC, and cubic BNC (h)

The temperature evolution of unit cell parameters may be used for the calculation of the thermal expansion coefficients. The temperature dependencies of the a and b-parameter were divided into low- and high-temperature ranges, corresponding to two different slopes in which two TECs were calculated. The obtained values of the thermal expansion coefficient are presented in Table 4.5. At high temperatures, TEC exhibit a higher value, because unit cell parameters change not only as a result of thermal vibrations but also a change in the stoichiometry of the material. The highest values of TECs at both low- and high-temperature ranges were observed in $BaLaCo_2O_{6-\delta}$, however the thermal expansion coefficient along c-axis is equal for all investigated lanthanides. Figure 4.14 shows the

relation between thermal expansion coefficient and lanthanide ionic radius, no direct relation between those two parameters is observed.

Table 4.5 Thermal expansion coefficients of BLC, BPC and BNC

Ln	Space group	direction	TEC ($\cdot 10^{-6}$)	
			T < 200°C	T > 200°C
La	Pmmm	a	17.8	26.5
		b	19.7	22.6
		c	19.7	19.7
	P4/mmm	a	20.6	20.6
		c	21.9	21.9
Pr	Pmmm	a	15.3	23.0
		b	15.5	22.1
		c	19.7	19.7
Nd	Pmmm	a	15.9	22.8
		b	13.4	22.6
		c	19.5	19.5
	$Pm\bar{3}m$	a	11.9	22.6

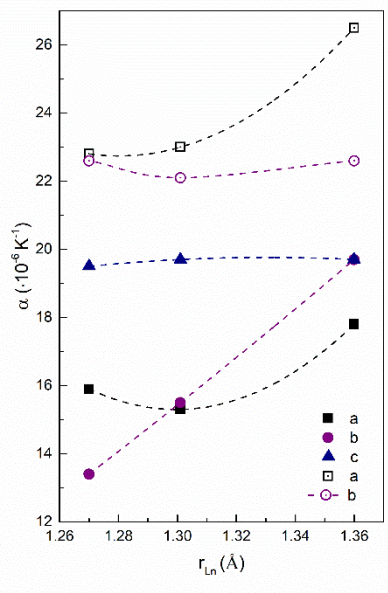

Figure 4.14 Thermal expansion coefficient as a function of lanthanide ionic radius for $BaLnCo_2O_{6-\delta}$ with orthorhombic double perovskite structure (space group Pmmm). Filled points are used to present the low-temperature TEC, while empty points for high-temperature TEC. The dashed lines are inserted as a guide for an eye

4.1.4 Scanning and transmission electron microscopy

Figure 4.15 shows the SEM images of $BaLaCo_2O_{6-\delta}$. The morphology of the material is uniform, and no contrast in the BSE image, which would indicate differences in chemical composition was observed. The sinterability of the investigated materials is high due to the cobalt, but materials may be easily fabricated with high open porosity. Such a morphology is especially desirable for electrode materials. Even with the high level of porosity the materials are mechanically strong, and the grains form a strongly fused framework.

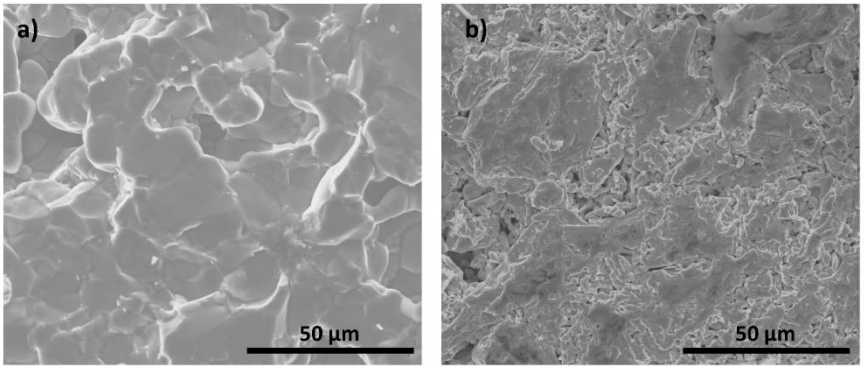

Figure 4.15 SEM pictures of $BaLaCo_2O_{6-\delta}$ imagined with secondary electrons (a), and backscattered electrons (b)

Transmission electron microscopy was used to investigate the crystal structure of double perovskite cobaltites in the hope to find evidence of A-site cations and oxygen vacancy ordering. During the measurement, the grains, oriented along the main pseudo-cubic zone axis towards the electron beam were searched.

Figure 4.16 a presents the typical TEM image of a double perovskite cobaltite grain, the corresponding Selective Area Electron Diffraction (SAED) pattern, presented in Figure 4.16b, indicates that the grain is oriented along the pseudo-cubic axis zone. The strongest diffraction spots correspond to the $\{100\}_c$ lattice planes associated with the lateral facets of the perovskite cubic unit cell. The distance between these planes determined based on the reciprocal space distance of diffraction spots is 0.39 nm, which corresponds to the a-parameter of the unit cell. Figure 4.16b shows that in halfway-between the strong $\{100\}_c$ reflections there are the weaker ones corresponding to the interplanar distance of 0.78 nm. That suggests the doubling of the unit cell parameter. Two exemplary weak spots are marked with arrows in Figure 4.16b. One of them is weaker than the other, which suggests that the nature of doubling in those two directions is different. The stronger of the weak doubled spots results from doubling along the c-axis, which confirms the A-site cations

ordering. The diffraction spots in the other direction may result either from doubling along the b-axis or the presence of two structural domains rotated at 90° with respect to each other. However, Rietveld refinement results clearly showed orthorhombic patterns thus the latter seems unlikely. What is more, a careful investigation of the outermost diffraction spots visible in the SAED pattern, presented in Figure 4.16, shows that they are split into two. The level of separation indicates a 1% variation of the interplanar distance, which perfectly fits the values of the b and c lattice parameters refined from the SR-PXD and NPD patterns for the orthorhombic structure of BLCO.

Figure 4.16c depicts the EDS spectrum of the investigated grain. Apart from barium, lanthanum, cobalt and oxygen, which come from the sample, other signals indicate the presence of Cu, C and Si. Copper and carbon come from the electron scattering on the TEM grid and carbon tape, while Si results from fluorescence processes inside the Si detector. The quantitative analysis of the elements of interest (except for O) gives the relative atomic ratio for Ba/La/Co on this grain the following values: 31.7/25.7/42.6 which is 1.2/1/1.7, slightly different from the nominal values 1/1/2.

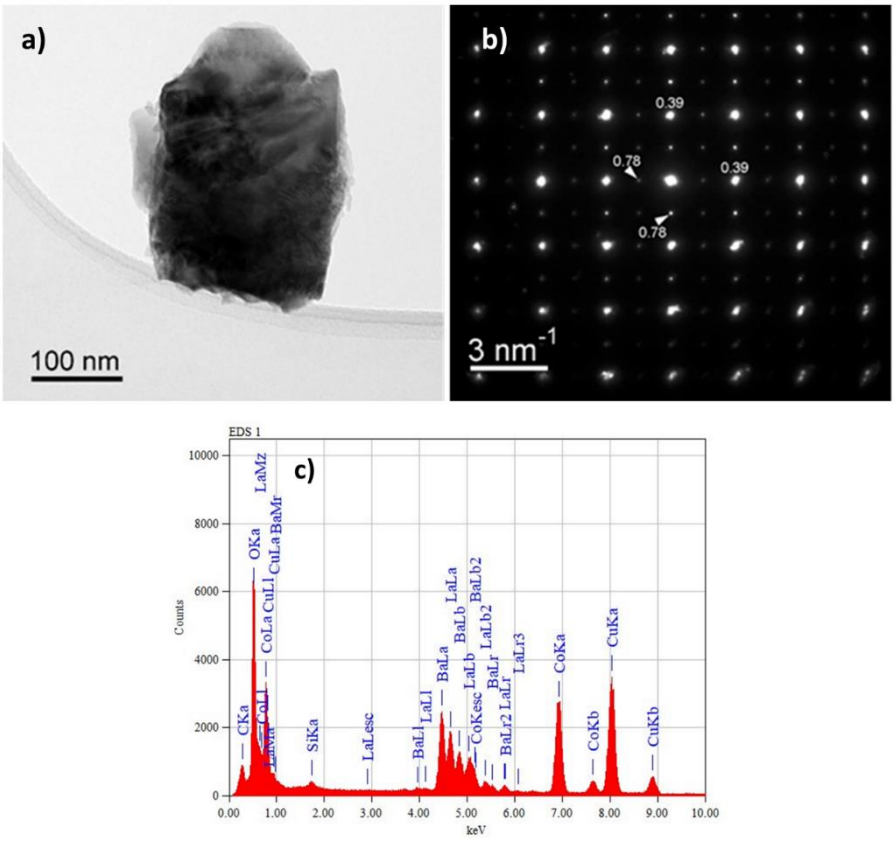

Figure 4.16 TEM images of $BaLaCo_2O_{6-\delta}$, TEM micrograph (a), SAED pattern (b), EDS spectra (c)

To understand whether the spot doubling results from oxygen vacancy ordering or the presence of two structural domains, the HRTEM studies were performed on the thinnest parts of the BLC grain. Figure 4.17 depicts the HRTEM image of the upper part of the $BaLaCo_2O_{6-\delta}$ grain, which is presented in Figure 4.16. Two areas were chosen for further analysis, and the corresponding SAED patterns of those two areas are presented next to the micrograph. The diffraction pattern of area 1 consists of strong spots with an interplanar distance of 0.39 Å, and weaker ones indicating 0.78 Å spacing. However, in contrast to Figure 4.16b, the spot doubling occurs only in one direction, which indicated the tetragonal structure of $BaLaCo_2O_{6-\delta}$. On the other hand, the spot doubling in area 2 occurs in two perpendicular directions. To investigate the nature of this doubling area 2 was enlarged. Figure 4.18 presents the enlargement image of area 2 shown in Figure 4.17. The intensity profile lines, which quantify the brightness of the spots confirm the periodicity of 0.78 Å along those two perpendicular directions.

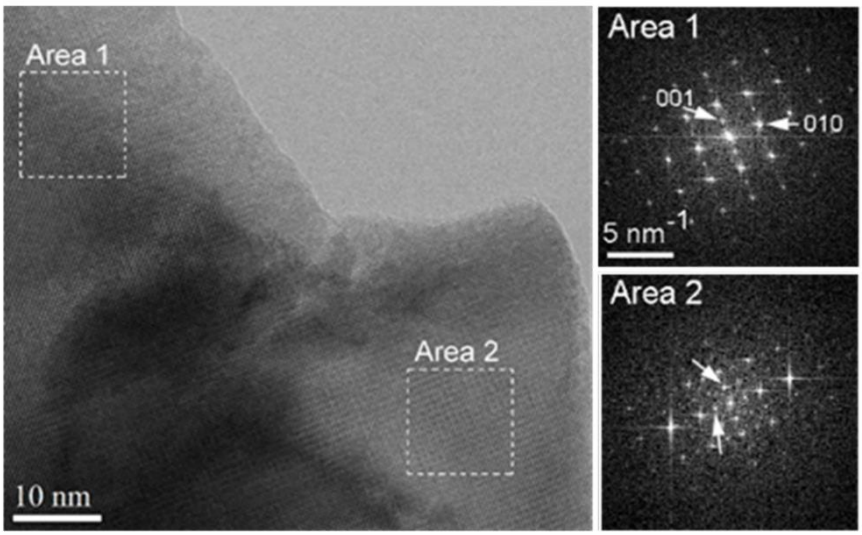

Figure 4.17 HRTEM image of BLC

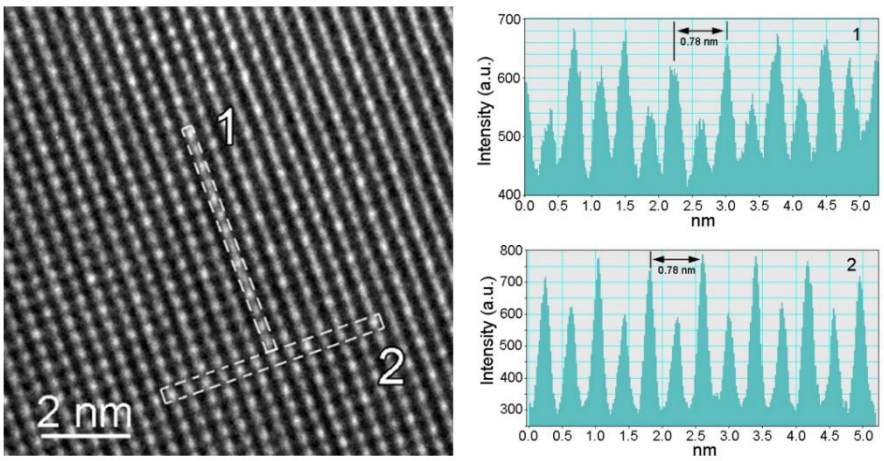

Figure 4.18 Enlarged HRTEM picture of BLC grain and intensity line profiles along two marked rows

The trace of different structural domains within one grain was spotted in $BaPrCo_2O_{6-\delta}$. Figure 4.19 presents the zoomed TEM image of the edge of the $BaPrCo_2O_{6-\delta}$ grain. The SAED patterns of the A and B areas are presented in Figure 4.19 b, and c, respectively. Both patterns can be indexed within the double perovskite structure with lattice parameters: a = 3.86 Å, b= 7.70 Å, and c = 7.50 Å, which is in good agreement with the SR-PXD and NPD results. Both diffraction patterns consist of rows of diffraction spots of alternating strong/soft intensity. These rows are disposed vertically in Figure 4.18b and horizontally in Figure 4.18c. The presence of soft diffraction spots with l odd in Figure 4.19b indicates the doubling of the c-parameter. In the SAED pattern presented in Figure 4.19c spots with k and l odds are visible, which indicates the doubling of both b- and c-parameters.

Based on the SAED pattern the orientation of each structural domain was determined. The A and B domains are oriented towards the **B** = [-210] and **B** = [0-11] zone axes, sharing the (122) family of planes. The crystallographic relation between A and B domains is $[-210]_A \parallel [0\text{-}11]_B$, $(001)_A \parallel (100)_B$.

The SAED patterns of both domains consist of weak spots marked with tilted arrows. Those spots are not allowed in the diffraction patterns along the two mentioned zones axes, however, as stated above, the investigated area is slightly larger than the single domain. Weak spots in the SAED pattern of the A domain are the trace of the B domain, and spots in the SAED pattern of the B domain come from A. The proximity of two different structural domains allows for their even more detailed analysis. It was possible to

make a high-resolution TEM image of the border of those two domains, which is presented in Figure 4.20a.

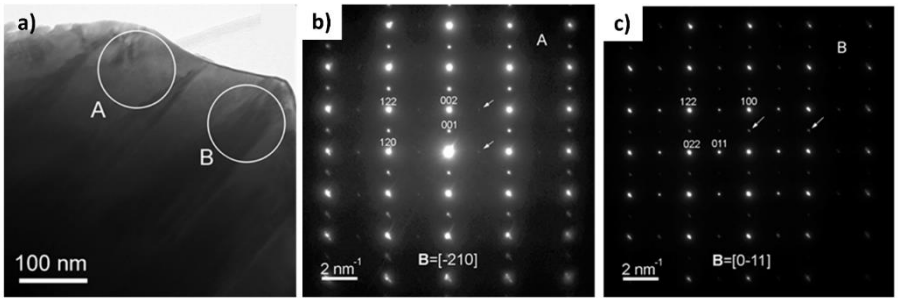

Figure 4.19 TEM image of the edge of Pr grain (a), SAED patterns corresponding to areas A and B (b), (c)

Figure 4.20 shows the grain boundary between two structural domains, differently oriented towards the electron beam. The areas of different atom arrangements are visible. The identified crystallographic directions are shown. In the picture, the areas of different orientations are marked in rectangles A and B, which correspond to the light and dark areas in Figure 4.19a. Figure 4.20b,c depicts the enlarged images of those two regions. Columns and rows of different brightness and contrast are visible along the marked direction. Intensity modulation points to the non-equivalency of the positions. This modulation may result from both different cations in these positions or differences in their occupancies. To explain the cause of these modulations the intensity line profiles were measured along the white arrows, and presented in Figure 4.20d, and c. In Figure 4.20d the modulation periodicity is 7.5 Å, which perfectly fits the c-parameter, resulting from the A site cations position. In the case of the B-domain, this periodicity is 5.4 Å, this value cannot be associated with the distance between Ba and Pr cations in this projection. What is more, also the spacing between Ba and Co cations in this orientation does not fit the periodicity.

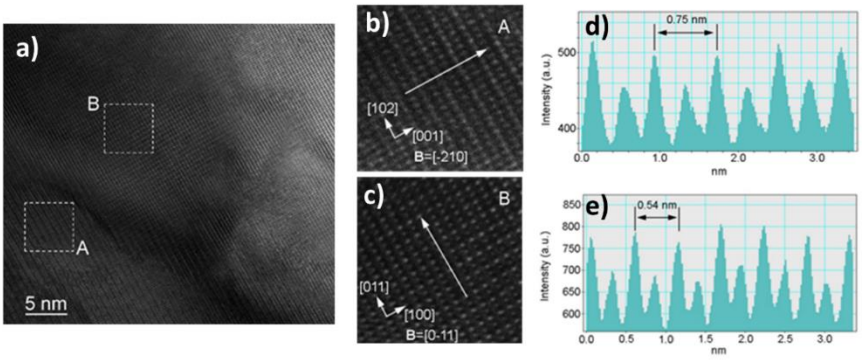

Figure 4.20 High-resolution TEM image of grain boundary between two structural domains (a), enlarged image of A domain oriented along B=[-210] (b), and B domain oriented along B=[0-11], line profiles measured along the white arrows (d,e)

Transmission electron microscopy was also used to find the element distribution in investigated materials. Figure 4.21 shows the EELS element mapping of $BaLaCo_2O_{6-\delta}$ (a), $BaNdCo_2O_{6-\delta}$ (b), and $BaGdCo_2O_{6-\delta}$ (c) with the vertical orientation of the c-axis. The element mapping was acquired by the scanning electron beam across the selected area (Figure 4.21). The EEL spectra of the whole investigated area (Fig Sxx) consist of the O K at 532 eV, Co $L_{3,2}$-edge with the two white lines at 779 and 794 eV, Ba $M_{5,4}$ white lines at 781 and 796 eV. What is more, the following lanthanide adsorption edges were present: La $M_{5,4}$ lines at 832 and 849 eV, Nd $M_{5,4}$ lines at 978 and 1000 eV, and Gd $M_{5,4}$ white lines at 1185 and 1217 eV. The intensities of these spectral lines have been used to determine the local chemical composition, presented in Figure 4.21. A-site cations ordering is visible in all the investigated materials; however, the barium and lanthanide separation is larger in $BaNdCo_2O_{6-\delta}$ and $BaGdCo_2O_{6-\delta}$, than in $BaLaCo_2O_{6-\delta}$. This suggests that barium and lanthanum form alternate layers, but the ordering is not perfect, they partially mix. The ionic radius of lanthanum is the closest to barium among all lanthanides, thus partial occupation of the same crystallographic positions introduces the weakest strain to the structure. As presented earlier, lanthanum barium cobaltite tends to form the cubic perovskite structure with a random distribution of La and Ba cations in the crystal structure. The cation ordering may be enforced by annealing the material in a reducing atmosphere, but the process of cation reorganization requires a long time to occur. Thus it may indicate that the reduction time was not long enough to complete the separation of the lanthanum and barium atoms.Figure 4.21 STEM images and EELS map of the BLC (a), BNC (b), and BGC (c). On the micrographs there are marked areas selected for TEM analysis.

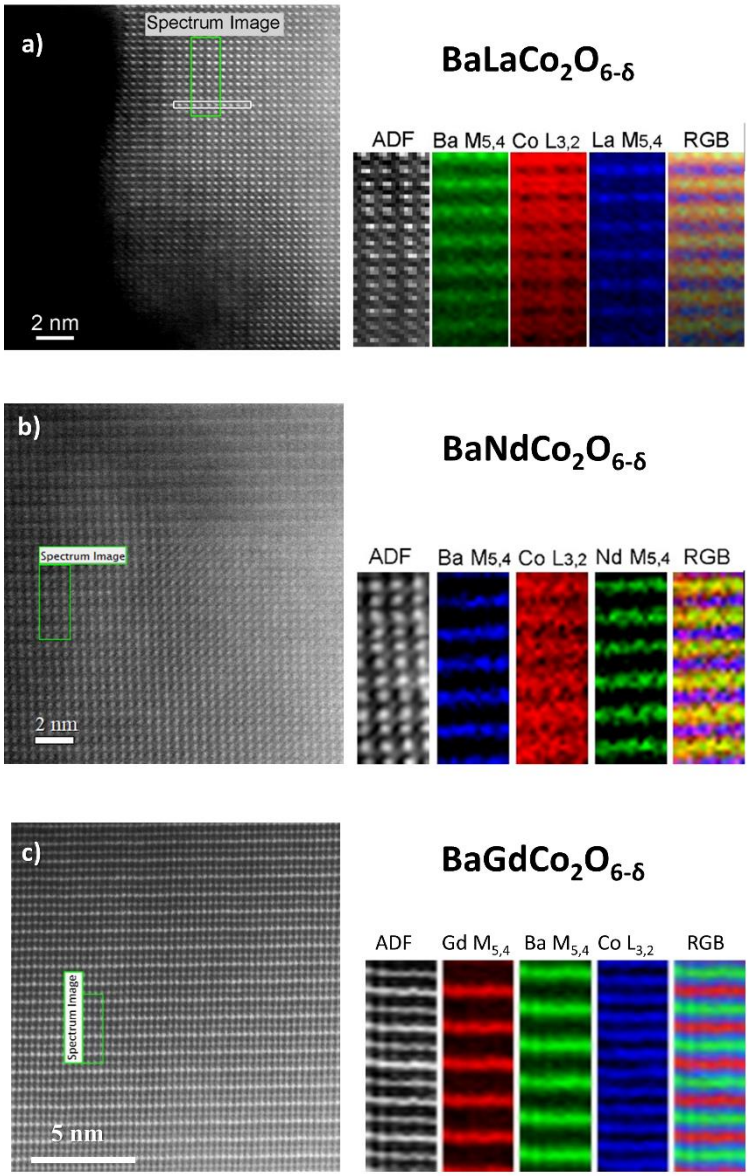

Figure 4.21 STEM images and EELS map of the BLC (a), BNC (b), and BGC (c). On the micrographs there are marked areas selected for TEM analysis

The quantitative analysis of EDS spectra (Figure I.12) allowed determining the relative atomic ratio, without taking into account the oxygen. The calculated atomic ratios are presented in Table 4.6 Chemical element atomic ratio in BaLnCo2O6-δ (Ln = La, Pr, Nd)For all investigated compounds the reduced atomic ratio of barium, lanthanide and cobalt slightly differs from the nominal value of 1/1/2, which suggests some deviation from expected stoichiometry. Nevertheless, it should be noted, that only one grain was the subject of the analysis. Some local changes in chemical stoichiometry may occur in the material. What is more, the EDS technique is based on the analysis of the absorption edges of each element. The maximum absorption edges of cobalt and barium are very close. The

spectral shift between Co $L_{3,2}$ and Ba $M_{5,4}$ white lines is only 2 eV, which strongly impedes the analysis.

Table 4.6 Chemical element atomic ratio in $BaLnCo_2O_{6-\delta}$ (Ln = La, Pr, Nd)

Ln	Ba/Ln/Co ratio	Ba/Ln/Co reduced ratio
La	31.7/25.7/42.6	1.2/1/1.7
Pr	25.2/26.7/48.1	0.9/1/1.8
Nd	19.6/22.3/58.1	0.9/1/2.6

Transmission electron microscopy was also used in search of amorphous or crystalline secondary phases on the surface of the materials exposed to the humidified atmosphere. Figure 4.22 shows the TEM images of two barium lanthanum cobaltite grains exposed to the humidified atmosphere. Those TEM images are typical of all investigated cobaltites, showing no significant changes upon hydration. The grain boundaries are not coated with any secondary phase, either crystalline or amorphous. The brightness modulation is a result of differences in the grain thickness.

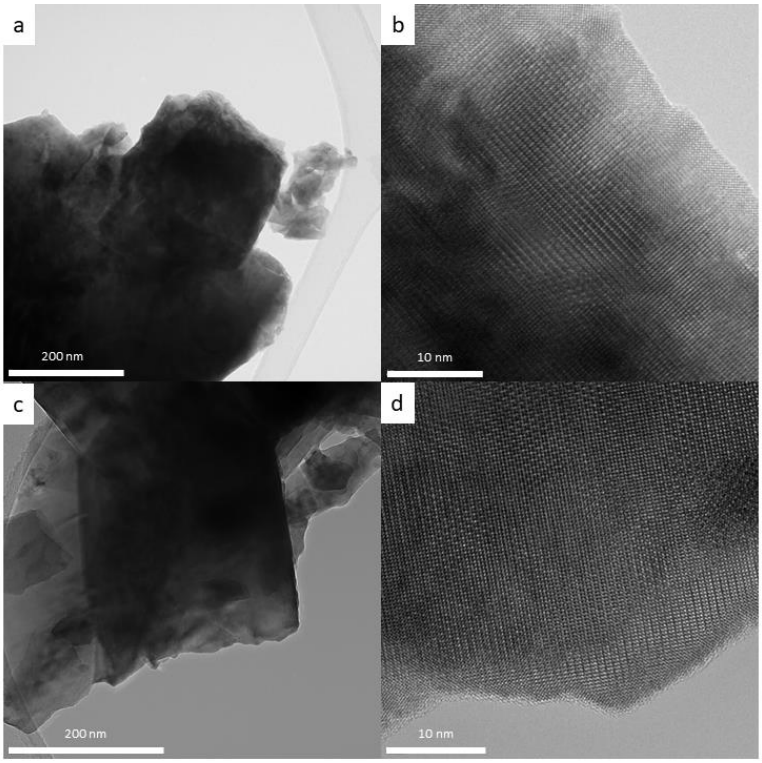

Figure 4.22 TEM images of two exemplary BLC grains which were exposed to humidified atmosphere (a,c) magnification of those images (b,d)

4.2 Thermal properties

4.2.1 Oxidation studies

The cobalt oxidation state strongly impacts the properties of double perovskites cobaltites. Thus, the knowledge of the average cobalt oxidation state and oxygen content is crucial for the property analysis of materials from this group. Iodometric titration was used to determine the level of cobalt oxidation at room temperature. The dependence of the average cobalt oxidation state and ionic radius of lanthanide is presented in Figure 4.23a. The oxygen content increases with the increasing ionic radius of lanthanide, reaching the highest value for BLC. The plot contains two points for $BaLaCo_2O_{6-\delta}$: one for the as-prepared material, with the cubic perovskite structure, and the other for the reduced compound with a layered structure. The former sample fits the trend well, while the latter has a lower cobalt oxidation state. This result appears significantly below the overall trend. Similarly, a significantly lower than expected value of the oxidation state was obtained for $BaPrCo_2O_{6-\delta}$ - marked as $Pr_{red.}$ To explain this result, another $BaPrCo_2O_{6-\delta}$ was synthesized – marked Pr_{ox} – which fits the trend well. A possible explanation is higher than in other lanthanides, the redox activity of Pr.

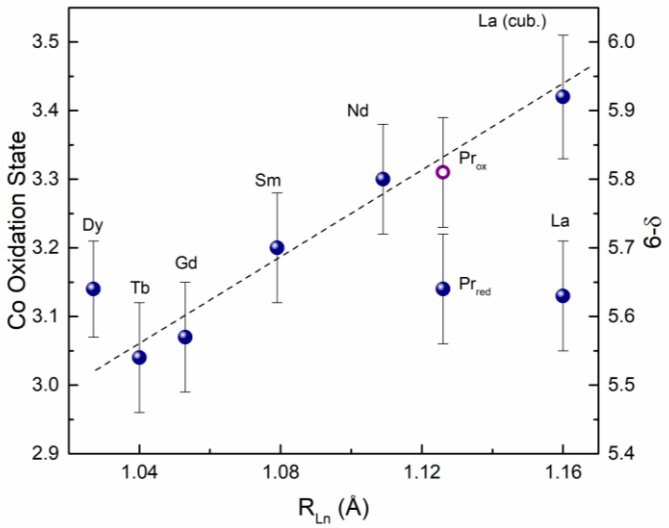

Figure 4.23 Average cobalt oxidation state and oxygen stoichiometry at room temperature of $BaLnCo_2O_{6-\delta}$ as a function of lanthanide ionic radius. Reprinted from Wachowski et al. 2020[246]

The average cobalt oxidation state determined by the means of iodometric analysis was used as an initial value for TGA studies. Figure 4.24 presents the average cobalt oxidation state and oxygen stoichiometry as a function of temperature. In all compositions, the oxygen stoichiometry remains constant up to 200-300°C. The onset temperature of oxygen release varies with the lanthanide, however, no clear trend between the temperature

at which reduction starts and the ionic radius of lanthanide was observed. Above this temperature, the oxygen content starts to decrease almost linearly with the temperature. A slightly different character is observed in $BaDyCo_2O_{6-\delta}$ and $BaTbCo_2O_{6-\delta}$, in which at the highest temperature the dependence changes the slope, or starts to increase, respectively. The average cobalt oxidation state and oxygen content increase with increasing ionic radius of the lanthanide. Such a dependence of oxygen stoichiometry of lanthanide ionic radius in double perovskite cobaltites was observed before[247],[248].

Figure 4.24a shows the oxidation curves of cubic and double perovskite BLC. Not only the initial oxygen nonstoichiometry of cubic $Ba_{0.5}La_{0.5}CoO_{3-\delta}$ but also the total mass change is lower than in its layered counterpart. However, the onset temperature of oxygen release is comparable for both polymorphs. Even though the cubic BLC is more stable than the double perovskite, no trace of oxidation of double perovskite lanthanum barium cobaltite was observed.

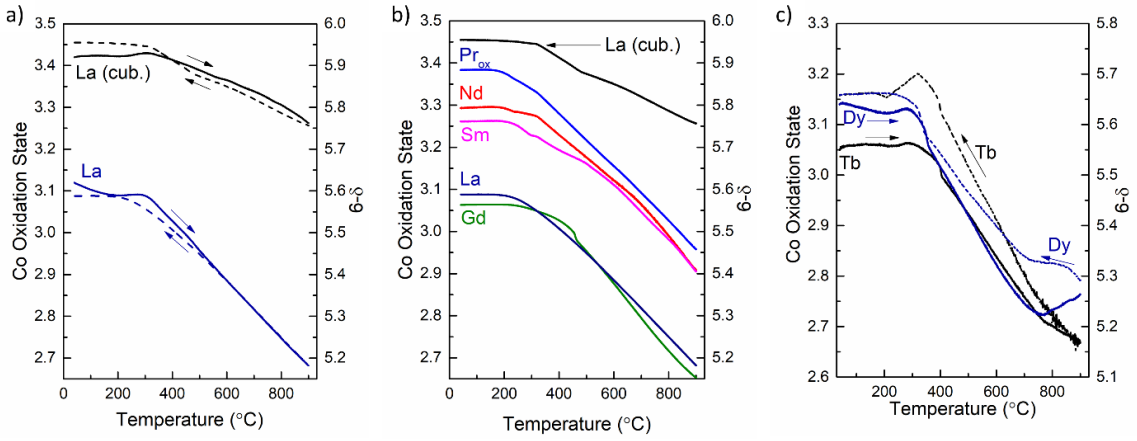

Figure 4.24 Average cobalt oxidation state and oxygen stoichiometry of $BaLnCo_2O_{6-\delta}$ as a function of temperature. Reprinted from Wachowski et al. 2020[246]

The comparison of oxygen stoichiometry determined by the means of neutron powder diffraction and iodometric titration is presented in Table 4.7. Both of these techniques gave consistent results within the limits of the measurement uncertainty.

Table 4.7 Oxygen stoichiometry determined by the means of powder neutron diffraction and iodometric titration

Ln	6-δ	
	PND	Iodometric titration
La (cubic)	6.0(1)	5.92(8)
La (double perovskite)	5.8(1)	5.63(7)
Pr	5.6(1)	5.64(7)
Nd	5.5(1)	5.57(8)
Sm	N/A	5.70(8)
Gd	5.55(8)	5.55(7)
Tb	5.5(1)	5.54(7)
Dy	N/A	5.64(7)

In both cubic and double perovskite BLC, the temperature at which the reduction of the material begins is roughly the same. Compliance between cubic and double perovskite BLC shows, that this temperature depends rather on the nature of the lanthanide not the initial value of oxygen stoichiometry. However, no direct correlation between lanthanide ionic radius and onset temperature was observed.

TGA was performed with a heating rate of 2°C/min, while the heating rate of HT SR-PXD studies was higher. To make sure, the level of oxidation in those two techniques is consistent, the TGA with the different heating rates was performed, which is presented in Figure 4.25. What can be seen, the temperature dependence of oxygen nonstoichiometry is identical for those two measurements. This is in the agreement with the studies of Aksenova et al.[249], in which the oxidation stoichiometry was measured under both dynamic conditions, and with isothermal 3-hour dwells. Both modes gave identical results, thus the results of TGA may be considered equilibrium values. This is also evidenced by the research on the diffusion coefficient carried out by Taskin et al[248],[250].

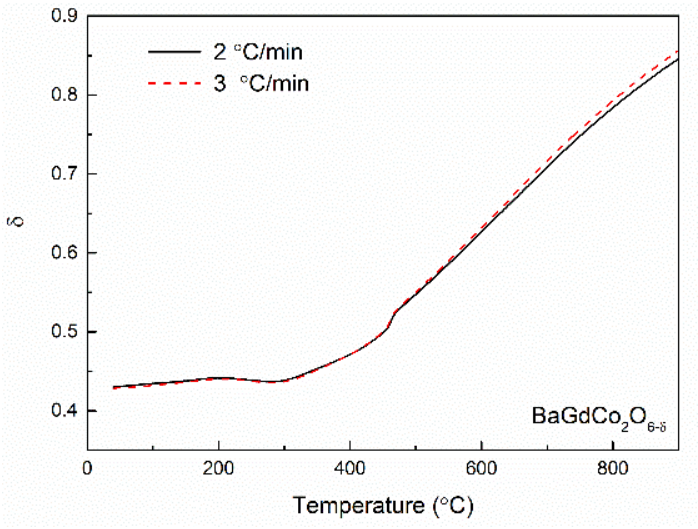

Figure 4.25 Oxygen nonstoichiometry as a function of time in $BaGdCo_2O_{6-\delta}$ with different heating rates. Reprinted from Wachowski et al. 2020[246]

4.2.2 Water uptake

The presence of mobile proton defects in the structure is a necessary condition for proton conduction. Proton defects in those compounds may be formed by water vapour incorporation from the atmosphere to the structure. The proton defect formation results in an increase of the material's mass under exposure to a humidified atmosphere, as water incorporates into the structure of the material. Figure 4.26a shows how the mass of each investigated cobaltite changes upon exposure to the humidified atmosphere. Before the atmosphere change mass of all compounds was constant, which suggests that the materials were equilibrated in those conditions. The mass of $BaPrCo_2O_{6-\delta}$, $BaNdCo_2O_{6-\delta}$, $BaSmCo_2O_{6-\delta}$, and $BaTbCo_2O_{6-\delta}$ remain constant after the switch to the humidified atmosphere. $BaDyCo_2O_{6-\delta}$ exhibits a minuscule mass gain of 0.004 %. A mass increase of 0.016%, and 0.021 % was observed in $BaLaCo_2O_{6-\delta}$ and $BaGdCo_2O_{6-\delta}$, respectively. As a function of time BLC and BGC masses increase linearly and are not reversible upon atmosphere switch back to dry conditions. The process was slow, and the total mass gain after 2 hours did not reached plateau, thus the total mass increase after this cannot be taken as an equilibrium value.

What is more, the influence of cation ordering on water uptake was investigated. Mass of both cubic and double perovskite lanthanum barium cobaltite was measured under humidified atmosphere, which is presented in Figure 4.26b. Similarly, to $BaLaCo_2O_{6-\delta}$, cubic BLC also exhibits linear mass increase, but the kinetics of this reaction is much

slower. After 2 hours mass gain of cubic BLC is four times smaller than that of orthorhombic/tetragonal BLC.

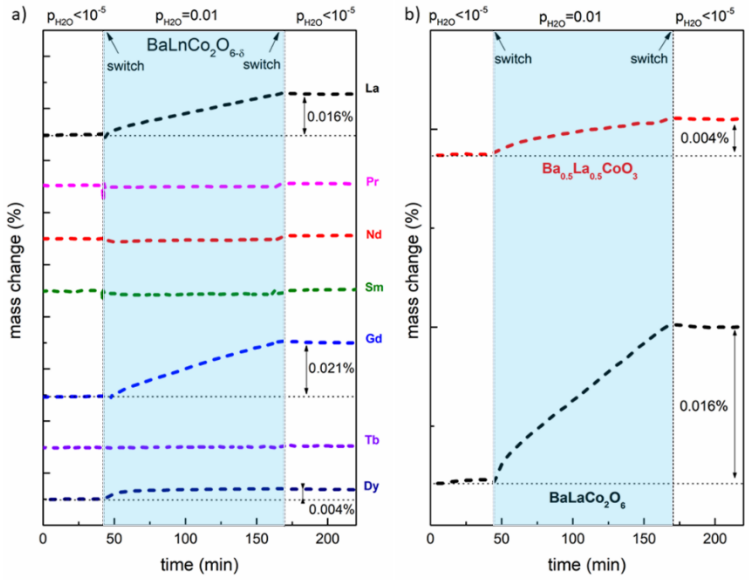

Figure 4.26 Mass as a function of time during water vapour pressure switches of $BaLnCo_2O_{6-\delta}$ (a), and cubic and double perovskite barium lanthanum cobaltite (b)

Figure 4.27 shows the mass increase under N_2 atmosphere. What can be clearly seen samples were not equilibrated and the mass was changing even before the switch. However, upon switching from dry to wet additional mass increase was observed which is related to water uptake. The process was partially reversible as the mass decreased after switching back to dry conditions. Thus, it may be stated that the mass change is an effect of two separate effects. The total mass increase related only to the water uptake was calculated by dividing those two effects, the procedure of which is described in Appendix 3. The total mass increase under humidified nitrogen is of the value 0.005% and 0.0016% for $Ba_{0.5}La_{0.5}CoO_{3-\delta}$ and $BaGdCo_2O_{6-\delta}$, respectively.

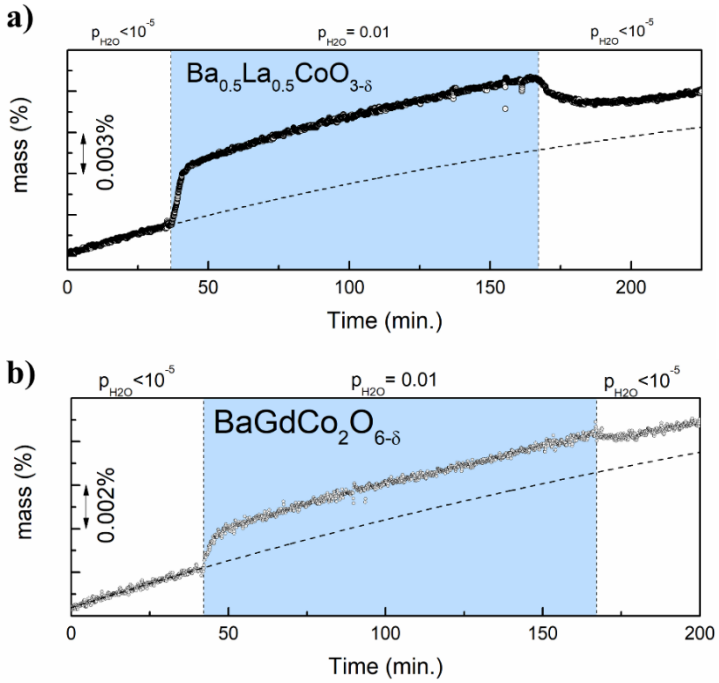

Figure 4.27 Mass increase as a function of time of $Ba_{0.5}La_{0.5}CoO_{3-\delta}$ (a), and $BaGdCo_2O_{6-\delta}$ (b) in nitrogen atmosphere

Figure 4.28 shows the mass change of $BaCo_{0.8}Gd_{0.2}O_{3-\delta}$, which is the compound that according to Malyshkin et al. is responsible for the water uptake in barium lanthanum gadolinium cobaltites[204]. In fact, this compound shows an exponential mass increase upon exposure to a humid atmosphere. The total mass gain reaches the value of 0.02%, which is of the same order of magnitude as the investigated double perovskite cobaltites $BaLaCo_2O_{6-\delta}$ and $BaGdCo_2O_{6-\delta}$.

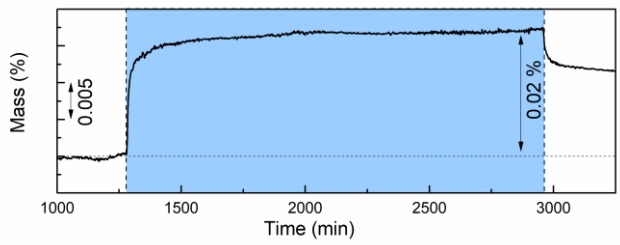

Figure 4.28 Mass increase as a function of time of $BaCo_{0.8}Gd_{0.2}O_{3-\delta}$

4.3 Electronic structure

4.3.1 X-ray absorption spectroscopy

Figure 4.29 shows x-ray absorption spectra of $BaLaCo_2O_{6-\delta}$, $BaPrCo_2O_{6-\delta}$, and $BaNdCo_2O_{6-\delta}$ on Co $L_{2,3}$ and Ba $M_{4,5}$ edges. The peak positions do not significantly change across all materials, however, the intensity of the peaks differs with the lanthanide. Since

Co $L_{2,3}$ edges are highly sensitive to cobalt oxidation state it may be postulated, that the cobalt valence in investigated materials is similar. This regime is dominated by the Co 2*p* core spin-orbit coupling, which causes the split of the signal into two spectral lines L_2 and L_3. The shape of the signal strongly depends on the multiplet structure resulting from Co 3*d*-3*d* and 2*p*-3*d* Coulomb and exchange interactions. It is also affected by the local crystal fields and O 2*p* ligands hybridization. With increasing cobalt average oxidation state the peak position should shift towards higher energies, no such significant shift was observed. The intensities of cobalt edges, Co L_3 and Co L_2 increase with decreasing ionic radius of lanthanide. The opposite relation was observed for barium Ba M_5 and Ba M_4 peaks, the intensity of which increases from neodymium to lanthanum. This indicates the increase in density of unoccupied states at 3*d* orbitals with simultaneous increase of occupied states at 4*f* Ba subshell. Figure 4.29b shows the Co L_3 edge of $BaLaCo_2O_{6-\delta}$, $BaPrCo_2O_{6-\delta}$, and $BaNdCo_2O_{6-}$ with the spectrum of CoO added as a reference, the prepeak characteristic of Co^{2+} ismarked as A in the graph. None of the investigated cobaltites exhibits a significant increase of absorbance in the range of Co^{2+}, which indicates, that the concentration of this specie at room temperature is negligible. The position of the C line is typical of Co^{3+} in both high and low spin states. The difference in pre-edge feature shape for these two electron configurations lays in the location of a shoulder (denoted as B). If the shoulder appears at energies lower than Co L_3 line then it indicates the presence of Co^{3+} in a high spin state.

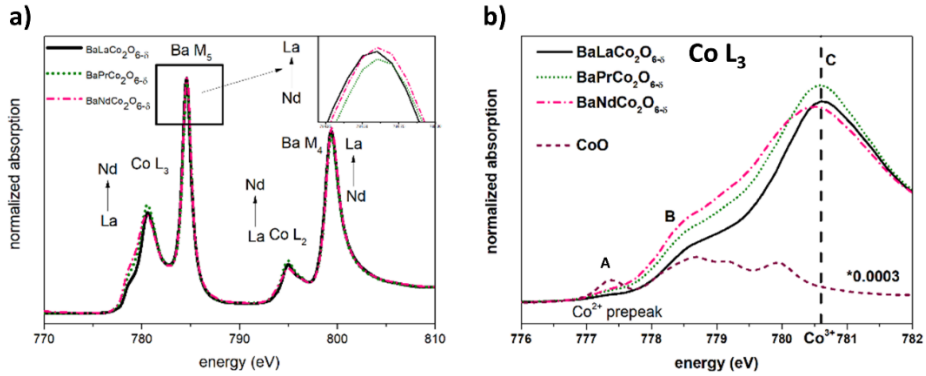

Figure 4.29 X-ray Absorption Spectra of investigated materials on Co $L_{2,3}$ and Ba $M_{4,5}$ edges (a), x-ray Absorption Near Edge Structure spectra of Co L_3 edge of investigated materials and reference. Reprinted from Szpunar et al. 2020[102]

Figure 4.30a shows the spectral line from 526 to 531 eV, which is pre-edge structure of oxygen K-edge. This regime consists of transitions from O 1*s* core level to O 2*p* orbitals that mixed with unoccupied Co 3*d* t_{2g} and e_g states. The first maximum is attributed to the

t_{2g} levels, its position shifts with oxidation and spin state, while an increase in its spectral weight indicates depopulation of the t_{2g} level. The higher energy signals came from the e_g orbitals, which splits in pyramidal coordination. In the literature, the peak around 530 eV is attributed to the unoccupied 3*d* x^2-y^2 orbitals[251]. The energies of spectral lines maximum marked in the figure for Co^{4+} IS, Co^{3+} HS, and Co^{3+} LS are the reported values for $SrCoO_3$[252]–[254], Sr_2CoO_3Cl[252], $EuCoO_3$[252], respectively. The spectral line at 529.5 eV may be assigned to the transition to the fourfold degenerate e_g holes of the LS Co^{3+} configuration. This line is not pronounced in any investigated materials; thus it may be stated that Co^{3+} exhibit a predominance of a high spin state. The white line of $BaLaCo_2O_{6-\delta}$ is shifted towards lower energies due to the higher cobalt oxidation state. Based on this data, it may be stated that at room temperature chemical state of cobalt is a mixture of Co^{4+} LS, and Co^{3+} HS, the proportion of which varies among the lanthanides. This is consistent with the observation made on the Co L_3 edge. The 1st derivative of normalized absorbance is presented in Figure 4.30b. This relation was used to determine the position of O K pre-peak maximum, which, as a function of lanthanide ionic radius, is presented in Figure 4.30c. The maximum pre-peak position decreases linearly with increasing ionic radius of lanthanide. This indicates the increasing valence of cobalt with increasing lanthanide radius because increasing cobalt oxidation state shifts the pre-peak maximum towards lower energies. This shift towards lower energies is accompanied by the enhancement of Co 3*d* – O 2*p* bond covalency[255], which may be attributed to the Co 3*d* – O 2*p* orbitals overlapping.

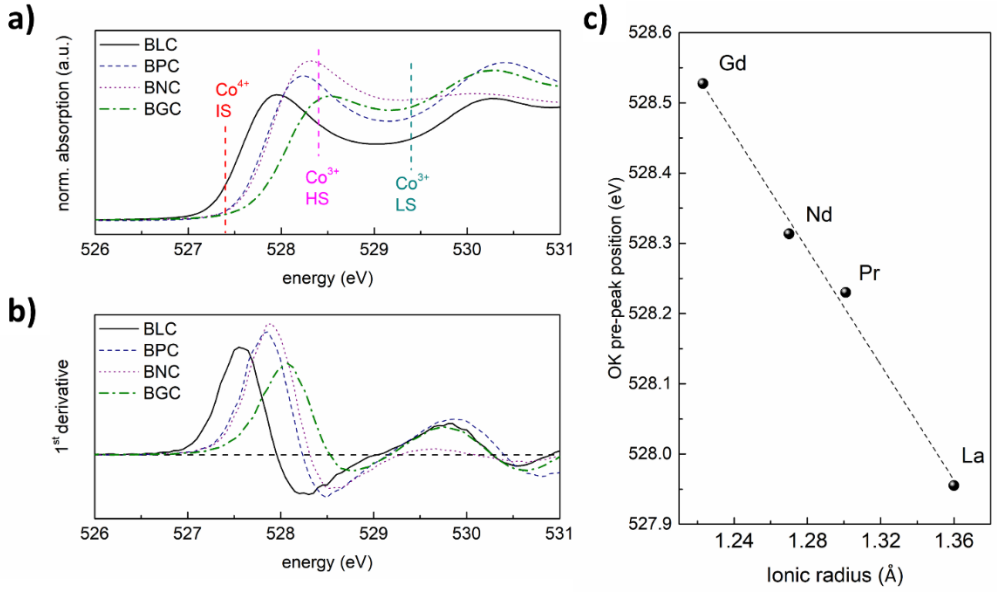

Figure 4.30 X-ray absorption spectra of oxygen K-edge in the Co 3d bands region (a), 1st derivative of normalized absorption (b), OK pre-peak position as a function of lanthanide ionic radius (c)

Figure 4.31 shows the O K pre-peak of cubic and double perovskite barium lanthanum cobaltite (a) and its derivative. The pre-peak position remains constant after material's reduction. This suggests that the change in cobalt valence must be accompanied by the transition to a higher spin state. The spectral weight of cubic BLC pre-peak is significantly higher in comparison to the reduced counterpart, which is a result of differences in oxygen vacancy and hole concentration. The enhancement of spectral weight is a result of the depopulation of the corresponding electronic states close to the Fermi level[255]. The higher intensity of OK pre-peak of cubic BLC points the higher average cobalt oxidation state of this polymorph.

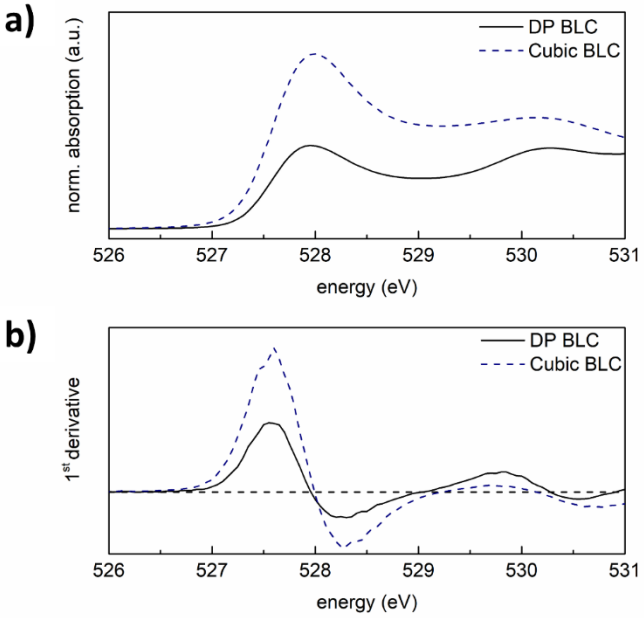

Figure 4.31 X-ray absorption spectra of oxygen K-edge in the Co 3d bands region of cubic and double perovskite BLC (a), 1st derivative of normalized absorption

No significant change of XAS spectra upon material reduction was observed in Co $L_{2,3}$ and Ba $M_{4,5}$ edges presented in Figure 4.32. Both the position and intensity of Ba $M_{4,5}$ and Co $L_{2,3}$ remain constant. However, the intensity of the shoulder at 778.5 eV is higher for cubic BLC, which indicates the increased concentration of cobalt in octahedral coordination. This is consistent with the higher oxygen content in as-prepared material.

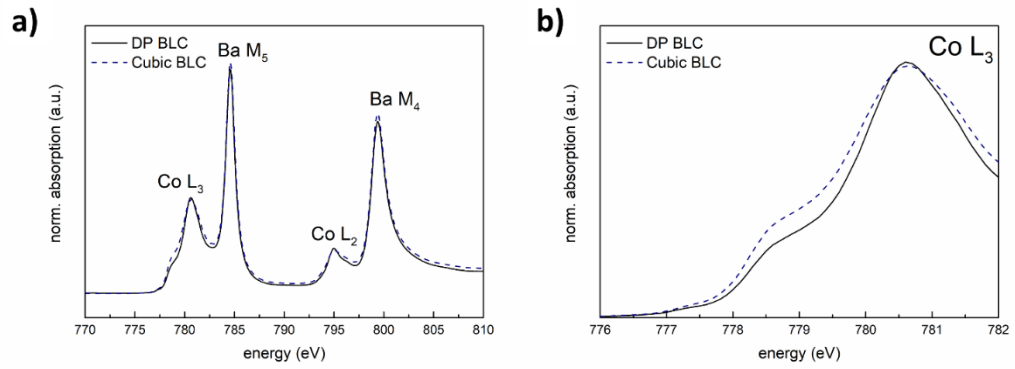

Figure 4.32 X-ray Absorption Spectroscopy spectra if cubic and double perovskite barium lanthanum cobaltites on Co $L_{2,3}$ and Ba $M_{4,5}$ edges (a), x-ray Absorption Near Edge Structure spectra of Co L_3 edge of cubic and double perovskite barium lanthanum cobaltites

The x-ray absorption spectrum of lanthanum in the energy range from 830 to 860 eV, presented in Figure 4.33, consists of two single lines. The M_4 and M_5 spectral lines correspond to the $3d_{3/2}$ and $3d_{5/2}$ states, respectively. Due to the singularity of spectral lines, it was possible to deconvolute the signal with two La M_5, La M_4 Lorentzian curves (cf. Appendix 1, figure I.9). This approach enabled the calculation of peak parameters, like FWHM, which are presented in Table 4.8. The M_4 and M_5 lines are separated with spin-orbit coupling. M_4 line of both cubic and double perovskite barium lanthanum cobaltite exhibits asymmetry at the higher energies. This tail is can be explained with the Fano effect[256], but since this effect is the same for both ordered, and disordered compounds it was not considered further. The peak positions (X_c) do not change upon reduction, similarly to FWHM. A significant change was observed in the intensity of the signal which is much lower for double perovskite barium lanthanum cobaltite, the peak area is also lower for reduced counterpart. Those spectral lines reflect the $3d^{10}4f^0 \rightarrow 3d^{10}4f^1$ transition, the decreasing spectral weight of these lines indicates the decreasing probability of those transitions in double perovskite barium lanthanum cobaltite.

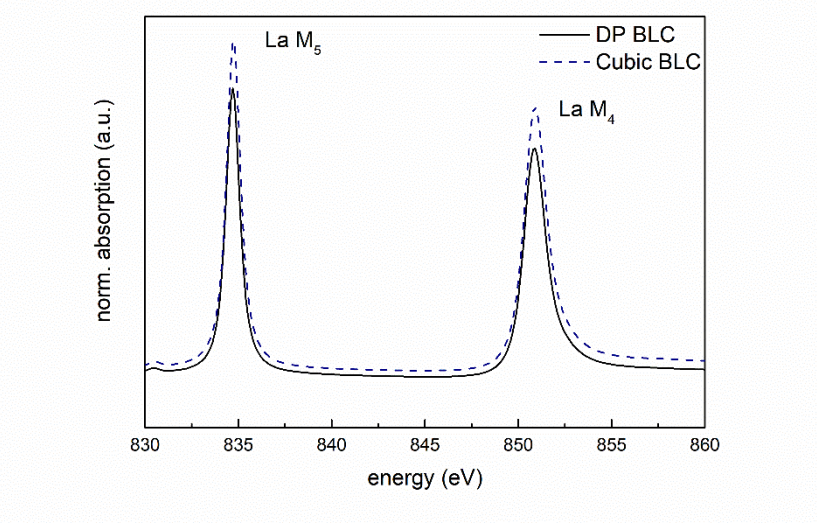

Figure 4.33 La $M_{4,5}$ edge of cubic and double perovskite $BaLaCo_2O_{6-\delta}$

Table 4.8 Peak parameters of $BaLaCo_2O_{6-\delta}$ La $M_{4,5}$ edges.

	X_c (eV)		FWHM (eV)		Area	
	Cubic	**DP**	**Cubic**	**DP**	**Cubic**	**DP**
La M_5	834.7	834.7	0.85(2)	0.85(1)	15.33(4)	13.37(2)
La M_4	850.9	850.9	1.39(1)	1.36(1)	19.90(8)	16.97(7)

Figure 4.34 shows the comparison of the pre-peak range on the O K edge of dried and hydrated barium lanthanum and gadolinium cobaltites. What can be clearly seen is the significant increase in the intensity of the line around 527.9 eV and 528.4 eV, for wet BLC and BGC, respectively. The position of the pre-peak maximum remains unchanged. A similar effect was observed in the cubic/double perovskite barium lanthanum cobaltite. The difference in the spectrum of dried and hydrated materials is visible also in the peak around 530.4 eV. In dried materials, this feature is much more pronounced. A decrease in spectral weight of this line suggests higher occupancy of this energy level. In other words, the protonic defect formation leads to the increase in the hole concentration on the t_{2g} level and a decrease on the e_g level. What is more, a less pronounced signal of $3d$ x^2-y^2, which arises from the splitting of e_g orbital in pyramidal coordination suggests, that the concentration of

cobalt in octahedral coordination increases. This is evidence of protonic defect influence on the electronic structure of the material.

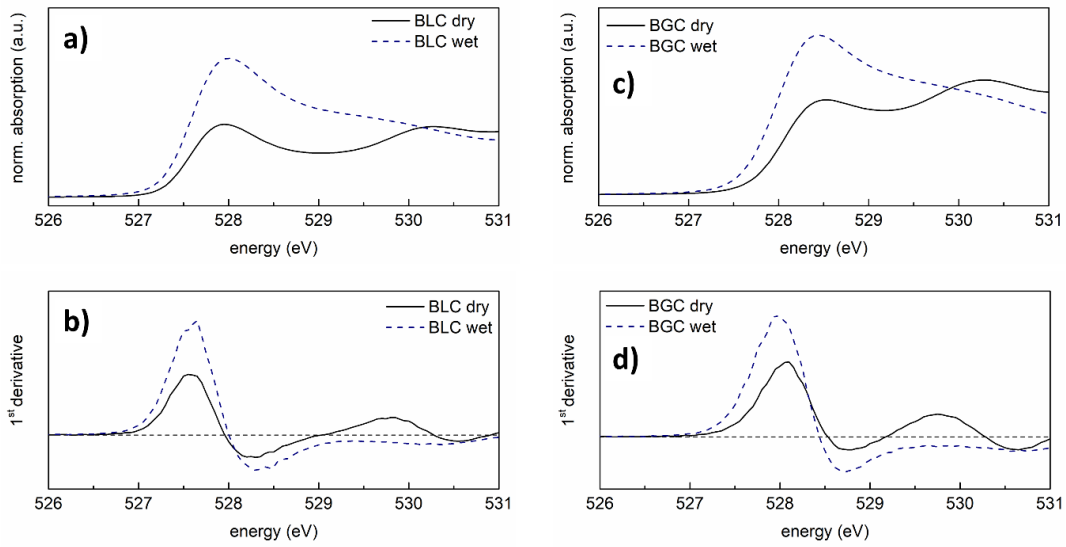

Figure 4.34 X-ray absorption spectra of oxygen K-edge pre-peak structure in the Co 3d bands region of dried and hydrated (wet) BLC (a), 1st derivative of normalized absorption of BLC (b), x-ray absorption spectra of oxygen K-edge pre-peak structure in the Co 3d bands region of as prepared (dry) and hydrated (wet) BGC (c), 1st derivative of normalized absorption of BGC (d)

The water incorporation strongly affects the Ba $M_{4,5}$ and Co $L_{2,3}$ edges of $BaLaCo_2O_{6-\delta}$ and $BaGdCo_2O_{6-\delta}$, presented in Figure 4.35 a,c, respectively. In the case of both barium lanthanum and barium gadolinium cobaltites, the intensity of Ba edges increases upon exposure to the humidified atmosphere, while on the Co $L_{2,3}$ edge the opposite effect is observed. This suggests that water incorporation causes the change in electron density around barium and cobalt. Since the x-ray absorption spectrum is sensitive to unoccupied states, it may be assumed that the electron clouds are moved towards the cobalt ions, namely, in hydrated materials the charge is more localized on cobalt ions. A closer look at the Co L_3 edge of BLC and BGC (Figure 4.35b,d, respectively) reveals that not only the intensity of this edge drops in hydrated materials but also the shoulder around 781.4 eV became more pronounced. This may be misinterpreted as the lowering of the spin state of cobalt, but the high level of overlapping of Ba and Co signals should be considered. This energy is characteristic of Ba $^3P_1$ final state[257], the intensity of which increases accordingly to the intensity of Ba $M_{4,5}$ edges.

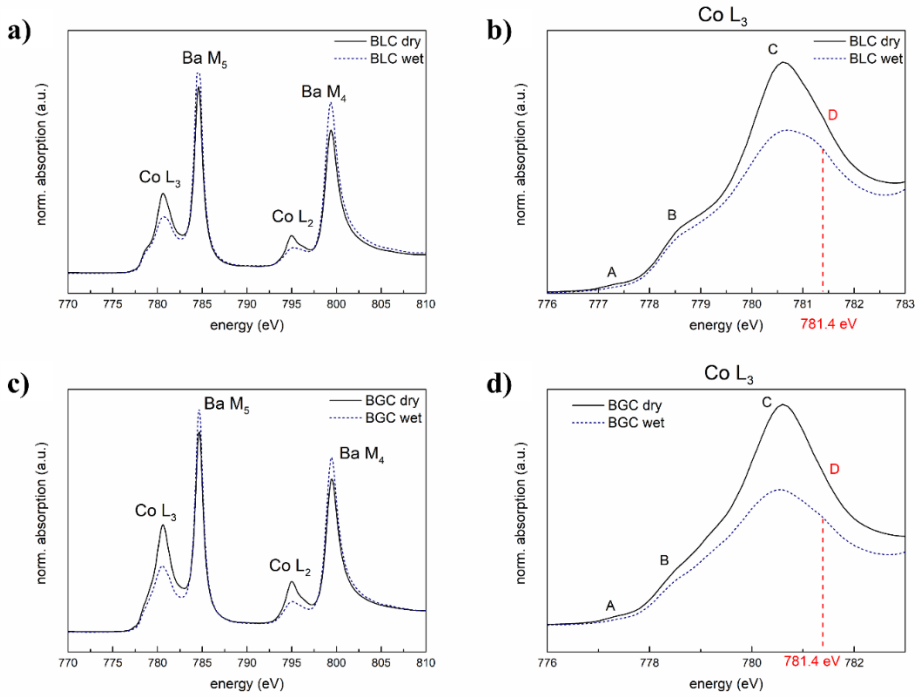

Figure 4.35 X-ray Absorption Spectroscopy spectra of barium lanthanum (a), and barium gadolinium (b) cobaltites on Co $L_{2,3}$ and Ba $M_{4,5}$ edges before and after exposure to humidifies atmosphere (a), X-ray Absorption Near Edge Structure spectra of Co L_3 edge of barium lanthanum (c), and barium gadolinium (d) cobaltites on Co $L_{2,3}$ and Ba $M_{4,5}$ edges before and after exposure to humidifies atmosphere

5 Discussion

The properties of $BaLnCo_2O_{6-\delta}$ (Ln=La, Pr, Nd, Sm, Gd, Tb, and Dy) are complex and depend not only on the Ln type but also on oxygen content, proton defect content and temperature. Cobalt in these compounds may adopt different oxidation state, coordination, and spin state, what strongly impedes the analysis of the fundamental properties. In the following sections, the influence of the cation and oxygen composition (5.1), temperature (5.2) and humidified atmosphere (5.3) on the crystal structure will be discussed.

5.1 Crystal structure

Cubic perovskite, tetragonal and orthorhombic double perovskite crystal structures were found in the studied family of $BaLnCo_2O_{6-\delta}$ oxides. The crystal structure will be discussed in relation to the A-site cation ordering, oxygen stoichiometry and oxygen vacancy ordering.

All the $BaLnCo_2O_{6-\delta}$ (Ln=Pr, Nd, Sm, Gd, Tb, Dy and Lu) compounds and reduced $BaLaCo_2O_{6-\delta}$, as the main phase, exhibit double perovskite structure with the A-site cations ordered, which was confirmed by the means of diffraction and microscopy studies. The combined Rietveld refinement of SR-PXD and NPD results clearly shows the lattice parameter doubling along the c-axis, while TEM measurement provided direct evidence of the barium and lanthanide cation separation into alternating Ba-O and Ln-O layers. This separation is a result of the mismatch in the A-site cations ionic radii, which introduce strain to the perovskite structure. What is more, unit cell volume and lattice parameters increase with the increasing lanthanide ionic radius, as does the equilibrium oxygen content in the material.

The majority phase fraction in all investigated materials, determined by the means of combined SR-PXD and NPD analysis was orthorhombic, suggesting ordering of oxygen vacancies along the b-direction. The oxygen vacancy ordering in double perovskite cobaltites has been a subject of intense discussion, mostly based on the results of diffraction studies. However, the diffraction techniques do not provide direct evidence of ordering. Solving the structure consists in modifying the parameters of the model so that it reflects the measured data in the best feasible way, but selecting a wrong model can also provide apparently satisfactory, but not necessarily physical, results. X-ray-based diffraction techniques are not very sensitive to differences in oxygen position occupancy. What is

more, the size of vacancy ordered domain may be smaller than the coherence length for x-ray scattering[258], thus the XRD pattern may falsely correspond to the structure with higher symmetry[184]. It is required to apply neutron powder diffraction to distinguish between tetragonal- non-ordered and orthorhombic – ordered structures. The direct evidence of oxygen vacancies ordering may be obtained by transmission electron microscopy.

Indeed, the combined TEM and NPD results obtained in this work confirmed the presence of oxygen vacancy ordering. Below, the $BaLaCo_2O_{6-\delta}$, and $BaPrCo_2O_{6-\delta}$ double perovskites will be discussed in detail.

$BaLaCo_2O_{6-\delta}$

First, the diffraction spots pointing to the b-parameter doubling were observed in the SAED pattern of $BaLaCo_2O_{6-\delta}$ (Figure 4.16). However, based only on this result it is difficult to distinguish if this is the evidence of oxygen vacancy ordering or the trace of the diffraction pattern from the different structural domains. Although, the careful analysis of HAADF contrast in the STEM image of $BaLaCo_2O_{6-\delta}$, presented in Figure 4.21a also reveals the lattice parameters doubling along with two perpendicular directions. Doubling along with c direction results from A-site cations ordering, which was confirmed with EELS mapping. The HAADF contrast pattern along the b-direction is observed in columns consisting of Co-O along the imaged [100] zone axis. What should be noted is the fact that HAADF contrast is not sensitive to light elements, thus the observed periodic pattern does not originate from differences in oxygen position occupancies. Nevertheless, the column consists also of cobalt ions, which are the source of the differences in intensities. Co^{3+} ions occupy two alternating positions along [010] direction. The presence of two different crystallographic positions of cobalt indicates b-parameter doubling, which gives a hint of oxygen vacancy ordering.

Based on transmission electron microscopy results, the atomic structural model of $BaLaCo_2O_{6-\delta}$ was constructed. The unit cell was built with VESTA software[159] and is presented in Figure 5.1. However, the periodicity along two perpendicular directions was observed, based on this data it is it cannot be unequivocally determined whether this is the result of oxygen vacancies ordering or the presence of two structural domains rotated by 90° relative to each other. Therefore, a tetragonal unit cell, with the uniform distribution of

oxygen vacancies in La-O layer was selected. The model shows the double perovskite unit cell with partially ordered A-site cations. It was estimated that 25% of lanthanum cations are situated in the barium layer, and vice versa. This structural model was applied to simultaneous Riveted refinement of SR-PXD and NPD data for both tetragonal and orthorhombic phases. This approach led to a slight decrease in R-factor from 5.60% to 5.55%, but it did not significantly affect the other fit parameters. This confirms the compliance of diffraction and microscopy data.

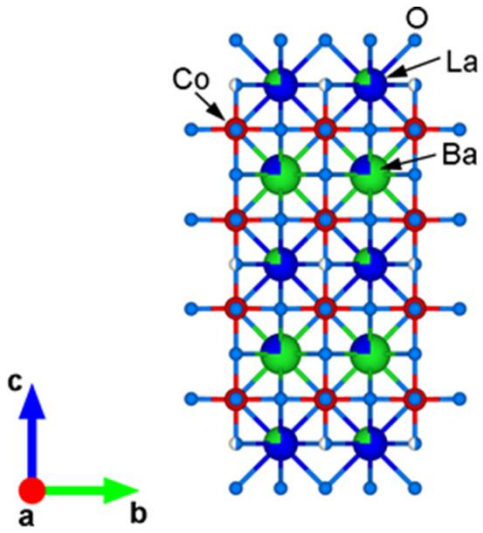

Figure 5.1 Model of $BaLaCo_2O_{6-\delta}$ unit cell. Reprinted from Wachowski et al. 2020[246]

In the case of barium lanthanum cobaltite the difference in ionic radii of lanthanum and barium is small enough ($\Delta R_{Ba,\ La} = 0.26$ Å)[153] for the cations to mix in the A-site sublattice. Because of random distribution and equal proportions of the A-site cations, positions of La and Ba are equivalent, and the structure of as-synthesised barium lanthanum cobaltite is cubic, with fully occupied oxygen positions. Annealing in the argon atmosphere leads to a reduction in cobalt average oxidation state and introduces oxygen vacancies to the system, which favours A-site cation separation. Under exposure to the Ar-atmosphere, the cation reorganisation takes place, and alternate layers of Ba-O and La-O along the c-axis are formed. Barium lanthanum reduction also affects the electronic structure of the material. The hole concentration on t_{2g} level is much higher in as-prepared material, which is a result of a higher average cobalt oxidation state and lower oxygen content. The reduction leads to the formation of cobalt in pyramidal coordination. Though the process of cation reorganisation was not studied in situ by the diffraction method, evidence of this process may be found during the electrical studies. The electrical conductivity of cubic

$Ba_{0.5}La_{0.5}CoO_{3-\delta}$ and double perovskite $BaLaCo_2O_{6-\delta}$ differ due to the difference in carriers' concentration and mobility[195],[259]. The continuous change of transport properties after the atmosphere switch from air to argon was observed in DC-conductivity measurements of cubic BLC[260]. Despite relatively high temperature t = 800°C, the stabilisation process after the atmosphere switch took around 8 hours. Such a long time indicates the cation reorganisation process, which was confirmed by comparing diffraction patterns before and after annealing. Cation reorganisation leads to the phase transition to a double perovskite structure. Oxygen vacancies formed upon reduction are located mostly in the Ln-O layer. O-site occupation in Co-O and Ba-O is close to unity. The favourable position of oxygen vacancies causes the formation of facilitated transportation channels, which strongly affect carriers' mobility.

$BaPrCo_2O_{6-\delta}$

TEM studies of $BaPrCo_2O_{6-\delta}$ revealed the unexpected periodicity along the [011] direction. This periodicity could not be explained by the Ba-Pr and Co-O distances in the presented projection. To fully understand the intensity modulation and correspond it to the crystal structure, HRTEM patterns were simulated using the multislice technique along the two-zone axes, **B**=[-210] and **B**=[0-11], with the aid of CrystalKit and Mac Tempas software kits. For two observed orientations, the series of HRTEM images were simulated with two parameters, sample thickness, and the defocus of the objective lens, Δf. The structural models, that were used for simulations are presented in Figure 5.2.

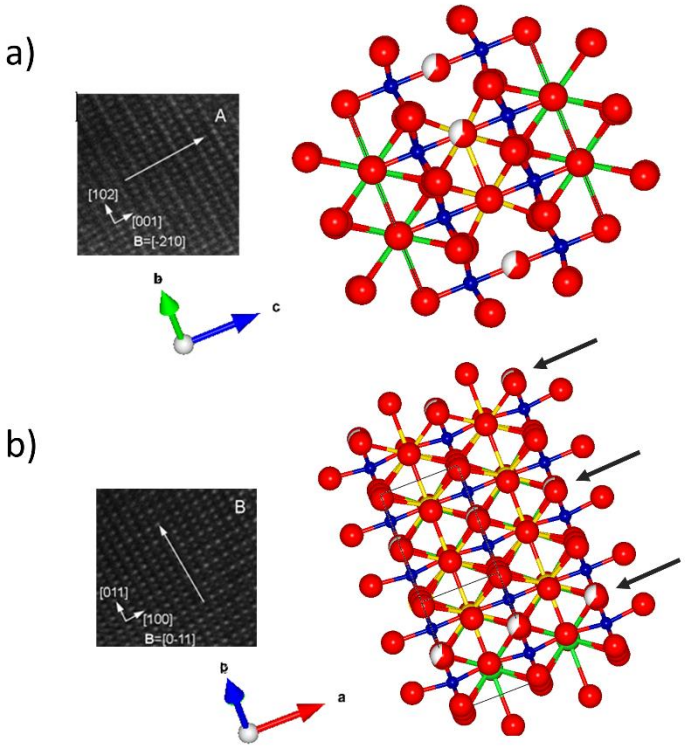

Figure 5.2 Structural models of $BaPrCo_2O_{6-\delta}$ double perovskite with the orientation determined in SAED pattern and HRTEM images

Figure 5.3 depicts the matrix of HRTEM images of $BaPrCo_2O_{6-\delta}$ with the orientation along $B = [\bar{2}10]$. Based on the image comparison it was decided that the micrograph obtained for a thickness t = 40 nm and a defocus Δf = -10 nm well corresponds to the measured image. Based on this simulation the structural model can be associated with the HRTEM image. Each point can be assigned to specific atoms in the crystal lattice. Thus, the praseodymium and barium positions were determined. The spacing between Ba-Pr corresponds to the periodicity that was detected in HRTEM studies. In this orientation, the A-site cations obscure the positions at which the localization of oxygen vacancies is expected, as they lie on one straight line concerning the incident electron beam.

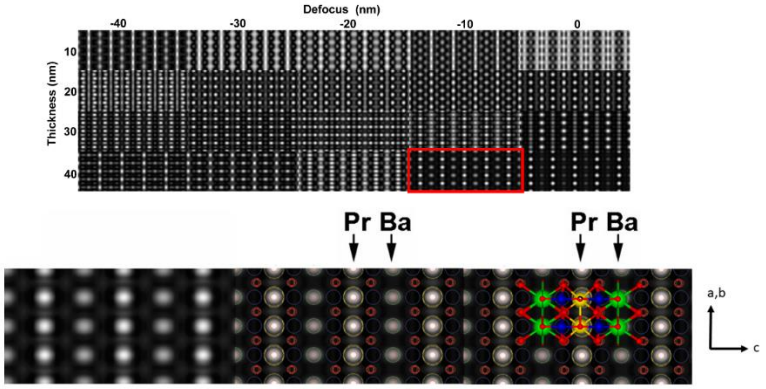

Figure 5.3 The matrix of HRTEM images simulated for BPC oriented towards B=[-210] direction. Reprinted from Wachowski et al. 2020[246]

Because of that the image of this structural domain oriented along $B = [0\bar{1}1]$ was also simulated. The matrix of simulated HRTEM images of this grain is presented in Figure 5.4. In this case t = 50 nm, and Δf = -20 nm fit the best experimental HRTEM. The layering of the structural model to the HRTEM image reveals that the intensity modulation is observed in the plain consisting of alternating rows of cobalt and oxygens. The positions of cobalt are represented by the dark dark spots while the light spots correspond to oxygen ions. The intensity of light spots is modulated in such a way that every second bright spot shows a higher intensity. This is evidence that oxygen position occupancies exhibit a repeatable order. Oxygen vacancies are located on alternating {010} planes along the b-axis. This leads to {011} planes containing oxygen vacancies alternating with fully occupied {011} planes. This corresponds to a period-doubling along the b-axis, but also along the [011] direction as noticed in the experimental SAED pattern and HRTEM images in [0–11] zone axis orientation (Figure 4.18c). Every second oxygen position has lower occupancies, which is a proof of oxygen vacancy ordering along the b-direction. Because of oxygen vacancy ordering, the b-parameter is doubled.

To understand why oxygen vacancies are visible in the grain oriented along $B = [0\bar{1}1]$, and not in $B = [\bar{2}10]$, the structural models, presented in Figure 5.4, should be carefully analysed. Oxygen vacancies in the grain oriented towards $B = [\bar{2}10]$ (Figure 5.2a) are located along the b-axis. The straight line of oxygen vacancies is visible in the model of the structure. As mentioned above oxygen positions are obscured by Ba cations, which give a bigger contribution to the HRTEM image, due to the larger atomic number of Ba. In the structural domain oriented along $B = [0\bar{1}1]$ the atomic columns containing only

oxygen are aligned parallel to the initial electron beam and the ordered vacancies are not masked by other atomic species. Thus, it may be assumed that this orientation is one of the few orientations in which the oxygen vacancies may be observed, giving evidence of oxygen vacancy ordering.

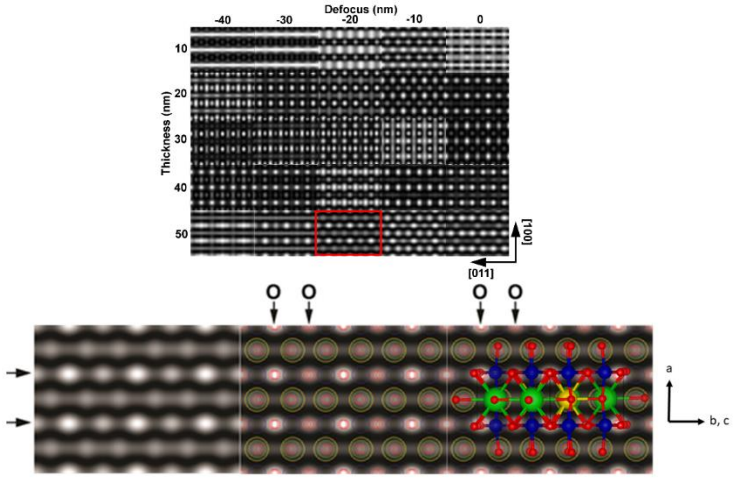

Figure 5.4 The matrix of HRTEM images simulated for BPC oriented towards B=[0-11] direction. Reprinted from Wachowski et al. 2020[246]

Summing up, the TEM results obtained for $BaLaCo_2O_{6-\delta}$ and $BaPrCo_2O_{6-\delta}$ confirm that the oxygen vacancies locate mainly in the Ln-O layer. The oxygen vacancy location in the Ln-O layers was also confirmed by the means of x-ray absorption spectroscopy, which revealed the presence of cobalt in both pyramidal and octahedral coordination. The ordering leads to a doubling of the b parameter of the perovskite unit cell. Thus, the space group that should be used to describe the structure of all investigated materials is orthorhombic Pmmm. Oxygen stoichiometry strongly impacts the double perovskite cobaltites properties, therefore the oxygen vacancy ordering also has a great influence on the materials' properties. Oxygen vacancy ordering may form a long-range magnetic ordering, which dramatically impacts the nature of the transition metal[261],[262].

The orthorhombic Pmmm space group was identified in $BaLaCo_2O_{6-\delta}$, $BaPrCo_2O_{6-\delta}$, and $BaNdCo_2O_{6-\delta}$ up to 1000°C. So far, the oxygen vacancy ordering has been believed to arise only in a specific range of oxygen stoichiometry. For example, Cox-Galhotra identified the tetragonal structure in $BaNdCo_2O_{6-\delta}$, for $5.51 < \delta < 5.11$[263], and $BaPrCo_2O_{6-\delta}$, for $5.57(1) < \delta < 5.17(2)$[264]. The results of studies presented in this thesis do not support this statement. At the highest investigated temperatures, the delta values go

beyond this range, and no phase transition was observed. What is more, if the structure was tetragonal, the a and b unit cell parameters should satisfy the dependence $a_{tetragonal} = a_{orthorhombic} = b_{tetragonal} = b_{othorhombic}/2$. As shown in Figure 5.5, this is not fulfilled in the whole studied temperature range. Therefore, we suggest that the orthorhombic perovskite structure may be stabilized in a wider range of oxygen stoichiometry than reported before[196],[240],[247].

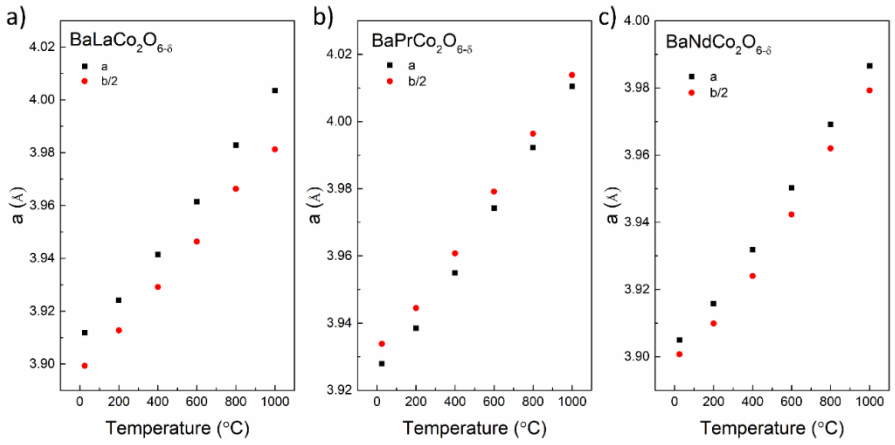

Figure 5.5 Comparison of unit cell parameters a and b/2. Reprinted from Wachowski et al. 2020[246]

$BaLaCo_2O_{6-\delta}$ and $BaSmCo_2O_{6-\delta}$ consist of two double perovskite polymorphs, tetragonal and orthorhombic. High-temperature synchrotron radiation x-ray diffraction revealed that also the $BaNdCo_2O_{6-\delta}$ consists of two phases, but only one of them has a double perovskite structure. The minority phase has a cubic perovskite structure with the space group $Pm\bar{3}m$. The formation of cubic $Ba_{0.5}Nd_{0.5}CoO_{3-\delta}$ is unlikely, due to the large difference in ionic radius of barium and neodymium. Although the coexistence of barium and neodymium, occupying the equivalent positions in the perovskite structure, was reported before[265], but, to our best knowledge, not in cobaltites. Even fully oxidised $BaNdCo_2O_6$ exhibits a double perovskite structure[196]. Diffraction studies do not provide the possibility to directly investigate the chemical composition, the compound identification is thus, indirect. Unit cell parameter of the cubic perovskite phase is a = 3.8848(2) Å. Among the perovskite structures that could be expected in this system, there are $BaCoO_{3-\delta}$ and $NdCoO_{3-\delta}$, or solid solutions of those two. Barium cobaltite in cubic perovskite structure is stabilised with high oxygen deficiency and exhibits a much higher unit cell parameter, a = 4.0887(5) Å[266]. $NdCoO_{3-\delta}$, in turn, exhibits a significantly lower unit cell parameter, a = 3.77 Å[28]. On this basis, it may be assumed that the minority cubic

perovskite phase is some solid solution of $BaCoO_{3-\delta}$ and $NdCoO_{3-\delta}$, however the attempt to refine the occupancies of barium and neodymium positions gave non-physical values.

The phase fraction of tetragonal $BaLaCo_2O_{6-\delta}$ remains constant up to 400°C and starts to decrease above this temperature. Such a relation was also observed in the temperature evolution of the mass of BLC under oxidising condition. Figure 5.6 shows the minority phase fraction as a function of temperature superimposed on the temperature dependency of the oxygen content. A significant correlation between the oxygen stoichiometry and the minority phase content is observed in BLC, while no such a correlation is present in BNC.

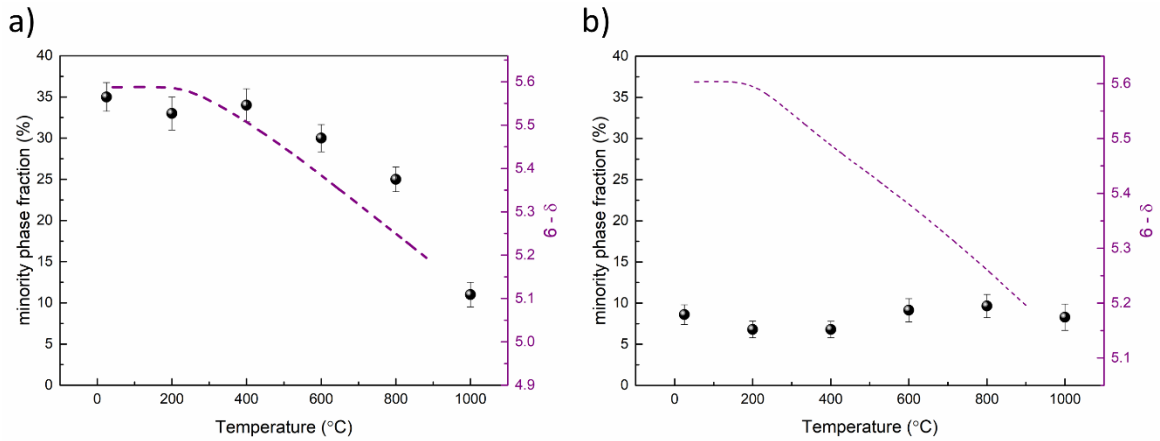

Figure 5.6 Temperature dependencies of minority phase fraction and oxygen stoichiometry in $BaLaCo_2O_{6-\delta}$ (a) *and $BaNdCo_2O_{6-\delta}$ (b). Reprinted from Szpunar et al. 2020*[102]

To understand the correlation between oxygen stoichiometry and phase composition, it should be noted that the average cobalt oxidation state, determined by the means of iodometric titration, is the mean for all component phases. Since $BaLaCo_2O_{6-\delta}$ is a mixture of tetragonal and orthorhombic phases it is impossible to determine the average cobalt oxidation state and oxygen stoichiometry for individual phases basing only on the iodometric titration, without making any additional assumptions. On the other hand, combined neutron powder diffraction, and synchrotron-radiation x-ray diffraction allows to calculate the oxidation state of cobalt in each phase. Based on the data of Wyckoff position occupancies presented in Tables 4.2 and 4.3. The chemical formulas of orthorhombic Pmmm and tetragonal P4/mmm BLC were determined as $BaLaCo_2O_{6.06}$ and $BaLaCo_2O_{5.66}$, respectively. This result is surprising because fully oxidised BLC is expected to have the tetragonal structure, while $\delta = 0.34$ indicates the orthorhombic phase. However, it should be emphasized the diffraction patterns of tetragonal and orthorhombic

BLC exhibit a very high level of overlapping, which strongly impedes the refinement. In contrast to the cobaltites containing other lanthanides total oxygen stoichiometry of BLC determined by the means of iodometric titration and diffraction studies differed.

The oxygen nonstoichiometry obtained by the iodometric titration method was considered for the analysis of the phase transformation. The average oxygen nonstoichiometry determined for the mixture of tetragonal and orthorhombic BLC phases at room temperature is $6-\delta = 5.63(7)$. The tetragonal phase is formed if the oxygen content is high, close to the stoichiometric value, or if the O3 positions are almost empty, and the oxygen content approaches the value $6-\delta = 5$. Under air atmosphere, at room temperature complete depletion of the Ln-O layer of oxygen is unlikely, thus it can be assumed that the tetragonal BLC is fully oxidised. Knowing the fraction of orthorhombic and tetragonal phases, the total oxygen content, and presuming that for tetragonal phase $\delta = 0$, the oxygen stoichiometry of the orthorhombic phase may be calculated. Thus, the chemical formula of orthorhombic BLC should be as follows: $BaLaCo_2O_{5.43}$, which is in good agreement with the δ values corresponding to the orthorhombic structure. At room temperature, BLC, therefore, consists of the fully oxidised tetragonal phase and orthorhombic phase with almost 0.5 occupancy of the O3 positions, which is presented schematically in Figure 5.7. Orthorhombic unit cells are marked with green colour, while the tetragonal ones with blue. With the increasing temperature, the materials start to reduce. Oxygen is released simultaneously from both the orthorhombic and tetragonal phases. When the oxygen ion is released from the tetragonal structure the oxygen vacancy is formed, which leads to the transformation of a particular unit cell to the orthorhombic one, increasing the majority phase content. Because of that, the oxygen stoichiometry of the remaining tetragonal phase remains constant.

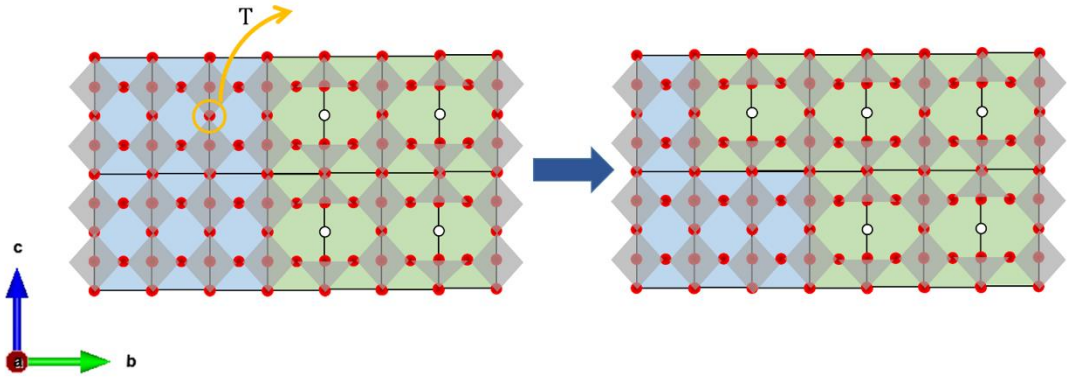

Figure 5.7 The scheme of phase transition between tetragonal and orthorhombic phases, showing what happens if the oxygen is released upon increasing temperature (T) from the tetragonal unit cell. Reprinted from Szpunar et al. 2020[102]

Such a correlation between phase composition and oxygen content was not observed in $BaNdCo_2O_{6-\delta}$, which consists of orthorhombic and cubic phases. In this case, the difference in cubic and orthorhombic perovskite structure does not lie in the oxygen stoichiometry and oxygen vacancy localization, but in the A-site cation distribution. Thus, oxygen stoichiometry does not influence the minority phase fraction. The constant phase fraction of the cubic perovskite phase suggests that under oxidising conditions in the whole studied temperature range the cation reorganization does not take place. Otherwise, the phase content of the material would change with temperature.

5.2 Chemical expansion

The expansion of the unit cell as a result of temperature change may not only be due to thermal expansion. Thermal expansion is related to the inherent vibrational properties, but in addition to it, chemical expansion may occur due to a change in the chemical composition, e.g. oxidation, or reduction. In the case of oxides with transition metals, change in temperature affects both. Therefore, the overall change of unit cell parameter reflects thermochemical expansion, which rarely can be deconvoluted into two separate factors.

Sometimes extraction of chemical expansion is possible, but several properties of the studied systems have to be analysed first. In the studied materials below 300 °C, the oxygen stoichiometry remains constant, thus the change of unit cell parameters results only from thermal expansion. The slope of unit cell parameter temperature dependence is constant. Above this temperature, a change in slope is observed, which suggests, that chemical

expansion starts to take place. This is consistent with the oxidation studies, in which the oxygen nonstoichiometry strongly increases above about 300 °C. With the increasing temperature the average ionic radius of cobalt changes, as well as oxygen vacancy concentration. The changes in average cobalt ionic radius result mainly from the change in average oxidation state of cobalt (Table II.2). The spin state may also affect the ionic radius, but the literature does not provide enough of data to quantify this contribution. Figure 5.8 presents the temperature evolution of the a-parameter of orthorhombic and tetragonal $BaLaCo_2O_{6-\delta}$. The deviation from linearity in the temperature dependence of the a-parameter in orthorhombic BLC increases with increasing temperature, while for tetragonal BLC dependency is linear in the whole investigated temperature range. It suggests that orthorhombic BLC undergoes both chemical and thermal expansion, while the tetragonal one shows only a thermal component. No chemical expansion in tetragonal $BaLaCo_2O_{6-\delta}$ indicates the constant oxygen nonstoichiometry. That supports the hypothesis describing the mechanism of phase transition between the tetragonal and orthorhombic phases, that is, if the oxygen is released from the material with the tetragonal structure, the phase is transformed into the orthorhombic structure, thus the oxygen stoichiometry in the remaining tetragonal phase remains constant (Figure 5.7).

Assuming that the thermal expansion coefficient is constant in the whole studied temperature range, the chemical expansion may be separated from the thermal one by subtracting the linear fit obtained from the data at low temperatures. The temperature evolution of the parameter resulting only from chemical expansion, calculated in the way described above is presented in Figure 5.8c. This dependence was compared to the temperature evolution oxygen vacancy concentration and a correlation between chemical expansion and the vacancy concentration was observed. The influence of the chemical expansion on the a-parameter, translates into a change in the volume of a unit cell under the influence of changes in the oxygen content. Those results were used to determine the chemical expansion coefficients.

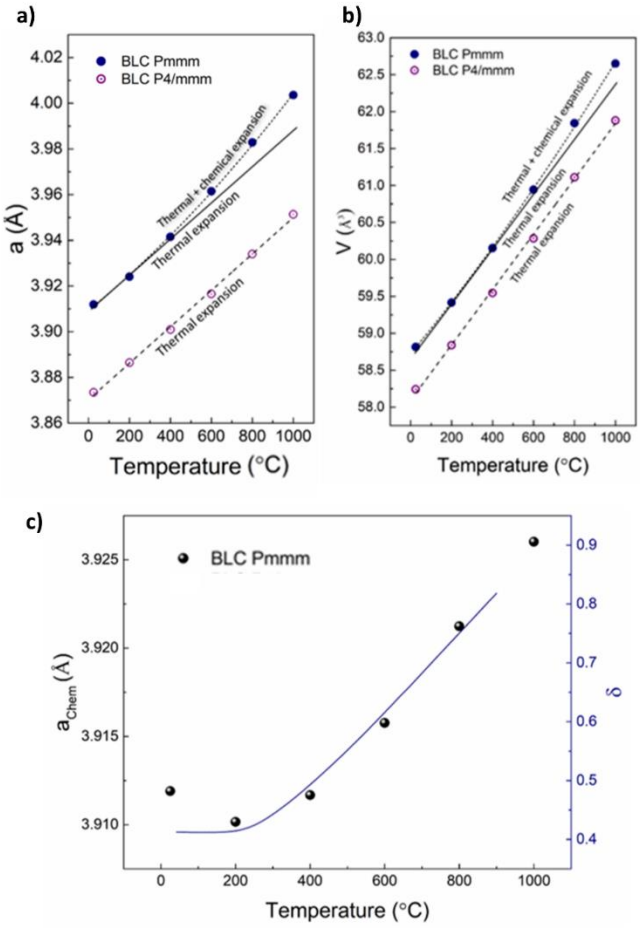

Figure 5.8 Thermal and chemical expansion of $BaLaCo_2O_{6-\delta}$. Temperature evolution of a-parameter (a) and unit cell volume (b) of orthorhombic and tetragonal $BaLaCo_2O_{6-\delta}$. The correlation between changes in a-parameter resulting from chemical expansion and oxygen nonstoichiometry. Reprinted from Szpunar et al. 2020[102]

5.2.1 Chemical expansion model

To calculate the chemical expansion coefficients the appropriate defect chemistry model must be applied. Temperature increase leads to cobalt ion reduction and oxygen vacancies formation[19],[259]. Chemical expansion results from the differences in ionic radii of cobalt at different oxidation states, and the effective ionic radius of oxygen vacancy in comparison to oxygen ion radius. In this study the total volumetric chemical expansion is modelled, assuming its isotropy.

In perovskite structure, cobalt can have three oxidation states: Co^{4+}, Co^{3+}, and Co^{2+}. Thus reduction from $Co^{4+} \rightarrow Co^{3+}$, and $Co^{3+} \rightarrow Co^{2+}$ may take place. The cobaltite $BaLnCo_2O_{6-\delta}$, without oxygen nonstoichiometry, may be used as an 'ideal' reference state to calculate the ideal oxidation state of cobalt, which in this case is equal to 3.5. Thus this value will be taken as a nominal charge of cobalt positions in the crystal lattice. Hence it is

necessary to introduce the half charges to the Kröger-Vink notation. Symbols used to describe Co^{2+}, Co^{3+}, and Co^{4+} are presented in Table 5.1. Such a notation is similar to the one introduced by T. Norby to describe oxides with inherently defective sublattices[267].

Table 5.1 Kröger-Vink symbols used to describe cobalt ions at each oxidation state

Ion	K-V symbol
$Co^{3.5+}$	Co_{Co}^{X}
Co^{2+}	$Co_{Co}^{\frac{3}{2}/}$
Co^{3+}	$Co_{Co}^{\frac{1}{2}/}$
Co^{4+}	$Co_{Co}^{\frac{1}{2}\bullet}$

Using Kröger-Vink notation the reactions of reduction may be written as follows:

$$2\,Co_{Co}^{\frac{1}{2}\bullet} + O_O^X \rightarrow 2\,Co_{Co}^{\frac{1}{2}/} + v_O^{\bullet\bullet} + \frac{1}{2}O_{2\,(g)} \tag{5.1}$$

$$2\,Co_{Co}^{\frac{1}{2}/} + O_O^X \rightarrow 2\,Co_{Co}^{\frac{3}{2}/} + v_O^{\bullet\bullet} + \frac{1}{2}O_{2\,(g)} \tag{5.2}$$

Therefore, the chemical expansion coefficient (β) consists of two parts: one originating from the formation of oxygen vacancies ($\beta_{V_O^{\bullet\bullet}}$) and the second from cobalt reduction (β_{Co}) (Eq. 5.3). The β_{Co} is doubled because there are two reduced cobalt ions per one oxygen vacancy.

$$\beta = \beta_{V_O^{\bullet\bullet}} + 2\,\beta_{Co} \tag{5.3}$$

The regimes of the dominance of each reaction can be distinguished. If the material is highly oxidised (δ <0.5) most cobalt ions should be at a 4+ oxidation state, thus reaction 5.1 dominates. Increasing the value of δ (δ > 0.5) leads to an increase in the concentration of Co^{3+}, which means that reaction 5.2 prevails. On this basis two regimes may be distinguished: oxidised state for δ < 0.5 and reduced state for δ > 0.5. In the former $\left[Co_{Co}^{\frac{1}{2}\bullet}\right] + \left[Co_{Co}^{\frac{1}{2}/}\right] \gg \left[Co_{Co}^{\frac{3}{2}/}\right]$ and in the latter $\left[Co_{Co}^{\frac{1}{2}/}\right] + \left[Co_{Co}^{\frac{3}{2}/}\right] \gg \left[Co_{Co}^{\frac{1}{2}\bullet}\right]$ relations must be fulfilled. The transition value of δ is 0.5, where the average cobalt oxidation state is 3.0.

The differences in ionic radii of cobalt at each oxidation state influence the unit cell volume, thus the chemical expansion coefficient of cobalt reduction may be defined in the way presented in Eq. 5.4, where V_0 is an initial unit cell volume at room temperature.

$$\beta_{Co} = \frac{1}{\Delta\delta} \cdot \frac{\Delta V_{Co}}{V_0} \tag{5.4}$$

Δδ in Eq. 5.4 stands for the change in oxygen nonstoichiometry. This equation can then be expanded to the form shown in equation 5.5.

$$\beta_{Co} = \frac{1}{\delta - \delta_0} \cdot \frac{V_{Co(\delta)} - V_{Co_0}}{V_0} \tag{5.5}$$

V_{Co_0} stands for the average volume of cobalt ion at room temperature, with the initial value of δ, and $V_{Co(\delta)}$ is the average volume occupied by Co at any given δ at elevated temperatures.

Reduction from Co^{4+} to Co^{3+}

The average volume of cobalt ions may be calculated as the weighted arithmetic mean volume of individual ions, where the weights are the concentration of cobalt ions in a particular oxidation state. Thus, concentrations of cobalt at each oxidation state are necessary for further calculation. Similarly, to average volume, the average cobalt oxidation state is a weighted arithmetic mean of each oxidation state according to Eq. 5.6

$$Co_{AVG} = \frac{2\left[Co_{Co}^{\frac{3}{2}/}\right] + 3\left[Co_{Co}^{\frac{1}{2}/}\right] + 4\left[Co_{Co}^{\frac{1}{2}\bullet}\right]}{2} \tag{5.6}$$

In the oxidised regime, where $\delta < 0.5$, the presence of Co^{2+} is unlikely, which was confirmed with XAS measurements (Figure 4.29). Equation 5.6 can be then simplified to the form presented in Eq 5.7.

$$Co_{AVG} = \frac{3}{2}\left[Co_{Co}^{\frac{1}{2}/}\right] + 2\left[Co_{Co}^{\frac{1}{2}\bullet}\right] \tag{5.7}$$

Assuming that in the oxidised regime cobalt in 2^+ oxidation state is absent, the sum of Co^{3+} and Co^{4+} concentrations must be equal to the total molar concentration of cobalt in double perovskite cobaltite. This relation is presented in Eq. 5.8.

$$\left[Co_{Co}^{\frac{1}{2}\bullet}\right] + \left[Co_{Co}^{\frac{1}{2}/}\right] = 2 \tag{5.8}$$

Moreover, the average cobalt oxidation state is be related to oxygen nonstoichiometry, according to Eq. 5.9.

$$Co_{AVG} = 3.5 - \delta \tag{5.9}$$

The combination of equations 5.7 - 5.9 gives the relations between the concentration of Co^{3+} and Co^{4+} with oxygen non-stoichiometry (eq.5.10, 5.11) in the oxidised regime.

$$\left[Co_{Co}^{\frac{1}{2}\bullet}\right] = 1 - 2\delta \tag{5.10}$$

$$\left[Co_{Co}^{\frac{1}{2}/}\right] = 2\delta + 1 \tag{5.11}$$

The expression for the mean volume of the cobalt ion, which is the weighted mean volume of the Co^{3+} and Co^{4+} ions, is given with the eq. 5.12.

$$V_{Co} = \frac{\left[Co_{Co}^{\frac{1}{2}\bullet}\right] \cdot V_{Co^{4+}} + \left[Co_{Co}^{\frac{1}{2}/}\right] V_{Co^{3+}}}{2} \tag{5.12}$$

Including equations 5.10, and 5.11 to equation 5.12 leads to the relation 5.13.

$$V_{Co}(\delta) = \frac{(1-2\delta)\cdot V_{Co^{4+}} + (2\delta+1)\cdot V_{Co^{3+}}}{2} \tag{5.13}$$

By analogy to equation 5.13, the expression for mean cobalt ion volume at room temperature can be written (eq. 5.14).

$$V_{Co_0} = \frac{(1-2\delta_0)\cdot V_{Co^{4+}} + (2\delta_0+1)\cdot V_{Co^{3+}}}{2} \tag{5.14}$$

The expressions of the chemical expansion coefficient of Co^{4+} to Co^{3+} reduction, presented in equations 5.15, and 5.16 are obtained by inserting equations 5.13, and 5.14 into equation 5.5.

$$\beta_{Co\ 4\to3} = \frac{1}{\Delta\delta} \cdot \frac{2((\delta_0 - \delta) \cdot V_{Co^{4+}} + (\delta - \delta_0) \cdot V_{Co^{3+}})}{V_0} \tag{5.15}$$

$$\beta_{Co\ 4\to3} = \frac{2 \cdot (V_{Co^{3+}} - V_{Co^{4+}})}{\mathrm{V_0}} \tag{5.16}$$

If the spherical shape of the cobalt ion is assumed, the expression of the chemical expansion coefficient of cobalt caused by reduction from Co^{4+} to Co^{3+} is described with equation 5.17.

$$\beta_{Co\ 4\to3} = \frac{2 \cdot \frac{4}{3}\pi \cdot (r^3_{Co^{3+}} - r^3_{Co^{4+}})}{\mathrm{V_0}} \tag{5.17}$$

Reduction of Co^{3+} to Co^{2+}

The analogous analysis may be conducted if the $\delta < 0.5$, namely in the highly reduced regime. When the oxygen vacancy concentration is high, it may be assumed that the cobalt is a mixture of Co^{3+}, and Co^{2+}, thus the relation between cobalt's average oxidation state is given with the equation 5.18. The sum of Co^{2+}, and Co^{3+} is equal to the total molar concentration of cobalt in $BaLnCo_2O_{6-\delta}$.

$$Co^{AVG} = \frac{3}{2} \cdot \left[Co^{\frac{1}{2}/}_{Co}\right] + \left[Co^{\frac{3}{2}/}_{Co}\right] \tag{5.18}$$

$$\left[Co^{\frac{1}{2}/}_{Co}\right] + \left[Co^{\frac{3}{2}/}_{Co}\right] = 2 \tag{5.19}$$

The relations between cobalt at each oxidation state concentration and oxygen nonstoichiometry are given with the equations 5.20 and 5.21.

$$\left[Co^{\frac{1}{2}/}_{Co}\right] = 3 - 2\delta \tag{5.20}$$

$$\left[Co^{\frac{3}{2}/}_{Co}\right] = 2\delta - 1 \tag{5.21}$$

Similarly, to the oxidised regime, the reduced cobalt volume can be calculated as a weighted mean of Co^{3+} and Co^{2+} volume, which is presented in equation 5.22.

$$V_{Co}(\delta) = \frac{(3-2\delta)\cdot V_{Co^{3+}} + (2\delta-1)\cdot V_{Co^{2+}}}{2} \tag{5.22}$$

The chemical expansion coefficient of cobalt associated with the reduction from Co^{3+} to Co^{2+} may be defined according to equation 5.22.

$$\beta_{Co\ 3\to2} = \frac{1}{\delta-\delta_0}\cdot\frac{\Delta V_{Co}}{V_0} \tag{5.23}$$

As an initial value of oxygen nonstoichiometry in this regime the value $\delta = 0.5$ is taken, and $V_{Co_0} = V_{Co^{3+}}$. On this basis, the equation 5.23 may be further transformed, to the form presented in equation 5.26

$$\beta_{Co\ 3\to2} = \frac{1}{\delta-0.5}\cdot\frac{(1-2\delta)\cdot V_{Co^{3+}} + (2\delta-1)\cdot V_{Co^{2+}}}{V_0} \tag{5.24}$$

$$\beta_{Co\ 3\to2} = \frac{1}{\delta-0.5}\cdot\frac{(0.5-\delta)\cdot V_{Co^{3+}} + (\delta-0.5)\cdot V_{Co^{2+}}}{V_0} \tag{5.25}$$

$$\beta_{Co\ 3\to2} = \frac{V_{Co^{2+}} - V_{Co^{3+}}}{V_0} \tag{5.26}$$

Relating cobalt ion volume to the ionic radius of cobalt, the expression of chemical expansion of cobalt corresponding to its reduction will be presented with equation 5.27

$$\beta_{Co\ 3\to2} = \frac{\frac{4}{3}\pi\cdot\left(r_{Co^{2+}}^3 - r_{Co^{3+}}^3\right)}{V_0} \tag{5.27}$$

Chemical expansion of oxygen vacancy formation

Simultaneously to cobalt reduction, the formation of oxygen vacancies takes place, which also influences the unit cell volume. In both, oxidised and reduced regimes the relation describing the chemical expansion of oxygen vacancy formation is believed to be the same, which may be described by equation 4.28.

$$\beta_{v_O^{\bullet\bullet}} = \frac{1}{\Delta\delta} \cdot \frac{\Delta V_O}{V_{O_0}} \tag{5.28}$$

V_O in equation 5.28 states for the average volume of oxygen site, which, similarly to the cobalt site may be calculated as a weighted mean of oxygen ion and oxygen vacancy volumes. This relation is presented in equation 5.29.

$$V_O = \frac{[O_O^X] \cdot V_{O_O^X} + [v_O^{\bullet\bullet}] \cdot V_{V_O^{\bullet\bullet}}}{6} \tag{5.29}$$

The δ value may be used to determine the molar concentrations of oxygen ions and oxygen vacancies. Thus, equation 5.29 may be written as Eq. 5.30.

$$V_O = \frac{(6-\delta) \cdot V_{O_O^X} + \delta \cdot V_{V_O^{\bullet\bullet}}}{6} \tag{5.30}$$

The equation of chemical expansion upon oxygen vacancy formation may be written by inserting equations 5.30 to equation 5.28, which is presented in equations 5.31 and 5.32.

$$\beta_{v_O^{\bullet\bullet}} = \frac{1}{\delta - \delta_0} \cdot \frac{(\delta_0 - \delta) \cdot V_{O_O^X} + (\delta - \delta_0) \cdot V_{V_O^{\bullet\bullet}}}{V_0} \tag{5.31}$$

$$\beta_{v_O^{\bullet\bullet}} = \frac{V_{V_O^{\bullet\bullet}} - V_{O_O^X}}{V_0} \tag{5.32}$$

5.2.2 Chemical expansion coefficient calculations

Figure 5.9 presents the relative change of unit cell volume resulting only from chemical expansion as a function of oxygen nonstoichiometry. This data was obtained by subtracting the fitted volume thermal expansion coefficient from the total change of unit cell volume upon temperature increase. The δ values at the specific temperature were drawn from the thermogravimetric studies. The oxidation was studied up to 900°C, while the high-temperature structural analyses were carried out up to 1000°C. Thus, there was a lack of data on oxygen nonstoichiometry at 1000°C, this value, therefore, was calculated by extrapolating the oxidation curve. What can be seen is that in all investigated compositions the change in slope is observed above δ = 0.5, which supports the existence of two regimes in which different processes dominate. The red dashed line is a linear fit to the data presented in the graphs, which represent the total chemical expansion. The slope of those lines may be used as a total chemical expansion coefficient upon reduction, which is

presented in Table 5.2. Total chemical expansion coefficients, presented in Table 5.2 consist of two-part, as shown in equation 5.3.

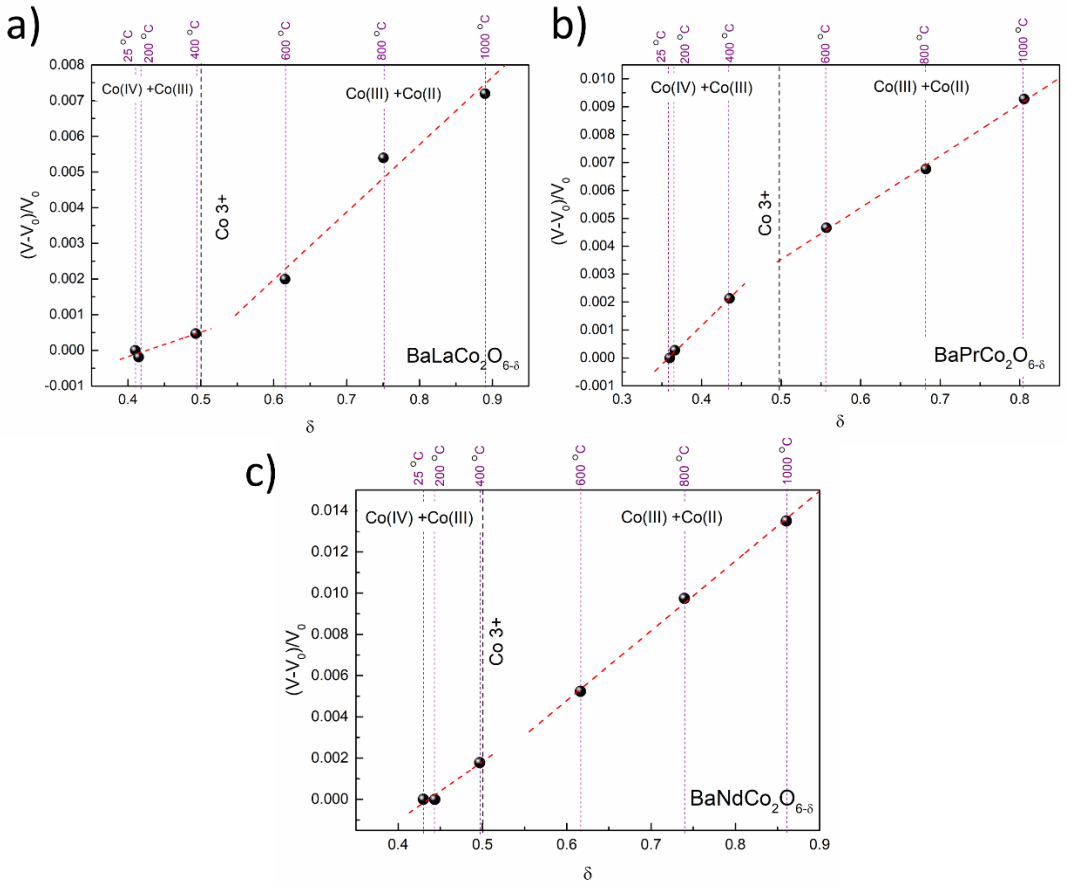

Figure 5.9 The relative change of unit cell volume resulting only from chemical expansion, obtained by subtracting thermal expansion from the total one. Reprinted from Szpunar et al. 2020[102]

Chemical expansion coefficient upon cobalt reduction in both, oxidised (eq. 5.17) and reduced (eq. 5.27) regimes, is dependent only on the initial unit cell volume and ionic radius of cobalt ion. Therefore, using the data determined by the means of iodometric titration and crystallographic data, each chemical expansion can be calculated. The calculated chemical expansion coefficients are summarized in Table 5.2. The calculation was conducted for the ionic radius of cobalt at each oxidation state in a high spin state. X-ray absorption spectroscopy studies confirmed that cobalt at room temperature exhibits a high spin state, which is also in agreement with the literature[158],[268]. The high spin of Co^{2+} is also stated to be more energetically favourable at room temperature[158],[268]. What is more, the general trend of the cobalt spin state is to increase with increasing temperature[269],[270]. For all the investigated lanthanides reduced regime is in the temperature range above 400°C, most Co^{2+} ions are believed to exhibit a high spin state.

Chemical expansion coefficient of oxygen vacancy formation was calculated accordingly to the equation 4.33.

$$\beta - 2\,\beta_{Co} = \beta_{V_O^{\bullet\bullet}} \tag{4.33}$$

The calculated values are presented in Table 5.2. In both oxidised and reduced regimes total chemical expansion coefficient β is positive, because of the unit cell volume increasing with increasing oxygen vacancy concentration. Nevertheless, the chemical expansion coefficient consists of two separate parts, giving the opposite effects. Chemical expansion coefficients of cobalt reduction exhibit positive values, while chemical expansion of oxygen vacancy formation is negative. The chemical expansion coefficient of oxygen vacancy formation in $BaNdCo_2O_{6-\delta}$ in contrast to others is positive. It should be emphasised, that the presented model takes into account the ionic radius of cobalt, which is not known for all spin states. Thus the calculated values are burdened with uncertainty. However, it does not significantly affect the correctness of the presented model, and unknown values could be easily implemented in it. A change in the cobalt oxidation state causes an increase in unit cell volume, while an oxygen vacancy formation causes its reduction. However, the influence of changes in the size of the cobalt ion radius is much stronger, therefore, along with the decrease in oxygen stoichiometry, an increase in the volume of the unit cell is observed.

Table 5.2 Total chemical expansion coefficients

Ln	Regime	β	β_{Co}	$\beta_{v_O^{\bullet\bullet}}$
La	δ < 0.5	$\beta = 0.007$	$\beta_{Co\,4\to3} = 0.0396$	$\beta_{v_O^{\bullet\bullet}} = -0.072$
	δ > 0.5	$\beta = 0.019$	$\beta_{Co\,3\to2} = 0.0133$	$\beta_{v_O^{\bullet\bullet}} = -0.0076$
Pr	δ < 0.5	$\beta = 0.028$	$\beta_{Co\,4\to3} = 0.0392$	$\beta_{v_O^{\bullet\bullet}} = -0.050$
	δ > 0.5	$\beta = 0.019$	$\beta_{Co\,3\to2} = 0.0132$	$\beta_{v_O^{\bullet\bullet}} = -0.0074$
Nd	δ < 0.5	$\beta = 0.029$	$\beta_{Co\,4\to3} = 0.0399$	$\beta_{v_O^{\bullet\bullet}} = -0.051$
	δ > 0.5	$\beta = 0.034$	$\beta_{Co\,3\to2} = 0.0134$	$\beta_{v_O^{\bullet\bullet}} = 0.0072$

So far, the phenomenon of chemical expansion has not been the subject of wide research on double perovskite cobaltites. Most of the available data is obtained with computer simulation since the experimental determination of the chemical expansion coefficient requires the use of sophisticated or combined measurement techniques. Two different approaches may be applied to determine the chemical expansion coefficient. The first is to observe changes in the unit cell parameters or the sample volume under the

influence of temperature changes at a constant partial pressure of oxygen. It is the approach that was applied within this study, but also in the literature[29],[271],[272]. The second approach is to conduct measurements under isothermal conditions by changing the oxygen partial pressure. The advantage of this approach is the elimination of the influence of the thermal expansion of the material. The observed changes in unit cell parameters result only from changes in the stoichiometry of the material. This approach was used to investigate the evolution of unit cell parameters of $BaNdCo_2O_{6-\delta}$[263] and $BaPrCo_2O_{6-\delta}$[264]. Both BNC and BPC exhibit the increase in a-parameter upon reduction, which agrees with this study. Cox-Galhotra, however, observed also the contraction along the c-axis, which has been explained by the high oxygen vacancy concentration in the Ln-O plane, which leads to the shift of Co and O2 towards the Ln-O plane[263],[264]. In this study, the localization of oxygen vacancies in Ln-O and anisotropy of chemical expansion were also observed, but no contraction of the c-parameter was present within this study. What is more, works of Cox-Galhorta do not contain calculated values of chemical expansion coefficient. Nevertheless, the general trend of changes in unit cell parameters can be compared, to what was done by Tsvetkov et.al[273]. Relative change of unit cell parameter is a measure of chemical lattice strain. The chemical lattice strain measured by Cox-Galhorta is lower than the one measured within this study, which may result from the fact that Cox-Galhorta conducted measurements under isothermal conditions, thus there was no need to separate chemical expansion from thermal. However, the chemical lattice strain presented in work of Cherepanov et. al[271]. is in a very good agreement to our studies[271],[273].

Since there is lack of reports on the chemical expansion coefficient in double perovskite cobaltites it is difficult to support those results. Although, chemical expansion coefficients were widely studied in $La_{1-x}Sr_xCo_yFe_{1-y}O_{3-\delta}$ (LSCF) system[181]. In this system total chemical expansion coefficient ranges from 0.022 for x = 0.4 and y = 0.8 to 0.059 for x = 0.5 and y = 0. The reported values refer to high temperatures, thus it should be compared to the reduced regime $\delta > 0.5$[181]. The results of chemical expansion coefficients in LCSF system is though comparable to the results presented within this thesis, what support the proposed model.

5.3 Water uptake

Three main questions arise from hydration studies of double perovskite cobaltites. The first question is whether the mass increase is a result of proton defect formation. The

second is what the mechanism of proton defect formation is, and finally what is the governing principle of hydration in double perovskite cobaltites. The goal is to establish a general rule, which could explain why some of those cobaltites hydrate, while the others do not.

Within this study water uptake was observed in $BaLaCo_2O_{6-\delta}$, $BaGdCo_2O_{6-\delta}$, and $BaDyCo_2O_{6-\delta}$. All of the investigated compounds exhibit the double perovskite structure; thus the water uptake phenomena cannot be related to the structure of the material, either to the ionic radius of lanthanide. As the cobalt average oxidation state and oxygen concentration increase linearly with the ionic radius of the lanthanide it also seems not to rule the water uptake. However, both the structure and oxygen content influence the level of water uptake, which is clearly visible in the studies of the cubic and double perovskite barium lanthanum cobaltite. The layered polymorph, which has a significantly higher concentration of oxygen vacancies, exhibits a four times higher mass increase in comparison to its cubic counterpart.

Contrary to literature reports no mass increase under humidified atmosphere was observed in $BaPrCo_2O_{6-\delta}$. However, that may be the result of a different experimental approach. Grimaud et al. observed water incorporation to $BaPrCo_2O_{6-\delta}$, which was assigned to proton defect formation and the authors stated that they managed to observe proton conductivity in BPC[190]. At first in Grimaud et al. approach, the sample was annealed in a wet atmosphere, and then the desorption of water was measured with thermogravimetric analysis. What is more, XRD measurements showed the formation of a secondary phase, which decomposed during TGA. A small amount of water absorbed by praseodymium barium cobaltite was also observed by Strandbakke et al.[192] and Hashimoto et al.[201] Goupil et al.[198] observed a mass increase of different cobaltites in the humidified atmosphere, but the amount absorbed water decreased with decreasing temperature below about 300°C, reaching value 0 at 0°C, what is inconsistent with the theory of hydration. This effect might be caused by water condensation in the thermobalance. Lozano et al.[274] applied secondary mass ion spectroscopy (SIMS) depth profiling to study the location of water in the BPC structure. This study concluded that water is located mainly close to the surface, which was related to hydrated layers in the interior walls of pores. However, they do not exclude the existence of a small number of proton defects in the material structure[274]. Malyshkin et al.[204] argued that although TGA and electrical conductivity

measurements are necessary to determine whether a material exhibits proton conductivity, they are not sufficient. Mass increase under humidified atmosphere may be incorrectly interpreted as proton defect formation, while it results from experimental error, hydration of impurities, or secondary phase formation[204].

Malyshkin et al.[204] and Lozano et al.[274] postulated that water uptake causes the formation of secondary phases on the surface of materials. In order to verify this statement XRD and TEM studies were performed on materials after exposure to the humidified atmosphere. Although the detection level and the resolution of laboratory scale XRD may not be sufficient to detect the small number of impurities, TEM clearly indicates that the humidified materials remain single-phase. What is more, as synthesised powders may also be considered as materials annealed under humidified atmosphere. The synthesis was performed in atmospheric air that was not dried. Typically, the relative humidity is around 40-60%, which translates into the partial pressure of water vapour of 0.01-0.015 bar. This value is comparable with the pH_2O used in the TG experiment. As-prepared powders, which may be then considered as hydrated, were investigated by the means of combined SR-PXD and NPD. As these techniques are characterized by very high resolution and did not indicate the presence of impurity phases, it can be clearly stated that in the investigated materials, no foreign phases are formed under the influence of a humid atmosphere. The investigated materials remain stable even under high water vapour pressure.

Malyshkin et al. postulated that $BaCo_{0.8}Gd_{0.2}O_{3-\delta}$ exhibits such a significant mass increase under exposure to the humidified atmosphere, that even if it is a minority phase, the water uptake is measurable. This study shows, that $BaCo_{0.8}Gd_{0.2}O_{3-\delta}$ hydrates, but the mass increase is of the same order of magnitude as that of $BaLaCo_2O_{6-\delta}$ and $BaGdCo_2O_{6-\delta}$. It is therefore impossible that the total mass gain of BGC and BLC is due to the hydration of the secondary cubic phase. It was shown, that in the investigated materials no secondary phase is formed upon the humidified condition, but even if BLC and BGC contain a secondary phase, its concentration is close to the detection level. The detection level of SR-PXD is around 3%, while for NPD it may be less than 1%[275]. If both BLC and BGC contain 5 wt. % of the impurity phase, and the whole mass increase is related to the hydration of this contamination, the relative mass increase of the impurity phase would be 0.32% and 0.42% for BLC and BGC, respectively. This value is one order of magnitude

higher than measured for $BaCo_{0.8}Gd_{0.2}O_{3-\delta}$. Therefore, the total increase in mass is not related to the hydration of the undetected contaminant.

Though the mass increase of $BaCo_{0.8}Gd_{0.2}O_{3-\delta}$ under humidified atmosphere reported by Malyshkin et al. reaches 0.2%, which could explain the total hydration, the differences in experimental approaches should be emphasised. Malyshkin et al.[204] measured the hydration as a function of temperature, under constant water vapour partial pressure, namely in isobaric conditions. In this study, isothermal water uptake is presented. Although in the case of pure proton conductors, isobaric and isothermal measurements give similar results[244], large differences may be observed in the water uptake of mixed conductors. Isothermal studies seem to be more relevant to mixed conducting materials, because more than one reaction contributing to mass increase may take place, which leads to an overestimation of calculated proton defect concentration.

Typically, the mass of proton conducting materials increases exponentially after exposure to the humidified atmosphere. In this study, a linear increase was observed. Such linear kinetics of mass relaxation is rather unusual[276]. Although the mass of BLC and BGC appears to increase linearly, more careful insight into the results reveals that in a short time after the change of water vapour partial pressure, the mass increase exponentially. On this basis, it can be stated that probably more than one reaction, with two different time constants, take place after the atmosphere switch.

More than one reaction contributing to water uptake is typical of mixed conducting oxides with three mobile carriers. As it was shown by Poetzsch et al.[132],[277] the diffusion in materials with three mobile carriers is a much more complicated problem than in materials with two mobile carriers. Thus, it is possible to observe two simultaneous reactions with different time constants, which together cause a linear increase in mass under exposure to the humidified atmosphere. Separating and identifying these processes is challenging. The calculation of proton concentration and determination of proton uptake mechanisms requires therefore great care.

A similar linear mass increase of equilibrated material was observed by Miruszewski et al.[278] in $Ba_{0.5}Sr_{0.5}Ti_{0.9}Fe_{0.1}O_{3-\delta}$, however, the initial exponential growth was much more pronounced. The fast process of mass increase was attributed to the hydrogenation due to a high hole concentration, while the slow process to the oxidation of the material. Since the

material was equilibrated in a dry atmosphere, it may be stated that water vapour partial pressure influences the kinetics of oxygen incorporation. A hypothetical reaction of simultaneous water and oxygen incorporation may therefore be written, which can be called 'hydroxylation' (eq. 5.34). This reaction involves two oxygen vacancies in the positions in which two proton defects are built-in, which is compensated by the creation of two electron holes.

$$H_2O_{(g)} + \frac{1}{2}O_{2_{(g)}} + 2V_O^{\bullet\bullet} \rightarrow \boldsymbol{2OH_O^{\bullet}} + 2h^{\bullet} \qquad (5.34)$$

$BaLaCo_2O_{6-\delta}$ and $BaGdCo_2O_{6-\delta}$ exhibit high p-type conductivity[165], thus it seems that proton incorporation in the reaction of hydrogenation is more probable. However, the determination of the proton formation mechanism should be further analysed.

In all investigated compound the oxygen vacancies locate in the Ln-O layer. $BaLaCo_2O_{6-\delta}$ and $BaGdCo_2O_{6-\delta}$ were not an exception in this respect. O1 and O2 positions in those compounds are fully occupied. Hence, the water uptake cannot be explained by the presence of oxygen vacancies outside the Ln-O layers, because they do not occur in any of the investigated materials. Although the oxygen vacancy concentration and structure affect the level of mass increase upon humidified atmosphere, what was shown on the cubic and double perovskite cobaltites, it does not determine whether the water uptake will take place or not. Similar observation were made by Zohourian et al.[24], who showed that differences in oxygen vacancy concentration are insufficient to explain the difference in proton uptake level in mixed conducting perovskites. According to this work, the degree of hydration is determined by the basicity of the oxide ions, which is only partially captured by the cation electronegativity[279]. The authors postulated that it is the B-site cation nature that determines the proton uptake. The hole transfer from the B-site transition metal to the oxygen, which increases the covalent nature of the B-O bond, impedes the protonic defect formation[279]. Bjørheim et al.[280] also suggested that the proton affinity is directly related to the electronic structure of both binary and ternary perovskite oxides. The authors observed a direct correlation between ionization potential and proton affinity. The lower ionization potential is, namely the higher the absolute position of the valence band maximum, the more favourable proton formation is[280].

X-ray absorption results showed that protonic defect formation influences the electronic structure, but the barium lanthanide cobaltites behave differently than the materials studied by Zohourian et al.[279]. In this case the water uptake is determined by the nature of the A-site cation since all the investigated materials are the cobaltites. Barium lanthanum and praseodymium cobaltites exhibit the significantly higher intensity of the pre-peak on O K edge, characteristic of overlap of Co 3*d* and O 2*p* ligand hole states, which indicates a higher concentration of holes localized close to the oxygen ion positions in BPC and BNC. By comparison, the intensity of the same pre-peak in barium lanthanum and gadolinium cobaltites is significantly lower. Therefore, it seems that in BPC and BNC the positive charge is more shifted toward oxygen and it is more difficult to incorporate the positively charged proton due to the Coulomb repulsion. The similar effect was observed in $BaFeO_{3-\delta}$ by Hoedl et al., who stated that the OH^- affinity increases with a decreasing ligand hole concentration[281].

The spectral weight of the overlapped state of Co 3*d* and O 2*p* ligand hole line increases as BGC and BLC materials were exposed to water vapour. This again indicates more holes on the oxygen sites thus it seems that proton defect formation causes the hole shift from cobalt to the oxygen. This is also visible on the Co L_3 edge. The intensity of this spectral line strongly decreases upon hydration, indicating the decreasing concentration of holes. A possible explanation is that when the proton defect is formed in be Co-O polyhedron the presence of its positive charge at one of the oxygen sites repulses the existing hole from the closest cobalt to other oxygen sites in the same polyhedron.

The question is why the properties of Co 3d and O 2p overlapped states change with the change of the lanthanide. It seems that there is some interaction between 4f states of Ln and 3d states of Co. Lanthanum and gadolinium at the third oxidation state, among other lanthanides have unique electronic structure having respectively empty and half full 4*f* sub-shell, which are most stable electronic configurations in the Ln series. It seems that such configurations interact with cobalt in a different way than other lanthanides. The difference may originate from the total angular momentum, L. In the case on unpaired electrons on 4f orbitals the total angular momentum of the ions $L \neq 0$ gives rise to a non-zero magnetic moment of the ion. This magnetic moment may affect the Co 3d states even at higher temperatures. On the other hand, La and Gd have $L = 0$ and this may cause weaker effect

on Co states, which in the end leverages the protonic defect formation. This may cause the formation of unique electronic structure that enables protonic defect to incorporate.

On the basis of the research presented in this dissertation, it was hypothesized that the possibility of the protonic defect formation is related to the electronic structure of the material, which is consistent with the latest studies of Hoedl et al[281]. Admittedly, this work does not consider the influence of the lanthanide on the ability of water incorporation. Although, we postulate that the interaction between Ln 4f and Co 3d states is crucial for the ability to incorporate water.

Summary

In the presented dissertation the materials from the family of $BaLnCo_2O_{6-\delta}$, where Ln stands for La, Pr, Nd, Sm, Gd, Tb, and Dy, were synthesised and characterized. The aim of this study was to identify the governing principles of hydration in the proposed group of materials. To verify the proposed research hypothesis. To verify the research hypotheses, a thorough analysis of the structural and thermal properties was carried out. The electronic structure of the materials was also examined. The following research techniques were used. Laboratory scale x-ray diffraction and combined synchrotron radiation x-ray diffraction with neutron powder diffraction were used to determine the crystallographic structure of investigated materials. The diffraction studies were analysed with Rietveld refinement. The transmission electron microscopy supported the structural studies. Scanning electron microscopy was used to investigate the morphology and phase uniformity of the materials. Oxygen nonstoichiometry at room and elevated temperatures were determined by the means of iodometric titration and thermogravimetry, respectively. Thermogravimetry was also used to verify the ability to incorporate the protonic defects. The electronic structure of the investigated materials was studied with x-ray absorption.

All of the synthesised materials, except $BaLaCo_2O_{6-\delta}$, exhibit double perovskite structure with A-site cations ordered in alternate layers along the c-axis. Rietveld refinement revealed the orthorhombic Pmmm unit cell of investigated materials. The unit cell parameter doubling along b-axis result from the oxygen vacancy ordering, what was directly confirmed with transmission electron microscopy. As synthesised barium lanthanum cobaltite has cubic perovskite structure, which is possible to form due to the small difference in ionic radius of barium and lanthanum. It has been observed that the orthorhombic double perovskite structure is stabilized over a wider range of oxygen stoichiometry than reported before. The unit cell parameters, and equilibrium oxygen content scale with the ionic radius of the lanthanide cation. The A-site cations ordering in BLC was achieved by annealing the material in an argon atmosphere. The reduced barium lanthanum cobaltite consists of two double perovskite polymorphs, tetragonal and orthorhombic structure. The temperature evolution of phase fraction of orthorhombic and tetragonal phases correlates well with the oxygen nonstoichiometry. This observation was the basis for formulating a model of the phase transition mechanism between orthorhombic and tetragonal double perovskite structures. The thermal and chemical expansion

contribution were separated from the temperature evolution of unit cell parameter. The thermal and volumetric chemical expansion coefficients of $BaLaCo_2O_{6-\delta}$, $BaPrCo_2O_{6-\delta}$, and $BaNdCo_2O_{6-\delta}$, were determined and the thermal expansion model was developed.

Mass increase upon water vapour partial pressure switch was observed only in $BaLaCo_2O_{6-\delta}$, $BaGdCo_2O_{6-\delta}$, and $BaDyCo_2O_{6-\delta}$. The signal from $BaDyCo_2O_{6-\delta}$, however, was very slight. It was excluded that the observed mass increase was related to the formation of secondary, also amorphous, phases on the surface of the grains. It was also not related to the presence of any impurity in the material. Since this it was concluded that the observed increase in mass is a volumetric effect resulting from protonic defects formation. However, it has not been decided whether proton defects are formed in the hydration or hydrogenation reaction. What is more, the observed mass increase is linear in time, instead of a typical exponential behaviour. This suggests that upon water vapour partial pressure switch more than process, with different time constants, take place. The hypothetical reaction of hydroxylation, being the simultaneous water and oxygen incorporation, was proposed.

The ability to incorporate water into the structure of the material could not be related to any structural feature, or oxygen vacancy concentration, since the structure of all investigated double perovskites is uniform and the oxygen vacancies concentration is proportional to lanthanide ionic radius. No oxygen vacancies were found in $BaLaCo_2O_{6-\delta}$ and $BaGdCo_2O_{6-\delta}$ on the different crystallographic position than in other investigated materials. This contradicts the stated research hypothesis, as proton defects will tend to build up on the position of the oxygen vacancy located in the Co-O layer. However, as shown in the example of cubic and double barium lanthanum cobaltite, although the crystallographic structure and the concentration of oxygen vacancies are not factors determining the ability to form protonic defects, they have an impact on the level of mass increase, which translates into the concentration of proton defects.

It seems that the key to explaining the ability of mixed conducting cobaltites with a double perovskite structure lies in the electronic structure of the material. The XAS studies revealed that the hole concentration on the mixed O2p and Co 3d t_{2g} orbital in $BaLaCo_2O_{6-\delta}$, $BaGdCo_2O_{6-\delta}$ is significantly lower than in other investigated materials. What is more, in hydrated materials this concentration significantly increases. The protonic defect, therefore, leads to a transfer of the electron hole towards oxygen, so it is not possible in materials

with a high ligand hole concentration. A hypothesis was made that the unique electronic structure of $BaLaCo_2O_{6-\delta}$, $BaGdCo_2O_{6-\delta}$ arises because of the interaction of lanthanum and gadolinium 4f orbitals with cobalt 3d orbitals. The 4f orbital of La^{3+} is empty, while the 4f orbital of Gd^{3+} is half full, and thus the total angular momentum of these lanthanides, unlike others with unpaired electrons on 4f orbital, is equal to 0. Such a configuration promotes the protonic defect formation.

In conclusion, this dissertation presents the detailed description of crystallographic structure of double perovskite cobaltites and verifies their ability to incorporate protonic defects into the materials structure. The study found that that the governing principle of hydration in mixed conducting perovskite oxides is an electronic structure of the material, which is determined by the nature of 4f orbital of the lanthanide. This statement is in agreement with the most recent literature reports.

This thesis was the part of the project „*Governing Principles in Hydration of Mixed Conducting Oxides*" co-financed by the National Science Centre under contract no. UMO-2016/22 / Z / ST5 / 00691. This project was carried out under the M-ERA.NET Joint Call 2016 agreement in cooperation with the University of Oslo and the Institute for Energy Technology in Norway, as well as Consejo Superior de Investigaciones in Spain.

References

1. Bjørheim, T. S. *et al.* A combined conductivity and DFT study of protons in $PbZrO_3$ and alkaline earth zirconate perovskites. *Solid State Ionics* **181**, 130–137 (2010).
2. Kreuer, K. D. Proton-Conducting Oxides. *http://dx.doi.org/10.1146/annurev.matsci.33.022802.091825* **33**, 333–359 (2003).
3. Norby, T., Widerøe, M., Glöckner, R. & Larring, Y. Hydrogen in oxides. *Dalt. Trans.* **0**, 3012–3018 (2004).
4. Brenner, T. M., Egger, D. A., Kronik, L., Hodes, G. & Cahen, D. Hybrid organic—inorganic perovskites: low-cost semiconductors with intriguing charge-transport properties. *Nat. Rev. Mater. 2016 11* **1**, 1–16 (2016).
5. Stoddart, A. Purely organic perovskites. *Nat. Rev. Mater. 2018 38* **3**, 226–226 (2018).
6. Yin, W. J., Yang, J. H., Kang, J., Yan, Y. & Wei, S. H. Halide perovskite materials for solar cells: a theoretical review. *J. Mater. Chem. A* **3**, 8926–8942 (2015).
7. George, G., Ede, S. R. & Luo, Z. Fundamentals of Perovskite Oxides : Synthesis, Structure, Properties and Applications. *Fundam. Perovskite Oxides* (2020) doi:10.1201/9780429351419.
8. Glazer, A. M. & IUCr. Perovskites modern and ancient. By Roger H. Mitchell.Thunder Bay, Ontario: AlmazPress, 2002. Price USD 70.00. ISBN0-9689411-0-9. *urn:issn:0108-7681* **58**, 1075–1075 (2002).
9. Chen, Z. X., Chen, Y. & Jiang, Y. S. Comparative Study of ABO3 Perovskite Compounds. 1. $ATiO_3$ (A = Ca, Sr, Ba, and Pb) Perovskites. *J. Phys. Chem. B* **106**, 9986–9992 (2002).
10. Bhalla, A. S., Guo, R. & Roy, R. The perovskite structure—a review of its role in ceramic science and technology. *http://dx.doi.org/10.1007/s100190000062* **4**, 3–26 (2016).
11. Aïssa, B., Ali, A. & El-Mellouhi, F. Oxide and Organic–Inorganic Halide Perovskites with Plasmonics for Optoelectronic and Energy Applications: A Contributive Review. *Catal. 2021, Vol. 11, Page 1057* **11**, 1057 (2021).
12. Juarez-Perez, E. J. *et al.* Photoinduced giant dielectric constant in lead halide perovskite solar cells. *J. Phys. Chem. Lett.* **5**, 2390–2394 (2014).
13. Yang, L. *et al.* Perovskite lead-free dielectrics for energy storage applications. *Prog. Mater. Sci.* **102**, 72–108 (2019).
14. Inaguma, Y., Chen, L., Itoh, M. & Nakamura, T. Candidate compounds with perovskite structure for high lithium ionic conductivity. *Solid State Ionics* **70**–**71**, 196–202 (1994).
15. Lan, R., Cowin, P. I., Sengodan, S. & Tao, S. A perovskite oxide with high conductivities in both air and reducing atmosphere for use as electrode for solid oxide fuel cells. *Sci. Reports 2016 61* **6**, 1–8 (2016).
16. Fukui, T., Ohara, S. & Kawatsu, S. Conductivity of $BaPrO_3$ based perovskite oxides.

J. Power Sources **71**, 164–168 (1998).

17. Kamata, H. *et al.* High temperature electrical properties of the perovskite-type oxide $La_{1-x}Sr_xMnO_{3-d}$. *J. Phys. Chem. Solids* **56**, 943–950 (1995).

18. Mizusaki, J. *et al.* Oxygen nonstoichiometry and defect equilibrium in the perovskite-type oxides $La_{1-x}Sr_xMnO_{3+d}$. *Solid State Ionics* **129**, 163–177 (2000).

19. Kuo, J. H., Anderson, H. U. & Sparlin, D. M. Oxidation-reduction behavior of undoped and Sr-doped $LaMnO_3$: Defect structure, electrical conductivity, and thermoelectric power. *J. Solid State Chem.* **87**, 55–63 (1990).

20. Bohnke, O., Bohnke, C. & Fourquet, J. L. Mechanism of ionic conduction and electrochemical intercalation of lithium into the perovskite lanthanum lithium titanate. *Solid State Ionics* **91**, 21–31 (1996).

21. Ishihara, T., Matsuda, H. & Takita, Y. Effects of rare earth cations doped for La site on the oxide ionic conductivity of $LaGaO_3$-based perovskite type oxide. *Solid State Ionics* **79**, 147–151 (1995).

22. Huang, W., Li, Y., Ding, Y. & Li, H. Preparation and conductive properties of double perovskite $Ba_3Sr_{1+x}Ta_{2-x}O_{9-\delta}$ and application for hydrogen sensor. *J. Alloys Compd.* **792**, 759–769 (2019).

23. Tarasova, N. *et al.* Novel mid-temperature $Y^{3+} \rightarrow In^{3+}$ doped proton conductors based on the layered perovskite BaLaInO4. *Ceram. Int.* **48**, 15677–15685 (2022).

24. Zohourian, R. *et al.* Mixed-Conducting Perovskites as Cathode Materials for Protonic Ceramic Fuel Cells: Understanding the Trends in Proton Uptake. *Adv. Funct. Mater.* **28**, 1801241 (2018).

25. Mastrikov, Y. A., Merkle, R., Heifets, E., Kotomin, E. A. & Maier, J. Pathways for oxygen incorporation in mixed conducting perovskites: A DFT-based Mechanistic analysis for (La, Sr)MnO3-δ. *J. Phys. Chem. C* **114**, 3017–3027 (2010).

26. Stevenson, J. W., Armstrong, T. R., Carneim, R. D., Pederson, L. R. & Weber, W. J. Electrochemical Properties of Mixed Conducting Perovskites $La_{1-x}M_xCo_{1-y}Fe_yO_{3-\delta}$ (M = Sr, Ba, Ca). *J. Electrochem. Soc.* **143**, 2722–2729 (1996).

27. Atou, T., Chiba, H., Ohoyama, K., Yamaguchi, Y. & Syono, Y. Structure Determination of Ferromagnetic Perovskite BiMnO3. *J. Solid State Chem.* **145**, 639–642 (1999).

28. Ali, Z. *et al.* Theoretical studies of structural and magnetic properties of cubic perovskites $PrCoO_3$ and $NdCoO_3$. *Phys. B Condens. Matter* **406**, 3800–3804 (2011).

29. Akahoshi, D. & Ueda, Y. Oxygen Nonstoichiometry, Structures, and Physical Properties of $YBaCo_2O_{5+x}$ ($0.00 \leq x \leq 0.52$). *J. Solid State Chem.* **156**, 355–363 (2001).

30. Shi, Y. G. *et al.* Continuous metal-insulator transition of the antiferromagnetic perovskite $NaOsO_3$. *Phys. Rev. B - Condens. Matter Mater. Phys.* **80**, 161104 (2009).

31. Goodenough, J. B., Longo, J. M. & Kafalas, J. A. Band antiferromagnetism and the new perovskite $CaCrO_3$. *Mater. Res. Bull.* **3**, 471–481 (1968).

32. Zhang, Y. *et al.* Properties of the ferrimagnetic double perovskites A_2FeReO_6 (A =

Ba and Ca). *J. Phys. Condens. Matter* **12**, 965 (2000).

33. Deschizeaux, M. N. *et al.* Synthesis and crystal structure of $(ThCu_3)(Mn^{3+}{}_2Mn^{4+}{}_2)O_{12}$, a new ferrimagnetic perovskite-like compound. *J. Solid State Chem.* **19**, 45–51 (1976).

34. Snyder, G. J. *et al.* Local structure, transport, and rare-earth magnetismin the ferrimagnetic perovskites. *Phys. Rev. B* **55**, 6453 (1997).

35. Takamura, Y. *et al.* Competing interactions in ferromagnetic/antiferromagnetic perovskite superlattices. *Phys. Rev. B - Condens. Matter Mater. Phys.* **80**, 180417 (2009).

36. De Teresa, J. M. *et al.* Spin-glass insulator state in $(Tb\text{-}La)_{2/3}Ca_{1/3}MnO_3$ perovskite *Phys. Rev. Lett.* **76**, 3392 (1996).

37. Zhang, J. *et al.* Kondo-like transport and its correlation with the spin-glass phase in perovskite manganites. *Phys. Rev. B* **72**, 054410 (2005).

38. Cai, J. W., Wang, C., Shen, B. G., Zhao, J. G. & Zhan, W. S. Colossal magnetoresistance of spin-glass perovskite $La_{0.67}Ca_{0.33}Mn_{0.9}Fe_{0.1}O_3$. *Appl. Phys. Lett.* **71**, 1727 (1998).

39. Moritomo, Y., Asamitsu, A., Kuwahara, H. & Tokura, Y. Giant magnetoresistance of manganese oxides with a layered perovskite structure. *Nat. 1996 3806570* **380**, 141–144 (1996).

40. Arulraj, A., Ramesha, K., Gopalakrishnan, J. & Rao, C. N. R. Magnetoresistance in the Double Perovskite Sr_2CrMoO_6. *J. Solid State Chem.* **155**, 233–237 (2000).

41. Jia, Y. X. *et al.* Pr-doping of the high-magnetoresistance perovskite $Nd_{23}Sr_{13}MnO_3$. *Solid State Commun.* **94**, 917–920 (1995).

42. Ginzburg, V. L. (Vitaliĭ L., Kirzhnit͡s, D. A. (David A., Agyei, A. K. & Birman, J. L. (Joseph L. High-temperature superconductivity. 364 (1982).

43. Tilley, R. J. D. *Perovskites : structure-property relationships*. (John Wiley & Sons, Ltd, 2016).

44. SEBASTIAN, M. T. CATION-DEFICIENT PEROVSKITES. *Dielectr. Mater. Wirel. Commun.* 335–360 (2008) doi:10.1016/B978-0-08-045330-9.00009-1.

45. Ishihara, T. Structure and Properties of Perovskite Oxides. 1–16 (2009) doi:10.1007/978-0-387-77708-5_1.

46. Mitchell, R. H. *Perovskites modern and ancient*. (Almaz Press Inc., 2002).

47. Bartel, C. J. *et al.* New tolerance factor to predict the stability of perovskite oxides and halides. *Sci. Adv.* **5**, (2019).

48. Cui, S. H., Li, Y., Wang, F. F., Wu, D. & Li, Z. R. Prediction and characterization of a new kind of alkali–superhalogen species with considerable stability: MBeX 3 (M = Li, Na; X = F, Cl, Br). *Phys. Chem. Chem. Phys.* **9**, 5721–5726 (2007).

49. Noheda, B., Gonzalo, J., Cross, L., Guo, R. & Park, S. Tetragonal-to-monoclinic phase transition in a ferroelectric perovskite: The structure of $PbZr_{0.52}Ti_{0.48}O_3$. *Phys. Rev. B* **61**, 8687 (2000).

50. Shim, S. H., Jeanloz, R. & Duffy, T. S. Tetragonal structure of $CaSiO_3$ perovskite above 20 GPa. *Geophys. Res. Lett.* **29**, 19–1 (2002).

51. Sasaki, S., Prewitt, C. T., Bass, J. D., Schulze, W. A. & IUCr. Orthorhombic perovskite $CaTiO_3$ and $CdTiO_3$: structure and space group. *urn:issn:0108-2701* **43**, 1668–1674 (1987).

52. Zhou, J. S. & Goodenough, J. B. Universal octahedral-site distortion in orthorhombic perovskite oxides. *Phys. Rev. Lett.* **94**, 065501 (2005).

53. Boudaya, C., Laroussi, L., Dhahri, E., Joubert, J. C. & Cheikh-Rouhou, A. Magnetic and magnetoresistance properties in rhombohedral perovskite-type compounds. *J. Phys. Condens. Matter* **10**, 7485 (1998).

54. Megaw, H. D. & Darlington, C. N. W. Geometrical and structural relations in the rhombohedral perovskites. *urn:issn:0567-7394* **31**, 161–173 (1975).

55. Nakamura, T., Sata, T. & Kose, S. Paramagnetism and Semiconductivity in a Triclinic Perovskite BaBiO3. *https://doi.org/10.1143/JPSJ.31.1284* **31**, 1284 (2013).

56. Ishiwata, S. *et al.* High pressure synthesis, crystal structure and physical properties of a new Ni(ii) perovskite BiNiO 3. *J. Mater. Chem.* **12**, 3733–3737 (2002).

57. Yu, J. *et al.* Monoclinic $SrIrO_3$: An Easily Synthesized Conductive Perovskite Oxide with Outstanding Performance for Overall Water Splitting in Alkaline Solution. *Chem. Mater.* **32**, 4509–4517 (2020).

58. Woodward, P. M. Octahedral Tilting in Perovskites. I. Geometrical Considerations. *urn:issn:0108-7681* **53**, 32–43 (1997).

59. Glazer, A. M. & IUCr. The classification of tilted octahedra in perovskites. *urn:issn:0567-7408* **28**, 3384–3392 (1972).

60. Howard, C. J. & Stokes, H. T. Group-Theoretical Analysis of Octahedral Tilting in Perovskites. *urn:issn:0108-7681* **54**, 782–789 (1998).

61. Kanamori, J. Crystal Distortion in Magnetic Compounds. *J. Appl. Phys.* **31**, S14 (2009).

62. Yin, W. J. *et al.* Oxide perovskites, double perovskites and derivatives for electrocatalysis, photocatalysis, and photovoltaics. *Energy Environ. Sci.* **12**, 442–462 (2019).

63. Aleksandrov, K. S. Structural phase transitions in layered perovskite-like crystals. *Crystallogr. Reports* **40**, 251–272 (1995).

64. Aleksandrov, K. S. & Beznosikov, B. V. Architecture of perovskite-like crystals. *Crystallogr. Reports* **42**, (1997).

65. Park, C. & Snyder, R. L. Structures of High-Temperature Cuprate Superconductors. *J. Am. Ceram. Soc.* **78**, 3171–3194 (1995).

66. Mitchell, R. H., Welch, M. D. & Chakhmouradian, A. R. Nomenclature of the perovskite supergroup: A hierarchical system of classification based on crystal structure and composition. *Mineral. Mag.* **81**, 411–461 (2017).

67. Fop, S., McCombie, K. S., Wildman, E. J., Skakle, J. M. S. & Mclaughlin, A. C. Hexagonal perovskite derivatives: a new direction in the design of oxide ion conducting materials. *Chem. Commun.* **55**, 2127–2137 (2019).

68. Darriet, J. & Subramanian, M. A. Structural relationships between compounds based on the stacking of mixed layers related to hexagonal perovskite-type structures. *J. Mater. Chem.* **5**, 543–552 (1995).

69. Nabi, M. & Gupta, D. C. Potential lead-free small band gap halide double perovskites Cs_2CuMCl_6 (M = Sb, Bi) for green technology. *Sci. Reports 2021 111* **11**, 1–13 (2021).

70. Das, N. & Kandimalla, S. Application of perovskites towards remediation of environmental pollutants: an overview. *Int. J. Environ. Sci. Technol. 2017 147* **14**, 1559–1572 (2017).

71. Bian, Z. *et al.* A review on perovskite catalysts for reforming of methane to hydrogen production. *Renew. Sustain. Energy Rev.* **134**, 110291 (2020).

72. Khan, R. *et al.* Role of perovskites as a bi-functional catalyst for electrochemical water splitting: A review. *Int. J. Energy Res.* **44**, 9714–9747 (2020).

73. Bin Adnan, M. A., Arifin, K., Minggu, L. J. & Kassim, M. B. Titanate-based perovskites for photochemical and photoelectrochemical water splitting applications: A review. *Int. J. Hydrogen Energy* **43**, 23209–23220 (2018).

74. Keav, S., Matam, S. K., Ferri, D. & Weidenkaff, A. Structured Perovskite-Based Catalysts and Their Application as Three-Way Catalytic Converters—A Review. *Catal. 2014, Vol. 4, Pages 226-255* **4**, 226–255 (2014).

75. Yang, Q., Liu, G. & Liu, Y. Perovskite-Type Oxides as the Catalyst Precursors for Preparing Supported Metallic Nanocatalysts: A Review. *Ind. Eng. Chem. Res.* **57**, 1–17 (2018).

76. Labhasetwar, N. *et al.* Perovskite-type catalytic materials for environmental applications. *http://www.tandfonline.com/action/journalInformation?show=aimsScope&journalCode=tsta20#.VmBmuzZFCUk* **16**, (2015).

77. Misono, M. Recent progress in the practical applications of heteropolyacid and perovskite catalysts: Catalytic technology for the sustainable society. *Catal. Today* **144**, 285–291 (2009).

78. Zhu, J. *et al.* Double Perovskite Cobaltites Integrated in a Monolithic and Noble Metal-Free Photoelectrochemical Device for Efficient Water Splitting. *ACS Appl. Mater. Interfaces* **13**, 20313–20325 (2021).

79. Vidyasagar, C. C., Muñoz Flores, B. M. & Jiménez Pérez, V. M. Recent Advances in Synthesis and Properties of Hybrid Halide Perovskites for Photovoltaics. *Nano-Micro Lett. 2018 104* **10**, 1–34 (2018).

80. Grancini, G. & Nazeeruddin, M. K. Dimensional tailoring of hybrid perovskites for photovoltaics. *Nat. Rev. Mater. 2018 41* **4**, 4–22 (2018).

81. Hoefler, S. F., Trimmel, G. & Rath, T. Progress on lead-free metal halide perovskites for photovoltaic applications: a review. *Monatshefte für Chemie - Chem. Mon. 2017*

1485 **148**, 795–826 (2017).

82. Chen, Y. *et al.* 2D Ruddlesden–Popper Perovskites for Optoelectronics. *Adv. Mater.* **30**, 1703487 (2018).

83. Liu, X. K. *et al.* Metal halide perovskites for light-emitting diodes. *Nat. Mater. 2020 201* **20**, 10–21 (2020).

84. Na Quan, L. *et al.* Perovskites for Light Emission. *Adv. Mater.* **30**, 1801996 (2018).

85. Veldhuis, S. A. *et al.* Perovskite Materials for Light-Emitting Diodes and Lasers. *Adv. Mater.* **28**, 6804–6834 (2016).

86. George, J. *et al.* Perovskite nanomaterials as optical and electrochemical sensors. *Inorg. Chem. Front.* **7**, 2702–2725 (2020).

87. Obayashi, H., Sakurai, Y. & Gejo, T. Perovskite-type oxides as ethanol sensors. *J. Solid State Chem.* **17**, 299–303 (1976).

88. Fergus, J. W. Perovskite oxides for semiconductor-based gas sensors. *Sensors Actuators B Chem.* **123**, 1169–1179 (2007).

89. Dimos, D. & Mueller, C. H. PEROVSKITE THIN FILMS FOR HIGH-FREQUENCY CAPACITOR APPLICATIONS1. *http://dx.doi.org/10.1146/annurev.matsci.28.1.397* **28**, 397–419 (2003).

90. Bellaiche, L. & Vanderbilt, D. Virtual crystal approximation revisited: Application to dielectric and piezoelectric properties of perovskites. *Phys. Rev. B* **61**, 7877 (2000).

91. Hao, J., Li, W., Zhai, J. & Chen, H. Progress in high-strain perovskite piezoelectric ceramics. *Mater. Sci. Eng. R Reports* **135**, 1–57 (2019).

92. Zheng, T., Wu, J., Xiao, D. & Zhu, J. Recent development in lead-free perovskite piezoelectric bulk materials. *Prog. Mater. Sci.* **98**, 552–624 (2018).

93. Wang, J. *et al.* Tunable Spin Characteristic Properties in Spin Valve Devices Based on Hybrid Organic–Inorganic Perovskites. *Adv. Mater.* **31**, 1904059 (2019).

94. Dahmen, K. H. & Carris, M. W. MOCVD of HTS and GMR perovskites by aerosol and liquid delivery MOCVD. *J. Alloys Compd.* **251**, 270–277 (1997).

95. Liu, X., Zhang, H. & Zhang, T. Recent advancements in manganite perovskites and spinel ferrite-based magnetic nanoparticles for biomedical theranostic applications. *Nanotechnology* **30**, 502001 (2019).

96. Sleight, A. W. Chemistry of High-Temperature Superconductors. *Science (80-.).* **242**, 1519–1527 (1988).

97. Jiang, S. P. & Li, Q. Introduction to Fuel Cells. *Introd. to Fuel Cells* (2022) doi:10.1007/978-981-10-7626-8.

98. Ormerod, R. M. Solid oxide fuel cells. *Chem. Soc. Rev.* **32**, 17–28 (2003).

99. Yamamoto, O. Solid oxide fuel cells: fundamental aspects and prospects. *Electrochim. Acta* **45**, 2423–2435 (2000).

100. Nobry Truls (University of Oslo). Personal communication. *19th Int. Conf. Solid*

State Protonic Conduct. (2018).

101. Sun, X., Simonsen, S. C., Norby, T. & Chatzitakis, A. Composite Membranes for High Temperature PEM Fuel Cells and Electrolysers: A Critical Review. *Membr. 2019, Vol. 9, Page 83* **9**, 83 (2019).

102. Szpunar, I. *et al.* High-Temperature Structural and Electrical Properties of $BaLnCo_2O_6$ Positrodes. *Materials (Basel).* **13**, 4044 (2020).

103. Mather, G. C. *et al.* Perspectives on Cathodes for Protonic Ceramic Fuel Cells. *Appl. Sci. 2021, Vol. 11, Page 5363* **11**, 5363 (2021).

104. Cao, J., Ji, Y. & Shao, Z. Perovskites for protonic ceramic fuel cells: a review. *Energy Environ. Sci.* **15**, 2200–2232 (2022).

105. Hussain, S. & Yangping, L. Review of solid oxide fuel cell materials: cathode, anode, and electrolyte. *Energy Transitions 2020 42* **4**, 113–126 (2020).

106. Hanif, M. B. *et al.* Recent progress of perovskite-based electrolyte materials for solid oxide fuel cells and performance optimizing strategies for energy storage applications. *Mater. Res. Bull.* **146**, 111612 (2022).

107. Ishihara, T. Low Temperature Solid Oxide Fuel Cells Using $LaGaO_3$-based Oxide Electrolyte on Metal Support. *J. Japan Pet. Inst.* **58**, 71–78 (2015).

108. Pelosato, R. *et al.* Co-precipitation in aqueous medium of $La_{0.8}Sr_{0.2}Ga_{0.8}Mg_{0.2}O_{3-\delta}$ via inorganic precursors. *J. Power Sources* **195**, 8116–8123 (2010).

109. Leng, Y., Chan, S. H. & Liu, Q. Development of LSCF–GDC composite cathodes for low-temperature solid oxide fuel cells with thin film GDC electrolyte. *Int. J. Hydrogen Energy* **33**, 3808–3817 (2008).

110. Zhou, X. & Zhou, F. Application of $La_{0.3}Sr_{0.7}Fe_{0.7}Ti_{0.3}O_{3-\delta}$/GDC electrolyte in LT-SOFC. *Int. J. Hydrogen Energy* **46**, 9988–9995 (2021).

111. Bae, K. *et al.* Demonstrating the potential of yttrium-doped barium zirconate electrolyte for high-performance fuel cells. *Nat. Commun. 2017 81* **8**, 1–9 (2017).

112. Kim, I. H. *et al.* Determination of partial conductivities and computational analysis of the theoretical power density of $BaZr_{0.1}Ce_{0.7}Y_{0.1}Yb_{0.1}O_{3-\delta}$ (BZCYYb1711) electrolyte under various PCFC conditions. *J. Mater. Chem. A* **7**, 21321–21328 (2019).

113. Shaikh, S. P. S., Muchtar, A. & Somalu, M. R. A review on the selection of anode materials for solid-oxide fuel cells. *Renew. Sustain. Energy Rev.* **51**, 1–8 (2015).

114. Andersson, M., Paradis, H., Yuan, J. & Sundén, B. Review of catalyst materials and catalytic steam reforming reactions in SOFC anodes. *Int. J. Energy Res.* **35**, 1340–1350 (2011).

115. Verbraeken, M. C. *et al.* Modified strontium titanates: from defect chemistry to SOFC anodes. *RSC Adv.* **5**, 1168–1180 (2014).

116. Tao, S. & Irvine, J. T. S. A redox-stable efficient anode for solid-oxide fuel cells. *Nat. Mater. 2003 25* **2**, 320–323 (2003).

117. Fergus, J. W. Oxide anode materials for solid oxide fuel cells. *Solid State Ionics* **177**,

1529–1541 (2006).

118. Ivers-Tiffée, E., Weber, A. & Herbstritt, D. Materials and technologies for SOFC-components. *J. Eur. Ceram. Soc.* **21**, 1805–1811 (2001).

119. Sun, C., Hui, R. & Roller, J. Cathode materials for solid oxide fuel cells: A review. *J. Solid State Electrochem.* **14**, 1125–1144 (2010).

120. Rembelski, D., Viricelle, J. P., Combemale, L. & Rieu, M. Characterization and Comparison of Different Cathode Materials for SC-SOFC: LSM, BSCF, SSC, and LSCF. *Fuel Cells* **12**, 256–264 (2012).

121. Wen, T. L., Tu, H., Xu, Z. & Yamamoto, O. A study of (Pr, Nd, Sm)$_{1-x}$Sr$_x$MnO$_3$ cathode materials for solid oxide fuel cell. *Solid State Ionics* **121**, 25–30 (1999).

122. Ishiham, T., Kudo, T., Matsuda, H. & Takita, Y. Doped Perovskite Oxide, PrMnO3, as a New Cathode for Solid-Oxide Fuel Cells that Decreases the Operating Temperature. *J. Am. Ceram. Soc.* **77**, 1682–1684 (1994).

123. Liu, M. *et al.* Enhanced performance of LSCF cathode through surface modification. *Int. J. Hydrogen Energy* **37**, 8613–8620 (2012).

124. Wang, W. G. & Mogensen, M. High-performance lanthanum-ferrite-based cathode for SOFC. *Solid State Ionics* **176**, 457–462 (2005).

125. Magnone, E. A systematic literature review on BSCF-based cathodes for solid oxide fuel cell applications. *J. Fuel Cell Sci. Technol.* **7**, (2010).

126. Liu, Q. L., Khor, K. A. & Chan, S. H. High-performance low-temperature solid oxide fuel cell with novel BSCF cathode. *J. Power Sources* **161**, 123–128 (2006).

127. Shao, Z. & Haile, S. M. A high-performance cathode for the next generation of solid-oxide fuel cells. *Mater. Sustain. Energy A Collect. Peer-Reviewed Res. Rev. Artic. from Nat. Publ. Gr.* 255–258 (2010) doi:10.1142/9789814317665_0036.

128. Mitsui, A., Miyayama, M. & Yanagida, H. Evaluation of the activation energy for proton conduction in perovskite-type oxides. *Solid State Ionics* **22**, 213–217 (1987).

129. Norby, T. Proton Conductivity in Perovskite Oxides. 217–241 (2009) doi:10.1007/978-0-387-77708-5_11.

130. Kreuer, K. D. *et al.* Proton conducting alkaline earth zirconates and titanates for high drain electrochemical applications. *Solid State Ionics* **145**, 295–306 (2001).

131. Norby, T. Solid-state protonic conductors: principles, properties, progress and prospects. *Solid State Ionics* **125**, 1–11 (1999).

132. Poetzsch, D., Merkle, R. & Maier, J. Proton uptake in the H + -SOFC cathode material Ba $_{0.5}$ Sr $_{0.5}$ Fe $_{0.8}$ Zn $_{0.2}$ O $_{3-\delta}$: transition from hydration to hydrogenation with increasing oxygen partial pressure. *Faraday Discuss.* **182**, 129–143 (2015).

133. Malyshkin, D., Novikov, A., Tsvetkov, D. & Zuev, A. Preparation, oxygen nonstoichiometry and defect structure of double perovskite LaBaCo$_2$O$_{6-\delta}$. *Mater. Lett.* **229**, 324–326 (2018).

134. Zhang, H. *et al.* An efficient and durable anode for ammonia protonic ceramic fuel cells. *Energy Environ. Sci.* **15**, 287–295 (2022).

135. Coors, W. G. Protonic ceramic fuel cells for high-efficiency operation with methane. *J. Power Sources* **118**, 150–156 (2003).

136. Choi, S. *et al.* Exceptional power density and stability at intermediate temperatures in protonic ceramic fuel cells. *Nat. Energy 2018 33* **3**, 202–210 (2018).

137. Chen, Y. *et al.* An In Situ Formed, Dual-Phase Cathode with a Highly Active Catalyst Coating for Protonic Ceramic Fuel Cells. *Adv. Funct. Mater.* **28**, 1704907 (2018).

138. Lin, B. *et al.* Intermediate-to-low temperature protonic ceramic membrane fuel cells with $Ba_{0.5}Sr_{0.5}Co_{0.8}Fe_{0.2}O_{3-\delta}$–$BaZr_{0.1}Ce_{0.7}Y_{0.2}O_{3-\delta}$ composite cathode. *J. Power Sources* **186**, 58–61 (2009).

139. Duan, C. *et al.* Readily processed protonic ceramic fuel cells with high performance at low temperatures. *Science (80-.).* **349**, 1321–1326 (2015).

140. Muñoz-García, A. B. & Pavone, M. First-Principles Design of New Electrodes for Proton-Conducting Solid-Oxide Electrochemical Cells: A-Site Doped $Sr_2Fe_{1.5}Mo_{0.5}O_{6-\delta}$ Perovskite. *Chem. Mater.* **28**, 490–500 (2016).

141. Bian, W. *et al.* Revitalizing interface in protonic ceramic cells by acid etch. *Nat. 2022 6047906* **604**, 479–485 (2022).

142. Raveau, B. (Bernard) & Seikh, M. M. *Cobalt oxides : from crystal chemistry to physics*. (Wiley-VCH, 2012).

143. Mizokawa, T. *et al.* Role of oxygen holes in Li_xCoO_2 revealed by soft X-ray spectroscopy. *Phys. Rev. Lett.* **111**, 056404 (2013).

144. Korotin, M. *et al.* Intermediate-spin state and properties of $LaCoO_3$. *Phys. Rev. B* **54**, 5309 (1996).

145. Señarís-Rodríguez, M. A. & Goodenough, J. B. $LaCoO_3$ Revisited. *J. Solid State Chem.* **116**, 224–231 (1995).

146. Kundu, A. K. *et al.* Spin-locking effect in the nanoscale ordered perovskite cobaltite La Ba Co 2 O 6. *Phys. Rev. B* **76**, 184432 (2007).

147. Sugiyama, J. *et al.* Dome-Shaped Magnetic Phase Diagram of Thermoelectric Layered Cobaltites. *Phys. Rev. Lett.* **92**, 4 (2004).

148. Maignan, A., Caignaert, V., Raveau, B., Khomskii, D. & Sawatzky, G. Thermoelectric power of $HoBaCo_2O_{5.5}$: Possible evidence of the spin blockade in cobaltites. *Phys. Rev. Lett.* **93**, 026401 (2004).

149. Nakajima, T., Ichihara, M. & Ueda, Y. New A-site ordered perovskite cobaltite $LaBaCo_2O_6$: Synthesis, structure, physical property and cation order-disorder effect. *J. Phys. Soc. Japan* **74**, 1572–1577 (2005).

150. Luo, W. & Wang, F. Powder X-ray diffraction and Rietveld analysis of $La_{1-x}Ba_xCoO_3$ (0<x≤0.5). *Powder Diffr.* **21**, 304–306 (2006).

151. Suard, E., Fauth, F. & Caignaert, V. Rhombohedral distortion in the new disordered $LaBaCo_2O_6$ perovskite. *Phys. B Condens. Matter* **276**–**278**, 254–255 (2000).

152. Garcés, D., Setevich, C. F., Caneiro, A., Cuello, G. J. & Mogni, L. Effect of cationic

order-disorder on the transport properties of $LaBaCo_2O_{6-\delta}$ and $La_{0.5}Ba_{0.5}CoO_{3-\delta}$ perovskites. *J. Appl. Crystallogr.* **47**, 325–334 (2014).

153. Shannon, R. D. & Prewitt, C. T. Effective ionic radii in oxides and fluorides. *Acta Crystallogr. Sect. B Struct. Crystallogr. Cryst. Chem.* **25**, 925–946 (1969).

154. Rautama, E. L. *et al.* Cationic Ordering and Microstructural Effects in the Ferromagnetic Perovskite $La_{0.5}Ba_{0.5}CoO_3$: Impact upon Magnetotransport Properties. (2008).

155. Pelosato, R., Cordaro, G., Stucchi, D., Cristiani, C. & Dotelli, G. Cobalt based layered perovskites as cathode material for intermediate temperature Solid Oxide Fuel Cells: A brief review. *J. Power Sources* **298**, 46–67 (2015).

156. Nakajima, T., Ichihara, M. & Ueda, Y. New A-site Ordered Perovskite Cobaltite $LaBaCo_2O_6$: Synthesis, Structure, Physical Property and Cation Order–Disorder Effect. doi:10.1143/JPSJ.74.1572.

157. Bernuy-Lopez, C., Høydalsvik, K., Einarsrud, M.-A. & Grande, T. Effect of A-Site Cation Ordering on Chemical Stability, Oxygen Stoichiometry and Electrical Conductivity in Layered $LaBaCo_2O_{5+\delta}$ Double Perovskite. *Mater. (Basel, Switzerland)* **9**, (2016).

158. Marshenya, S. N. *et al.* Improved structural stability, electron transport and defect formation in $PrBaCo_2AlO_{6-\delta}$. *J. Alloys Compd.* **767**, 1041–1047 (2018).

159. Momma, K. & Izumi, F. VESTA 3 for three-dimensional visualization of crystal, volumetric and morphology data. *J. Appl. Crystallogr.* **44**, 1272–1276 (2011).

160. Kim, J.-H. & Manthiram, A. $LnBaCo_2O_{5+\delta}$ Oxides as Cathodes for Intermediate-Temperature Solid Oxide Fuel Cells. *J. Electrochem. Soc.* **155**, B385 (2008).

161. Zhang, K., Ge, L., Ran, R., Shao, Z. & Liu, S. Synthesis, characterization and evaluation of cation-ordered $LnBaCo_2O_{5+\delta}$ as materials of oxygen permeation membranes and cathodes of SOFCs. *Acta Mater.* **56**, 4876–4889 (2008).

162. Zhao, H. *et al.* Electrochemical performance of $Pr_{1-x}Y_xBaCo_2O_{5+\delta}$ layered perovskites as cathode materials for intermediate-temperature solid oxide fuel cells. *Int. J. Hydrogen Energy* **38**, 16365–16372 (2013).

163. Kim, J. H. & Manthiram, A. Layered $LnBaCo_2O_{5+\delta}$ perovskite cathodes for solid oxide fuel cells: an overview and perspective. *J. Mater. Chem. A* **3**, 24195–24210 (2015).

164. Gao, Z., Mogni, L. V., Miller, E. C., Railsback, J. G. & Barnett, S. A. A perspective on low-temperature solid oxide fuel cells. *Energy Environ. Sci.* **9**, 1602–1644 (2016).

165. Maignan, A., Martin, C., Pelloquin, D., Nguyen, N. & Raveau, B. Structural and Magnetic Studies of Ordered Oxygen-Deficient Perovskites$LnBaCo_2O_{5+\delta}$, Closely Related to the "112" Structure. *J. Solid State Chem.* **142**, 247–260 (1999).

166. Søgaard, M., Hendriksen, P. V., Mogensen, M., Poulsen, F. W. & Skou, E. Oxygen nonstoichiometry and transport properties of strontium substituted lanthanum cobaltite. *Solid State Ionics* **177**, 3285–3296 (2006).

167. Garcés, D., Leyva, A. G. & Mogni, L. V. High temperature transport properties of $La_{0.5-x}Pr_xBa_{0.5}CoO_{3-\delta}$ perovskite (x = 0, 0.2, 0.5). *Solid State Ionics* **347**, 115239 (2020).

168. Suntsov, A. Y., Leonidov, I. A., Patrakeev, M. V. & Kozhevnikov, V. L. High-temperature electron–hole transport in $PrBaCo_2O_{5+\delta}$. *J. Solid State Chem.* **184**, 1951–1955 (2011).

169. Grimaud, A. *et al.* Double perovskites as a family of highly active catalysts for oxygen evolution in alkaline solution. *Nat. Commun. 2013 41* **4**, 1–7 (2013).

170. Vøllestad, E., Schrade, M., Segalini, J., Strandbakke, R. & Norby, T. Relating defect chemistry and electronic transport in the double perovskite $Ba_{1-x}Gd_{0.8}La_{0.2+x}Co_2O_{6-\delta}$ (BGLC). *J. Mater. Chem. A* **5**, 15743–15751 (2017).

171. Telegin, S. V., Zuev, A. Y., Naumov, S. V., Patrakov, E. I. & Tsvetkov, D. S. Synthesis, Single Crystal Growth, and Properties of Cobalt Deficient Double Perovskite $EuBaCo_{2-x}O_{6-\delta}$ (x = 0-0.1). *J. Chem.* **2017**, (2017).

172. Martin A Maignan, C., Pelloquin, D., Nguyen, N. & Raveau, B. Magnetoresistance in the oxygen deficient $LnBaCo_2O_{5.4}$ (Ln=Eu, Gd) phases. *Appl. Phys. Lett.* **71**, 1421 (1998).

173. Wang, Y. *et al.* Oxygen isotope effect on metal–insulator transition in layered cobaltites$RBaCo_2O_{5.5}$ (R = Pr,Dy, Ho and Y). *J. Phys. Condens. Matter* **17**, 5813 (2005).

174. Antipinskaya, E. A., Marshenya, S. N., Politov, B. V. & Suntsov, A. Y. The interplay of oxygen non-stoichiometry and defects in Ga-doped layered cobaltites. *Solid State Ionics* **339**, 115002 (2019).

175. Tsvetkov, D. S., Sereda, V. V. & Zuev, A. Y. Defect structure and charge transfer in the double perovskite $GdBaCo_2O_{6-\delta}$. *Solid State Ionics* **192**, 215–219 (2011).

176. Suntsov, A. Y., Politov, B. V., Leonidov, I. A., Patrakeev, M. V. & Kozhevnikov, V. L. Improved stability and defect structure of yttrium doped cobaltite $PrBaCo_2O_{6-\delta}$. *Solid State Ionics* **295**, 90–95 (2016).

177. Parfitt, D., Chroneos, A., Tarancón, A. & Kilner, J. A. Oxygen ion diffusion in cation ordered/disordered $GdBaCo_2O_{5+\delta}$. *J. Mater. Chem.* **21**, 2183–2186 (2011).

178. Chen, Y. C., Yashima, M., Peña-Martínez, J. & Kilner, J. A. Experimental visualization of the diffusional pathway of oxide ions in a layered perovskite-type cobaltite PrBaCo2O5+δ. *Chem. Mater.* **25**, 2638–2641 (2013).

179. Hu, Y. *et al.* Oxygen diffusion mechanism in the mixed ion-electron conductor $NdBaCo_2O_{5+x}$ †. *J. Mater. Chem* **22**, 18744 (2012).

180. Zhukov, V. P. *et al.* Structural stability, defects and competitive oxygen migration in $Pr_{1-x}Y_xBaCo_2O_{6-\delta}$. *Solid State Ionics* **347**, (2020).

181. Løken, A., Ricote, S. & Wachowski, S. Thermal and Chemical Expansion in Proton Ceramic Electrolytes and Compatible Electrodes. *Crystals* **8**, 365 (2018).

182. Bai, S., Zhang, N., Gao, C. & Xiong, Y. Defect engineering in photocatalytic materials. *Nano Energy* **53**, 296–336 (2018).

183. Jangizehi, A., Schmid, F., Besenius, P., Kremer, K. & Seiffert, S. Defects and defect engineering in Soft Matter. *Soft Matter* **16**, 10809–10859 (2020).

184. Merkulov, O. V. *et al.* Oxygen nonstoichiometry and defect chemistry of perovskite-structured $SrFe_{1-x}Mo_xO_{3-\delta}$ solid solutions. *Solid State Ionics* **292**, 116–121 (2016).

185. Kröger, F. A. & Vink, H. J. Relations between the Concentrations of Imperfections in Crystalline Solids. *Solid State Phys. - Adv. Res. Appl.* **3**, 307–435 (1956).

186. Kroger, F. A. Defect Chemistry in Crystalline Solids. *http://dx.doi.org/10.1146/annurev.ms.07.080177.002313* **7**, 449–475 (2003).

187. Smyth, D. M. *The Defect Chemistry of Metal Oxides*. *System* (Oxford University Press, 2000).

188. Kreuer, K. D. Proton conductivity: Materials and applications. *Chem. Mater.* **8**, 610–641 (1996).

189. Poetzsch, D., Merkle, R. & Maier, J. Proton uptake in the H+-SOFC cathode material $Ba_{0.5}Sr_{0.5}Fe_{0.8}Zn_{0.2}O_{3-\delta}$: transition from hydration to hydrogenation with increasing oxygen partial pressure. *Faraday Discuss.* **182**, 129–143 (2015).

190. Grimaud, A. *et al.* Hydration Properties and Rate Determining Steps of the Oxygen Reduction Reaction of Perovskite-Related Oxides as H + -SOFC Cathodes . *J. Electrochem. Soc.* **159**, B683–B694 (2012).

191. Klyndyuk, A. I., Chizhova, E. A., Kharytonau, D. S. & Medvedev, D. A. Layered Oxygen-Deficient Double Perovskites as Promising Cathode Materials for Solid Oxide Fuel Cells. *Mater. 2022, Vol. 15, Page 141* **15**, 141 (2021).

192. Strandbakke, R. *et al.* Gd- and Pr-based double perovskite cobaltites as oxygen electrodes for proton ceramic fuel cells and electrolyser cells. *Solid State Ionics* **278**, 120–132 (2015).

193. Pang, S. *et al.* Characterization of cation-ordered perovskite oxide $LaBaCo_2O_{5+\delta}$ as cathode of intermediate-temperature solid oxide fuel cells. *Int. J. Hydrogen Energy* **37**, 6836–6843 (2012).

194. Tsvetkov, D. S. *et al.* Double perovskites $REBaCo_{2-x}M_xO_{6-\delta}$ (RE=La, Pr, Nd, Eu, Gd, Y; M=Fe, Mn) as energy-related materials: An overview. *Pure Appl. Chem.* **91**, 923–940 (2019).

195. Bernuy-Lopez, C., Høydalsvik, K., Einarsrud, M.-A. & Grande, T. Effect of A-Site Cation Ordering on Chemical Stability, Oxygen Stoichiometry and Electrical Conductivity in Layered $LaBaCo_2O_{5+\delta}$ Double Perovskite. *Materials (Basel).* **9**, 154 (2016).

196. Pralong, V., Caignaert, V., Hebert, S., Maignan, A. & Raveau, B. Soft chemistry synthesis and characterizations of fully oxidized and reduced $NdBaCo_2O_{5+\delta}$ phases $\delta = 0, 1$. *Solid State Ionics* **177**, 1879–1881 (2006).

197. Strandbakke, R. *et al.* Gd-and Pr-based double perovskite cobaltites as oxygen electrodes for proton ceramic fuel cells and electrolyser cells. *Solid State Ionics* **278**, 120–132 (2015).

198. Goupil, G., Delahaye, T., Sala, B., Lefebvre Joud, F. & Gauthier, G. Selection and

study of basic layered cobaltites as mixed ionic–electronic conductors for proton conducting fuel cells. *Solid State Ionics* **263**, 15–22 (2014).

199. Leonard, K., Druce, J., Thoreton, V., Kilner, J. A. & Matsumoto, H. Exploring mixed proton/electron conducting air electrode materials in protonic electrolysis cell. *Solid State Ionics* **319**, 218–222 (2018).

200. Brieuc, F., Dezanneau, G., Hayoun, M. & Dammak, H. Proton diffusion mechanisms in the double perovskite cathode material $GdBaCo_2O_{5.5}$: A molecular dynamics study. *Solid State Ionics* **309**, 187–191 (2017).

201. Hashimoto, D., Han, D. & Uda, T. Dependence of lattice constant of Ba, Co-contained perovskite oxides on atmosphere, and measurements of water content. *Solid State Ionics* **262**, 687–690 (2014).

202. Téllez Lozano, H., Druce, J., Cooper, S. J. & Kilner, J. A. Double perovskite cathodes for proton-conducting ceramic fuel cells: are they triple mixed ionic electronic conductors? *Sci. Technol. Adv. Mater.* **18**, 977–986 (2017).

203. Goupil, G., Delahaye, T., Sala, B., Lefebvre Joud, F. & Gauthier, G. Selection and study of basic layered cobaltites as mixed ionic–electronic conductors for proton conducting fuel cells. *Solid State Ionics* **263**, 15–22 (2014).

204. Malyshkin, D. *et al.* The origin of triple conductivity and water uptake in layered double perovskites: A case study on lanthanum-substituted $GdBaCo_2O_{6-\delta}$. *J. Alloys Compd.* **845**, 156309 (2020).

205. Kreuer, K. -D, Rabenau, A. & Weppner, W. Vehicle Mechanism, A New Model for the Interpretation of the Conductivity of Fast Proton Conductors. *Angew. Chemie Int. Ed. English* **21**, 208–209 (1982).

206. Marrony, M. - Proton-Conducting Oxide Materials. *Proton-Conducting Ceram.* 96–195 (2015) doi:10.1201/B18921-5/PROTON-CONDUCTING-OXIDE-MATERIALS-MATHIEU-MARRONY.

207. Mao, Y., Banerjee, S. & Wong, S. S. Hydrothermal synthesis of perovskite nanotubes. *Chem. Commun.* **0**, 408–409 (2003).

208. Wu, L., Mei, X. & Zheng, W. Hydrothermal synthesis and characterization of double perovskite Ba2YSbO6. *Mater. Lett.* **60**, 2326–2330 (2006).

209. Navas, D., Fuentes, S., Castro-Alvarez, A. & Chavez-Angel, E. Review on Sol-Gel Synthesis of Perovskite and Oxide Nanomaterials. *Gels 2021, Vol. 7, Page 275* **7**, 275 (2021).

210. Huízar-Félix, A. M., Hernández, T., de la Parra, S., Ibarra, J. & Kharisov, B. Sol–gel based Pechini method synthesis and characterization of $Sm_{1-x}Ca_xFeO_3$ perovskite $0.1 \leq x \leq 0.5$. *Powder Technol.* **229**, 290–293 (2012).

211. Reis, J. V. *et al.* Synthesis of $CeNb_3O_9$ perovskite by Pechini method. *Mater. Lett.* **227**, 261–263 (2018).

212. Yafarova, L. V. *et al.* Sol–gel synthesis and investigation of catalysts on the basis of perovskite-type oxides $GdMO_3$ (M = Fe, Co). *J. Sol-Gel Sci. Technol.* **92**, 264–272 (2019).

213. Huang, K., Feng, M. & Goodenough, J. B. Sol-Gel Synthesis of a New Oxide-Ion Conductor Sr- and Mg-Doped $LaGaO_3$ Perovskite. *J. Am. Ceram. Soc.* **79**, 1100–1104 (1996).

214. Algueró, M., Ricote, J. & Castro, A. Mechanosynthesis and Thermal Stability of Piezoelectric Perovskite $_{0.92}Pb(Zn_{1/3}Nb_{2/3})O_3$–$0.08PbTiO_3$ Powders. *J. Am. Ceram. Soc.* **87**, 772–778 (2004).

215. Zyryanov, V. V. *et al.* Mechanosynthesis of complex oxides with fluorite and perovskite-related structures and their sintering into nanocomposites with mixed ionic–electronic conductivity. *Solid State Ionics* **176**, 2813–2818 (2005).

216. Evans, J. X-Ray Absorption Spectroscopy for the Chemical and Materials Sciences. *X-Ray Absorpt. Spectrosc. Chem. Mater. Sci.* (2018) doi:10.1002/9781118676165.

217. Ermrich, M. & Opper, D. *XRD for the analyst - Getting acquainted with the principle*. (PANalytical GmbH, 2013).

218. Clearfield, A., Reibenspies, J. H. & Bhuvanesh, N. Principles and Applications of Powder Diffraction. *Princ. Appl. Powder Diffr.* 1–386 (2009) doi:10.1002/9781444305487.

219. Pecharsky, V. K. & Zavalij, P. Y. Fundamentals of powder diffraction and structural characterization of materials. *Fundam. Powder Diffr. Struct. Charact. Mater.* 1–741 (2005) doi:10.1007/978-0-387-09579-0.

220. Powder Diffraction. *Powder Diffr.* (2008) doi:10.1039/9781847558237.

221. Sun, H. & Zhou, W. Progress on X-ray Absorption Spectroscopy for the Characterization of Perovskite-Type Oxide Electrocatalysts. *Energy & Fuels* **35**, 5716–5737 (2021).

222. van Bokhoven, J. A. & Lamberti, C. X-Ray Absorption and X-Ray Emission Spectroscopy: Theory and Applications. *X-Ray Absorpt. X-Ray Emiss. Spectrosc. Theory Appl.* **1**–**2**, 1–845 (2015).

223. Henke, B. L., Gullikson, E. M. & Davis, J. C. X-Ray Interactions: Photoabsorption, Scattering, Transmission, and Reflection at E = 50-30,000 eV, Z = 1-92. *At. Data Nucl. Data Tables* **54**, 181–342 (1993).

224. Dyadkin, V., Pattison, P., Dmitriev, V. & Chernyshov, D. A new multipurpose diffractometer PILATUS@SNBL. *urn:issn:1600-5775* **23**, 825–829 (2016).

225. Abdala, P. M., Mauroy, H. & Van Beek, W. A large-area CMOS detector for high-energy synchrotron powder diffraction and total scattering experiments. *J. Appl. Crystallogr.* **47**, 449–457 (2014).

226. Thompson, S. P. *et al.* Beamline I11 at Diamond: A new instrument for high resolution powder diffraction. *Rev. Sci. Instrum.* **80**, 075107 (2009).

227. Kisi, E. H. & Howard, C. J. Applications of Neutron Powder Diffraction. *Appl. Neutron Powder Diffr.* **9780198515944**, 1–504 (2009).

228. Sears, V. F. Neutron scattering lengths and cross sections. *https://doi.org/10.1080/10448639208218770* **3**, 26–37 (2006).

229. Rietveld Refinement. *Rietveld Refinement* (2018)

doi:10.1515/9783110461381/HTML.

230. Goldstein, J. I. *et al.* Electron Beam—Specimen Interactions: Interaction Volume. *Scanning Electron Microsc. X-Ray Microanal.* 1–14 (2018) doi:10.1007/978-1-4939-6676-9_1.

231. Williams, D. B. & Carter, C. B. Transmission electron microscopy: A textbook for materials science. *Transm. Electron Microsc. A Textb. Mater. Sci.* 1–760 (2009) doi:10.1007/978-0-387-76501-3.

232. Ilyin, A. M. Auger Electron Spectroscopy A2 - Thomas, Sabu. *Micro Nano Technol.* 363–381 (2017).

233. Goldstein, J. I. *et al.* Secondary Electrons. *Scanning Electron Microsc. X-Ray Microanal.* 29–37 (2018) doi:10.1007/978-1-4939-6676-9_3.

234. Goldstein, J. I. *et al.* Backscattered Electrons. *Scanning Electron Microsc. X-Ray Microanal.* 15–28 (2018) doi:10.1007/978-1-4939-6676-9_2.

235. Goldstein, J. I. *et al.* X-Rays. *Scanning Electron Microsc. X-Ray Microanal.* 39–63 (2018) doi:10.1007/978-1-4939-6676-9_4.

236. Goldstein, J. I. *et al.* Cathodoluminescence. *Scanning Electron Microsc. X-Ray Microanal.* 481–489 (2018) doi:10.1007/978-1-4939-6676-9_28.

237. Potapov, P. temDM - Software for TEM in digital micrograph. http://temdm.com/web/ (2019).

238. Weil, J. A. & Bolton, J. R. Electron Paramagnetic Resonance. (2006) doi:10.1002/0470084987.

239. Wongjamras, A., Schlachter, A. S. & Stolte, W. C. Progress of Soft-x-ray Absorption Endstation for Environmental Samples. *Energy Procedia* **9**, 56–62 (2011).

240. Frontera, C., Caneiro, A., Carrillo, A. E., Oró-Solé, J. & García-Muñoz, J. L. Tailoring oxygen content on $PrBaCo_2O_{5+\delta}$ layered cobaltites. *Chem. Mater.* **17**, 5439–5445 (2005).

241. Karvonen, L. *et al.* O-K and Co-L XANES study on oxygen intercalation in parasite $SrCoO_{3-\delta}$. *Chem. Mater.* **22**, 70–76 (2010).

242. Meyiwa, B. Iodometric and Iodimetric Titration Methods. *J. Wet. Heal.* **1**, 5–8 (2020).

243. Conder, K., Pomjakushina, E., Soldatov, A. & Mitberg, E. Oxygen content determination in perovskite-type cobaltates. *Mater. Res. Bull.* **40**, 257–263 (2005).

244. Mielewczyk-Gryń, A. *et al.* Water uptake analysis of acceptor-doped lanthanum orthoniobates. *J. Therm. Anal. Calorim.* **138**, 225–232 (2019).

245. Pouchard, M., Villesuzanne, A. & Doumerc, J. P. Spin state behavior in some cobaltites (III) and (IV) with perovskite or related structure. *J. Solid State Chem.* **162**, 282–292 (2001).

246. Wachowski, S. L. *et al.* Structure and water uptake in $BaLnCo_2O_{6-\delta}$ (Ln =La, Pr, Nd, Sm, Gd, Tb and Dy). *Acta Mater.* **199**, 297–310 (2020).

247. Aksenova, T. V., Gavrilova, L. Y., TsvetkoV, D. S., Voronin, V. I. & CherepanoV,

V. A. Crystal structure and physicochemical properties of layered perovskite-like phases $LnBaCo_2O_{5+\delta}$. *Russ. J. Phys. Chem. A 2011 853* **85**, 427–432 (2011).

248. Taskin, A. A., Lavrov, A. N. & Ando, Y. Fast oxygen diffusion in A-site ordered perovskites. *Prog. Solid State Chem.* **35**, 481–490 (2007).

249. Aksenova, T. V., Gavrilova, L. Y., Yaremchenko, A. A., Cherepanov, V. A. & Kharton, V. V. Oxygen nonstoichiometry, thermal expansion and high-temperature electrical properties of layered $NdBaCo_2O_{5+\delta}$ and $SmBaCo_2O_{5+\delta}$. *Mater. Res. Bull.* **45**, 1288–1292 (2010).

250. Taskin, A. A., Lavrov, A. N. & Ando, Y. Achieving fast oxygen diffusion in perovskites by cation ordering. *Appl. Phys. Lett.* **86**, 091910 (2005).

251. Hu, Z. *et al.* Different look at the spin state of Co^{3+} ions in a CoO_5 pyramidal coordination. *Phys. Rev. Lett.* **92**, 207402 (2004).

252. Sun, H. & Zhou, W. Progress on X-ray Absorption Spectroscopy for the Characterization of Perovskite-Type Oxide Electrocatalysts. *Energy and Fuels* **35**, 5716–5737 (2021).

253. Hu, Z. *et al.* Spin-state order/disorder and metal–insulator transition in $GdBaCo_2O_{5.5}$: experimental determination of the underlying electronic structure. *New J. Phys.* **14**, 123025 (2012).

254. Potze, R. H., Sawatzky, G. A. & Abbate, M. Possibility for an intermediate-spin ground state in the charge-transfer material $SrCoO_3$. *Phys. Rev. B* **51**, 11501 (1995).

255. Guan, D. *et al.* Searching General Sufficient-and-Necessary Conditions for Ultrafast Hydrogen-Evolving Electrocatalysis. *Adv. Funct. Mater.* **29**, 1900704 (2019).

256. Fano, U. Effects of Configuration Interaction on Intensities and Phase Shifts. *Phys. Rev.* **124**, 1866 (1961).

257. Galakhov, V. R. *et al.* Insight into the Electronic States of Co Ions in Octahedra and Pyramids of $EuCaCo_2O_{5.5}$ and $EuBaBo_2O_{5.25}$ Cobaltites Through Soft X-Ray Absorption Spectroscopy. *SSRN Electron. J.* (2022) doi:10.2139/SSRN.4113970.

258. Nemudry, A. & Uvarov, N. Nanostructuring in composites and grossly nonstoichiometric or heavily doped oxides. *Solid State Ionics* **177**, 2491–2494 (2006).

259. Pang, S. L., Jiang, X. N., Li, X. N., Wang, Q. & Zhang, Q. Y. Structural stability and high-temperature electrical properties of cation-ordered/disordered perovskite LaBaCoO. *Mater. Chem. Phys.* **131**, 642–646 (2012).

260. Szpunar, I. *et al.* Electric and magnetic properties of Lanthanum Barium Cobaltite. *J. Am. Ceram. Soc.* **0**, (2019).

261. Mehta, V. V. *et al.* Long-range ferromagnetic order in $LaCoO_{3-\delta}$ epitaxial films due to the interplay of epitaxial strain and oxygen vacancy ordering. *Phys. Rev. B - Condens. Matter Mater. Phys.* **91**, 144418 (2015).

262. Seema, K. & Kumar, R. Effect of Dopant Concentration on Electronic and Magnetic Properties of Transition Metal-Doped ZrO_2. *J. Supercond. Nov. Magn.* **28**, 2735–2742 (2015).

263. Cox-Galhotra, R. A. *et al.* Visualizing oxygen anion transport pathways in $NdBaCo_2O_{5+\delta}$ by in situ neutron diffraction. *J. Mater. Chem. A* **1**, 3091–3100 (2013).

264. Cox-Galhotra, R. A. *et al.* An in-situ neutron diffraction study of the crystal structure of $PrBaCo_2O_{5+\delta}$ at high temperature and controlled oxygen partial pressure. *Solid State Ionics* **249**–**250**, 34–40 (2013).

265. Gilev, A. R., Hossain, A., Kiselev, E. A., Korona, D. V. & Cherepanov, V. A. High-temperature studies on crystal structure, properties and electrochemical performance of $Nd_{0.5}Ba_{0.5}Mn_{0.5}Fe_{0.5}O_{3-\delta}$. *Mater. Lett.* **238**, 298–300 (2019).

266. Mentré, O. *et al.* $BaCoO_{2.22}$: the most oxygen-deficient certified cubic perovskite. *Dalt. Trans.* **44**, 10728–10737 (2015).

267. Norby, T. A Kröger-Vink Compatible Notation for Defects in Inherently Defective Sublattices. *J. Korean Ceram. Soc.* **47**, 19–25 (2010).

268. Korotin, M. *et al.* Intermediate-spin state and properties of $LaCoO_3$. *Phys. Rev. B* **54**, 5309 (1996).

269. Vankó, G., Rueff, J. P., Mattila, A., Németh, Z. & Shukla, A. Temperature- and pressure-induced spin-state transitions in $LaCoO_3$. *Phys. Rev. B - Condens. Matter Mater. Phys.* **73**, 024424 (2006).

270. Taguchi, H. Spin State of Cobalt Ion in $Nd(Cr_{1-x}Co_x)O$=. *J. Solid State Chem.* **122**, 297–302 (1996).

271. Cherepanov, V. A., Aksenova, T. V., Gavrilova, L. Y. & Mikhaleva, K. N. Structure, nonstoichiometry and thermal expansion of the $NdBa(Co,Fe)_2O_{5+\delta}$ layered perovskite. *Solid State Ionics* **188**, 53–57 (2011).

272. Tsvetkov, D. S., Ivanov, I. L., Malyshkin, D. A. & Zuev, A. Y. Oxygen content, crystal structure and chemical expansion of $PrBaCo_{2-x}Fe_xO_{6-\delta}$ double perovskites. *Dalt. Trans.* **43**, 11862–11866 (2014).

273. Tsvetkov, D. S., Sereda, V. V., Malyshkin, D. A., Ivanov, I. L. & Zuev, A. Y. Chemical lattice strain in nonstoichiometric oxides: an overview. *J. Mater. Chem. A* (2022) doi:10.1039/D1TA08407K.

274. Téllez Lozano, H., Druce, J., Cooper, S. J. & Kilner, J. A. Double perovskite cathodes for proton-conducting ceramic fuel cells: are they triple mixed ionic electronic conductors? *http://www.tandfonline.com/action/journalInformation?show=aimsScope&journalCode=tsta20#.VmBmuzZFCUk* **18**, 977–986 (2017).

275. Tsvetkov, M. *et al.* Phase composition and crystal structure determination of cobalt ferrite, modified with Ce, Nd and Dy ions by X-ray and neutron diffraction. *J. Mol. Struct.* **1179**, 233–241 (2019).

276. Poetzsch, D., Merkle, R. & Maier, J. Stoichiometry Variation in Materials with Three Mobile Carriers—Thermodynamics and Transport Kinetics Exemplified for Protons, Oxygen Vacancies, and Holes. *Adv. Funct. Mater.* **25**, 1542–1557 (2015).

277. Poetzsch, D., Merkle, R. & Maier, J. Stoichiometry Variation in Materials with Three Mobile Carriers—Thermodynamics and Transport Kinetics Exemplified for Protons, Oxygen Vacancies, and Holes. *Adv. Funct. Mater.* **25**, 1542–1557 (2015).

278. Miruszewski, T. *et al.* Structure and transport properties of triple-conducting $Ba_xSr_{1-x}Ti_{1-y}Fe_yO_{3-\delta}$ oxides. *RSC Adv.* **11**, 19570–19578 (2021).

279. Zohourian, R., Merkle, R., Raimondi, G. & Maier, J. Mixed-Conducting Perovskites as Cathode Materials for Protonic Ceramic Fuel Cells: Understanding the Trends in Proton Uptake. *Adv. Funct. Mater.* **28**, 1801241 (2018).

280. Bjørheim, T. S., Hoedl, M. F., Merkle, R., Kotomin, E. A. & Maier, J. Proton, Hydroxide Ion, and Oxide Ion Affinities of Closed-Shell Oxides: Importance for the Hydration Reaction and Correlation to Electronic Structure. *J. Phys. Chem. C* **124**, 1277–1284 (2020).

281. Hoedl, M. F., Ertural, C., Merkle, R., Dronskowski, R. & Maier, J. The Orbital Nature of Electron Holes in $BaFeO_3$ and Implications for Defect Chemistry. *J. Phys. Chem. C* (2022) doi:10.1021/ACS.JPCC.2C02545.

List of figures

List of tables

I. Appendix 1

This chapter complements the results presented in chapter 3. For the sake of readability, it was decided not to include all the results, charts and tables in the main text of the thesis. The main text consist of only representative results and graphs, while the rest is placed in this chapter. However, the full set of results was analyzed and discussed in the main text.

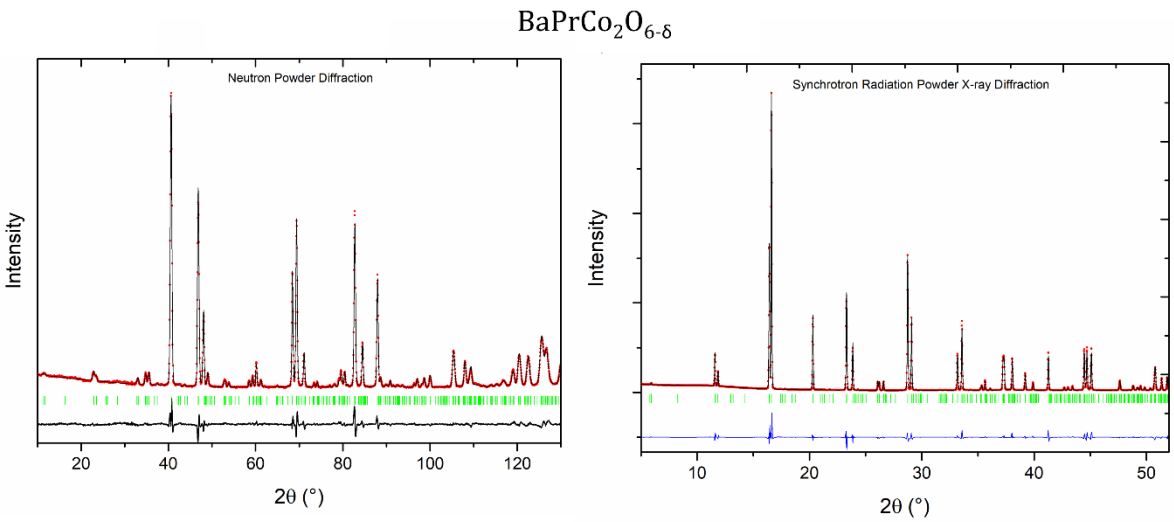

Figure I.1 NPD and SR-PXD patterns of $BaPrCo_2O_{6-\delta}$. Reprinted from Wachowski et al. 2020[246]

Table I.1 Refined structural parameters of orthorhombic $BaPrCo_2O_{6-\delta}$, Wyckoff position, atomic coordinates, and site occupancies

ID	Wyck	Position			Atom	Occ	Layer
		X	Y	Z			
Pr1	*2p*	½	0.2570(4)	½	Pr^{3+}	1	Pr-O
Ba1	*2o*	½	0.2494(4)	0	Ba^{2+}	1	Ba-O
Co1	*2r*	0	½	0.2496(8)	Co^{3+}	1	Co-O
Co2	*2q*	0	0	0.2524(9)	Co^{3+}	1	Co-O
O1a	*1a*	0	0	0	O^{2-}	1	Ba-O
O1b	*1e*	0	½	0	O^{2-}	1	Ba-O
O2a	*2r*	½	0	0.2933(8)	O^{2-}	0.98(2)	Co-O
O2b	*2t*	½	½	0.2702(9)	O^{2-}	1.02(2)	Co-O
O2c	*4u*	0	0.2435(2)	0.2760 (7)	O^{2-}	0.92(2)	Co-O
O3a	*1g*	0	½	½	O^{2-}	0.94(2)	Pr-O
O3b	*1c*	0	0	½	O^{2-}	0.58(2)	Pr-O

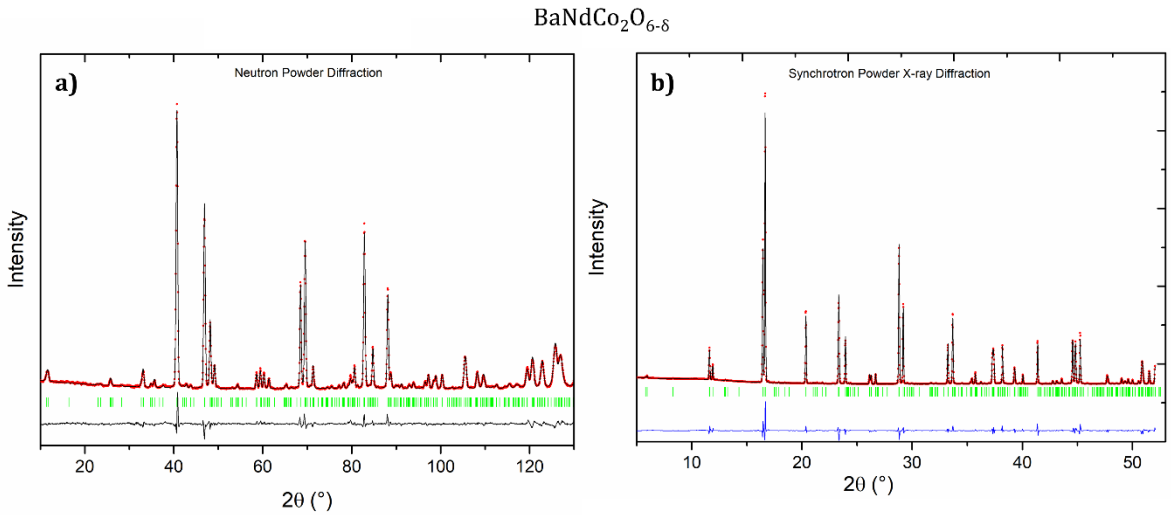

Figure I.2 NPD and SR-PXD patterns of $BaNdCo_2O_{6-\delta}$. Reprinted from Wachowski et al. 2020[246]

Table I.2 Refined structural parameters of orthorhombic $BaNdCo_2O_{6-\delta}$, Wyckoff position, atomic coordinates, and site occupancies

ID	Wyck	Position			Atom	Occ	Layer
		X	Y	Z			
Nd1	*2p*	½	0.2616(6)	½	Nd^{3+}	1	Nd-O
Ba1	*2o*	½	0.2506(8)	0	Ba^{2+}	1	Ba-O
Co1	*2r*	0	½	0.2517(6)	Co^{3+}	1	Co-O
Co2	*2q*	0	0	0.2530(7)	Co^{3+}	1	Co-O
O1a	*1a*	0	0	0	O^{2-}	1	Ba-O
O1b	*1e*	0	½	0	O^{2-}	1	Ba-O
O2a	*2r*	½	0	0.2965(9)	O^{2-}	1.01(2)	Co-O
O2b	*2t*	½	½	0.270(1)	O^{2-}	1.02(2)	Co-O
O2c	*4u*	0	0.2416(5)	0.280(9)	O^{2-}	0.91(1)	Co-O
O3a	*1g*	0	½	½	O^{2-}	0.93(2)	Nd-O
O3b	*1c*	0	0	½	O^{2-}	0.45(1)	Nd-O

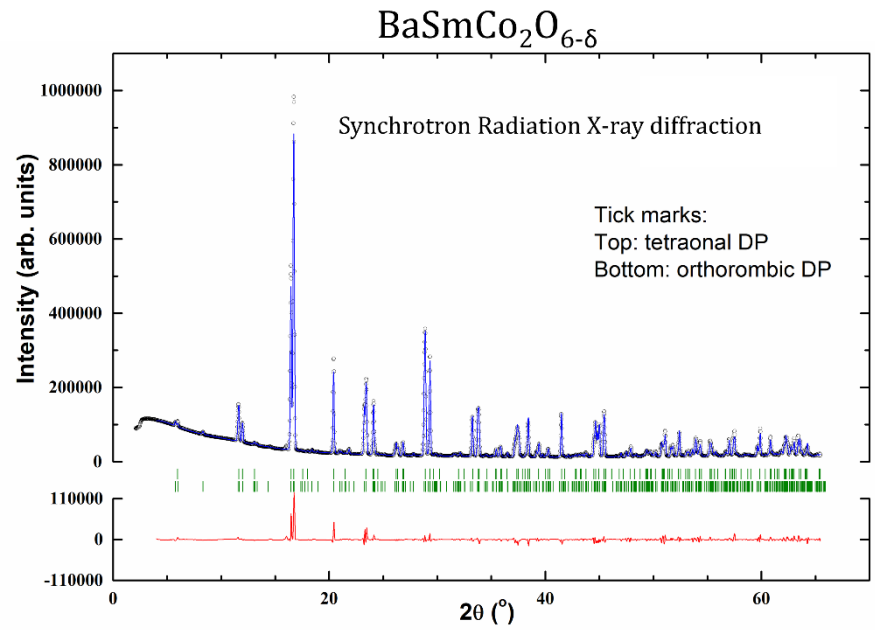

Figure I.3 SR-PXD pattern of $BaSmCo_2O_{6-\delta}$. Reprinted from Wachowski et al. 2020[246]

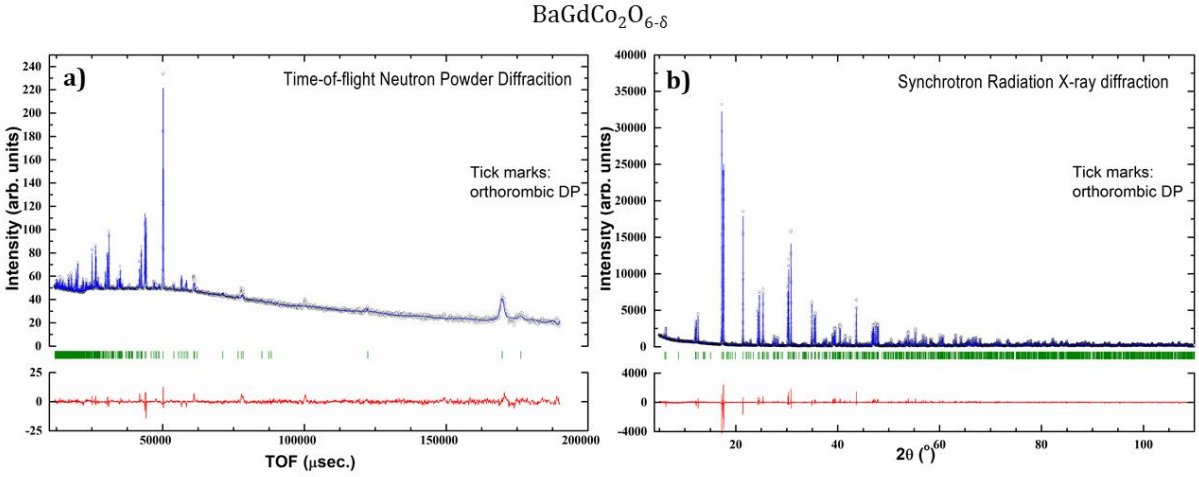

Figure I.4 NPD and SR-PXD patterns of $BaGdCo_2O_{6-\delta}$. Reprinted from Wachowski et al. 2020[246]

Table I.3Refined structural parameters of orthorhombic $BaGdCo_2O_{6-\delta}$, Wyckoff position, atomic coordinates, and site occupancies

ID	Wyck	Position			Atom	Occ	Layer
		X	Y	Z			
Gd1	*2p*	½	0.2722(1)	½	$^{160}Gd^{3+}$	1	Gd-O
Ba1	*2o*	½	0.2500(1)	0	Ba^{2+}	1	Ba-O
Co1	*2r*	0	½	0.2517(3)	Co^{3+}	1	Co-O
Co2	*2q*	0	0	0.2558(3)	Co^{3+}	1	Co-O
O1a	*1a*	0	0	0	O^{2-}	1	Ba-O
O1b	*1e*	0	½	0	O^{2-}	1	Ba-O
O2a	*2r*	½	0	0.3099(6)	O^{2-}	0.99(1)	Co-O
O2b	*2t*	½	½	0.2684(6)	O^{2-}	0.99(1)	Co-O
O2c	*4u*	0	0.2388(4)	0.2940(4)	O^{2-}	0.978(8)	Co-O
O3a	*1g*	0	½	½	O^{2-}	1.00(2)	Gd-O
O3b	*1c*	0	0	½	O^{2-}	0.20(1)	Gd-O

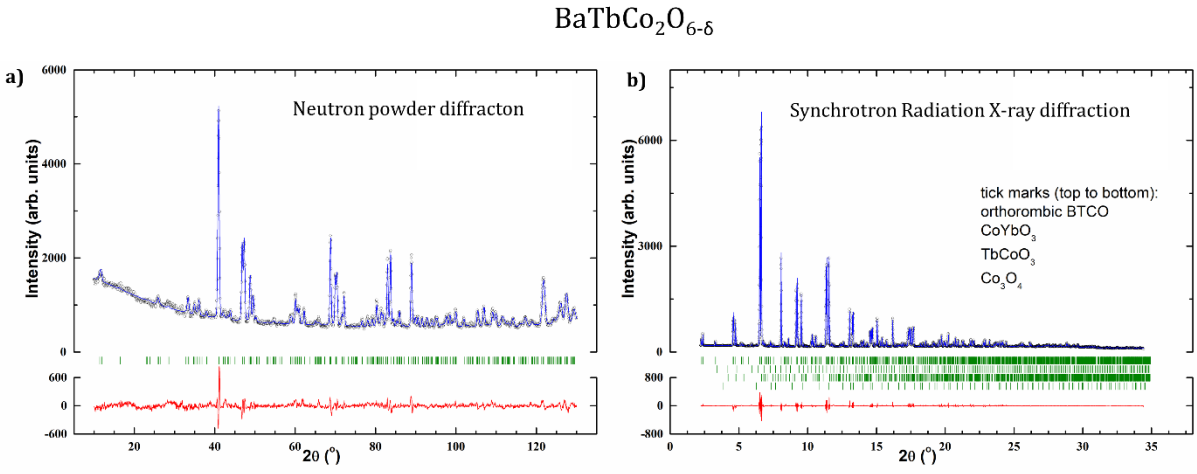

Figure I.5 NPD and SR-PXD patterns of $BaTbCo_2O_{6-\delta}$. Reprinted from Wachowski et al. 2020[246]

Table I.4Refined structural parameters of orthorhombic $BaTbCo_2O_{6-\delta}$, Wyckoff position, atomic coordinates, and site occupancies

ID	Wyck	Position			Atom	Occ	Layer
		X	Y	Z			
Tb1	*2p*	½	0. 2730(1)	½	Tb^{3+}	1	Tb-O
Ba1	*2o*	½	0.2494(1)	0	Ba^{2+}	1	Ba-O
Co1	*2r*	0	½	0.2532(4)	Co^{3+}	1	Co-O
Co2	*2q*	0	0	0.2582(4)	Co^{3+}	1	Co-O
O1a	*1a*	0	0	0	O^{2-}	1	Ba-O
O1b	*1e*	0	½	0	O^{2-}	1	Ba-O
O2a	*2r*	½	0	0.313(1)	O^{2-}	1.00 (1)	Co-O
O2b	*2t*	½	½	0.2723(1)	O^{2-}	1.00 (1)	Co-O
O2c	*4u*	0	0.2371(7)	0.2928(6)	O^{2-}	1.00 (1)	Co-O
O3a	*1g*	0	½	½	O^{2-}	0.95(2)	Tb-O
O3b	*1c*	0	0	½	O^{2-}	0.09(1)	Tb-O

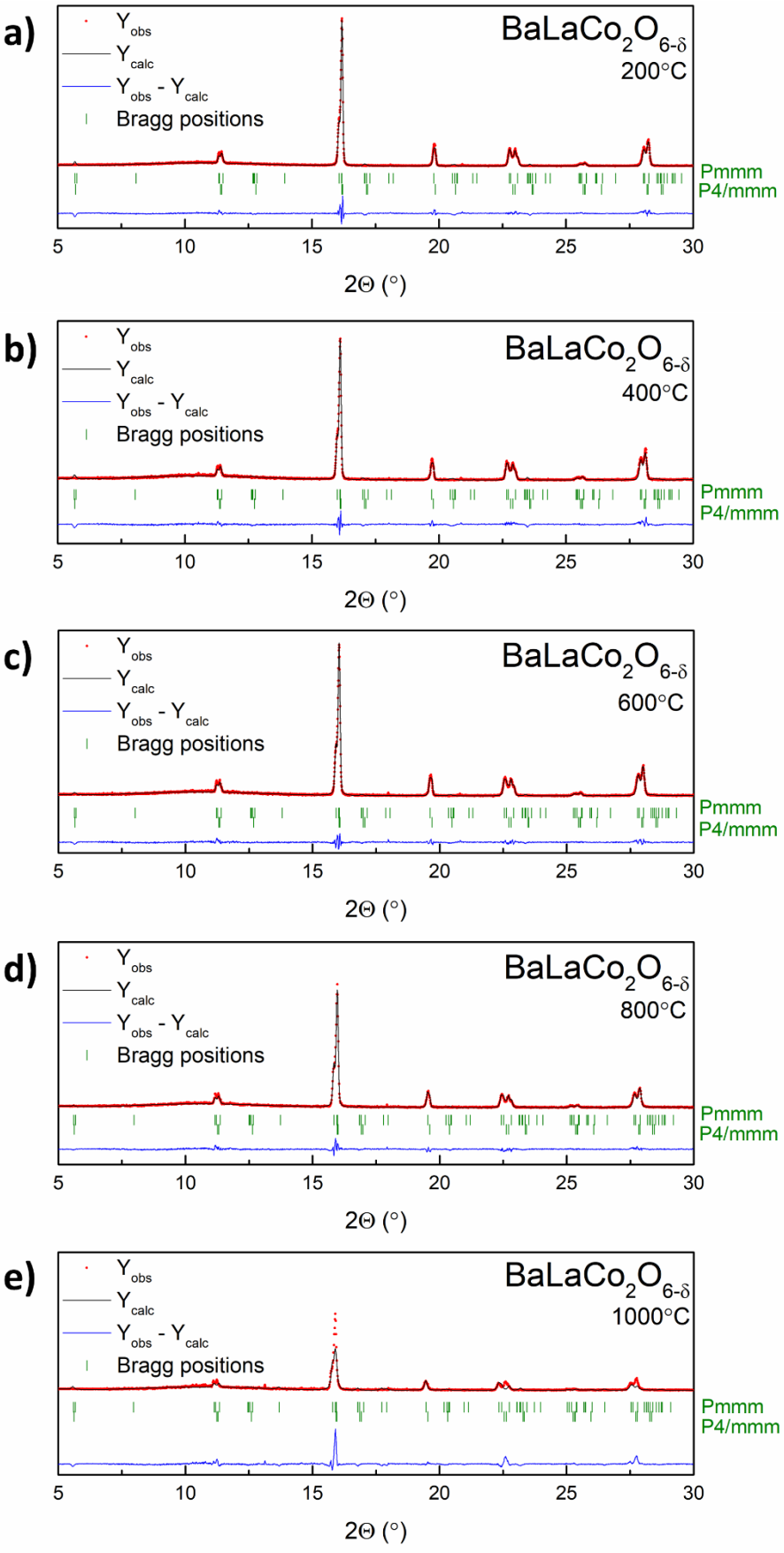

Figure I.6 High-temperature SR-PXD diffraction patterns of $BaLaCo_2O_{6-\delta}$

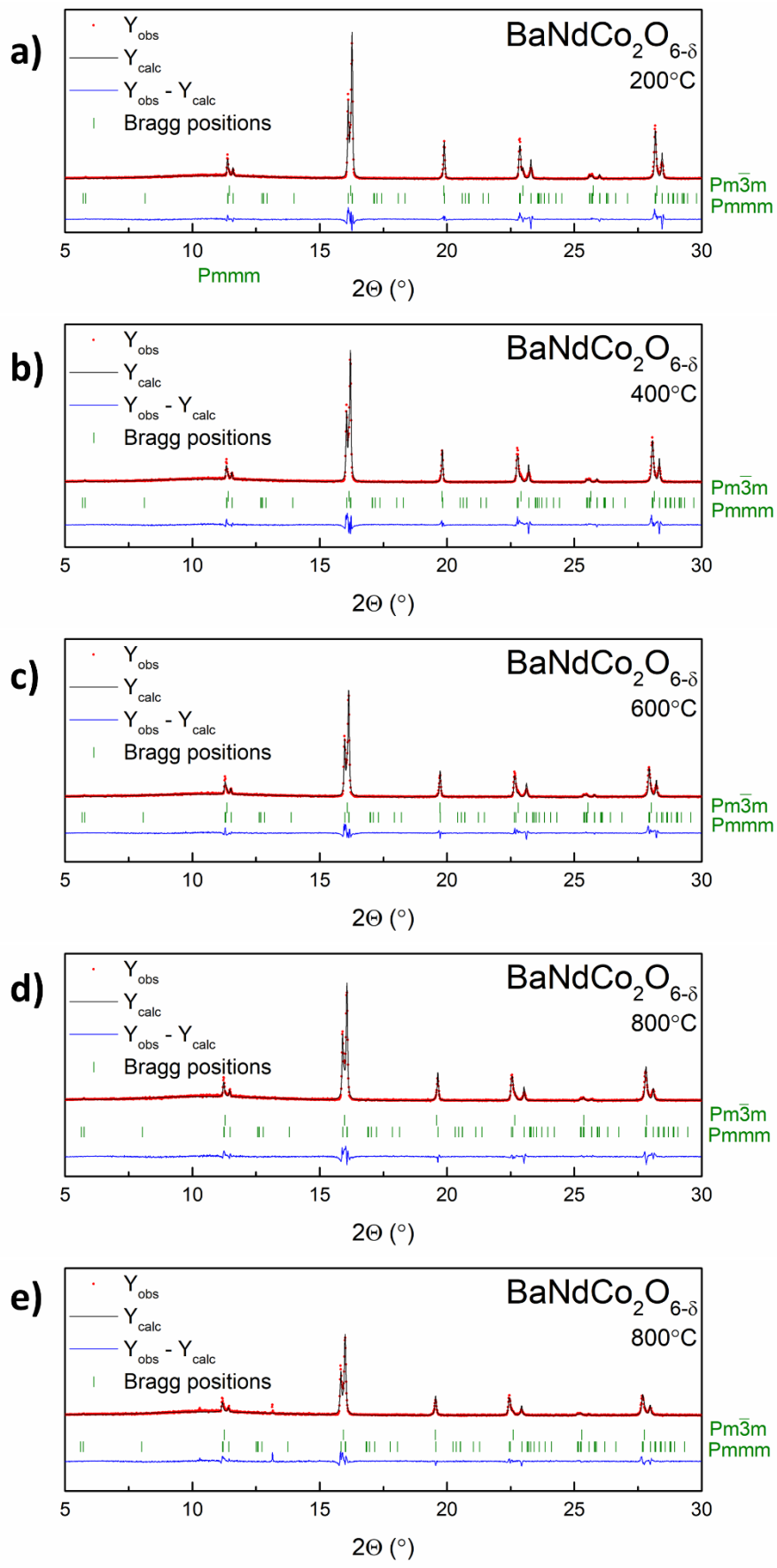

Figure I.7 High-temperature SR-PXD diffraction patterns of $BaNdCo_2O_{6-\delta}$

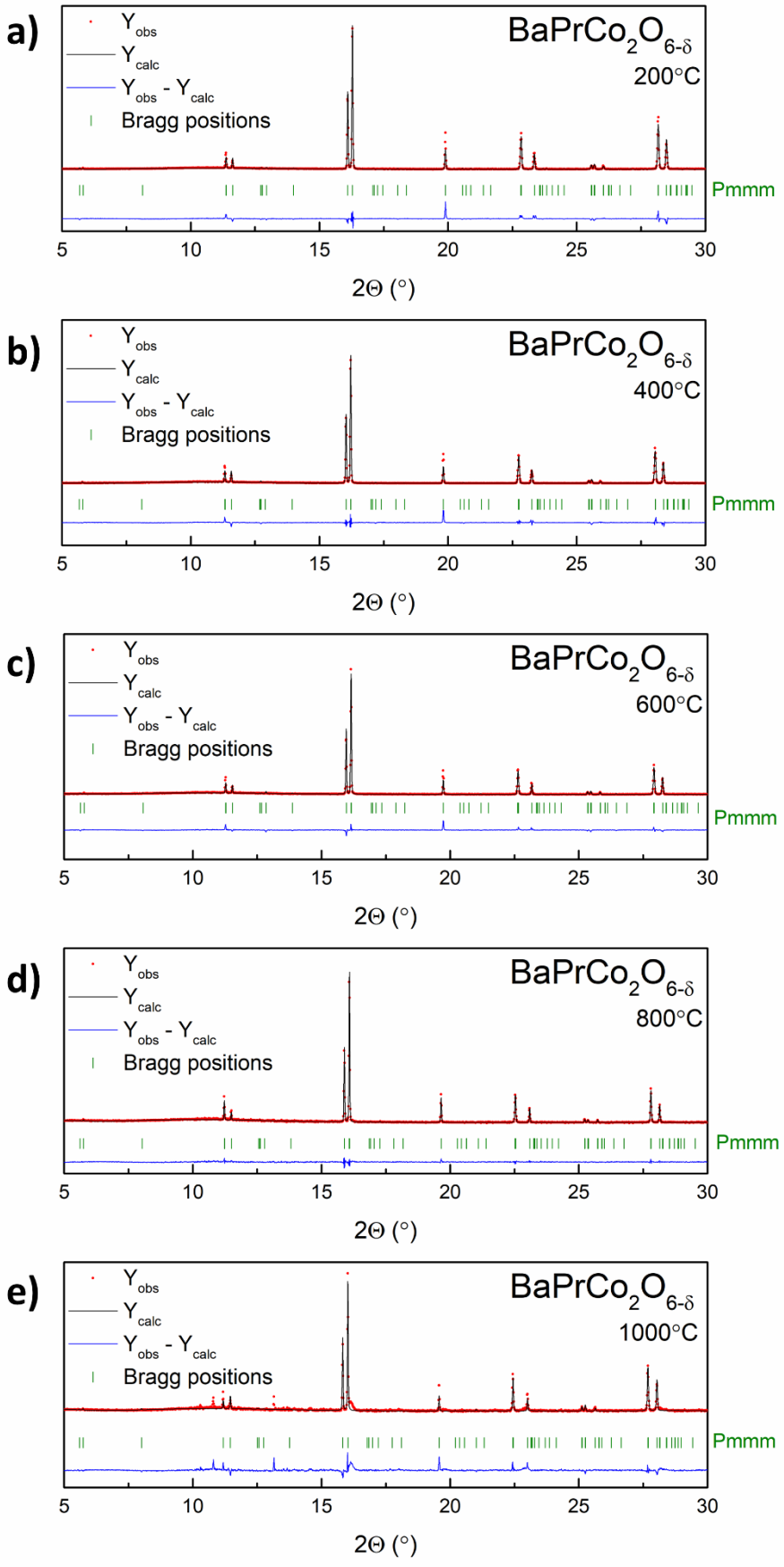

Figure I.8 High-temperature SR-PXD diffraction patterns of $BaPrCo_2O_{6-\delta}$

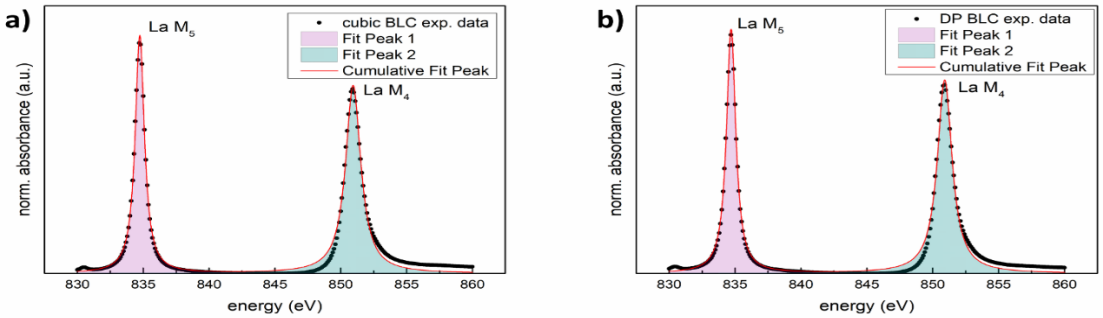

Figure I.9 Deconvolution of La edges of cubic (a) and double perovskite (b) $BaLaCo_2O_{6-\delta}$

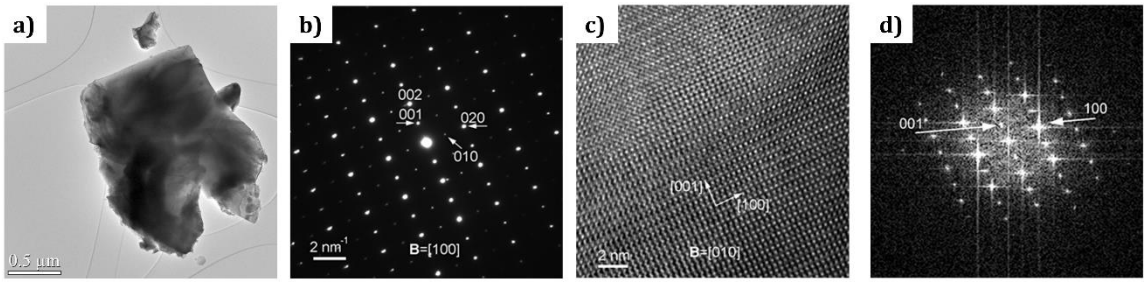

Figure I.10 TEM image (a) and the associated SAED pattern (b) of a BNCO crystal grain oriented along a pseudocubic zone axis; (c) HRTEM image and the associated FFT pattern (d) proving the doubling of the lattice parameter along [001]. Reprinted from Wachowski et al. 2020[246]

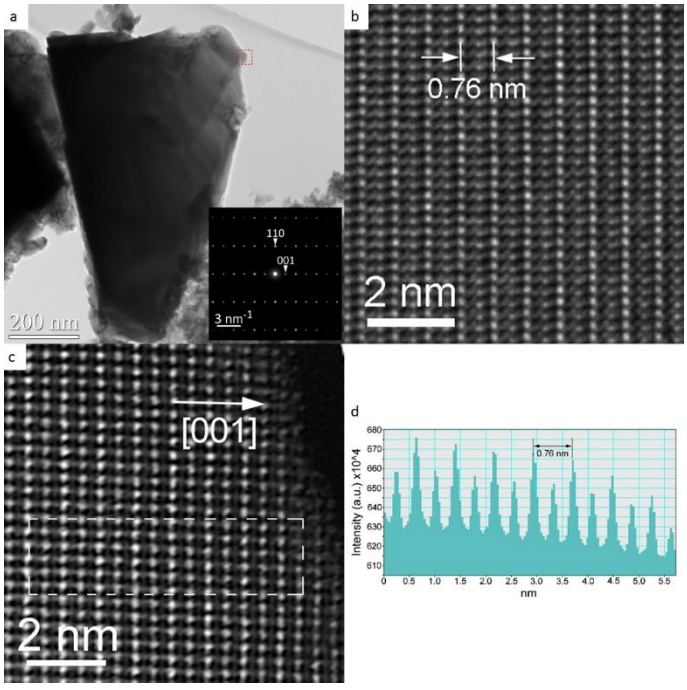

Figure I.11 Low magnification TEM image and the corresponding SAED pattern in the B=[- 110] orientation (inserted) of a typical crystal grain from the sample BaGdCo2O6-δ; (b) HRTEM micrograph from the area marked with a red frame in (a); (c) HAADF-STEM image from the same area; (d) Intensity line profile along the [001] direction inside the dashed-line frame on the HAADF image in (c). Reprinted from Wachowski et al. 2020[246]

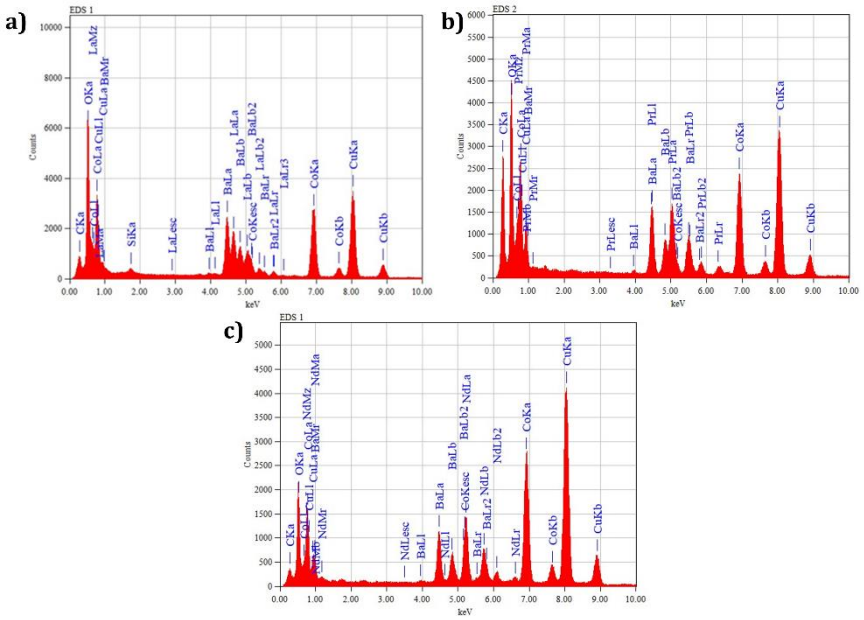

Figure I.12 Elemental composition determined by EDS for BaLaCo2O6-δ (a), BaPrCo2O6-δ (b) and BaNdCo2O6-δ (c). Reprinted from Wachowski et al. 2020[246]

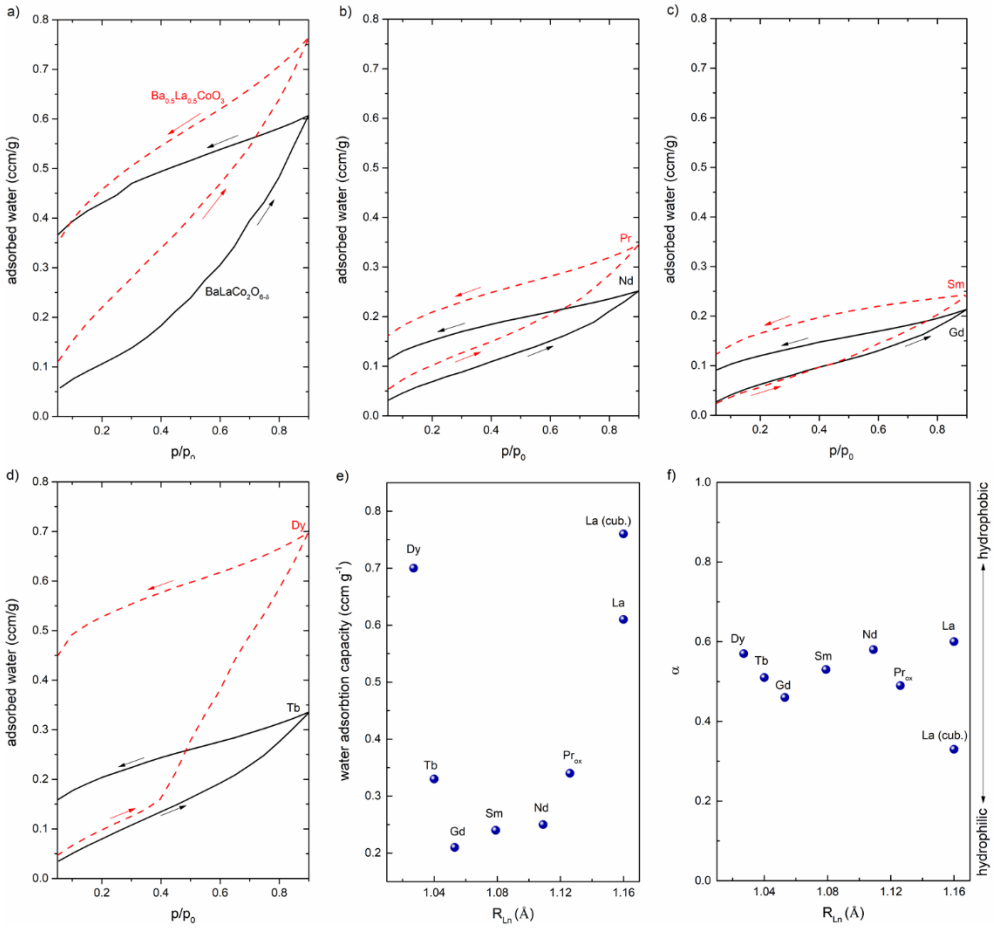

Figure I.13 Water adsorption studies results. Isotherms at room temperature of $Ba_{0.5}La_{0.5}CoO_{3-\delta}$ and $BaLaCo_2O_{6-\delta}$ (a), $BaPrCo_2O_{6-\delta}$ and $BaNdCo_2O_{6-\delta}$ (b), $BaSmCo_2O_{6-\delta}$ and $BaGdCo_2O_{6-\delta}$ (c), $BaTbCo_2O_{6-\delta}$ and $BaDyCo_2O_{6-\delta}$ (d), total volume of water adsorbed at the highest vapour pressure (e) and α parameter plotted as a function of RLn radius (f). Arrows indicate the direction of the process: to the right – sorption, to the left – desorption

II. Appendix 2

The ionic radius of lanthanides decreases with increasing atomic number, as a consequence the difference between barium and lanthanide radii increases. Strain-induced by the mismatch in A-site cations radii causes cations ordering along the c-axis. The distortion from ideal cubic perovskite structure may be parametrized by the classical Goldschmidt tolerance factor t, as well as new tolerance factor τ, introduced by Bartel et al[47]. The greater the deviation of the parameter t from the value equal to 1 the highest deviation from the cubic structure. To calculate the Goldschmidt tolerance factor it is required to know the exact value of each cation ionic radius, which strongly depends on the coordination number and oxidation state[1]. In perovskite structure, A-site cations exhibit 12-fold coordination. Not for all Ln^{3+}, the value of ionic radius for coordination number equal to 12 is reported in the literature, however, there is plenty of data for different CNs. Figure II.1 depicts the relation between the ionic radii and coordination number of each investigated lanthanide. Ionic radius for 12-fold coordination is reported only for La, Nd, and Sm. The ionic radius of the lanthanide increase with the coordination number, but this relation is not linear. This knowledge may be used to extrapolate the ionic radius of the rest lanthanides in 12-fold coordination. Second-order polynomials were fitted to the available data to estimate unavailable values of ionic radii. Table II.1 contains the list of all investigated lanthanides ionic radii. Values marked with * are the estimated ones. Those values were used to calculate the Goldschmidt tolerance factor for all investigated compounds, which are also presented in Table II.1.

The Goldschmidt tolerance factor consists of the geometric relation between ionic radii of A-, B-site cations and anion. In this case, the A-site cation sublattice is half-occupied by barium and lanthanide, thus the A-site cation radius is calculated as an arithmetic average of Ln and Ba radii. Size of cobalt ions changes with not only coordination number and oxidation state, but also the spin state, which is summarised in Table II.2. To check the general trend of the t factor the calculations were carried out for Co^{4+} at a high spin state, and CN = 6. The T parameter calculated in that way decreases with increasing atomic number, getting closer to a value equal to one. This suggests that the smaller lanthanide is introduced to the $BaLnCo_2O_{6-\delta}$, the weaker strain should be, and the structure should be less distorted from the ideal perovskite structure. However, the observed trend is the opposite. The only compound, which adapt the cubic perovskite structure was lanthanum

barium cobaltite. The variable nature of cobalt should also be considered. The average oxidation state of cobalt in cubic BLC is Co_{AVG} = 3.42(9). XAS studies did not reveal the presence of cobalt in the second oxidation state Co^{2+}, thus at room temperature, the B-sublattice consists of the mixture of Co^{3+} and Co^{4+}. What is more, the position of pre-peak at oxygen K-edge indicates the high spin of cobalt. On this basis, the effective Goldschmidt tolerance factor may be calculated. Similarly, to the previous calculation, the effective cobalt ionic radius was calculated as an arithmetic average of Co^{3+} and Co^{4+} at a high spin state. This approach lowers the tolerance factor to t_{eff} = 1.0322. For higher lanthanides calculation of t_{eff} is impossible due to unknown concentration of cobalt at each spin state and lack of data on cobalt ionic radius.

Although, the Goldschmidt tolerance factor, as a simple geometry relation, is widely used as a parameter describing the distortion from cubic perovskite structure, is not applicable in the case of this study. This parameter is too simplified, does not include the A-site cations ordering, and is impossible to be precisely calculated due to the lack of crystallographic data. What is more, the sum of ionic radii may not be a sufficient estimation of the interatomic bond length.

In the literature the new tolerance factor τ was presented. This parameter was described in subsection 2.1.1. The calculation of the τ parameter requires the knowledge of the ionic radius of the cobalt. At room temperature the mixture of Co^{3+} and Co^{4+} occupies the B-sublattice, thus the ionic radius of cobalt can be calculated as the weighted average of Co^{3+} and Co^{4+} ionic radii, in a similar way as shown in the chemical expansion model.

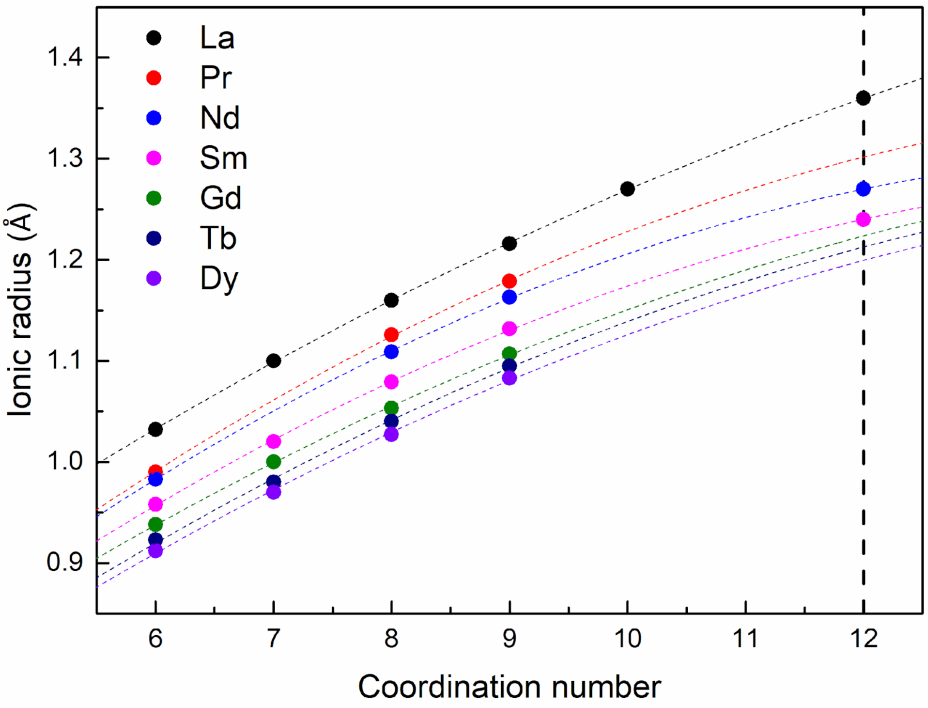

Figure II.1 Relation of ionic radius of lanthanides as a function of coordination number

Table II.1 The list of ionic radii, Goldschmidt parameters, and new tolerance factor τ calculated for $BaLnCo_2O_{6-\delta}$

Ln	**Ionic Radius[153] (Å)**	**t**	**τ**
La	1.36	1.0534	2.95
Pr	1.301*	1.0427	2.96
Nd	1.27	1.0371	2.96
Sm	1.24	1.0317	2.99
Gd	1.223*	1.0286	2.98
Tb	1.212*	1.0266	2.98
Dy	1.199*	1.0242	3.00

Table II.2 Ionic radius of cobalt in 6-fold coordination

Oxidation state	Spin state	Ionic Radius (Å)
Co^{2+}	LS	0.65
	IS	-
	HS	0.745
Co^{3+}	LS	0.545
	IS	-
	HS	0.61
Co^{4+}	LS	-
	IS	-
	HS	0.53

III. Appendix 3

Under nitrogen atmosphere the mass increase was observed even before the atmosphere was switched from dry to wet. In dry atmosphere the mass increase may be attributed to the change in oxygen stoichiometry, while under humidified conditions the mass increase may be related to proton defect formation. Therefore, in order to determine the increase in mass under the influence of a change in the partial pressure of water vapor in the atmosphere, it was necessary to separate these two effects.

For this purpose, the following procedure was used. The exponential function, presented with the equation III.1, was fitted to the data before the atmosphere switch, which is presented in Figure III.1 as a baseline. Then, this base line was subtracted from the measurement data. The fit parameters are presented in Table III.1.

$$y = y_0 + A \cdot e^{R_0 \cdot x} \tag{III.1}$$

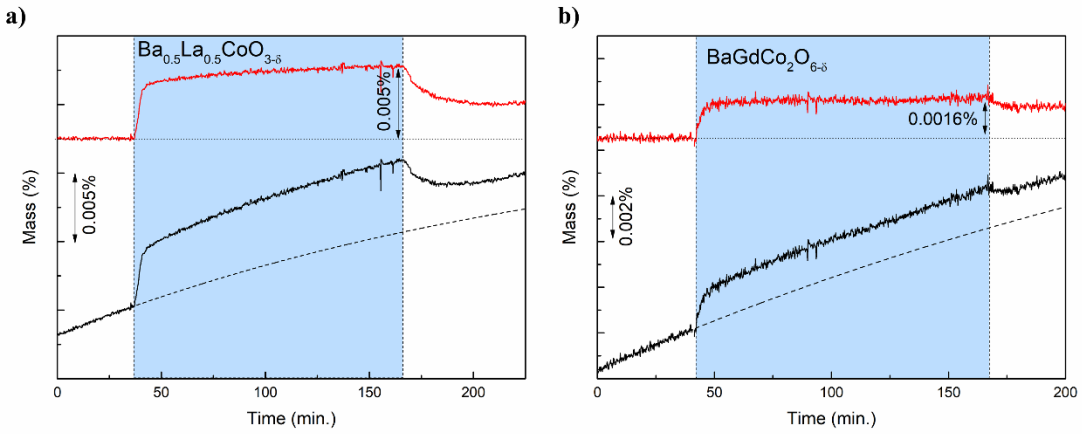

Figure III.1 Water uptake of B (a) and (b). Lower curves show the experimental data with fitted exponential function presented with the dashed line. The upper curves show the data with the subtracted exponent

Table III.1 The exponential fit parameters

	$Ba_{0.5}La_{0.5}CoO_{3-\delta}$	$BaGdCo_2O_{6-\delta}$
y_0	98.1134	98.11774
A	-0.01302	-0.01736
R_0	-0.00356	-0.00265